PHASE TRANSITIONS, MAGNETISM AND SURFACE ADSORPTIONS ASSESSED BY META-GGA FUNCTIONALS AND RANDOM PHASE APPROXIMATION

A Dissertation
Submitted to
the Temple University Graduate Board

In Partial Fulfillment
of the Requirements for the Degree
DOCTOR OF PHILOSOPHY

By

Bing Xiao

Aug 2014

Examining Committee Members:

John P. Perdew, Advisory Chair, Department of Physics

Adrienn Ruzsinszky, Department of Physics

Xifan Wu, Department of Physics

Tan Yuen, Department of Physics

Jianmin Tao, Department of Chemistry, University of Pennsylvania

ProQuest LLC.
789 East Eisenhower Parkway
P.O. Box 1346
Ann Arbor, MI 48106 - 1346

ABSTRACT

The meta-GGA functionals and random phase approximation are tested for phase transitions and a strongly correlated transition metal oxide in this dissertation. One of the latest meta-GGA functionals is also employed to study the van der Waals bound system in surface science. Our main purpose is to reveal the performance of new exchange-correlation functionals on various properties and systems. We are also interested in seeking the possible relationship between the performance of a semilocal functional and its exchange enhancement factor.

We have studied the structural phase transitions in crystalline Si (insulator to metal), SiO_2 (insulator to insulator) and Zr (metal to metal) systems, as a test of exchange energy semilocal functionals on Jacob's ladder. Our results confirm the energy-geometry delimma of GGAs in three systems. The most sophisticated non-empirical meta-generalized gradient approximations (meta-GGAs) such as TPSS (Tao-Perdew-Staroveov-Scuseria) and revTPSS (revised TPSS) give better lattice constants than PBE, but the phase transition parameters (energy difference and transition pressure) are smaller and less realistic than those from the latter GGA. However, the recent functionals of meta-GGA made simple family (MGGA_MS) behave differently to those previous meta-GGAs, predicting larger and more realistic phase transition parameters. Meanwhile, MGGA_MS also delivers the equilibrium geometry of crystalline materials similar to previous non-empirical meta-GGAs.

In contrast to semilocal functionals, the nonlocal functionals such as the range-separated hybrid functional HSE06 (Heyd-Scuseria-Ernzerhof) and non-self consistent

random phase approximation (RPA) are not only able to give the accurate equilibrium geometry , but also predict the realistic phase transition parameters for Si and SiO_2 systems.

The ground state of rutile-type vanadium dioxide (R-VO_2) represents a great challenge to the current density functional theory. In this dissertation, we investigated the electronic structures and magnetism of R-VO_2 using exchange-correlation functionals of all five rungs on Jacob's ladder. Our calculations show that all semilocal functionals (LSDA, GGAs and meta-GGAs) and hybrid functionals (HSE06) stabilize the spin-polarized states (ferromagnetic and anti-ferromagnetic states) over non-magentic state, which are completely opposite to experimental observation. Suprisingly, LSDA gives the best energetic descriptions for magnetic and non-magnetic phases of R-VO_2 among semilocal functionals and HSE06. Othwerwise, RPA calculations are highly dependent on the inputs in the spin polarized case. With PBE inputs, RPA also fails, giving lower energies for spin-polarized states than for the non-magnetic phase. Meawhile, the results are reversed using LSDA inputs. From the computed equilibrium cell volume, we observe the error cancellation in the exchange-correlation hole of most semilocal functionals in the spin-polarized calculations. LSDA and RPA do not fit to this picture. By analyzing the local magnetic moments of vanadium atoms, it is found that the magnetic property predicted from meta-GGA can be related to its exchange enhancement factor.

The physisorption of a molecule on a transition metal surface is also another difficult problem in DFT because of the long-range van der Waals interactions. The recently developed MGGA_MS family of density functionals is able to capture a portion

of intermediate range dispersion interactions. Therefore, we employed MGGA_MS2 to study the physisorption of CO_2 on Pt (111) surface, and the results are compared to those of PBE, PBE+D2 and optB88-vdW methods. The computed binding curves comfirm that that MGGA_MS2 indeed captures the van der Waals interactions near the equilibrium binding distance, and the obtained binding distance is also in good agreement with PBE+D2 and optB88-vdW calculations. By computing the electron density difference map (EDDM), we find that the electron densities of CO_2 and Pt (111) surface are strongly polarized in optB88-vdW, creating the dipole moments in two subsystems. Such effect is reduced in MGGA_MS2. For PBE, the polarization of electron density is very weak, but not negligible. The α dependence in the exchange enhancement factor of a meta-GGA is the key to capture the intermediate range van der Waals interactions.

In summary, a meta-GGA functional can step out of the famous "energy-geometry dilemma" , predicting good lattice constants and phase transition parameters at the same time. With the proper construction, a meta-GGA can even capture a portion of van der Waals interactions. The RPA is usually more accurate than semilocal functionals for many ground state properties. The strongly correlated systems like R-VO_2 are still a big challenge to present-day density functional theory. We will continue to seek more accurate exchange-correlation functionals.

ACKNOWLEDGMENTS

First of all, I want to thank my advisor Prof John P. Perdew who has very kindly provided the opportunity for me to work with him. Although I have been mainly working on the testing of different density functionals on the solids rather than developing the new density functional method, I still learned a lot about the theories of exchange-correlation functionals by his enlightenment. This knowledge will definitely benefit my future research in related fields.

In particular, I would also like to thank Prof Adrienn Rusinszky and Prof Jianwei Sun at Temple University. They enlightened me a lot in my research projects. Most importantly, with their generous help, I was able to solve the hardware and software problems in the numerical calculations, and which are crucial to my Ph.D research. Many thanks also to Jianmin Tao (University of Pennsylvania) , Pan Hao (Tulane University), Yuan Fang (Tulane University) and Hongwei Wang (Temple University), we had a lot of interesting discussions about the various topics in physics and computational materials sciences.

Prof Theodore W. Burkhardt and Prof Rongjia Tao at Temple University should be specifically acknowledged. Without their efforts on paperwork, I would not have been able to successfully transfer to Temple University in the summer of 2013 quickly and smoothly.

Special thanks to my colloborators Jing Feng (Harvard University), Yefei Li (Xi'an Jiaotong University) and Yingchun Ding (Chendu University of Information Technology) . We worked on several interesting areas in the past several years. These

fruitful colloborations greatly extended my knowledge from pure theoretical physics to the colorful applications.

Also, many thanks to Physics Department at Tulane University, I spent a lot of good time there during my Ph.D study from 2010 to 2013, and their crawfish festival reminds me many sweet moments in New Orleans. I also want to acknowledge the Department of Physics at Temple University for their great support, allowing me to complete my research and earn the degree.

Finally, I truly appreciate my wife Chunting, who accompanied me for most of my graduate career. My extremely supportive parents, parents-in-law and brother also deserve a lot of thanks from me.

TABLE OF CONTENTS

Page

LIST OF TABLES

LIST OF FIGURES

CHAPTER 1

DENSITY FUNCTIONAL THEORY

In 1929, Paul Dirac made a famous statement about the status of quantum mechanics at that time. In the paper entitled "Quantum mechanics of many-electron systems", he wrote down the following famous words [1]:

"The general theory of quantum mechanics is now complete… The underlying physical laws necessary for the mathematical theory of a large part of physics and the whole of chemistry are thus completely known."

1.1 Many-Body Hamiltonian

In quantum mechanics, all possible interactions between particles in a many body system are given by its Hamiltonian. Typically, for a system with many electrons and nuclei such as a molecule or solid, the full Hamiltonian in the non-relativistic quantum mechanics is expressed as [2]:

$$\hat{H} = -\sum_{i=1}^{n}\frac{\hbar^2}{2m}\nabla_i^2 - \sum_{I=1}^{N}\frac{\hbar^2}{2M_I}\nabla_i^2 - \sum_{i=1}^{n}\sum_{I=1}^{N}\frac{1}{4\pi\varepsilon_0}\frac{Z_I e^2}{|r_i - R_I|} + \frac{1}{2}\sum_{i=1}^{n}\sum_{j,j\neq i}^{n-1}\frac{1}{4\pi\varepsilon_0}\frac{e^2}{|r_i - r_j|} + \frac{1}{2}\sum_{I=1}^{N}\sum_{J,J\neq I}^{N-1}\frac{1}{4\pi\varepsilon_0}\frac{Z_I Z_J e^2}{|R_I - R_J|} \quad (1.1)$$

where $\hat{H}$ is the Hamiltonian operator; m and M are the masses of electron and nucleus; n and N represent the total number of electrons and nuclei in the system; r_i and R_I give the positions of i electron and I nucleus; e is the elementary charge; Z is the total charge of the nucleus and ε_0 is the static dielectric constant in vacuum; $\hbar$ denotes the reduced

Planck constant. The first two terms in the above equation are the kinetic energies for electrons ($\hat{T}_e$) and nuclei ($\hat{T}_n$). The Coulomb attraction between electrons and nuclei is given by the third term ($\hat{V}_{en}$). The last two terms represent the Coulomb replusions among eletrons ($\hat{V}_{ee}$) and nuclei ($\hat{V}_{nn}$), respectively.

1.2 Born-Oppenheimer Approximation

In principle, the stationary properties of a many body system can be obtained by solving the Schrödinger equation given below.

$$\hat{H}\Psi(\underset{\sim}{r},\underset{\sim}{R}) = E\Psi(\underset{\sim}{r},\underset{\sim}{R}) \tag{1.2}$$

In the equation, the many body Hamiltonian is given by Equation 1.1; E is the eigenenergy and $\Psi(\underset{\sim}{r},\underset{\sim}{R})$ is the many body wavefunction; $\underset{\sim}{r}$ and $\underset{\sim}{R}$ can be expressed as $\{r_1, r_2, \ldots, r_N\}$ and $\{R_1, R_2, \ldots, R_N\}$, which are the positions of electrons and nuclei, respectively.

Practically, equation 1.2 is not exactly solvable even for a multi-electron atom [1, 2]. Therefore, one must find the way to simplify the many-body Hamiltonian before doing any realistic calculation for molecules and solids. First of all, we can easily notice that the mass of an electron is significantly smaller than for nuclei (Note that even in Hydrogen atom, the ratio $m_e/m_n \approx 1/1836$). Generally, the electrons can follow the motion of heavy "sluggish" nuclei at any moment during the electron-nucleus dynamics. Otherwise, we may also treat the two subsytems adiabatically, i.e., electrons and nuclei, assuming that either there is no energy transfer or the energy flows in an ordered way

between two subsystems. Due to these two postulates, the many-body wave function given in equation 1.2 can be rexpressed as the multiplication of the wave functions of two subsystems

$$\Psi_{BO}(\underset{\sim}{r},\underset{\sim}{R}) = \Phi(\underset{\sim}{R})\psi_e(\underset{\sim}{r},\underset{\sim}{R}) \tag{1.3}$$

where for eletrons and nuclei, their wave functons are given by $\Phi(\underset{\sim}{R})$ and $\psi_e(\underset{\sim}{r},\underset{\sim}{R})$, respectively. At any moment, for a given configuration of nuclei, the electronic wave function $\psi_e(\underset{\sim}{r},\underset{\sim}{R})$ is the eigenstate of electronic Hamiltonian or at least approximately the ground state wave function of electronic part.

$$\hat{H}_e\psi_e(\underset{\sim}{r},\underset{\sim}{R}) = E_e\psi_e(\underset{\sim}{r},\underset{\sim}{R}) \tag{1.4}$$

The electronic Hamiltonian is given as:

$$\hat{H}_e = \hat{T}_e + \hat{V}_{ee} + \hat{V}_{en} + \hat{V}_{nn} \tag{1.5}$$

where all the terms are defined in equation 1.1 for electronic part. Based on Equations 1.2-1.5, we can rewirte equation 1.2 as:

$$(\hat{T}_n + \hat{H}_e)\Phi(\underset{\sim}{R})\psi_e(\underset{\sim}{r},\underset{\sim}{R}) = E\Phi(\underset{\sim}{R})\psi_e(\underset{\sim}{r},\underset{\sim}{R}) \tag{1.6}$$

This equation can be recognized as the famous Born-Oppenheimer approximation which decouples electronic degrees of freedom from the total electron-nucleus wavefunction [3]. Under the Born-Oppenheimer approximation, the Schrödinger equation for nuclei is written as:

$$(\hat{T}_n + \hat{H}_e)\Psi_{\mathrm{BO}}(\underset{\sim}{r},\underset{\sim}{R}) = \mathrm{E}\,\Psi_{\mathrm{BO}}(\underset{\sim}{r},\underset{\sim}{R}) + \{\text{small corrections}\} \tag{1.7}$$

The “small corrections” usually refer to phonon-electron coupling and a small correction to nucleus kinetic energy. In most cases, they are simply ignored or treated as

high order perturbations in quantum mechanics. It is generally true that the kinetic energy spectrum of electrons is not significantly overlapped with that of nuclei. The Born-Oppenhemier approximation is accurate enough for the many-body Hamiltonian in most quantum mechanical calculations [2].

1.3 Thomas-Fermi Density Functional

Theoretically, the ground state properties of a many-body system can be obtained by minimizing the total energy with respect to the many-body wavefunction under the Born-Oppenhemier approximation. In reality, this strategy requires tremendous efforts to make it work numerically even for small systems like atoms and simple molecules. The main difficulty is that the total degrees of freedom embedded in the many-body wavefunction are huge, and the computational costs scale expontentially as the system grows. This is a fundamental bottleneck for applying any wave function based optimization method to the large system [2].

In 1927, Thomas [4] and Fermi [5] independently employed the electron density rather than wave function to compute the total energy of many-body system. The relationship between electron density and many-body wave function is usually expressed as:

$$\begin{aligned} n(\vec{r}) &= N\sum_{\sigma}\sum_{\sigma_2}....\sum_{\sigma_N}\int d^3\vec{r}_2.....\int d^3\vec{r}_N \{\cdots\} \\ \{\cdots\} &= \psi_e^*(\vec{r},\sigma;\vec{r}_2,\sigma_2.....\vec{r}_N,\sigma_N)\psi_e(\vec{r},\sigma;\vec{r}_2,\sigma_2.....\vec{r}_N,\sigma_N) \end{aligned} \tag{1.8}$$

where $n(\vec{r})$ is the electron density, σ_i represents the spin direction of i electron, r is the position of each electron. Clearly, for a system with N electrons, the total spacial degrees

of freedom are *3N*. Meanwhile, using the electron density as the variable, the degrees of freedom are always 3 [2]. In Thomas-Fermi density functional, the energy functional, which has been drived from the uniform electron gas, is given by

$$E_{TF}[n] = \frac{3}{10}(3\pi^2)^{2/3}\int d^3\vec{r}[n(\vec{r})]^{5/3} + \frac{1}{2}\int d^3\vec{r}\int d^3\vec{r}'\,\frac{n(\vec{r})n(\vec{r}')}{\left|\vec{r}-\vec{r}'\right|} \tag{1.9}$$

where, the first term on the right hand side of equation 1.9 gives the kinetic energy for the given electron density distribution; while the second term is the classic Coulomb interaction between two electron density distributions. It has been shown that Thomas-Fermi energy functional can give reasonable results for heavy atoms; however, it is not accurate for molecules and solids. The molecules in Thomas-Fermi theory are unbound, because the exchange-correlation energy which responsible for most of the cohesive energy in condensed phases, is completely ignored in this energy functional [6, 7]. Later, the exchange-correlation effects were indeed included in several other earlier versions of density functionals such as Thomas-Fermi-Dirac approximation (with local exchange only) [6, 8], Thomas-Fermi-Dirac-Gombas approximation (local exchange-correlation) [8] and Thomas-Fermi-Dirac-Gombas-Weizsäcker (semilocal correction to kinetic energy and local exchange-correlation) [9]. Those earlier energy functionals are considered to be still very rough approximations for molecules and solids. They do not predict very accurate cohesive energies and equilibrium geometries for condensed phases. Therefore, they have never been widely used in any practical calculations for condensed phases [6].

1.4 Hohenbergy-Kohn Theorem

In the Thomas-Fermi energy functional, the electron density is used as the only variable which determines the total energy in a unique way. Using the variational principle for equation 1.9 under the constraint that the integration of electron density $n(r)$ gives the correct total number of electrons in the system, we can minimize the total energy density functional with respect to electron density. It is possible that the ground state total energy and electron density can be obtained. However, this is not guaranteed, because it is not clear if one can actually use electron density to characterize ground state properties of a many-body system completely, compared to wave function method [10, 11]. The possible connection between Schrödinger equation (Equation 1.4) and density functional (Equation 1.9) was not clear before the publication of the Hohenberg-Kohn theorem in 1960s [12, 13].

The Hohenberg-Kohn formulation of density functional theory was proposed in 1964. Two fundamental principles have been established for the ground state properties of an interacting electrons gas in an external potential.

Hohenberg-Kohn theorem I: Using the density as the basic variable [12].

The first theorem states that the full many-body ground state is an unique functional of electron density $n(\vec{r})$. In other words, if the ground state electron density $n_g(\vec{r})$ is known, then it determines the total electron number N ($N = \int n_g(\vec{r}) d^3\vec{r}$), the external potential ($V_{ext}(\vec{r})$), the Hamiltonian ($\widehat{H}_e$) and all eigenstate wavefunctions ($\psi_g(\vec{r})$) of $\widehat{H}_e$. The first theorem is mathematically rigorous and can be proved using *reductio ad absurdum* [2].

Hohenberg-Kohn theorem II: The variational principle [12].

The total energy of an interacting many-body system is given as:

$$E_v[n] = Q[n] + \int v(\vec{r})n(\vec{r})d^3r \tag{1.10}$$

where $E_v[n]$ is the total energy of the many-particle system for a given external potential $v(\vec{r})$; $Q[n]$ represents a universal density functional of electron kinetic energy and Coulomb interactions, and which can be expressed as

$$Q[n] \equiv \langle \psi_e(\underset{\sim}{r}, \underset{\sim}{R}) | (\hat{T}_e + \hat{V}_{ee}) | \psi_e(\underset{\sim}{r}, \underset{\sim}{R}) \rangle \tag{1.11}$$

Applying the variational principle, the minimum of equation 1.10 is obtained with the constraint given below for the electron density $n(\vec{r})$.

$$N[n] \equiv \int n(\vec{r})d^3\vec{r} = N \tag{1.12}$$

Note that the electron density is computed from Equation 1.8 using the electron wave-function. In the wave-function method, the ground state energy is evaluated as $E_g = \min_{\psi_e \to N} \langle \psi_e | \hat{H}_e | \psi_e \rangle$. ψ_e can be any normalized trial wavefunction satisfying equation 1.12. In density functional method, we minimize equation 1.10 using the normalized trial electron densities rather than wavefunctions. The special minimization strategy, called the Levy-Lieb constrained search method, was firstly given independently by Levy [14] and Lieb [10] in their works. As shown in equation 1.13, this method adopts two different steps. In the first step, the normalized trial wave-function minimizes the Hamiltonian $\hat{H}_e$ for the given density $n(\vec{r})$. Then, for the given external potential and the fixed number of electrons , we minimize the equation 1.10 for any possible trial density distribution.

$$E_g = \min_{\psi_e \to N} \langle \psi_e | \hat{H}_e | \psi_e \rangle = \min_{n(\vec{r}) \to N} \min_{\psi_e \to n(\vec{r})} \langle \psi_e | \hat{H}_e | \psi_e \rangle$$
$$= \min_{n(\vec{r}) \to N} \langle \psi_e^{\min} | \hat{H}_e | \psi_e^{\min} \rangle \tag{1.13}$$

The second step of Levy-Leib constrained search can be rewritten in a more familiar density functional form using equation 1.10.

$$E_g = \min_{n(\vec{r}) \to N} \langle \psi_e^{\min} | \hat{H}_e | \psi_e^{\min} \rangle = \min_{n(\vec{r}) \to N} \left\{ Q[n] + \int v(\vec{r}) n(\vec{r}) d^3 r \right\} \tag{1.14}$$

The universal density functional $Q[n]$ is given by:

$$Q[n] = \langle \psi_e^{\min} | \hat{T}_e + \hat{V}_{ee} | \psi_e^{\min} \rangle \tag{1.15}$$

For the N electron system, the minimizing of equation 1.13 by varying the many-body wave-function in $3N$ space is almost a formidable task. Using the Levy-Leib constrained search, the problem of optimizing the wavefunction has been transformed into the minimization of equation 1.14 by trial electron density $n(\vec{r})$ in 3-dimensional space [2].

1.5 Kohn-Sham Theorem

The Levy-Leib two-step constrained search indicates that the normalized trial wave-function ψ_e^{min} can be obtained from the first step. However, it is still unclear how it is computed from the density functional theory. The complete answer for this question was provided in the works of Kohn and Sham [13] in 1965, later known as the Kohn-Sham theorem.

1.5.1 Adiabatic Connection with Fully Interacting System

In the Kohn-Sham density functional theory, the total energy functional of an interacting system is eventually mapped onto a system with non-interacting electrons moving in the effective external potential. It is required that the ground state energy and electron density obtained from such a non-interacting model system are exactly the same as those of fully interacting system. Therefore, one has to adjust the kinetic energy and external potential in the Kohn-Sham system such that it gives the same ground state properties as the true interacting many-body system. Thermodynamically, the Kohn-Sham system can be adiabatically connected to the fully interacting system within the following expression [15].

$$E_g = \int_0^1 d\lambda \left\langle \psi_e^\lambda \middle| \hat{H}_e^\lambda \middle| \psi_e^\lambda \right\rangle \tag{1.16}$$

with

$$\hat{H}_e^\lambda = \hat{T}_\lambda + \lambda \hat{V}_{ee} + \hat{V}_{ext}^\lambda \tag{1.17}$$

note that $\hat{H}_e^\lambda$ represents the electronic Hamiltonian for a fictitious λ interacting system. In the adiabatic connection, by varying λ smoothly from 0 to 1, we require that for each λ system on the path, the ground state electron density ($n_g^\lambda(\vec{r})$) is equivalent $n_g^{\lambda=1}(\vec{r})$. The ground state energy now can be calculated as the coupling constant (λ) averaged expectation value of the Hamiltonian ($\hat{H}_e^\lambda$) going from Kohn-Sham non-interacting system (with $\lambda = 0$) to the fully interacting system ($\lambda = 1$). The relationship between Kohn-Sham and true interacting systems is given in equation 1.18.

$$\hat{H}_e^{\lambda} = \begin{cases} \hat{H}_e^{\lambda=1} = \hat{T} + \hat{V}_{ee} + \hat{V}_{ext} \\ \hat{H}_e^{\lambda=0} = \hat{T}_s + \hat{V}_{eff} \end{cases} \tag{1.18}$$

In the Kohn-Sham system, the Coulomb interactions of electrons are completely turned off, and $\hat{T}_s$ refers to the kinetic energy of non-interacting electrons. The true external potential $\hat{V}_{ext}$ is replaced by an effective potential $\hat{V}_{eff}$. The difference between $\hat{T}$ and $\hat{T}_s$ can be built into the $\hat{V}_{eff}$. As a result, the two kinetic energies are considered to be the same in euqation 1.18.

1.5.2 Kohn-Sham Equation

From equations 1.10 and 1.12, it is straightforward to show that the minimization of equation 1.14 can be achieved using the conventional Euler-Lagrange multiplier. The new energy density functional is given by

$$F[n] = \left\{ Q[n] + \int v(\vec{r}) n(\vec{r}) d^3\vec{r} \right\} - \mu \left[\int n(\vec{r}) d^3\vec{r} - N \right] \tag{1.19}$$

where μ is the Euler-Lagrange multiplier and $F[n]$ is simply a functional of density. The minimizing of $F[n]$ with respect to electron density $n(\vec{r})$ is obtained when the following condition is fulfilled.

$$\delta[F[n]] = \left\{ \frac{\delta Q[n]}{\delta n} + v(\vec{r}) - \mu \right\} \delta n = 0 \tag{1.20}$$

The obtained Euler-Lagrange equation now can be written as

$$\frac{\delta Q[n]}{\delta n} + v(\vec{r}) = \mu \tag{1.21}$$

here $v(\vec{r})$ is actually the external potential $v_{ext}(\vec{r})$, and μ is the chemical potential which ensures that the total electron number is always correct in the non-interacting system. The form of the universal density functional $Q[n]$ is known [12, 13].

$$Q[n] = T_s[n] + E_H[n] + E_{xc}[n] \tag{1.22}$$

In this equation, the kinetic energy density functional is represented by $T_s[n]$, and $E_H[n]$ is the classical electrostatic energy of non-interacting electrons. The last term refers to the exchange-correlation energy, mainly accounting for the missing many-body effects in Kohn-Sham system. Substituting equation 1.22 into 1.21, we can show that

$$\frac{\delta T_s[n]}{\delta n} + V_H(\vec{r}) + \frac{\delta E_{xc}[n]}{\delta n} + v_{ext}(\vec{r}) = \mu \tag{1.23}$$

where $V_H(\vec{r})$ represents the classic Coulomb potential (Hartree potential) of electrons and which can be computed as

$$V_H(\vec{r}) = \frac{\delta E_H[n]}{\delta n} = \int \frac{n(\vec{r}')}{|\vec{r} - \vec{r}'|} d^3\vec{r}' \tag{1.24}$$

Finally, combining equations 1.18 and 1.23, the effective potential of Kohn-Sham system is obtained as

$$\frac{\delta T_s[n]}{\delta n} + v_{eff}(\vec{r}) = \mu \tag{1.25}$$

with

$$v_{eff}(\vec{r}) = V_H(\vec{r}) + V_{xc}(\vec{r}) + V_{ext}(\vec{r}) \tag{1.26}$$

and the exchange-correlation potential

$$V_{xc}(\vec{r}) = \delta E_{xc}[n] / \delta n \tag{1.27}$$

Clearly, equation 1.25 is similar to the single-particle Schrödinger equation where each electron moves in a universal effective potential. If we multiple both sides of equation 1.25 by the Kohn-Sham single particle wave function $\psi_\alpha^{KS}(\vec{r})$, the Kohn-Sham equation is obtained.

$$\left[-\frac{1}{2}\nabla^2 + V_{eff}(\vec{r})\right]\phi_\alpha^{KS}(\vec{r}) = \varepsilon_\alpha \phi_\alpha^{KS}(\vec{r}) \tag{1.28}$$

Here the chemical potential μ has the same meaning as the eigenenergy of Kohn-Sham orbital. Meanwhile, the kinetic energy energy functional is defined in the following way

$$T_s[n] = \int d^3\vec{r}\,\hat{\tau}[\vec{r}]n(\vec{r}) \tag{1.29}$$

where the kinetic energy operator $\hat{\tau}[\vec{r}] = 2\sum_\alpha |\nabla\phi_\alpha^{KS}|^2/2$, and the electron density $n(r)$ $= 2\sum_\alpha f_\alpha |\phi_\alpha^{KS}|^2$, where f_α is the Fermi-Dirac distribution function for α Kohn-Sham single particle orbital with eigenenergy ε_α. Within this definition for $T_s[n]$, equation 1.28 can be easily validated using equations 1.25 and 1.29. Similar to Hartree-Fock theory, the total ground state energy of the non-interacting system is not equivalent to the sum of all eigenenergies of Kohn-Sham single particle orbitals. The exact relationship between them is given by

$$E = \sum_{\alpha=1}^{M}\varepsilon_\alpha - \frac{1}{2}\int\int \frac{n(\vec{r})n(\vec{r}')}{|\vec{r}-\vec{r}'|}d^3\vec{r}d^3\vec{r}' + \left\{E_{xc}[n] - \int V_{xc}[n]n(\vec{r})d^3\vec{r}\right\} \tag{1.30}$$

here M denotes the highest occupied Kohn-Sham single particle orbital and in the spin degenerated case $M = N/2$, with N the total number of eletrons in the system. The exchange-correlation potential is already defined in equation 1.27. The possible expression for $E_{xc}[n]$ will be discussed in the next section. Now, the wavefunction of the

non-interacting system ψ_e^{min} can be constructed from all occupied Kohn-Sham orbitals using the following expression.

$$\psi_e^{\min}(\vec{r}) = \frac{1}{\sqrt{M!}} \begin{vmatrix} \phi_1(\vec{r}_1) & \phi_2(\vec{r}_1) & \cdots & \cdots & \phi_M(\vec{r}_1) \\ \phi_1(\vec{r}_2) & \phi_2(\vec{r}_2) & \cdots & \cdots & \phi_M(\vec{r}_2) \\ \vdots & \vdots & \cdots & \cdots & \vdots \\ \vdots & \vdots & \cdots & \cdots & \vdots \\ \phi_1(\vec{r}_N) & \phi_2(\vec{r}_N) & \cdots & \cdots & \phi_M(\vec{r}_N) \end{vmatrix} \tag{1.31}$$

Note that the ϕ_i represents the ith occupied Kohn-Sham single particle orbital. equation 1.31 is a typical single Slater determiant for non-interacting, identical and indistinguishable Fermions, representing a single reference configuration for *N* electrons.

1.5.3 Exchange-Correlation Energy Functional

The exchange-correlation energy is given by the third term in the Equation 1.26. The exact mathematical form of this energy functional is unknown in density functional theory. Therefore, one must construct its form from a model system. The most well-known model system is the uniform electron gas. If the electron density of the system varies sufficiently slow, then Hohenberg and Kohn [13] showed that the exchange-correlation energy functional has the following form

$$E_{xc}[n] = \int n(\vec{r}) \varepsilon_{xc}^{unif}[n] d^3\vec{r} \tag{1.32}$$

where $\varepsilon_{xc}^{unif}[n]$ is the exchange-correlation energy per particle of uniform electron gas. Equation 1.32 is enssentially the local density approximation (LDA). However, the analytical expression of $\varepsilon_{xc}^{unif}[n]$ was not known in the 1960s. The actual breakthrough of applying DFT to realistic condensed matters (atoms, molecules and solids) happened

much later in 1970s. Within equation 1.32, the local exchange-correlation potential is given by

$$V_{xc}(\vec{r}) = \varepsilon_{xc}^{unif}[n(\vec{r})] + n(\vec{r})\frac{d\varepsilon_{xc}^{unif}[n]}{dn} \tag{1.33}$$

and euqation 1.30 can be written as

$$E = \sum_{\alpha=1}^{M}\varepsilon_{\alpha} - \frac{1}{2}\int\int\frac{n(\vec{r})n(\vec{r}')}{|\vec{r}-\vec{r}'|}d^3\vec{r}d^3\vec{r}' + \left\{\int(\varepsilon_{xc}^{unif}[n] - V_{xc}[n])n(\vec{r})d^3\vec{r}\right\} \tag{1.34}$$

1.6 Exchange-Correlation Functionals

In this section, a comprehensive review is presented for the exchange-correlation functionals, which play the central role in density functional theory.

1.6.1 Exchange-Correlation Hole

The exchange-correlation can be revealed from the joint probability interpretation of many-body wavefunction [6]. The joint density probability refers to a two particle density distribution, which is given by

$$\rho_2(\vec{r}_1,\sigma_1;\vec{r}_2,\sigma_2) = \mathrm{N(N-1)}\sum_{\sigma_3}\cdots\sum_{\sigma_N}\int d^3\vec{r}_3\cdots\int d^3\vec{r}_N\left|\psi_e(\vec{r}_1,\sigma_1;\vec{r}_2,\sigma_2\cdots\vec{r}_N,\sigma_N)\right|^2 \tag{1.35}$$

where $\rho_2(\vec{r}_1,\sigma_1;\vec{r}_2,\sigma_2)$ is the joint density probability, referring to the probability of finding the first partice at r_1 with spin index σ_1 as well as the second particle at r_2 with spin σ_2 at the same time. Due to the Pauli exclusive principle, it is known that the probability of finding two particles with the same spin ($\sigma_1 = \sigma_2$) in the same position ($r_1 = r_2$) is zero. This is basically the origin of the exchange hole surrounding a electron.

On the other hand, the electrons also try to avoid getting close to each other, because the singularity of on-top Coulomb repulsion between them. Therefore, electrons are correlated with each other due to the Coulomb interactions. In contrast to the exchange hole, the Coulomb correlation applies to all electrons, no matter what their spins are. The two particle distribution function given in equation 1.35 can be rewritten as

$$\rho_2(\vec{r}_1,\sigma_1;\vec{r}_2,\sigma_2) = n_{\sigma_1}(\vec{r}_1) n_2(\vec{r}_2,\sigma_2;\vec{r}_1,\sigma_1) \tag{1.36}$$

Here the one particle density distribution function $n_{\sigma_1}(\vec{r}_1)$ gives the probability of finding the particle with spin σ_1 in $d^3\vec{r}_1$ at $\vec{r}_1$. It can be obtained using the expression given below.

$$n_{\sigma_1}(\vec{r}_1) = \mathrm{N}\sum_{\sigma_2}\sum_{\sigma_3}\cdots\sum_{\sigma_N}\int d^3\vec{r}_2\int d^3\vec{r}_3\cdots\int d^3\vec{r}_N \left|\psi_e(\vec{r}_1,\sigma_1;\vec{r}_2,\sigma_2\cdots\vec{r}_N,\sigma_N)\right|^2 \tag{1.37}$$

Otherwise, the two particle conditional probability $n_2(\vec{r}_2,\sigma_2;\vec{r}_1,\sigma_1)$ provides the probability of finding the second electron with spin σ_2 at $\vec{r}_2$, given the first electron of spin σ_1 at $\vec{r}_1$. The relationship between exchange-correlation hole and two particle distribution function is usually defined as

$$\rho_2(\vec{r}_1,\sigma_1;\vec{r}_2,\sigma_2) = n_{\sigma_1}(\vec{r}_1)\left[n_{\sigma_2}(\vec{r}_2) + n_{xc}(\vec{r}_2,\sigma_2;\vec{r}_1,\sigma_1)\right] \tag{1.38}$$

here $n_{xc}(\vec{r}_2,\sigma_2;\vec{r}_1,\sigma_1)$ is the exchange-correlation hole. Combining equations 1.36 and 1.38, we find that

$$n_{xc}(\vec{r}_2,\sigma_2;\vec{r}_1,\sigma_1) = n_2(\vec{r}_2,\sigma_2;\vec{r}_1,\sigma_1) - n_{\sigma_2}(\vec{r}_2) \tag{1.39}$$

We should note that the exchange hole surrounding the electron of spin σ_1 at $\vec{r}_1$ is a negative value, because the Pauli exclusive principle. On the other hand, the total $n_{xc}(\vec{r}_2,\sigma_2;\vec{r}_1,\sigma_1)$ has no restriction on the sign of its values. The physical interpretation

of equation 1.39 is that the probability of finding a second electron of spin σ_2 at $\vec{r}_2$, given first electron of spin σ_1 at $\vec{r}_1$, is decreased due to the exchange-correlation hole surrounding the first electron. Since the exchange hole has a different origin than the correlation hole, one can study the properties of exchange and correlation holes separately.

$$n_{xc}(\vec{r}_2,\sigma_2;\vec{r}_1,\sigma_1) = n_x(\vec{r}_2,\sigma_2;\vec{r}_1,\sigma_1)\delta_{\sigma_1,\sigma_2} + n_c(\vec{r}_2,\sigma_2;\vec{r}_1,\sigma_1) \tag{1.40}$$

The exchange-correlation energy now can be computed from exchange-correlation hole by

$$E_{xc}[n] = \frac{1}{2}\int d^3\vec{r}_1 n(\vec{r}_1)\int d^3\vec{r}_2 \frac{n_{xc}(\vec{r}_1,\vec{r}_2)}{|\vec{r}_1-\vec{r}_2|} \tag{1.41}$$

here we use the spin un-resolved quantities in the equation. Substituting equation 1.40 into 1.41, we can calculate exchange and correlation enerigies independently. The exchange hole satisfies several physical constraints which can be shown from Hartree-Fock theory. In Hartree-Fock theory, the exact exchange energy is calculated by

$$E_x[n] = -\frac{1}{2}\int d^3\vec{r}_1\int d^3\vec{r}_2 \frac{n_1(\vec{r}_1,\vec{r}_2)n_1(\vec{r}_2,\vec{r}_1)}{|\vec{r}_1-\vec{r}_2|} \tag{1.42}$$

with the one electron density matrix $n_1(\vec{r}_1,\vec{r}_2)$

$$n_1(\vec{r}_1,\vec{r}_2) = \sum_{\sigma_1}\sum_{\sigma_2}\sum_{\sigma_3}\cdots\sum_{\sigma_{N+1}}\int d^3\vec{r}_3\cdots\int d^3\vec{r}_{N+1}\{\cdots\} \tag{1.43}$$

and $\{\cdots\}$ stands for

$$\psi_e^*(\vec{r}_1,\sigma_1;\vec{r}_3,\sigma_3\cdots\vec{r}_{N+1},\sigma_{N+1})\psi_e(\vec{r}_2,\sigma_2;\vec{r}_3,\sigma_3\cdots\vec{r}_{N+1},\sigma_{N+1}) \tag{1.44}$$

while using the exchange hole, it is obtained by

$$E_x[n] = \frac{1}{2}\int d^3\vec{r}_1 n(\vec{r}_1)\int d^3\vec{r}_2 \frac{n_x(\vec{r}_1,\vec{r}_2)}{|\vec{r}_1-\vec{r}_2|} \tag{1.45}$$

Thus, from equations 1.42 and 1.45, it can be easily seen that

$$-\frac{1}{2}\int d^3\vec{r}_1\int d^3\vec{r}_2 \frac{n_1(\vec{r}_1,\vec{r}_2)n_1(\vec{r}_2,\vec{r}_1)}{|\vec{r}_1-\vec{r}_2|} = \frac{1}{2}\int d^3\vec{r}_1 n(\vec{r}_1)\int d^3\vec{r}_2 \frac{n_x(\vec{r}_1,\vec{r}_2)}{|\vec{r}_1-\vec{r}_2|} \tag{1.46}$$

and

$$n_x(\vec{r}_1,\vec{r}_2) = -\frac{|n_1(\vec{r}_1,\vec{r}_2)|^2}{n(\vec{r}_1)} \tag{1.47}$$

since the one particle electron density $n(\vec{r}_1)$ and the absolute square of the density matrix $n_1(\vec{r}_1,\vec{r}_2)$ are non-negative numbers. Therefore, the first constraint for exchange hole density is

$$n_x(\vec{r}_1,\vec{r}_2) \le 0 \tag{1.48}$$

Additionally, the integration of equation 1.47 for $\vec{r}_2$ gives the second constraint.

$$\int n_x(\vec{r}_1,\vec{r}_2)d^3\vec{r}_2 = -\int \frac{|n_1(\vec{r}_1,\vec{r}_2)|^2}{n(\vec{r}_1)}d^3\vec{r}_2 = -\frac{n(\vec{r}_1)}{n(\vec{r}_1)} = -1 \tag{1.49}$$

Finally, the last constraint is that the on-top exchange hole at $\vec{r}_1$ is given by

$$n_x(\vec{r}_1,\vec{r}_1) = -\frac{|n_1(\vec{r}_1,\vec{r}_1)|^2}{n(\vec{r}_1)} = -n(\vec{r}_1) \tag{1.50}$$

where $n_1(\vec{r}_1,\vec{r}_1) = n_1(\vec{r}_1)$ in a fully spin-polarized system. The exchange hole makes the second electron vanish at $\vec{r}_1$, given that both electrons have the same spin index. In Figure 1.1, we plot the exchange hole distributions of uniform (s = 0) and non-uniform (s = 1) cases from the gradient expansion approximation (GEA).

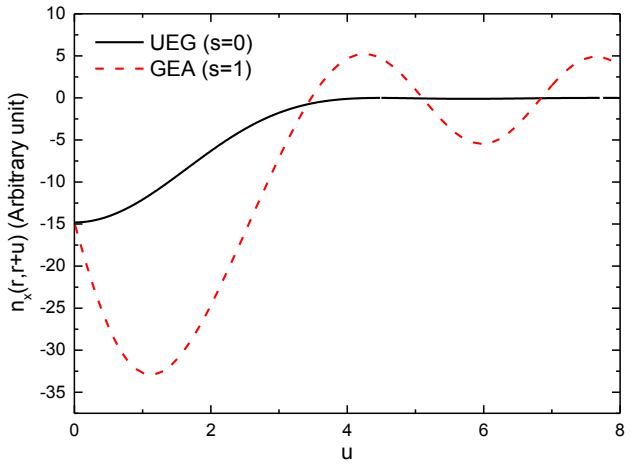

Figure 1.1: The exchange holes of uniform (s = 0) and non-uniform (s = 1) electron densities. The reference electron is located at the origin. The data for plots are generated by GEA.

On the other hand, the electron density is rearranged by the correlation hole, but the total number of electrons is conserved. Thus, the only constraint for correlation hole is given in equation 1.51, implying that the correlation hole does not have any restriction on its sign. Usually, the value of correlation hole is negative at short range around a reference electron, and it can be positive far away from $\vec{r}_1$.

$$\int n_c(\vec{r}_1,\vec{r}_2)d^3\vec{r}_2 = 0 \tag{1.51}$$

Similar to the evaluation of exchange energy from exchange hole using equation 1.45, the correlation energy can be calculated from correlation hole as

$$E_c[n] = \frac{1}{2}\int d^3\vec{r}_1 n(\vec{r}_1)\int d^3\vec{r}_2 \frac{n_c(\vec{r}_1,\vec{r}_2)}{|\vec{r}_1-\vec{r}_2|} \tag{1.52}$$

Finally, using euquations 1.49 and 1.51, we get the constraint for total exchange-correlation hole.

$$\int n_{xc}(\vec{r}_1,\vec{r}_2)d^3\vec{r}_2 = -1 \tag{1.53}$$

In density functional theory, the constraints for exchange-correlation hole shown in this section are considered as the fundamental guildlines when building the exchange-correlation density functionals [16].

1.6.2 Jacob's Ladder of Density Functionals

The most well-known classification of exchange-correlation functionals used in modern first principles calculations based on density functional theory has been proposed by Perdew and Schmidt [16, 17]. The ingredients, which can be incorporated in the construction of an exchange-correlation functional, are the electron density $n(r)$, density gradient $\nabla n(r)$ and orbital kinetic energy density ($\tau = \sum_\sigma \tau_\sigma$) for semilocal functionals. Meanwhile, the non-local exchange-correlation functionals also use the Kohn-Sham single particle orbitals as the input information. In Figure 1.2, the basic idea of sorting exchange-correlation functionals by their ingredients on Jacob's ladder is illustrated.

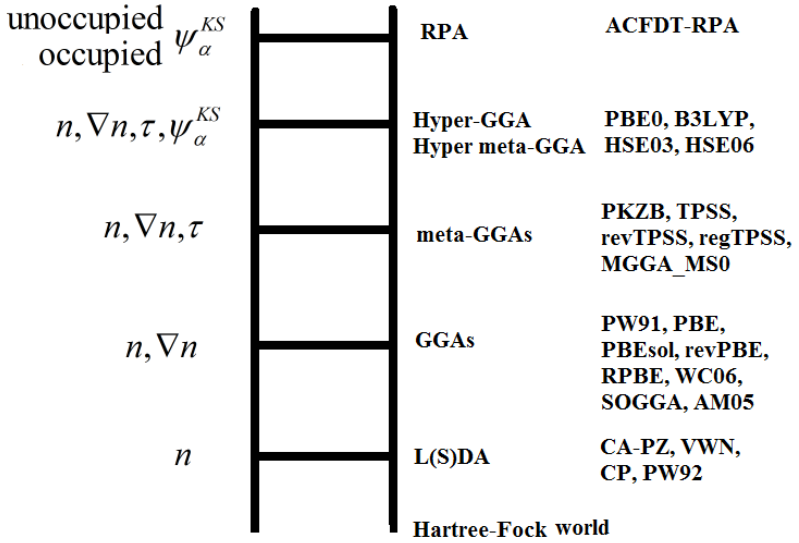

Figure 1.2: The Jacob's ladder of density functionals.

The first rung on Jacob's ladder is the local spin density approximation (LSDA or LDA for simplicity in spin non-polarized case) which uses only the local spin electron densities to compute the exchange-correlation energy. The general expression of LSDA is given by

$$E_{\mathrm{xc}}^{\mathrm{LSDA}}[n_{\uparrow}, n_{\downarrow}] = \int n(\vec{r}) \varepsilon_{\mathrm{xc}}^{\mathrm{unif}}(n_{\uparrow}(\vec{r}), n_{\downarrow}(\vec{r})) d^3\vec{r} \tag{1.54}$$

where the spin unresolved density $n(\vec{r}) = n_{\uparrow}(\vec{r}) + n_{\downarrow}(\vec{r})$, and $\varepsilon_{xc}^{unif}(n_{\uparrow}(\vec{r}), n_{\downarrow}(\vec{r}))$ is already defined as the exchange-correlation energy per particle of uniform electron gas in equation 1.32. The most widely used forms of L(S)DA are Vosko-Wilk-Nusair (VWN) [18], Perdew-Zunger (PZ) [19], Cole-Perdew (CP) [20] and Perdew-Wang (PW92) [21].

The second rung on Jacob's ladder is the generalized gradient approximation or GGA. The exchange-correlation functional of GGA level uses both the local spin density $n_{\sigma}(\vec{r})$ and the density gradient $\nabla n_{\sigma}(\vec{r})$ infinitesimally close to $\vec{r}$ as the variables in its construction. The expression of exchange-correlation energy of a GGA-level functional can be calculated as

$$E_{\mathrm{xc}}^{\mathrm{GGA}}[n_{\uparrow}, n_{\downarrow}] = \int n(\vec{r}) \varepsilon_{\mathrm{xc}}^{\mathrm{GGA}}(n_{\uparrow}, n_{\downarrow}, \nabla n_{\uparrow}, \nabla n_{\downarrow}) d^3\vec{r} \tag{1.55}$$

here $\varepsilon_{xc}^{GGA}(n_{\uparrow}, n_{\downarrow}, \nabla n_{\uparrow}, \nabla n_{\downarrow})$ is the exchange-correlation energy per particle of GGA. It might be constructed from $\varepsilon_{xc}^{unif}(n_{\uparrow}(\vec{r}), n_{\downarrow}(\vec{r}))$. Some well-known GGA exchange-correlation functionals are gradient expansion approximations (GEA) [13, 22, 23], Perdew-Wang (PW91) [24], Perdew-Burke-Ernzerhof (PBE) [25], revised PBE (revPBE) [26], RPBE [27], Armiento-Mattsson (AM05) [28], Wu-Cohen (WC) [29], PBE revised for solid (PBEsol) [30] and Zhao-Truhlar (SOGGA) [31].

Meta-generalized gradient approximation or meta-GGA is the third rung on Jacob's ladder. Besides spin-resolved density $n_\sigma(\vec{r})$ and density gradient ∇n_σ, the exchange-correlation energy functional of meta-GGA also employs the orbital kinetic energy density ($\tau_\sigma(\vec{r}) = \frac{1}{2}\sum_\alpha |\nabla \phi_{\alpha\sigma}(\vec{r})|^2$) as another ingredient. The exchange-correlation energy is calculated as

$$E_{\mathrm{xc}}^{\text{meta-GGA}}[n_\uparrow, n_\downarrow] = \int n(\vec{r}) \varepsilon_{\mathrm{xc}}^{\text{meta-GGA}}(n_\uparrow, n_\downarrow, \nabla n_\uparrow, \nabla n_\downarrow, \tau_\uparrow, \tau_\downarrow) d^3\vec{r} \tag{1.56}$$

here $\varepsilon_{xc}^{meta-GGA}(n_\uparrow, n_\downarrow, \nabla n_\uparrow, \nabla n_\downarrow, \tau_\uparrow, \tau_\downarrow)$ is the exchange-correlation energy per particle of meta-GGA. The GGA exchange-correlation energy has been used in meta-GGA construction. Many different forms are available for meta-GGA, including Perdew [32], Ghosh-Parr [33], Becke-Roussel [34], Van Voorhis-Scuseria [35], Perdew-Kurth-Zupan-Blaha (PKZB) [36], Tao-Perdew-Staroverov-Scuseria (TPSS) [37], Zhao-Truhlar (M06-L) [38], revised Tao-Perdew-Staroverov-Scuseria (revTPSS) [39], regularized TPSS (regTPSS) [40], meta-GGA made simple family (MGGA_MS) [41-43], Campo-Gázquez-Trickey-Vela (meta-VT{8, 4}) [44] and Constantin-Fabiano-Sala (BLOC) [45].

The exchange-correlation functional at the fourth rung on Jacob's ladder is called hyper-GGA or hyper-meta-GGA. The strategy adopted to hyper-GGA (meta-GGA) is the mixing of semilocal exchange-correlation functionals on the first three rungs with non-local exchange or correlation functional. Therefore, the exchange-correlation functional obtained in this way is usually referred as hybrid functional. A typical hybrid functional contains a portion of Hartree-Fock like exact exchange in its exchange energy functional, and the correlation energy functional usually keeps the same form as that of a semilocal functional (PBE correlation in most cases). All hybrid functionals are nonlocal and

orbital dependent. Mathematically, it is more transparent than some semilocal functionals. Computationally, it can be 10 to 100 times more expensive than semilocal functionals on the first three rungs. In quantum chemistry, the mostly widely used hybrid functionals are B3LYP (Becke, three parameter, Lee-Yang-Parr) [46] and the M06 suite of meta-hybrid GGA [47, 48]. Meanwhile, the PBE0 [49] and Heyd-Scuseria-Ernzerhof (HSE) [50-52] are very popular in structural calculations for solids.

On the top of Jacob's ladder, we have the random phase approximation (RPA) [15, 53-66]. RPA uses both occupied and unoccupied Kohn-Sham orbitals in its exchange-correlation energy functionals. Additionally, RPA is also completely non-local in both exchange and correlation functionals, in constrast to hybrid functional where only the exchange part is nonlocal. The most intriguing property of RPA is that the long range van der Waals interactions can be described naturally due to its non-local construction of correlation energy. RPA is supposed to be the most accurate method for isolectronic energy differences in solids in the framework of density functional theory. Some earlier tests of RPA on transition metals [58, 64, 66], bulk materials [53-58, 65, 66], molecules [59, 62] and surfaces [60, 61, 63] indicated that the method is highly reliable and accurate. However, the main disadvantage of RPA is its high computational costs. Typically, RPA is 100 times slower than semilocal functionals. For large system, it is almost not affordable for most modern supercomputers.

1.6.3 Mathematical Forms

Since we are aiming to test exchange-correlation functionals of all five rungs on Jacob's ladder and to use their exchange enhancement factors to explain the performances on different properties, it is necessary to review some of them from the point of view of their mathematical constructions.

1.6.3.1 Local Spin Density Approximation

The local spin density approximation (LSDA) plays the fundamental role in the construction of other exchange-correlation functionals on Jacob's ladder. The starting point of LSDA is the exchange-correlation energy functional of uniform electron gas. In the earlier 1980s, Ceperley and Alder published the computed exchange-correlation energy of uniform electron gases at finite temperature using Green's-function Monte-Carlo simulation [67, 68]. The total energy density per particle for uniform electron gas is given as

$$\varepsilon_{\mathrm{t}}^{\mathrm{unif}} = t_s(n) + \varepsilon_{\mathrm{x}}^{\mathrm{unif}}(n) + \varepsilon_{\mathrm{c}}^{\mathrm{unif}}(n) \tag{1.57}$$

with the kinetic energy per particle $t_s(n)$, exchange energy $\varepsilon_x^{unif}(n)$ and correlation energy $\varepsilon_x^{unif}(n)$ per particle. We define the Wigner-Seitz radius of uniform electron gas as $r_s = (3/[4\pi n])^{1/3}$. The analytical expressions for the first two terms in equation 1.57 are known.

$$t_s(n) = \frac{3}{10}\left(3\pi^2 n\right)^{2/3} = \frac{1.105}{r_s^2} \tag{1.58}$$

$$\varepsilon_{\mathrm{x}}^{\mathrm{unif}}(n) = -\frac{3}{4\pi}\left(3\pi^2 n\right)^{1/3} = \frac{-0.458}{r_s} \tag{1.59}$$

The formulation of correlation energy comes from the Monte-Carlo simulations of the total energy for uniform electron gas with different r_s values. The analytical expressions used in LSDA are actually the numerical fitting forms of uniform electron gas, starting from Monta-Carlo data [67, 68]. The correlation energy per particle of uniform electron gas is dependent on r_s and spin polarizibility (ξ). The latter quantity is defined as $\xi = (n_\uparrow - n_\uparrow)/n$, where $n = n_\uparrow + n_\downarrow$. For spin non-polarized ($n_\uparrow = n_\uparrow = n/2$ or $\xi = 0$) and spin fully polarized ($\xi = 1$) cases, the correlation energies per particle are given by Ceperly's parametrizations of correlation energy for $r_s \geq 1$

$$\varepsilon_{\mathrm{c}}^{\mathrm{unif}}(r_s, \xi = 0) \approx \frac{-0.1423}{(1 + 1.0529\sqrt{r_s} + 0.334 r_s)} \tag{1.60}$$

and

$$\varepsilon_{\mathrm{c}}^{\mathrm{unif}}(r_s, \xi = 1) \approx \frac{-0.0843}{(1 + 1.398\sqrt{r_s} + 0.2611 r_s)} \tag{1.61}$$

then the correlation energy per particle for an arbitrary ξ is calculated by the interpolation of euqations 1.60 and 1.61 in the following way:

$$\varepsilon_{\mathrm{c}}^{\mathrm{unif}}(\mathrm{r}_s, \xi) = \varepsilon_{\mathrm{c}}^{\mathrm{unif}}(\mathrm{r}_s, \xi = 0) + \frac{g(\xi) - 1}{2^{1/3} - 1}\left[\varepsilon_{\mathrm{c}}^{\mathrm{unif}}(\mathrm{r}_s, \xi = 1) - \varepsilon_{\mathrm{c}}^{\mathrm{unif}}(\mathrm{r}_s, \xi = 0)\right] \tag{1.62}$$

here $g(\xi) = [(1+\xi)^{4/3}+(1-\xi)^{4/3}]/2$. Note that $g(\xi = 0) = 1$ and $g(\xi = 1) = 2^{1/3}$. On the other hand, the kinetic energy and exchange energy per particle of uniform electron gas in spin polarized case are computed as

$$\varepsilon_{\mathrm{x}}^{\mathrm{unif}}(r_s, \xi) = \frac{-0.458}{r_s} g(\xi) \tag{1.63}$$

$$t_s(r_s, \xi) = \frac{1.105}{r_s^2} f(\xi) \tag{1.64}$$

with $f(\xi) = [(1+\xi)^{5/3}+(1-\xi)^{5/3}]/2$. In analogy to $g(\xi)$, we have $f(\xi = 0) = 1$ and $f(\xi = 1) = 2^{2/3}$. The total exchange-correlation energy per particle given in equation 1.54 can be easily obtained from equations 1.62-64. It is worth noting that the expressions 1.60 and 1.61 for uniform electron gas are appropriate for most applications. Perdew and Zunger [19] found that for atomic calculations, the correlation energy per particle at high density is needed. They have shown that for $r_s \leq 1$ and arbitrary ξ, the correlation energy of uniform electron is obtained in a similar way to equation 1.62, but with the following expressions for correlation energy in two special cases (See equations 1.60 and 1.61).

$$\varepsilon_{\mathrm{c}}^{\mathrm{unif}}(r_s, \xi = 0) = 0.0311 \ln r_s - 0.048 + 0.0020 r_s \ln r_s - 0.0116 r_s \tag{1.65}$$

$$\varepsilon_{\mathrm{c}}^{\mathrm{unif}}(r_s, \xi = 1) = 0.01555 \ln r_s - 0.0269 + 0.0007 r_s \ln r_s - 0.0048 r_s \tag{1.66}$$

Using the equations 1.59-62, the exchange and correlation energies of uniform electron gas in two different limits are

$$\begin{cases} \lim\limits_{r_s \to 0} \varepsilon_{\mathrm{x}}^{\mathrm{unif}}(r_s) = -\infty \\ \lim\limits_{r_s \to \infty} \varepsilon_{\mathrm{x}}^{\mathrm{unif}}(r_s) = -0 \end{cases} \tag{1.67}$$

and

$$\begin{cases} \lim\limits_{r_s \to 0} \varepsilon_{c}^{\mathrm{unif}}(r_s, \xi) = -C \\ \lim\limits_{r_s \to \infty} \varepsilon_{c}^{\mathrm{unif}}(r_s, \xi) = -0 \end{cases} \tag{1.68}$$

where C is a positive number. Note that $r_s \longrightarrow \infty$ and $r_s \longrightarrow 0$ correspond to low density and high density limits. In the high density limit, equations 1.65 and 1.66 give -∞ for correlation energy, and obviously they do not exhibit the correct behavior in this case [22, 25]. Note that equations 1.65 and 1.66 are correct for the uniform gas. Equations 1.67

and 1.68 are not correct for this system, although they are correct for systems that have fully non-degenerate ground states at the Kohn-Sham level.

The electron density of any system can be varied by a strategy called uniform scaling. The relationship between scaled and initial electron densities is given by $n_\gamma = \gamma^3 n(\gamma r)$, where γ is the scaling parameter. In Figure 1.3, the radial density distribution of hydrogenic 1s wave-function is shown for several different scaling parameters. The total number of particles is conserved before and after scaling. For the uniform electron gas, we can see that when the electron density is scaled, the kinetic energy and exchange energy per particle can be calculated from the un-scaled one. The scaling properties of correlation are not as simple as exchange energy.

$$\begin{cases} t_s(n_\gamma) = \gamma^2 t_s(n) \\ \varepsilon_{\mathrm{x}}^{\mathrm{unif}}(n_\gamma) = \gamma \varepsilon_{\mathrm{x}}^{\mathrm{unif}}(n) \end{cases} \tag{1.69}$$

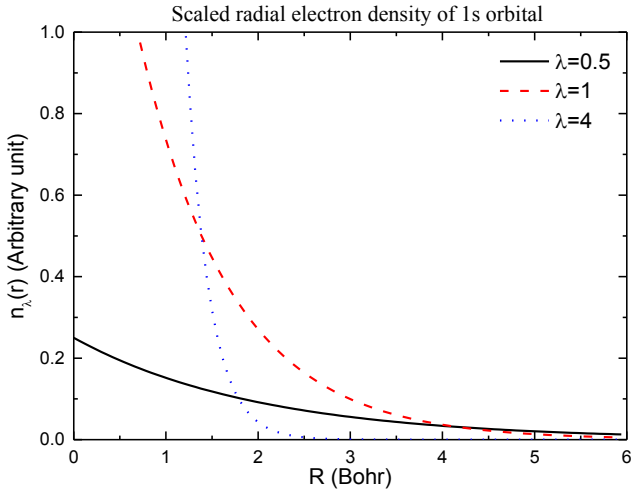

Figure 1.3: The radial density distributions of the hydrogenic 1s orbital using different scaling parameters. The analytical expression for radial density of 1s orbital is $n_\lambda = 2\gamma^3 e^{-\gamma r}$.

LSDA starts from the exchange-correlation energy of spin-resolved uniform electron gas (UEG), so it preserves many good scaling properties of UED. Practically, LSDA is also a great success, and it is used in electronic structure calculations nowadays. It is found that LSDA is more accurate for compact structures with slowly varying densities than it is for atoms and loosly bonded crystals where the electron density distribution is less uniform. For extended structures like crystals, the exchange-correlation hole of LSDA is pretty accurate, but it is too diffuse for atoms where the electron densities are more localized than solids [59]. As a result, LSDA usually overestimates the cohesive energy for molecules and solids. The lattice constants of crystal structures are also underestimated by LSDA. In the surface science, LSDA gives good surface energy for metals, but the computed adsorption energy is too large.

Gunnarsson and Lundqvist [69] discovered that the exchange-correlation hole of LSDA satisfies all constraints for the exact hole (See section 1.6.1). To some extent, this explains why LSDA gives quite reasonable resutls for condensed phases.

1.6.3.2 Generalized Gradient Approximation

The earliest version of GGA is the gradient expansion approximation (GEA). The exchange-correlation energy functional is given as [22, 69]

$$E_{\mathrm{xc}}^{\mathrm{GEA}}[n_{\uparrow},n_{\downarrow}] = E_{\mathrm{xc}}^{\mathrm{LSDA}}[n_{\uparrow},n_{\downarrow}] + \int C_{xc}^{\uparrow\uparrow}(n_{\uparrow},n_{\downarrow})\frac{\left|\nabla n_{\uparrow}\right|^2}{n_{\uparrow}^{4/3}}d^3\vec{r} + \int C_{xc}^{\downarrow\downarrow}(n_{\uparrow},n_{\downarrow})\frac{\left|\nabla n_{\downarrow}\right|^2}{n_{\downarrow}^{4/3}}d^3\vec{r} + \int C_{xc}^{\downarrow\downarrow}(n_{\uparrow},n_{\downarrow})\frac{\left|\nabla n_{\downarrow}\right|^2}{n_{\uparrow}^{2/3}n_{\downarrow}^{2/3}}d^3\vec{r} \quad (1.70)$$

where $C_{xc}^{\sigma\sigma'}(n_{\uparrow},n_{\downarrow})$ is the derived coefficients.

The GEA is supposed to be more accurate than LSDA for the slowly varying densities satisfying the following conditions:

$$\begin{cases} \dfrac{\nabla n}{n} \ll k_F \\ \dfrac{\nabla n}{n} \ll k_s \end{cases} \tag{1.71}$$

here, we define the local Fermi wave vector $k_F = (3\pi^2 n)^{1/3} = 2\pi/\lambda_F$ and local Thomas-Fermi screening wave vector $k_s = \sqrt{4k_F/\pi a_0} = 1/\lambda_s$, where λ_F and λ_s are local Fermi wave-length and local Thomas-Fermi screening length, and a_0 is the Bohr radius (0.529 Å). However, equation 1.71 is never fulfilled by real atoms, molecules and solids. As a result, GEA works badly for those systems. Later, it was found that the exchange and correlaton holes of GEA violate many constraints which are satisfied by LSDA and exact holes [22].

PW91 and PBE are the two most important and representative exchange-correlation functionals at GGA level [24, 25]. PBE is a simplified version of PW91. The exchange and correlation functionals are constructed separately. The exchange energy of a GGA functional for the spin non-polarized density is usually expressed as:

$$E_x^{GGA}[n] = \int n\varepsilon_{\mathrm{x}}^{\mathrm{unif}}(n)F_x(s)d^3\vec{r} \tag{1.72}$$

where $\varepsilon_x^{unif}(n)$ is the exchange energy of spin non-polarized UEG, given in Equation 1.59; *s* is the reduced density gradient, another dimensionless quantiy evaluated by *s* = $|\nabla n|/(2k_F n)$. $F_s(s)$ is the gradient enhancement factor, playing the central role in exchange energy functional. A general expression for $F_s(s)$ is given by:

$$F_x(\mathrm{s}) = 1 + \kappa - \frac{\kappa}{1 + \mu s^2 / \kappa} \tag{1.73}$$

A non-empirical GGA exchange functional must satisfy as many contraints as possible. Those constraints are [25, 31]:

1. The spin scaling relation for exchange energy

$$E_x[n_\uparrow, n_\downarrow] = \frac{1}{2} E_x[2n_\uparrow, 0] + \frac{1}{2} E_x[2n_\downarrow, 0] \tag{1.74}$$

2. Uniform density scaling (See also equation 1.69 for UEG)

$$E_x[n_\lambda] = \lambda E_x[n] \tag{1.75}$$

3. Lieb-Oxford bound

$$E_x[n_\uparrow, n_\downarrow] \geq E_{xc}[n_\uparrow, n_\downarrow] \geq -1.679 \int n^{4/3} d^3\vec{r} \tag{1.76}$$

with $E_x^{LDA}[n] = -1.679 \int n^{4/3} d^3\vec{r}$.

4. Density in the slow varying limit

$$E_{\mathrm{x}}^{\mathrm{GGA}}[n] = \int n \varepsilon_{\mathrm{x}}^{\mathrm{unif}}(n)(1 + \mu_{\mathrm{GE}} s^2) d^3\vec{r} \tag{1.77}$$

with $\mu_{GE} = 10/81 \approx 0.12345679$ for the GEA in equation 1.70.

The enhancement factors of PW91 and PBE are expressed as:

PW91 [24]

$$F_x(s) = \frac{1 + 0.19645 s \sinh^{-1}(7.7956 s) + (0.2743 - 0.1508 e^{-100 s^2}) s^2}{1 + 0.19645 s \sinh^{-1}(7.7956 s) + 0.004 s^4} \tag{1.78}$$

PBE [25]

$$F_x(s) = 1 + 0.804 - \frac{0.804}{1 + \frac{0.21951 s^2}{0.804}} \tag{1.79}$$

It can be shown that the exchange energy functional of PW91 satisfies all four constraints given in equations 1.74-77. Meanwhile, PBE violates the fourth constraint, indicating that it does not recover the second order gradient expansion for the density in the slow varying limit. Note that in equation 1.73, recovering equation 1.77 requires $\mu = \mu_{GE}$, and PBE value (0.21951) are two times larger than the correct number. The reasons why PBE adopts such value are based on two facts. First of all, the PBE exchange energy functional gives the better exchange energy for neutral atoms when using the current μ in its form [30]; otherwise, the μ in PBE was also chosen to make second order gradient expansion of exchange to cancel that of correlation, because it is believed that LSDA is more accurate than GEA for linear response of the uniform gas [31]. In Figure 1.4, the gradient enhancement factors of PW91 and PBE are compared to LDA and GEA (See equation 1.77). LDA is represented by horizontal line, becase it is not dependent on *s*; GEA violates the sum rule of exchange hole, its profile increases monotonically with *s* without upper limit; PW91 and PBE give similar profiles in most *s* range. For very large *s* (which energetically may not important), PW91 decreases with *s* and then approaches zero when $s \longrightarrow \infty$. The large *s* behavior of GGA exchange enhancement factor is determined by the Leib-Oxford bound. This constraint can be satisfied by a GGA in two different ways. The global Leib-Oxford bound is given by equation 1.76 as an integration form, requiring $F_x(s) \leq 2.273$ or $\kappa \leq 1.273$; meanwhile, PBE and PW91 fulfill the local Leib-Oxford bound, requiring $F_x(s) \leq 1.804$ or $\kappa \leq 0.804$. The local Leib-Oxford bound is given by

$$n\varepsilon_{\mathrm{x}}^{\mathrm{unif}}(n)F_x(s) \geq -1.679n^{4/3} \tag{1.80}$$

Zhang and Yang [26] showed that for the given eletron density, the fulfillment of equation 1.80 is sufficient but not a necessary condition for satisfying global Leib-Oxford bound. In contrast, Perdew and coworkers showed that it is also a necessary condition [70].

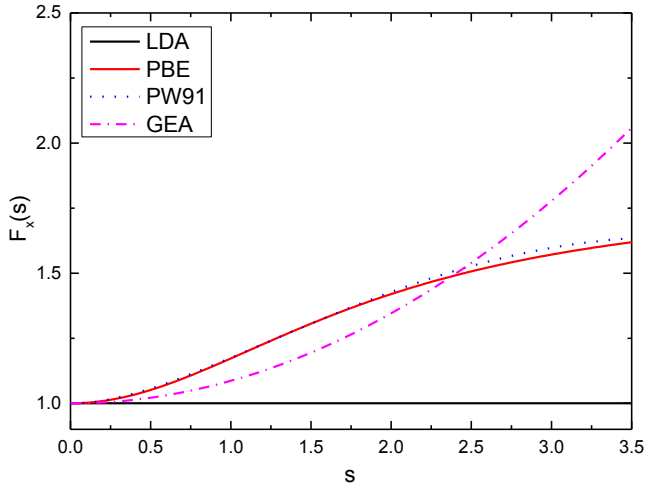

Figure 1.4: The plots of gradient enhancement factor of LDA, GEA, PW91 and PBE.

The correlation functionals of PW91 and PBE are much complicated than their exchange part. The starting points are LSDA and GEA. The general expression of correlation energy functional is written by [24, 25]

$$E_c^{GGA}[n_\uparrow, n_\downarrow] = \int n\left[\varepsilon_c^{unif}(r_s,\xi) + H(r_s,\xi,t)\right]d^3\vec{r} \qquad (1.81)$$

where t is another scaled density gradient, and it is computed by $t = |\nabla n|/[2g(\xi)k_s n]$. k_s is local Thomas-Fermi screening wave-vector as defined in equation 1.71, and g(ξ) is given in equation 1.63, a function related to local spin polarization. $H(r_s,\xi,t)$ is the gradient correction to correlation energy per particle, and it has different forms in PW91 and PBE.

The constraints for correlation energy functional are not as simple and transparent as those of exchange energy functional. Some well-known constraints are [25, 30, 31]:

1. Second order gradient expansion in slow varying limit ($t \longrightarrow 0$)

$$E_c^{\mathrm{GGA}}[n] = \int n\varepsilon_c^{\mathrm{unif}}(n)(1+\beta_{\mathrm{GE}}t^2)d^3\vec{r} \tag{1.82}$$

where the GEA second order expansion coefficient $\beta_{GE} = 0.066725$.

2. The rapid varying limit ($t \longrightarrow \infty$)

$$E_c^{GGA}[n_\uparrow, n_\downarrow] = 0 \tag{1.83}$$

3. High density limit ($r_s \longrightarrow \infty$)

$$E_c^{GGA}[n_\uparrow, n_\downarrow] = -C \tag{1.84}$$

where C is a positive constant (See equation 1.68). The second constraint is required by the sum rule of correlation hole (equation 1.51). In the rapid varying limit, the only way to satisfy the sum rule is to make the GEA correlation hole vanish.

The correlation functional of PW91 is given by [24]:

$$H(r_s, \xi, t) = H_0 + H_1 \tag{1.85}$$

where

$$H_0(r_s, \xi, t) = \mathrm{g}^3 \frac{\beta^2}{2\alpha} \ln\left[1 + \frac{2\alpha}{\beta}\frac{t^2 + At^4}{1 + At^2 + A^2t^4}\right] \tag{1.86}$$

$$H_1(r_s, \xi, t) = \nu\left[C_c(r_s) - C_c(0) - \frac{3C_x}{7}\right] g^3 t^2 e^{-100g^4(k_s^2/k_F^2)t^2} \tag{1.87}$$

with $\alpha = 0.09$, $\nu = (16/\pi)(3\pi^2)^{1/3}$, $C_c(0) = 0.004235$, $C_x = -0.001667$, $\beta = \nu C_c(0)$ and

$$A = \frac{2\alpha}{\beta}\frac{1}{e^{-2\alpha\varepsilon_c^{unif}(r_s,\xi)/(\mathrm{g}^3\beta^2)} - 1} \tag{1.88}$$

$$C_c(r_s) = C_{xc}(r_s) - C_x \tag{1.89}$$

$$C_{xc}(r_s) = \frac{2.568 + ar_s + br_s^2}{1 + cr_s + dr_s^2 + 10br_s^3} \times 10^{-3} \tag{1.90}$$

here $a = 23.266$, $b = 7.389\times10^{-3}$, $c = 8.723$ and $d = 0.472$. In equation 1.88, $\varepsilon_c^{unif}(r_s, \xi)$ is given in equation 1.62. Note that PW91 uses the expressions of correlation energy of UEG in the high density case to interpolate the value at arbitrary ξ (See also equations 1.65 and 1.66).

On the other hand, the correlation energy of PBE is a simplified version of PW91 case, and which is given by [22, 25]:

$$H(r_s, \xi, t) = \mathrm{g}^3 \gamma \ln\left\{1 + \frac{\beta}{\gamma} t^2 \left[\frac{t^2 + At^4}{1 + At^2 + A^2t^4}\right]\right\} \tag{1.91}$$

and

$$A = \frac{\beta}{\gamma}\left[e^{\frac{-\varepsilon_c^{unif}(r_s,\xi)}{\gamma g^3}} - 1\right]^{-1} \tag{1.92}$$

here $\gamma = 0.031091$ and $\beta = 0.066725$.

It can be shown that PBE satisfies all three constraints given in equations 1.82-84 [22]. While, PW91 violates the third constraint, because it uses euqations 1.65-66 rather than 1.60-61. Since LSDA correlation is also built from equations 1.65-66, therefore, both LSDA and PW91 do not scale properly in the high density limit [22].

Once the expressions for exchange and correlation functional are known, the total exchange-correlation energy of GGA can be evaluated as [24]:

$$E_{\mathrm{xc}}^{\mathrm{GGA}}[n_\uparrow, n_\downarrow] = \int n\varepsilon_{\mathrm{x}}^{\mathrm{unif}}(r_s, \xi = 0) F_{\mathrm{xc}}^{\mathrm{GGA}}(\mathrm{r}_s, s, \xi) d^3\vec{r} \tag{1.93}$$

where $\varepsilon_x^{unif}(r_s, \xi = 0)$ is the exchange energy per particle of spin non-polarized UEG, given in equation 1.59, and exchange-correlation gradient enhancement factor $F_{xc}^{GGA}(r_s, s, \xi)$ is given by

$$F_{\mathrm{xc}}^{\mathrm{GGA}}(r_s, s, \xi) = \frac{\varepsilon_{\mathrm{xc}}^{\mathrm{GGA}}(r_s, s, \xi)}{\varepsilon_{\mathrm{x}}^{\mathrm{unif}}(\mathrm{r}_s, \xi = 0)} \tag{1.94}$$

here the exchange-correlation energy of GGA per particle is computed as

$$\varepsilon_{\mathrm{xc}}^{\mathrm{GGA}}(r_s, s, \xi) = \varepsilon_{\mathrm{x}}^{\mathrm{unif}}(r_s, \xi = 0) F_x(s, \xi) + [\varepsilon_{\mathrm{c}}^{\mathrm{unif}}(r_s, \xi) + \mathrm{H}(\mathrm{r}_s, \xi, \mathrm{t})] \tag{1.95}$$

With

$$F_x(s, \xi) = \frac{1}{2}\left[(1+\xi)^{4/3} F_x(\mathrm{x}) + (1-\xi)^{4/3} F_x(\mathrm{y})\right] \tag{1.96}$$

and x = $s/(1+\xi)^{1/3}$ and y = $s/(1-\xi)^{1/3}$.

In Figures 1.5 and 1.6, the three-dimensional contours of exchange-correlation gradient enhancement factor are displayed for PW91 and PBE in the spin non-polarized case ($\xi = 0$). In the spin fully polarized case ($\xi = 1$), the shapes of those contours are similar to those of the spin non-polarized situation. Although, PW91 satsifies the second order gradient expansion for both exchange and correlation energies, PBE and PW91 curves in this limit are qualitively similar to each other. The main difference between PW91 and PBE in their exchange enhancement factors is attributed to the large *s* behavior. Again, both GGAs fulfill the local Leib-Oxford constraint, but when *s* goes to infinity, $F_x(s)$ of PW91 is reduced to zero rather than 1.804 in PBE. The main reason is due to another less well-known constraint for exchange-correlation at large *s* under the non-uniform scaling of electron density [44]. The non-uniform scaling of electron density

is related to the dimensional crossover, and which could be important for low-dimensional materials such as carbon nanotubes and layered crystalline structures.

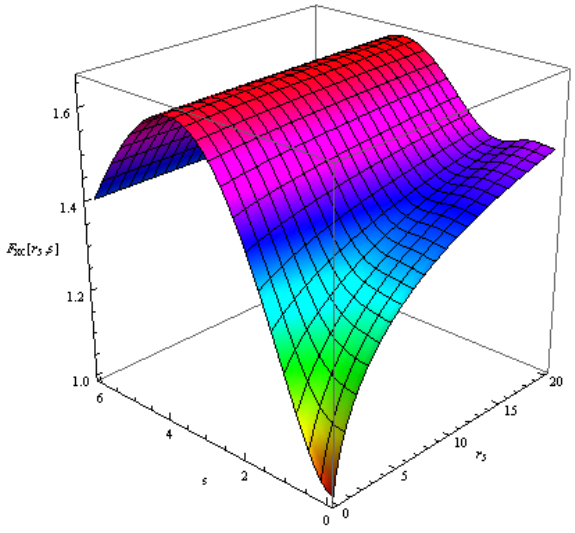

Figure 1.5: The three-dimensional (3-D) contour plot of exchange-correlation enhancement factor of PW91 in spin non-polarized case ($\xi = 0$).

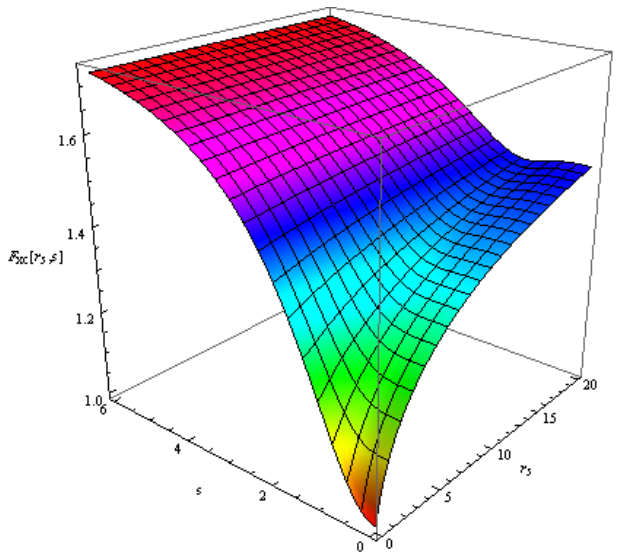

Figure 1.6: The 3-D contour plot for exchange-correlation enhancement factor of PBE in spin non-polarized case ($\xi = 0$).

Several other widely used exchange-correlation functionals of GGA level will be briefly reviewed here.

In 1998, Zhang and Yang [26] slightly revised the exchange part of PBE functional, keeping $F_x(s)$ the same as PBE, but using $\kappa = 1.245$. The correlation energy functional is completely identical to PBE form. This new GGA is named revised PBE or revPBE. For any spin polarized physical density, in order to fulfill Leib-Oxford bound for exchange energy, the upper limit of $\kappa = 0.804$. However, it is found that revPBE does not violate equation 1.76 in many calculations for atoms, molecules and surfaces [27]. Otherwise, revPBE also does not satisfy equation 1.77.

Hammer *et al*. [27] revisited PBE and revPBE, and the new PBE exchange gradient enhancement factor proposed by them is given by

$$F_x(s) = 1 + \kappa(1 - e^{-\mu s^2/\kappa}) \tag{1.97}$$

here $\kappa = 0.804$ and $\mu = 0.21951$. Note that μ is the same as PBE. The PBE correlation is adopted in this new PBE known as RPBE. The exchange enhancement factor of RPBE imitates the behavior of revPBE for s in the range of 0 to 2.5. For large s, it recovers PBE profile. Similarly to PBE and revPBE, RPBE violates the second order gradient expansion in small s limit.

In 2006, Wu and Cohen [29] derived another GGA type exchange enhancement factor given below:

$$F_x = 1 + \kappa - \frac{\kappa}{1 + x/\kappa} \tag{1.98}$$

With

$$x = \frac{10}{81}s^2 + (\mu - \frac{10}{81})s^2 \, e^{-s^2} + \ln(1 + cs^4) \tag{1.99}$$

here $\kappa = 0.804$, $\mu = 0.21951$ and $c = 0.0079325$. Constant c was chosen to recover the gradient expansion of Svendsen and von Barth [71] for slowly varying density. This expansion is given by:

$$F_x(s) = 1 + \frac{10}{81}p + \frac{146}{2025}q^2 - \frac{73}{405}qp + Dp^2 + O(\nabla^6) \tag{1.100}$$

with $p = s^2$, $q = \nabla^2 n/[4(3\pi^2)^{\frac{2}{3}} n^{\frac{5}{3}}]$ and $D = 0$ from the best numerical estimation. Obviously, WC06 exchange functional fulfill all four constraints mentioned before.

In 2008, Perdew *et al*. [30] slightly modified some coefficients of PBE exchange and correlation functionals. The obtained new GGA functional is known as PBE revised for solids or PBEsol. The exchange enhancement factor of PBEsol recovers the second order gradient expansion for small s, requiring that $\mu = \mu_{GE} = 10/81$. It is also believed that the gradient expansion of correlation energy for small s is not quite relevant to real systems. Therefore, PBEsol correlation energy was refitted to exchange-correlation energy of jellium surface computed from TPSS [37]. PBEsol uses $\beta = 0.046$ rather than β_{GE} in PBE.

In the same year, Zhan and Truhlar [38] published SOGGA (second order generalized gradient approximation). SOGGA recovers the second order gradient expansion in both exchange and correlation parts (See equations 1.77 and 1.82). The PBE correlation functional was used without further modification, because it respects the equation 1.82. The exchange gradient enhancement factor of SOGGA is written as:

$$F_x(s) = 1 + \kappa \left(1 - \frac{1}{2} \frac{1}{1 + \mu s^2 / \kappa} - \frac{1}{2} e^{-\mu s^2 / \kappa} \right) \tag{1.101}$$

where μ = 10/81 and κ = 0.552.

The exchange gradient enhancement factors of GGA-level functionals discussed here are plotted in Figure 1.7. The large s behaviour of $F_x(s)$ is determined by κ. Those GGA functionals with large κ values (revPBE, RPBE and etc.), their profiles are increased faster than others with the increasing of s. PBEsol, WC06 and SOGGA curves at small s are close to GEA profile. SOGGA is very "soft" at large s due to its smallest κ value.

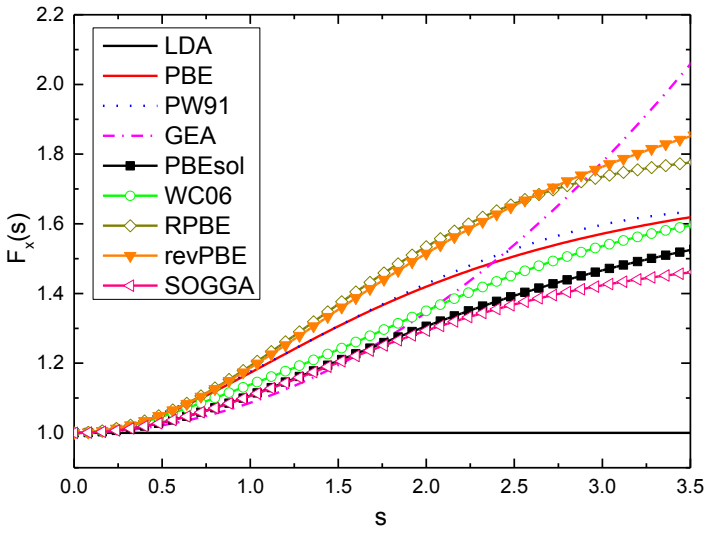

Figure 1.7: The profiles of exchange gradient enhancement factor of GGA-level functionals.

The improvement of GGA over LSDA for many properties of atoms, molecules and crystal structrues is significant. First of all, GGA-level functionals correct the over-binding problem of LSDA: The GGA atomization energy (cohesive energy) is close to experiment. Because the GGA correction to LSDA lowers the total energy of

atoms more than that of molecules and solids. GGA level functionals suffer from the famous dilemma that the geometry and energetics can not be described accurately at the same time [60, 72]. For example, PBEsol, SOGGA and WC06, which recover the second order expansion in exchange energy, usually give the good description for lattice constants and bulk moduli, but the computed cohesive energy and energy barrier are less accurate than PBE. In addition, RPBE and revPBE give the good results for surface adsorption energy, but they perform even worse than PBE for lattice geometry. At GGA-level, there is no universal functional which is good for all properties (surface adsorption, energetics and geometry).

1.6.3.3 Meta-Generalized Gradient Approximation

Generally, the formulation of the meta-GGA exchange-correlation functional is more flexible than GGA and LSDA, because the orbital kinetic energy density is also incorporated in its construction (See equation 1.56). In other words, meta-GGAs can be much more complicated than GGAs and LSDA. In this dissertation, we will only test several non-emiprical meta-GGAs forms such as PKZB [36], TPSS [37], revTPSS [39], regTPSS [40] and MGGA_MS variants [41, 42]. Therefore, the discussions here are mainly focused on those meta-GGA functionals. Otherwise, we are particularly interested in the exchange part of meta-GGAs, because it is found that the performance of meta-GGAs on geometry and energetics can be explained using their exchange enhancement factors. Since the total exchange-correlation energy is dominated by

exchange energy for normal solids, it is expected to see the correlation between performance of a meta-GGA and its exchange enhancement factor.

The Perdew, Kurth, Zupan and Blaha (PKZB) meta-GGA was constructed following the philosophy of PBE GGA-level functional [36]. Besides those constraints given in equations 1.74-77, the exchange enhancement factor of PKZB recovers the fourth order gradient expansion coefficient of Svendsen and von Barth [71] (See equation 1.100). The exchange energy of the meta-GGA for a spin non-polarized density can be written as

$$E_{\mathrm{x}}^{\mathrm{MGGA}}[n]=\int n\varepsilon_{\mathrm{x}}^{\mathrm{unif}}(n)F_x(n,\nabla n,\tau)d^3\vec{r} \tag{1.102}$$

where $F_x(n,\nabla n,\tau)$ is the exchange enhancement factor, τ is the kinetic energy density. In PKZB meta-GGA, the exact form is

$$F_x(p,\tilde{q})=1+\kappa-\frac{\kappa}{1+x/\kappa} \tag{1.103}$$

and

$$x=\frac{10}{81}p+\frac{146}{2025}\tilde{q}^2-\frac{73}{405}\tilde{q}p+\left[\mathrm{D}+\frac{1}{\kappa}\left(\frac{10}{81}\right)^2\right]p^2 \tag{1.104}$$

with

$$p=\left|\nabla n\right|^2/[4(3\pi^2)^{2/3}n^{8/3}]=s^2 \tag{1.105}$$

$$\tilde{q}=3\tau/[2(3\pi^2)^{2/3}n^{5/3}]-9/20-p/12 \tag{1.106}$$

where κ = 0.804, and D = 0.113. Note that D was fixed to zero in equation 1.98.

Euqation 1.103 is plotable in two special cases:

1. The single orbital region or one (two) electron density

$$\tau = \tau_W = \frac{|\nabla n|^2}{8n} \tag{1.107}$$

$$\tilde{q} = \frac{2}{3} p - \frac{9}{20} \tag{1.108}$$

where τ is equivalent to Weizsäcker kinetic energy density (τ_W), which is the lower bound of τ and it is exact for one-electron system.

2. The slow varying limit of electron density

$$\tau = \tau_{\text{unif}} = \frac{3}{10}(3\pi^2)^{2/3} n^{5/3} \tag{1.109}$$

$$\tilde{q} = -\frac{1}{12} p \tag{1.110}$$

In Figure 1.8, the profiles of equation 1.103 in two cases are shown for PKZB. Although, PKZB respects the Leib-Oxford bound, we can see that its exchange enhancement factor grows much faster than PBE for relatively large s ($s >$ 1).

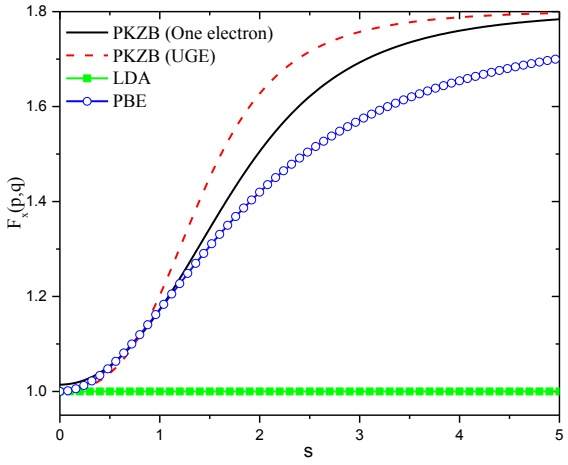

Figure 1.8: The profiles of the exchange enhancement factor of PKZB in two special cases: the single orbital region ($\tau = \tau_W$) and the UEG ($\tau = \tau_{\text{unif}}$). For the convinence, PBE and LSDA are also shown in the figure.

The correlation energy of PKZB is built based on PBE correlation energy, preserving all good properties of PBE (Equations 1.82-84). Another extra advantage of a meta-GGA correlation functional is that it can be self-interaction free for spin polarized one-electron density. PKZB employs the following expression to compute the correlation energy [36].

$$E_{\mathrm{c}}^{\mathrm{MGGA}}[n_{\uparrow},n_{\downarrow}]=\int\left\{\begin{array}{l} n\varepsilon_{\mathrm{c}}^{\mathrm{GGA}}(n_{\uparrow},n_{\downarrow},\nabla n_{\uparrow},\nabla n_{\downarrow})\left[1+C\left(\frac{\sum_{\sigma}\tau_{\sigma}^{W}}{\sum_{\sigma}\tau_{\sigma}}\right)^{2}\right] \\ -(1+C)\sum_{\sigma}\left(\frac{\tau_{\sigma}^{W}}{\tau_{\sigma}}\right)^{2} n_{\sigma}\varepsilon_{\mathrm{c}}^{\mathrm{GGA}}(n_{\uparrow},0,\nabla n_{\uparrow},0) \end{array}\right\} d^{3}\vec{r} \qquad (1.111)$$

Here the ε_c^{GGA} is the correlation energy of GGA per particle, and it can be compute from equation 1.81. The spin resolved orbital kinetic energy density is computed as $\tau_\sigma = \sum_\alpha |\nabla\phi_{\alpha\sigma}(\vec{r})|^2/2$ and the Weizsäcker kinetic energy density (τ_W^σ) of equation 1.107. The constant $C = 0.53$, so that the computed surface correlation energies for jellium models by PKZB are in close agreement with those of PBE. It is easy to verify that for the one-electron system, $\tau_\sigma = \tau_\sigma^W$ and the term in the curly braket of equation 1.111 vanishes. In contrast to GGAs, equation 1.111 is not plottable.

The first widely used non-empirical meta-GGA is TPSS [37]. The main idea in the construction of TPSS exchange energy is that the exchange potential must be finite at the nucleus for the ground one- and two-electron densities. TPSS exchange also respects the constraints which are are already satisfied by PKZB. The exchange energy of TPSS is also computed from equation 1.102, but with the following exchange enhancement factor

$$F_x(p,z) = 1 + \kappa - \frac{\kappa}{1 + \frac{x(p,z)}{\kappa}} \tag{1.112}$$

where $\kappa = 0.804$ and the function $x(p,z)$ is given as

$$x(p,z) = \frac{\left\{\left[\frac{10}{81} + c\frac{z^2}{(1+z^2)^2}\right]p + \frac{146}{2025}\tilde{q}_b^2 - \frac{73}{405}\tilde{q}_b\sqrt{\frac{1}{2}\left(\frac{3}{5}z\right)^2 + \frac{1}{2}p^2}\right\}}{(1+\sqrt{e}p)^2} \tag{1.113}$$
$$\left\{+\frac{1}{\kappa}\left(\frac{10}{81}\right)^2 p^2 + 2\sqrt{e}\frac{10}{81}\left(\frac{3}{5}z\right)^2 + e\mu p^3\right\}$$

and

$$\tilde{q}_b = \frac{9}{20}\frac{(\alpha-1)}{[1+b\alpha(\alpha-1)]^{1/2}} + \frac{2p}{3} \tag{1.114}$$

$$\alpha = \frac{\tau - \tau_W}{\tau_{\text{unif}}} \tag{1.115}$$

$$z = \frac{\tau_W}{\tau} = \frac{5p}{5p + 3\alpha} \tag{1.116}$$

here $\mu = 0.21951$, $c = 1.59096$, $e = 1.537$ and $b = 0.40$. Note that p is given in Equation 1.105, τ_W is defined in equation 1.107 and τ_{unif} is given by equation 1.109. Due to the relationships given in equations 1.105, 1.115 and 1.116, the exchange enhancement factor of TPSS can be also written as a function of s and α or $F_x(s,\alpha)$. Simialr to PKZB (Equation 1.104), some coefficients in equation 1.113 of TPSS are identical to those of equation 1.100, because both meta-GGAs recover the fourth order gradient expansion of Svendsen and von Barth [71] in slowly varying limit. The values of α and z in two special cases should be checked further. In the UEG, $\tau = \tau_{\text{unif}}$ and $\tau_W \to 0$,

then $\alpha = 1$ and $z = 0$; for the one- or two-electron densities, $\tau = \tau_W$, we have $\alpha = 0$ and $z = 1$. Therefore, a meta-GGA level density functional can distinguish two different types of electron density in space. The two densities may have the same reduced density gradient, thus GGA-level functionals treat them as the same density. The convergence of exchange potential at the nucleus for one- or two electron densities in TPSS is achieved by requiring that

$$\left.\frac{dF_x(p=s^2, z=1)}{ds}\right|_{s=0.376} = 0 \tag{1.117}$$

here, $s = 0.376$ refers to a two-electron exponential density at the nucleus.

In contrast to PKZB, the exchange enhancement factor of TPSS is plottable for arbitrary s and α values. In Figure 1.9, the profiles of equation 1.112 are given for two cases, i.e., UGE and one- or two electron densities. They are also compared to PBE and LDA curves. Meanwhile, we also plot the 3-D contour of $F_x(s, \alpha)$ for TPSS in Figure 1.10. The main difference between TPSS and PBE is that in the single orbital region ($\alpha = 0$), TPSS gives more negative exchange energy per particle than PBE. This is reasonable, because the electron density in the single orbital region is usually more localized than uniform electron gas. Therefore, the exchange hole is also expected to be more deep and localized aroung the reference electron. The meta-GGA functionals can distinguish single orbital region from other electron densities, giving better description for exchange energy than GGA functionals do. This is the main advantage of the meta-GGA level functional.

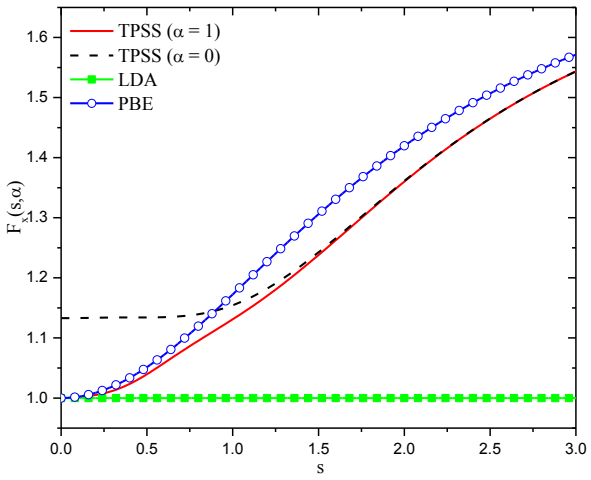

Figure 1.9: The profiles of exchange enhancement factor of TPSS in two different densities are compared to PBE and LDA. Note that $\alpha = 0$ refers to one- or two electron densities, and $\alpha = 1$ corresponds to UEG case.

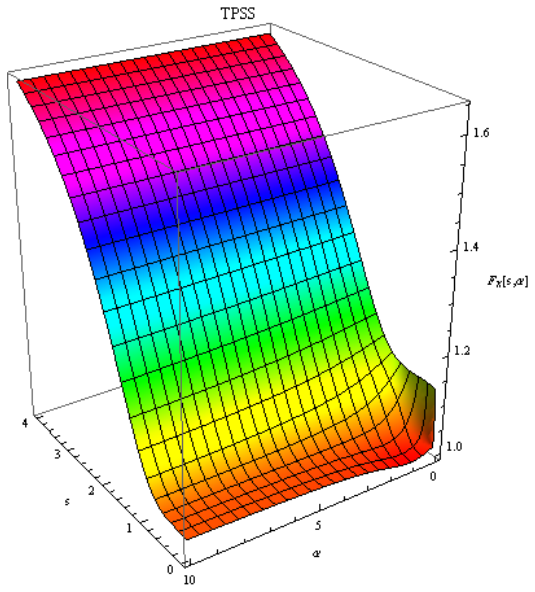

Figure 1.10: The 3-D contour plot of the exchange enhancement factor of TPSS.

The correlation energy of TPSS was constructured from a revised PKZB correlation energy functional, and can be expressed as

$$E_c^{\mathrm{MGGA}}[n_\uparrow, n_\downarrow] = \int n\varepsilon_c^{\mathrm{revPKZB}}[1 + d\varepsilon_c^{\mathrm{revPKZB}}(\tau_W/\tau)^3]d^3\vec{r} \qquad (1.118)$$

where d = 2.8 hartree^{-1}, and $\varepsilon_c^{revPKZB}$ the revised PKZB correlation energy functional per particle [37].

$$\varepsilon_{\mathrm{c}}^{\mathrm{revPKZB}} = \left\{ \begin{array}{l} \varepsilon_{\mathrm{c}}^{\mathrm{PBE}}(n_\uparrow, n_\downarrow, \nabla n_\uparrow, \nabla n_\downarrow)[1 + C(\zeta,\xi)(\tau_W/\tau)^2] \\ -[1 + \mathrm{C}(\zeta,\xi)](\tau_W/\tau)^2 \sum_\sigma \frac{n_\sigma}{n} \tilde{\varepsilon}_c \end{array} \right\} \tag{1.119}$$

and

$$C(\zeta,\xi) = \frac{C(0,\xi)}{\left\{1 + \zeta^2[(1+\xi)^{-4/3} + (1-\xi)^{-4/3}]/2\right\}^4} \tag{1.120}$$

$$\tilde{\varepsilon}_c = \max\left[\varepsilon_{\mathrm{c}}^{\mathrm{PBE}}(n_\uparrow, 0, \nabla n_\uparrow, 0), \varepsilon_{\mathrm{c}}^{\mathrm{PBE}}(n_\uparrow, n_\downarrow, \nabla n_\uparrow, \nabla n_\downarrow)\right] \tag{1.121}$$

$$C(0,\xi) = 0.53 + 0.87\xi^2 + 0.50\xi^4 + 2.26\xi^6 \tag{1.122}$$

where $\zeta = |\nabla\xi|/2(3\pi^2 n)^{1/3}$. Note that in PKZB correlation energy functional (Equation 1.111), the C = 0.53. It is treated as function in TPSS.

In 2009, Perdew *et al*. [39] slightly modified the original TPSS exchange-correlation functional and named the new meta-GGA as revised TPSS or revTPSS. The main argument is that TPSS gives good energetics, but the lattice constants are too large. The new functional was supposed to give the good results for both geometry and energetics (surface energies and cohesive energy). The expressions for exchange and correlation functionals of revTPSS are basically the same as those of TPSS. For exchange energy, the term $cz^2p/(1+z^2)^2$ in equation 1.113 is replaced by $cz^3p/(1+z^2)^2$, and set μ = 0.14, c = 2.35204 and e = 2.1677. In Figure 1.11, we plot the exchange enhancement factor of revTPSS in two limits, and compare them to TPSS, PBE and LDA. Since revTPSS respects PBEsol exchange enhancement factor,

and uses a smaller μ than PBE and TPSS. For relatively large s, its profiles grow less rapidly than those of TPSS and PBE.

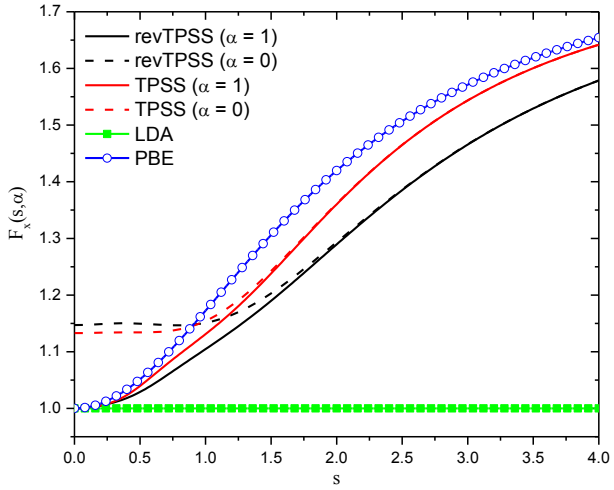

Figure 1.11: The profiles of exchange enhancement factor of revTPSS, TPSS, PBE and LDA.

In Figure 1.12, the 3-D contour plot of exchange enhancement factor is illustrated for revTPSS.

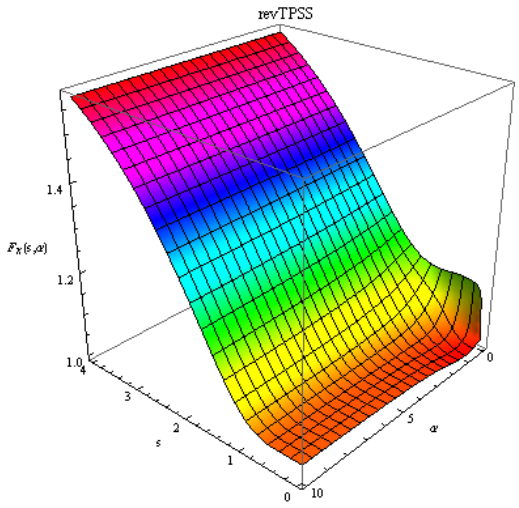

Figure 1.12: The 3-D contour plot of the exchange enhancement factor of revTPSS.

The correlation energy of revTPSS is simply obtained from TPSS by requiring that

$$\beta(r_s) = \frac{0.066725(1+0.1r_s)}{(1+0.1778r_s)} \tag{1.123}$$

and

$$C(0,\xi) = 0.59 + 0.9269\xi^2 + 0.6225\xi^4 + 2.1540\xi^6 \tag{1.124}$$

where $\beta = 0.066725$ in PBE and TPSS.

The regularized TPSS or regTPSS was proposed by Ruzsinszky *et al*. [40] in 2012. The main motivation is to remove the order of limits problem in TPSS and revTPSS. Both meta-GGAs employ z and s in their exchange enhancement factors (Equation 1.112). However, equation 1.116 implies that the actual value of z is dependent on whether s or α tends to zero first.

$$\begin{cases} \lim\limits_{s\to 0}\lim\limits_{\alpha\to 0} z = 1 \\ \lim\limits_{\alpha\to 0}\lim\limits_{s\to 0} z = 0 \end{cases} \tag{1.125}$$

As a result, the values of exchange enhancement factor of TPSS or revTPSS are different in two limits. In Table 1.1, the exchange enhancemet in different limits is given for several meta-GGAs. In the second and third columns, the order of limits problem is clearly seen for TPSS and revTPSS.

Table 1.1: The exchange enhancement factor of meta-GGAs in different limits.

$F_x(s,\alpha)$	TPSS	revTPSS	regTPSS	MGGA_MS0
$\lim_{\alpha\to\infty}\lim_{s\to 0}$	1.035	1.035	1	0.856
$\lim_{\alpha\to 0}\lim_{s\to 0}$	1.014	1.014	1.147	1.144
$\lim_{s\to 0}\lim_{\alpha\to 0}$	1.133	1.147	1.147	1.144
$\lim_{\alpha\to 0}\lim_{s\to\infty}$	1.804	1.804	1.804	1.290

In regTPSS, the exchange enhancement factor is obtained by the interpolation of revTPSS exchange enhancement factor for $\alpha = 0$ and ordinary α values [40]:

$$F_x(s,\alpha) = \mathrm{F_x^{revTPSS}}(s,\alpha) + f\exp(-cs^2)[\mathrm{F_x^{revTPSS}}(s,\alpha=0) - \mathrm{F_x^{revTPSS}}(s,\alpha)] \quad (1.126)$$

and

$$f = \frac{(1-\alpha)^3}{(1+d\alpha)^3} \quad (1.127)$$

where $c = 3$ and $d = 1.475$. Note that the correlation part of regTPSS is identical to revTPSS, and thus the discussion is omitted here.

In Figure 1.13, the exchange enhancement factors of regTPSS and revTPSS are illustrated. For small s and α, revTPSS profiles drop surprisingly fast, compared to regTPSS curves, due to the order of limits problem. In regTPSS, the order of limits issue in revTPSS (also in TPSS) has been successfully eliminated.

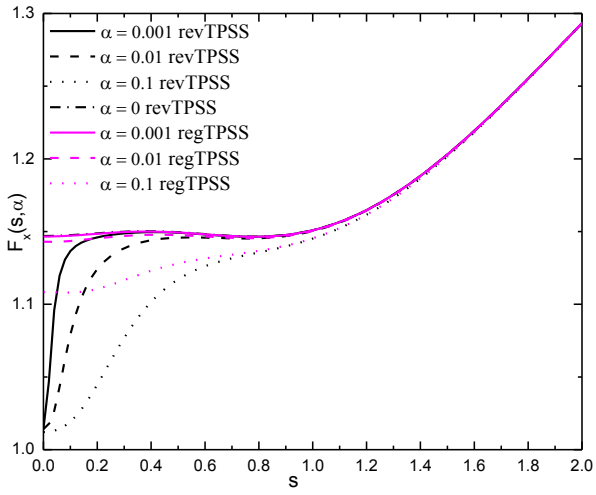

Figure 1.13: The order of limits problem in meta-GGAs.

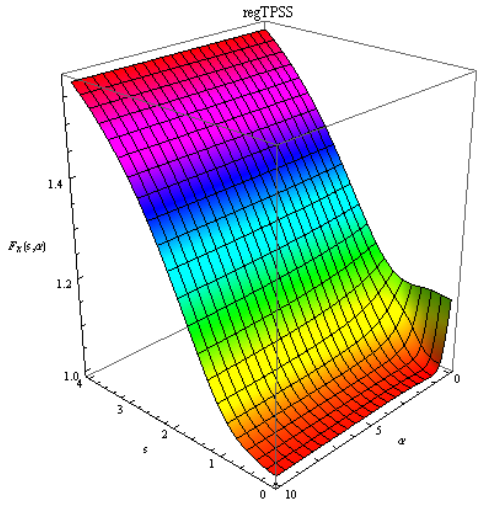

Figure 1.14: The 3-D contour plot of exchange enhancement factor of regTPSS.

Recently, there is another breakthrough in the developing of meta-GGAs. Sun *et al*. [41-43] discovered that α (See equation 1.115) is able to distinguish three different types of chemical interactions in solids, i.e., single covalent bond ($\alpha = 0$), metallic bond ($\alpha \approx 1$) and van der Waals interactions ($\alpha \rightarrow \infty$). Based on this observation, the new meta-GGA form, known as meta-GGA made simple or

MGGA_MS, was proposed. In contrast to previous meta-GGAs such as TPSS, revTPSS and regTPSS, the importance of α in a meta-GGA exchange enhancement factor is emphasized. The α dependence of $F_x(s,\alpha)$ in this new meta-GGA is completely distangled from its s dependence. Otherwise, the PBE-type exchange enhancement factor (Equation 1.73) is used in this meta-GGA. Similar to regTPSS, MGGA_MS also adopts an interpolation form, but using $\alpha = 1$ and $\alpha = 0$ values. The exchange enhancement factor of MGGA_MS is expressed as [41, 42]

$$F_{\mathrm{x}}^{\mathrm{MGGA\_MS}}(s,\alpha) = F_x^1(s) + f(\alpha)[F_x^0(p) - F_x^1(p)] \tag{1.128}$$

where

$$F_x^1(s) = 1 + \kappa - \kappa / (1 + \mu_{\mathrm{GE}} s^2 / \kappa) \tag{1.129}$$

$$F_x^0(s) = 1 + \kappa - \kappa / [1 + (\mu_{\mathrm{GE}} s^2 + \mathrm{c}) / \kappa] \tag{1.130}$$

$$f(\alpha) = \frac{(1-\alpha^2)^3}{(1+\alpha^3 + b\alpha^6)} \tag{1.131}$$

here μ_{GE} = 10/81; while, in MGGA_MS0, c = 0.28771, b = 1.0 and κ = 0.29; for MGGA_MS1, c = 0.18150, b = 1.0 and κ = 0.404; for MGGA_MS2, c = 0.14601, b = 4.0 and κ = 0.504.

The correlation part of MGGA_MS variants use PBE form, but replacing constant β by equation 1.123 [41]. The exchange enhancement factors of MGGA_MS, TPSS, revTPSS are shown in Figure 1.15. In Figure 1.16, the 3-D contour plot of the exchange enhancement factor for MGGA_MS0 is illustrated. From Figure 1.15, the most intriguing property of MGGA_MS0 is that its exchange enhancement factor increases much slower than TPSS and revTPSS. In addition, the large s limit of

MGGA_MS0 is far below that of the other meta-GGAs. The main reason is all MGGA_MS variants have very small κ values in their exchange enhancement factors. Such small κ is also used in SOGGA functional (See equation 1.99) [31]. Otherwise, $F_x^{MGGA}(s,\alpha)$ of MGGA_MS0 decreases with the increasing of α for small s. Other meta-GGAs like TPSS, revTPSS and regTPSS are increased in the same region for s.

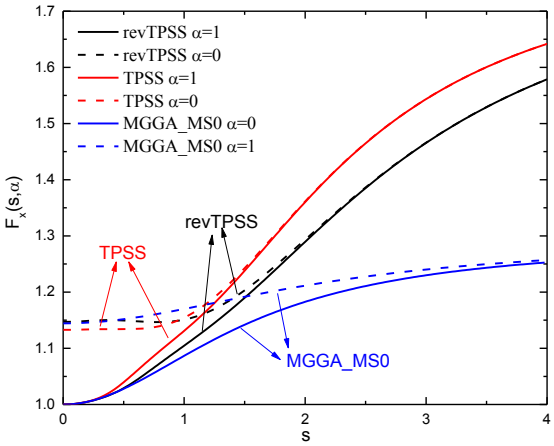

Figure 1.15: The exchange enhancement factors of TPSS, revTPSS and MGGA_MS0 are shown for two α values.

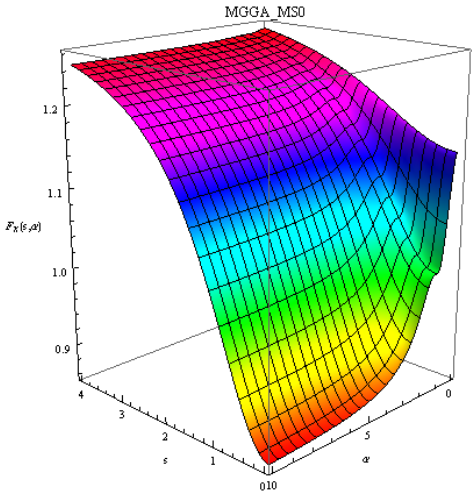

Figure 1.16: The 3-D contour plot of exchange enhancement factor of MGGA_MS0.

The meta-GGA functionals PKZB, TPSS, revTPSS, regTPSS and MGGA_MS variants have been tested for the equilibrium geometries and energetics of molecules and crystal structures, and the results were also compared with L(S)DA and GGA functionals [73, 74]. These earlier calculations indeed showed that meta-GGAs can predict the good structural properties and energetics at the same time. However, most meta-GGAs are not widely used in solid structural calculations so far. One possible reason is that they are only abailable in some main stream plane wave codes very recently.

1.6.3.4 Hyper-Generalized Gradient Approximation

The most widely tested two forms of hyper-GGA are PBE0 [49] and two HSE variants (HSE03 and HSE06) [50, 51]. The HSE family belongs to the range-separated hybrid functionals. In this dissertation, only HSE06 will be used in our calculations. The general ideal of building a hyper-GGA (or hyper-meta-GGA) is to introduce the Hartree-Fock like exact exchange into the exchange energy functional. Usually, the exchange energy of hyper-GGA is the mixture of Hartree-Fock like exact exchange with the semilocal exchange energy functional. The total exchange-correlation energy functionals of PBE0 and HSE06 are given by:

$$E_{\mathrm{xc}}^{\mathrm{PBE0}}[n] = a(E_{\mathrm{x}}^{\mathrm{HF}} - E_{\mathrm{x}}^{\mathrm{PBE}}) + E_{\mathrm{xc}}^{\mathrm{PBE}} \tag{1.132}$$

$$E_{xc}^{HSE}[n] = a(E_{\mathrm{x}}^{\mathrm{HF_{SR}}} - E_{\mathrm{x}}^{\mathrm{PBE_{SR}}}) + (1-a)E_{\mathrm{x}}^{\mathrm{PBE_{SR}}} + E_{\mathrm{x}}^{\mathrm{PBE_{LR}}} + E_{\mathrm{c}}^{\mathrm{PBE}} \tag{1.133}$$

where a is an empirical parameter, and usually taken as 0.25. SR and LR refer to the short range and long range parts of exchange hole. The partion of exchange energy into SR and LR parts is done by decomposing the Coulomb kernel according to

$$\frac{1}{r} = S_\mu(r) + L_\mu(r) = \frac{erfc(\mu r)}{r} + \frac{erf(\mu r)}{r} \tag{1.134}$$

here μ is the range separation parameter, $erf(r)$ and $erfc(r)$ are the error and complementary error functions, respectively.

The main advandage of using range-separation for exchange part is that the high computational costs of PBE0 can be significantly reduced, especially for metallic systems where PBE0 does not converge efficiently [51]. Semilocal functionals also underestimate the fundamental band gap for semiconductors and insulators, the hyrid functionals give more accurate band gaps for those systems [52].

1.6.3.5 Random Phase Approximation

The random phase approximation is the fifth rung on Jacob's ladder. The exchange-correlation energy functional is completely non-local for both parts. The RPA-level functional is believed to be the most accurate method in the framework of density functional theory, and it is the "heaven" of chemical accuracy [75, 76]. In an RPA calculation, the conventional DFT results (charge density, wave-function and Kohn-Sham single particle energies) are used as the inputs. The RPA method will be briefly reviewed here for two reasons: firstly, the formulation of RPA method has been done [15]; on the other hand, the expressions of RPA exchange-correlation functional

are too complicated and not plottable, compared to semilocal functionals. For more technique details, we may refer the readers to the related literature [15, 53-64].

In RPA, the total energy is computed as the sum of two different parts: the Hartree-Fock energy (E_{HF}) and the correlation energy obtained from adiabatic-connection fluctuation-dissipation theorem (ACFDT). The expressions of these two parts are given as:

$$E_{\mathrm{t}}^{\mathrm{RPA}} = E_{\mathrm{HF}} + E_{\mathrm{c}} \tag{1.135}$$

$$E_{\mathrm{HF}} = T_{KS}[n] + E_{ion-el} + E_H[n] + E_x\left[\left\{\psi_\alpha^{KS}\right\}\right] \tag{1.136}$$

$$E_{\mathrm{c}} = -\frac{1}{2}\int_0^1 d\lambda \int_0^\infty \frac{d\omega}{2\pi} \int d^3\vec{r} \int d^3\vec{r}\, \upsilon(\vec{r},\vec{r}')\left[\chi^\lambda(\vec{r},\vec{r}';i\omega) - \chi^0(\vec{r},\vec{r}';i\omega)\right] \tag{1.137}$$

$$\begin{aligned} E_x\left[\left\{\psi_{\alpha\sigma}^{KS}\right\}\right] &= \frac{1}{2}\sum_\alpha \sum_\beta \sum_{\sigma,\sigma'} \int d^3\vec{r} \int d^3\vec{r}'\, f_{\alpha\sigma} f_{\beta\sigma'} \{\cdots\} \\ \{\cdots\} &= \frac{\psi_{\alpha\sigma}^*(\vec{r})\psi_{\beta\sigma'}^*(\vec{r}')\psi_{\alpha\sigma}(\vec{r}')\psi_{\beta\sigma'}(\vec{r})}{\left|\vec{r}-\vec{r}'\right|}\delta_{\sigma\sigma'} \end{aligned} \tag{1.138}$$

where $T_{KS}[n]$ is the total kinetic energy of Kohn-Sham system; E_{ion-el} is the electrostatic pontential energy of electron-ions system; $E_H[n]$ gives the Hartree energy among electrons (See equation 1.9); $E_x[\{\psi_{\alpha\sigma}^{KS}\}]$ represents the Hartree-Fock like exact exchange energy, and which is computed from Kohn-Sham single particle orbtials. Meanwhile, the correlation energy in RPA is obtained by equation 1.137 where λ refers to the coupling constant (See section 1.5.1) that switches the Kohn-Sham non-interacting system ($\lambda = 0$) to fully interacting system ($\lambda = 1$). The adiabatic connection ensures that transition between two systems is always smooth and the integration of λ in equation 1.137 can be done analytically. $\chi^\lambda(\vec{r},\vec{r}';i\omega)$ and $\chi^0(\vec{r},\vec{r}';i\omega)$ are the

linear response functions of fictitious λ-interacting system and non-interacting Kohn-Sham system, respectively. The calculation of E_{HF} is straightforward using equation 1.138, because Kohn-Sham single particle orbitals are easily obtained from any standard DFT calculation. For the correlation energy, the linear response functions must be evaluated first. The linear response functions of fully interacting and Kohn-Sham systems are defined as

$$\chi^1(\vec{r},\vec{r}';t-t') = \frac{\delta n(\vec{r},t)}{\delta v_{ext}(\vec{r}',t')} \tag{1.139}$$

$$\chi^0(\vec{r},\vec{r}';t-t') = \frac{\delta n(\vec{r},t)}{\delta v_{eff}(\vec{r}',t')} \tag{1.140}$$

with

$$v_{eff}(\vec{r}',t') = v_H(\vec{r}',t') + v_{xc}(\vec{r}',t') + v_{ext}(\vec{r}',t') \tag{1.141}$$

where the three terms on the right hand side of equation 1.141 are Hartree potential (Equation 1.24), exchange-correlation potential (Equation 1.27) and external potential, respectively. By requiring that equations 1.139 and 1.140 are the same, then we have

$$\chi^1(\vec{r},\vec{r}';t-t')\delta v_{ext}(\vec{r}',t') = \chi^0(\vec{r},\vec{r}';t-t')\delta[v_H(\vec{r}',t') + v_{xc}(\vec{r}',t') + v_{ext}(\vec{r}',t')] \tag{1.142}$$

then applying the chain rule for the expressions on the right hand side of equation 1.142,

$$\delta v_H(\vec{r}',t') = \int dt_1 \int dt_2 \int d^3\vec{r}_1 \int d^3\vec{r}_2 \frac{\delta v_H(\vec{r}',t')}{\delta n(\vec{r}_1,t_1)} \frac{\delta n(\vec{r}_1,t_1)}{\delta v_{ext}(\vec{r}_2,t_2)} \delta v_{ext}(\vec{r}_2,t_2) \tag{1.143}$$

$$\delta v_{xc}(\vec{r}',t') = \int dt_1 \int dt_2 \int d^3\vec{r}_1 \int d^3\vec{r}_2 \frac{\delta v_{xc}(\vec{r}',t')}{\delta n(\vec{r}_1,t_1)} \frac{\delta n(\vec{r}_1,t_1)}{\delta v_{ext}(\vec{r}_2,t_2)} \delta v_{ext}(\vec{r}_2,t_2) \tag{1.144}$$

with

$$\begin{cases} \dfrac{\delta v_H(\vec{r}',t')}{\delta n(\vec{r}_1,t_1)} = v(\vec{r}_1,\vec{r}') = \dfrac{1}{|\vec{r}'-\vec{r}_1|} \\ \dfrac{\delta v_{xc}(\vec{r}',t')}{\delta n(\vec{r}_1,t_1)} = f_{xc}(\vec{r}_1,\vec{r}';t'-t_1) \\ \dfrac{\delta n(\vec{r}_1,t_1)}{\delta v_{ext}(\vec{r}_2,t_2)} = \chi^1(\vec{r}_1,\vec{r}_2;t_1-t_2) \end{cases} \quad (1.145)$$

substituting equations 1.143-145 into 1.142, and changing the integration variables, and also doing the Fourier transformation from time domain to frequency domain, the following relationship is obtained [15].

$$\chi^1(\vec{r},\vec{r}';i\omega) = \left\{ \begin{array}{l} \chi^0(\vec{r},\vec{r}';i\omega) + \\ \int d^3\vec{r}_1 \int d^3\vec{r}_2 \chi^0(\vec{r},\vec{r}_1;i\omega)\left[v(\vec{r}_1,\vec{r}_2) + f_{xc}(\vec{r}_1,\vec{r}_2;i\omega)\right]\chi^1(\vec{r}_2,\vec{r}';i\omega) \end{array} \right\} \quad (1.146)$$

The relationship given in equation 1.146 is named as Dyson equation. It shows that the linear response function of a fully interacting system is obtained from the Kohn-Sham system self-consistently. For an arbitrary λ-interacting system, its linear response function $\chi^\lambda(\vec{r},\vec{r}';i\omega)$ is computed in a similar way to equation 1.146.

$$\chi^\lambda(\vec{r},\vec{r}';i\omega) = \left\{ \begin{array}{l} \chi^0(\vec{r},\vec{r}';i\omega) + \\ \int d^3\vec{r}_1 \int d^3\vec{r}_2 \chi^0(\vec{r},\vec{r}_1;i\omega)\left[\lambda v(\vec{r}_1,\vec{r}_2) + f_{xc}(\vec{r}_1,\vec{r}_2;i\omega)\right]\chi^\lambda(\vec{r}_2,\vec{r}';i\omega) \end{array} \right\} \quad (1.147)$$

Under the framework of RPA, it is assumed that f_{xc}= 0. It can be shown that

$$\chi^\lambda = \chi^0 + \chi^0 \lambda v \chi^\lambda \quad (1.148)$$

with the correlation energy computed by

$$E_c = \int_0^\infty \frac{d\omega}{2\pi} Tr\left\{\ln\left[1-\chi^0 v\right] + \chi^0 v\right\} \quad (1.149)$$

where χ^0 is computed from the Kohn-Sham occupied and virtual single particle orbitals as

$$\chi^0(\vec{r},\vec{r}';\mathrm{i}\omega) = -\sum_n^{occ}\sum_m^{uocc} 2\left(\frac{\psi_m^*(\vec{r}')\psi_n(\vec{r}')\psi_n^*(\vec{r})\psi_m(\vec{r})}{\varepsilon_m - \varepsilon_n - i\omega} + \frac{\psi_n^*(\vec{r}')\psi_m(\vec{r}')\psi_m^*(\vec{r})\psi_n(\vec{r})}{\varepsilon_m - \varepsilon_n + i\omega}\right) \quad (1.150)$$

where ψ_m and ψ_n are unoccupied and occupied Kohn-Sham single particle orbitals; ε_m and ε_n are the Kohn-Sham single particle energies. Note that the orbitals and energies required for RPA calculations are calculated from equation 1.28.

1.7 DFT+U Correction

DFT+U is often considered as an empirical method for treating the strong correlated system in a better way than conventional semilocal exchange-correlation functionals [77-80]. In a strong correlated system, the electron hopping between two different lattice sites of a localized orbital is suppressed due to the strong on-site Coulomb repulsion. Therefore, the electrons are localized on the lattice site (Wigner crystal). However, the semilocal functionals (L(S)DA, GGAs and meta-GGAs) underestimate such interaction. Thus, those electrons are too delocalized and can easily hop between different sites. The simplest remediation to semilocal functionals is adding a penalty functional to them, and the U is actually the penalty function [79]. Since, the semilocal functionals give reasonable electronic states for those delocalized bonding orbitals. Thus, U is usually only applied to the particularly selected orbitals. The total energy of DFT+U is computed as

$$E_{\mathrm{t}}^{\mathrm{DFT+U}}[n,\{\psi_\alpha\}] = E_t^{DFT}[n] + E_t^U[\{\psi_\alpha\}] - E^{dc}[n,\{\psi_\alpha\}] \quad (1.151)$$

where $E_t^{DFT}[n]$ is the total energy computed from any ordinary DFT method, $E_t^U[\{\psi_\alpha\}]$ is the U correction to a group of selected Kohn-Sham orbitals, $E^{dc}[n,\{\psi_\alpha\}]$

accounts the portion of U correction that has been already included in DFT calculation for those orbitals. The last two terms of equation 1.151 are usually combined together. The resulting expression for DFT+U method is given by

$$E_{\mathrm{t}}^{\mathrm{DFT+U}}[n,\{\psi_\alpha\}] = E_t^{DFT}[n] + \Delta E^U \tag{1.152}$$

$$\Delta E^U = \left[\begin{array}{l} \frac{1}{2}\sum_{m,m',\sigma} U(n_{im\sigma} - n^0)(n_{im'-\sigma} - n^0) \\ +\frac{1}{2}\sum_{\substack{m,m',\sigma \\ m\neq m'}} (U-J)(n_{im\sigma} - n^0)(n_{im'\sigma} - n^0) \end{array} \right] \tag{1.153}$$

where U and J are the on-site Coulomb repulsion energy and inter-orbital exchange parameter, respectively. The average occupancy of a localized orbital is obtained by $n^0 = N^0/p$, where $N^0 = \sum_{m,\sigma} n_{im\sigma}$ is the number of localized electrons at site i, and p is the degeneracy of the localized spin-orbitals, i.e., for *3d*, p = 10, and *4f*, p = 14. Finally, it can be shown that the Kohn-Sham one-particle effective potential in DFT+U is expressed by

$$V^{DFT+U} = V^{DFT} + \sum_{m,\sigma} U(n_{im\sigma} - n^0) + \sum_{\substack{m,\sigma \\ m\neq m'}} (U-J)(n_{im\sigma} - n^0) \tag{1.154}$$

Usually, U and J two empirical parameters, and might be determined from XPS spectra of strong correlated systems [81]. Recently, Mosey *et al*. [82] and Cococcioni *et al*. [83] showed that U and J can be calculated from *ab-inito* methods.

1.8 DFT+D2 Correction

The DFT+D2 method aims to treat the long-range van der Waals interacting energy in an empirical way on top of a DFT structural calculation [84-86]. This method is empirical for two reasons. On one hand, the van der Waals interactions between two atoms are computed using a pairwise potential form, similar to the classic force field method. On the other hand, the van der Waals coefficients of atoms are estimated from the London relationship for the dispersion [84], and those coefficients for atomic pairs are obtained from a geometric average of coefficients of components [84, 85].

The total energy in the DFT+D2 method is expressed by

$$E^{\mathrm{DFT+D2}} = E^{\mathrm{DFT}} + E^{\mathrm{D2}} \tag{1.155}$$

with

$$E^{\mathrm{D2}} = -s_6 \sum_{i=1}^{N_{at}-1} \sum_{j=i+1}^{N_{at}} \frac{C_6^{ij}}{R_{ij}^6} f_{dmp}(R_{ij}) \tag{1.156}$$

$$f_{dmp}(R_{ij}) = \frac{1}{1+e^{-d(R_{ij}/R_r-1)}} \tag{1.157}$$

$$\begin{cases} C_{ij}^6 = \sqrt{C_i^6 C_j^6} \\ R_r = R_i + R_j \end{cases} \tag{1.158}$$

where s_6 is a global scaling constant, and its value is known for some exchange-correlation functionals, i.e., 0.75 (PBE), 1.0 (TPSS), 1.2 (BLYP) and 1.05 (B3LYP); C_i^6 and C_{ij}^6 are the van der Waals coefficients of atom and atomic pair, respectively; R_r is the sum of two van der Waals radii of *i* and *j* atoms. The roles of the damping

function $f_{dmp}(R_{ij})$ are to remove the mathematical singularity at small R_{ij} and to scale down the van der Waals interactions of atomic pairs in the short distance where the DFT methods are able to describe. In this dissertation, DFT+D2 method will be applied to phase transition problem in solid structures.

1.9 Non-Empirical van der Waals Density Functionals

The main purpose for developing the non-empirical van der Waals density functionals (or vdW-DFs) is the same as that of empirical DFT+D2 approach. The vdw-DFs are more advanced than DFT+D2 in the sense that, in the former method, there is no empirically determined parameter in its formulation. The most well-known vdW-DF was proposed by Langreth-Lundqvist group [87] in 2004. The exchange-correlation energy in vdW-DF is given by

$$E_{\mathrm{xc}}^{\mathrm{vdW\text{-}DF}} = E_{\mathrm{x}}^{\mathrm{DFT}} + E_{\mathrm{c}}^{\mathrm{LDA}} + E_{\mathrm{c}}^{\mathrm{nl}} \tag{1.159}$$

where E_x^{DFT} represents the exchange energy functional of a DFT method [88]; E_c^{LDA} is the correlation energy functional of LDA; the last term E_c^{nl} stands for the non-local correlation functional for van der Waals interactions. The general form of E_c^{nl} is written as

$$E_c^{nl} = \frac{1}{2}\int d^3\vec{r}\int d^3\vec{r}' n(\vec{r})\Phi(\vec{r},\vec{r}')n(\vec{r}') \tag{1.160}$$

Here the key ingredient is the non-local correlation kernel $\Phi(\vec{r},\vec{r}')$. For the details of its construction, one may refer to the works of Dion *et al*. [87], Thonhasuser *et al*. [89] and Vydrov and Voorhis [90].

CHAPTER 2

PLANE WAVES AND PAW METHOD

2.1 Plane Waves

Nowadays, most structural calculations based on density functional theory (DFT) for solids are performed using periodic boundary condition (PBC). The plane waves are the natural basis set of PBC.

2.1.1 Bloch Theorem

The crystal structure is completely defined by its lattice constants and atomic positions. In 3-dimensional space, the the lattice constants are given by

$$\begin{pmatrix} \vec{a}_1 \\ \vec{a}_2 \\ \vec{a}_3 \end{pmatrix} = \begin{pmatrix} a_{11} & a_{12} & a_{13} \\ a_{21} & a_{22} & a_{23} \\ a_{31} & a_{32} & a_{33} \end{pmatrix} \tag{2.1}$$

where $\vec{a}_1, \vec{a}_2$ and $\vec{a}_3$ are lattice vectors in x, y and z directions of Cartesian coordinates; a_{ij} is the component of each lattice vector in each of three directions. In Figure 2.1, the definition of the lattice vectors is shown. For any lattice site, the translational symmetry applies.

$$\vec{R} = \vec{R}_0 + \vec{T} \tag{2.2}$$

here $\vec{R}_0$ is the coordinates of a lattice site, and after applying the translational operation ($\vec{T}$), the new position is given by $\vec{R}$. Note that $\vec{T}$ is expressed as

$$\vec{T} = u\vec{a}_1 + v\vec{a}_2 + w\vec{a}_3 \tag{2.3}$$

where *u*, *v* and *w* are integers.

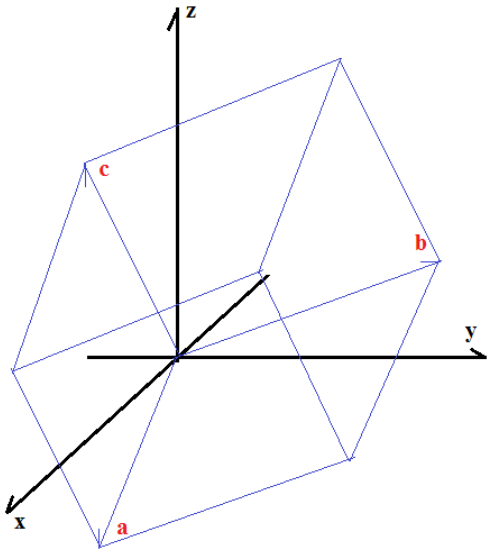

Figure 2.1: The lattice vectors and Cartersian coordinates.

The reciprocal lattice vectors of a crystal structure can be defined in a similar way to equation 2.1, but now the reciprocal lattice vectors are computed from

$$\begin{cases} \vec{b}_1 = \dfrac{2\pi(\vec{a}_2 \times \vec{a}_3)}{\vec{a}_1 \cdot (\vec{a}_2 \times \vec{a}_3)} \\ \vec{b}_2 = \dfrac{2\pi(\vec{a}_1 \times \vec{a}_3)}{\vec{a}_1 \cdot (\vec{a}_2 \times \vec{a}_3)} \\ \vec{b}_3 = \dfrac{2\pi(\vec{a}_2 \times \vec{a}_1)}{\vec{a}_1 \cdot (\vec{a}_2 \times \vec{a}_3)} \end{cases} \tag{2.4}$$

where $\vec{b}_1$, $\vec{b}_2$ and $\vec{b}_3$ are the reciprocal lattice vectors. Note that $\vec{a}_1 \cdot (\vec{a}_2 \times \vec{a}_3) = V$, where V is the volume of the lattice. It is easy to verify that $\vec{a}_i \vec{b}_j = 2\pi\delta_{ij}$. In the reciprocal space, the translational symmetry is preserved as that in real space:

$$\vec{G} = h\vec{b}_1 + m\vec{b}_2 + l\vec{b}_3 \tag{2.5}$$

here *h*, *m* and *l* are integers.

The Bloch wave of a crystal structure is given by

$$\psi_{n,k}(\vec{r}) = u_{n,k}(\vec{r})\exp(i\vec{k}\cdot\vec{r}) \tag{2.6}$$

with $\vec{k}$ is the wave vector in the first Brillouin zone, and n is the band index; $u_{n,k}(\vec{r})$ is the periodic part of the Bloch wave, the phase factor of Bloch wave is given by the expontential function or plane wave. If we replace $\vec{r}$ in equation 2.6 by $\vec{r}' = \vec{r} + \vec{R}$, it can be rewritten as

$$\psi_{n,k}(\vec{r}+\vec{R}) = u_{n,k}(\vec{r}+\vec{R})\exp[i\vec{k}\cdot(\vec{r}+\vec{R})] \tag{2.7}$$

since the periodic part satisfies $u_{n,k}(\vec{r}+\vec{R}) = u_{n,k}(\vec{r})$, then we have

$$\psi_{n,k}(\vec{r}+\vec{R}) = \left[u_{n,k}(\vec{r})\exp(i\vec{k}\cdot\vec{r})\right]\exp(i\vec{k}\cdot\vec{R}) \tag{2.8}$$

which can be simplified as

$$\psi_{n,k}(\vec{r}+\vec{R}) = \psi_{n,k}(\vec{r})\exp(i\vec{k}\cdot\vec{R}) \tag{2.9}$$

This is the famous Bloch theorem for electron waves in a crystal structure, which shows the translational symmetry under PBC.

2.1.2 Schrödinger Equation in Reciprocal Space

Here, we would like to have a little discussion about the Schrödinger equation in reciprocal space. The main reason is that most ab-inito computing codes are required to solve the a set of linear equations to get the eigenstates and engenenergies for single particle band dispersions. Those linear equations are derived from Schrödinger equation in reciprocal space.

The Schrödinger equation in a crystal structure is written as

$$\hat{H}\psi_{n,k}(\vec{r}) = \varepsilon_{n,k}\psi_{n,k}(\vec{r}) \tag{2.10}$$

$$\hat{H} = -\frac{\hbar^2}{2m}\nabla^2 + V(\vec{r}) \tag{2.11}$$

where the first term in equation 2.11 is kinetic energy of a Bloch electron, and $V(\vec{r})$ is the crystal potential, and it might be constructed from superposition of individual atomic potential in the crystal structure by

$$V(\vec{r}) = \sum_{\tau}\sum_{m} V[\vec{r} - (\vec{\tau} + \vec{R}_m)] \tag{2.12}$$

here $\vec{\tau}$ is the atomic position in the unit cell.

The Hamiltonian given in equation 2.11 is translational invariant. From the Fourier theorem, the Bloch state and crystal potential are the periodic functions. Therefore, both can be expanded as Fourier series in reciprocal space.

$$u_{n,k}(\vec{r}) = \sum_{G} C_{k+G} \exp[-\mathrm{i}(\vec{\mathrm{k}} + \vec{\mathrm{G}})\cdot\vec{r}] \tag{2.13}$$

$$V(\vec{r}) = \sum_{G'} C_{G'} \exp[-\mathrm{i}\vec{\mathrm{G}}'\cdot\vec{\mathrm{r}}] \tag{2.14}$$

here C_{k+G} and $C_{G'}$ are the Fourier expansion coefficients of Bloch wave and crystal potential. Substituting equations 2.13 and 2.14 into 2.10, we get the central equation:

$$\begin{aligned} &\frac{\hbar^2}{2m}\sum_{G,G} C_{k+G}(k+G)^2 \exp[-i(\vec{k}+\vec{G})\cdot\vec{r}]\delta_{G,G'} \\ &+\sum_{G}\sum_{G'}\left\{C_{k+G}\exp[-i(\vec{k}+\vec{G})\cdot\vec{r}]\right\}\left\{C_{G'}\exp[-i\vec{G}'\cdot\vec{r}]\right\} \\ &= \varepsilon_{n,k}\sum_{G} C_{k+G}\exp[-i(\vec{k}+\vec{G})\cdot\vec{r}] \end{aligned} \tag{2.15}$$

For a fixed G of the Bloch state, a set of linear equation should be solved for G' as

$$[\frac{\hbar^2}{2m}(k+G)^2 - \varepsilon_{n,k}]C_{k+G} + \sum_{G'} C_{G'}C_{k+G'} = 0 \tag{2.16}$$

this is the central equation of Schrödinger equation in PBC. In DFT, the Kohn-Sham equation in reciprocal space can be written in a similar form for crystal structure. Finally, it is worth noting that the largest expansion coefficient of equation 2.13 is determined by $\left|\vec{k}+\vec{G}\right|$. In plane wave based DFT codes, the expansion coefficient C_{k+G} is truncated by the following expression.

$$\frac{\hbar^2}{2m}(k+G)^2 \le E_{cut} \tag{2.17}$$

In Figure 2.2, the Fourier expansion of crystal potential or Bloch wave is illustrated. All expansion coefficients larger than the radius of the circle are set to zero.

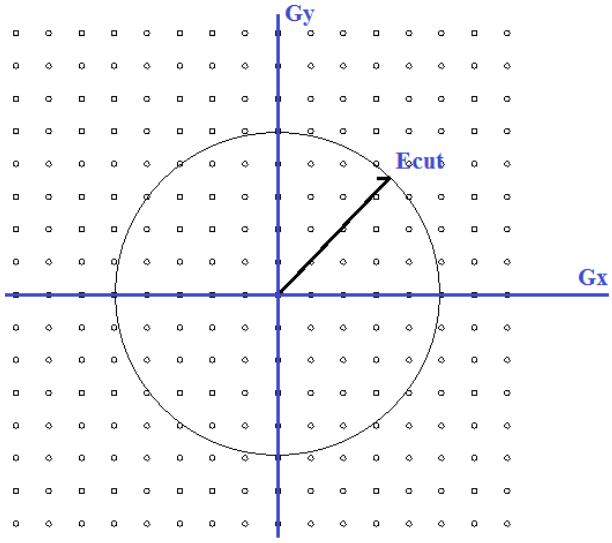

Figure 2.2: The Fourier expansion of Bloch wave or crystal potential in reciprocal space.

2.2 Pseudopotentials

2.2.1 Introduction to Pseudopotentials

We would like to present a brief review of pseudopotential theory. This is a well-established field. Many codes are published and available online for generating different types of pseudopotentials for one's own purpose.

The principles behind the development of pseudopotentials are based on two facts [91-95]. Firstly, for valence orbitals, near the nucleus, the radial distribution of electron density in the core region shows strong oscillations because of the wave-function is constrained by orthogonality. The Fourier transformation of density in the real space near the core region to reciprocal space is numerically too expensive, requiring a lot of expansion coefficients to be stored during the calculation. Otherwise, recovering the exact nodes of them in the core region is not a "must" requirement for many electronic calculations, because the core region is simply not involved in chemical bonding between atoms. As a result, the nodes in the core region are not important if we are only interested in chemical bonds of solids. Secondly, the kinetic energy of the electron in the core region is large, and to some extent, the strong Coulomb attraction between electron and pseudo-ion is partially or completely cancelled by positive kinetic energy. The resulting total potential in the core region for a valence orbital is smooth and without showing the singularity. The conclusion we can draw from these two facts is that both the wave-function and potential in the core region can be nodeless and smooth. In Figure 2.3, the differences between pseudized wave-function, potential and those of all-electron results are depicted.

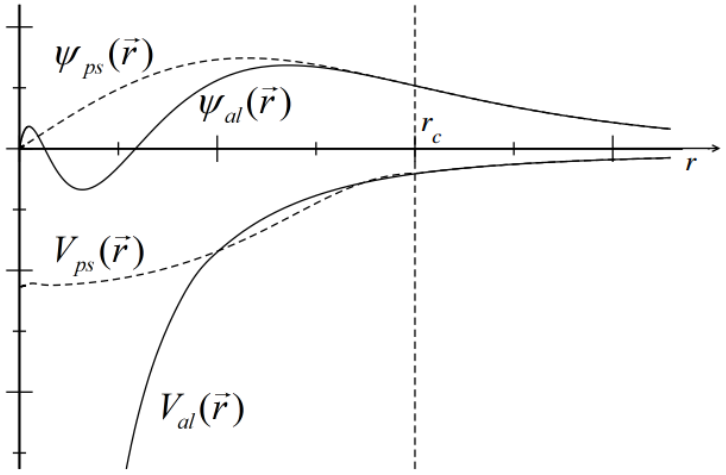

Figure 2.3: The pseudized wave-function and potential are compared to all-electron results.

Numerically, this can be done by solving two Schrödinger equations: one for all-electron with full potential, and another for pseudo-wavefunction and pseudopotential.

$$\left[\hat{T}+V_{al}(\vec{r})\right]\psi_{al}(\vec{r})=\varepsilon_{al}\psi_{al}(\vec{r}) \tag{2.18}$$

$$\left[\hat{T}+V_{ps}(\vec{r})\right]\psi_{ps}(\vec{r})=\varepsilon_{ps}\psi_{ps}(\vec{r}) \tag{2.19}$$

$$\left.\begin{aligned} V_{al}(\vec{r})&=V_{ps}(\vec{r}) \\ \psi_{al}(\vec{r})&=\psi_{ps}(\vec{r}) \end{aligned}\right\} \rightarrow \vec{r}\geq\vec{r}_c \tag{2.20}$$

where ps and al stand for "pseudo" and "all electron", respectively; $\vec{r}_c$ defines the cut-off radius where the pseudo-wavefunction and pseudopotential are coincide with all-electron resutls; for the pseudized orbital, requiring both Schrödinger equations give the same eigenenergy. The most widely used two types of pseudopotentials are normal conserving pseudopotentials (NCPPs) [91-94] and ultra-soft pesudopotentials (USPPs) [95]. The strating point for their constructions is the same, as shown in equations 2.18 and 2.19, but

there are some additional conditions which must be fulfilled in each case. Thedetailed discussions are omitted here, because in this dissertation, the first principles calculations are performed using the more complicated projector augement wave (PAW) method.

2.2.2 PAW Method

In NCPPs and USPPs, the wave-function and Coulomb potential of valence orbital are artificially smoothed. The resulting pseudo-wavefunction and pseudopotential are accurate for general DFT calculations. However, the "nodes" in the core region are important in other applications like spin-orbital coupling effects. The PAW method is designed to recover the all-electron properties of pseudo-wavefunction and potential in the core region on one hand, and also reducing the computational costs at the same time on the other hand.

The PAW method was firstly propsed by Blöchl in 1994 [96, 97]. In this method, the space is devided into two sub-regions as shown in Figure 2.4. The total PAW wave-function is computed as

$$\left|\psi_n^{PAW}\right\rangle = \left|\tilde{\psi}_n\right\rangle + \sum_i \left(\left|\phi_i\right\rangle - \left|\tilde{\phi}_i\right\rangle\right)\left\langle \tilde{p}_i \middle| \tilde{\psi}_n \right\rangle \tag{2.21}$$

where $\left|\psi_n^{PAW}\right\rangle$ is the PAW wave-function which recovers the exact behavior of all-electron wave-function in the core region; $\left|\tilde{\psi}_n\right\rangle$ is the pseudo wave-function expanded in plane waves, and which is nodeless in the core region; $|\phi_i\rangle$ is the all-electron partial wave-function; $\left|\tilde{\phi}_i\right\rangle$ and $|\tilde{p}_i\rangle$ are atom centered localized functions. The all-electron partial wave function is obtained from the radial relativistic Schrödinger equation for the

speherical non-spin polarized atom (similar to equation 2.18). Meanwhile, the pseudo-partial wave function is computed by

$$\left(\frac{1}{2}\nabla^2+\tilde{\upsilon}_{\text{eff}}+\sum_{ij}\left|\tilde{p}_i\right\rangle D_{ij}\left\langle\tilde{p}_j\right|\right)\left|\tilde{\phi}_k\right\rangle=\varepsilon_k\left(1+\sum_{ij}\left|\tilde{p}_i\right\rangle Q_{ij}\left\langle\tilde{p}_j\right|\right)\left|\tilde{\phi}_k\right\rangle \tag{2.22}$$

where D_{ij} and Q_{ij} are the characteristic PAW parameters, and they are computed as

$$Q_{ij}=\left\langle\phi_i\middle|\phi_j\right\rangle-\left\langle\tilde{\phi}_i\middle|\tilde{\phi}_j\right\rangle \tag{2.23}$$

$$D_{ij}=\left\langle\phi_i\middle|-\frac{1}{2}\nabla^2+\upsilon_{\text{eff}}\middle|\phi_j\right\rangle-\left\langle\tilde{\phi}_i\middle|-\frac{1}{2}\nabla^2+\tilde{\upsilon}_{\text{eff}}\middle|\tilde{\phi}_j\right\rangle \tag{2.24}$$

Note that the pseudo-partial wave functions $\left|\tilde{\phi}_i\right\rangle$ are equivalent to all-electron partial wave functions $\left|\phi_i\right\rangle$ outside the cutoff radius, and they match continuously onto the all-electron ones inside the core region. The projector functions $\left|\tilde{p}_i\right\rangle$ are dual to the partial waves:

$$\left\langle\tilde{p}_i\middle|\tilde{\phi}_j\right\rangle=\delta_{ij} \tag{2.25}$$

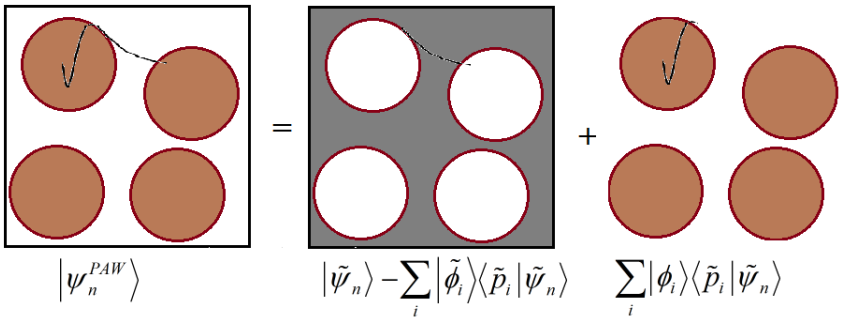

Figure 2.4: The pseudization of wave-function in PAW method.

2.3 Self-consistent Cycle

In a typical DFT calculation, the self-consistency is shown in Figure 2.5 [98]. Note that the initial charge density is obtained from the superposition of pseudo-atomic charge densities.

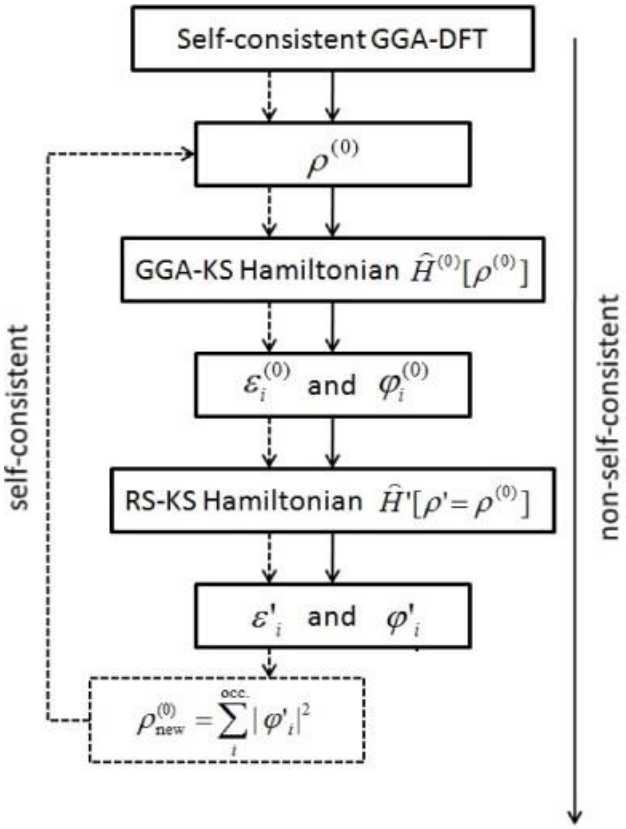

Figure 2.5: The self-consistent cycle of a DFT calculation.

CHAPTER 3

ASSESSING SEMILOCAL AND HYBRID FUNCTIONALS FOR PRESSURE INDUCED PHASE TRANSITONS IN Si, SiO_2 AND Zr SYSTEMS

Phase transitons are important in condensed matter physics, and they are also relavant to the geometry-energy dilemma of semilocal functionals. Indeed, it was earlier work by Hamann [99] on the SiO_2 phase transition under the pressure that motivated many solid state physicists to switch from LSDA to the PBE GGA. It is known that LSDA usually favors the high density phase, and overestimates its stability. Otherwise, the GGA PBE predicts good phase transition pressure and energy difference between high and low pressures in many cases. The non-empirical meta-GGAs have been rarely tested for phase transitions in solids before. We are particularly interested in one question: Can meta-GGAs predict good results for equilibrium lattice constants for two polymorphs of a solid, as well as the phase transiton parameters such as the energy difference between polymorphs and the transition pressure? In order to address this issue, we select three different types of phase transition induced by pressure. In the Si system, the low pressure phase diamond-structure Si (D-Si) transforms into a high pressure β-tin Si phase by compressuring the crystal structure above 10 GPa [100, 101]. This is an insulator to metal transition. Meanwhile, the α-quartz to stishovite phase transformation is a normal insulator-to-insulator transition. Finally, in the Zr system, both high and low pressure phases are metallic; thus, the ω-Zr to β-Zr transition is a normal transformation between two metallic phases. We also would like to compare the computed phase

transition parameters of meta-GGAs to those of LDA, GGAs and hybrid functional. We can see that a meta-GGA has the great potential to give both the geometry and energetics correct in solids.

3.1 Introduction to Si, SiO_2 and Zr Systems

Si, SiO_2 and Zr systems have been chosen in this dissertation as the model systems for testing the pressure induced phase transitions, because they are well-known to the scientific community and the accurate experimental transiton pressure is also available in each system.

In Figure 3.1, the crystal structures of two Si polymorphs are shown. In Si system, the D-Si is the most stable form at low pressure and temperature [100]. Under the hydrostatic pressure, it transforms into a metallic β-tin Si phase at nearly 10 GPa [101]. The D-Si has a faced centered cubic conventional cell with space group F$d\bar{3}m$ (227). Each conventional cell has eight Si atoms, occupying two special Wyckoff sites 16c (0, 0, 0) and 8a (0.25, 0.25, 0.25). On the other hand, the high pressure phase β-tin Si has a body-centered tetragonal conventional cell with space group I$4_1/amd$ (141). The conventional cell has 4 atoms occupying a special Wyckoff site 8c (0, 0, 0). Chang and Cohen [100], and Hu et al. [101] also studied several other high pressure phases of Si. Their works showed that at least other three different Si phases exist in the range of 0 to 40 GPa, i.e., body centered cubic (Si-III, ~10 to 0 GPa), primitive hexagonal (Si-IV, ~14 to 40 GPa) and hexagonal close-packed (Si-V, ~40 GPa).

In SiO_2 system, α-quartz and stishovite are the two most well-known ploymorphs. α-quartz is aboundant in earth crust, and stishovite is famous because the only way to create it on the surface of the earth is due to the meteorite impact [99]. The space group of α-quartz is $P3_221$ (152), and the unit cell has three SiO_2 units. The three Si atoms are located at 3a (x, 0, 1/3) Wyckoff site and the remaining six O atoms occupy 6c (x, y, z) site, where x, y and z are internal degrees of freedom. The α-quartz and stishovite are wide band gap insulators ($>$ 8 eV), and the phase transformation of the former to the latter structure is associated with the change of coordinate numbers for both Si and O atoms. In α-quartz phase, the basic structural unit is SiO_4 tetrahedral, forming a 3-dimensional network by sharing corners. The coordinate numbers for Si and O are 4 and 2, respectively. In stishovite, each Si atom is surrounded by six nearest O atoms, forming a SiO_6 octahedral aligned in $[\bar{1}10]$ direction. Meanwhile, each O atom is linked with other three Si atoms. Experimentally, it has been verified that Si-O bonds in stishovite show stronger ionic character than those in α-quartz. This can explain why the coordinate number of Si in α-quartz is larger than stishovite. The crystal structures of α-quartz and stishovite are illustrated in Figure 3.2.

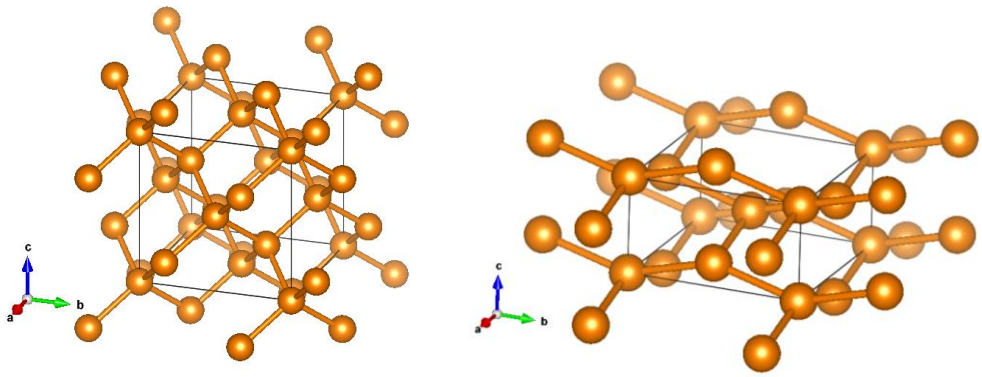

(a) (b)

Figure 3.1: The crystal structures of two Si polymorphs. (a) diamond-structure Si (LP); (b): β-tin Si (HP). Note that LP and HP refer to low pressure and high pressure, respectively.

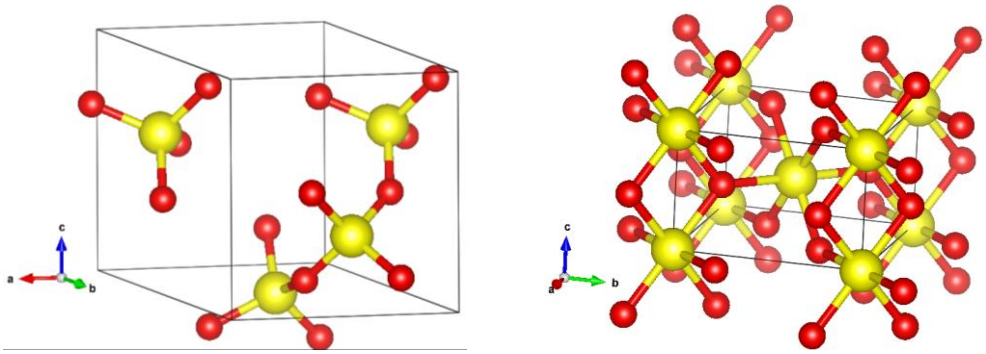

(a) (b)

Figure 3.2: The crystal structures of SiO_2 polymorphs. (a): α-quartz (LP); (b): stishovite (HP). The small red balls are oxygen atoms, and the large yellow ones are Si atoms.

Zr has three well-known crystal structures, i.e., the hexagonal close-packed α-phase, the hexagonal ω-phase with AlB_2-type structure and the centered cubic β-phase [102-105]. The most stable phase at room tempertature and ambient pressure is α-Zr. The α-Zr also transforms into ω-Zr in the range of 2-7 GPa at room temperature [103]. Meanwhile, the ω-Zr to β-Zr transition occurs at 30 $\pm$ 2 GPa, determined from energy-

dispersive x-ray diffraction [105]. Ostanin *et al.* [102] found that the transition pressure is 35 ± 5 GPa in another experiment. The crystal structures of ω-Zr and β-Zr are shown in Figure 3.3. The space group of hexagonal ω-Zr is P6/mmm (191), and each unit cell has three Zr atoms. Zr atoms occupy two special Wyckoff positions, 1a (0, 0, 0) and 2d (1/3, 2/3, 1/2). On the other hand, the β-Zr has space group $Im\bar{3}m$ (229), and two Zr atoms are placed at 2a (0, 0, 0) position.

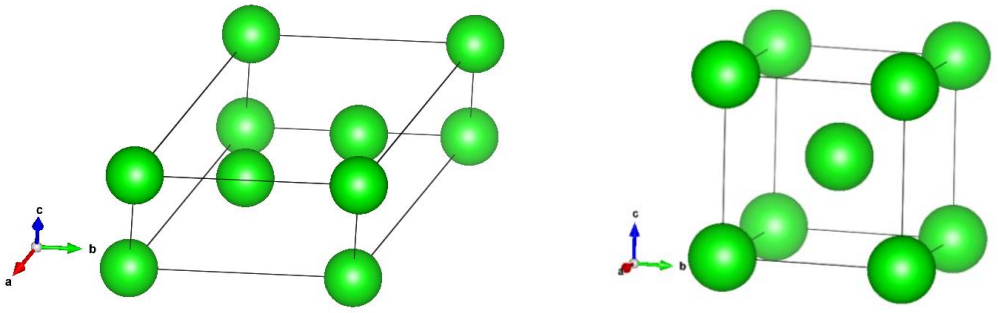

(a) (b)

Figure 3.3: The crystal structures of two Zr polymorphs. (a): ω-Zr (LP); (b): β-Zr (HP).

3.2 Computational Details

3.2.1 Density Functional Calculations

All first-principles calculations with periodic boundary conditions employed the *VASP* program (Vienna *ab-initio* simulation program), which uses the projector augmented wave (PAW) method [97]. In the PAW method, the frozen-core approximation is used, and the pseudo-atom is described by PAW pseudopotentials. For the plane-wave expansions, the kinetic energy cutoff was set to 500 eV for all calculations. The GW-type PAW potentials for Si, O, Zr were employed in this work:

Si_{3s3p3d}, O_{2s2p} and $Zr_{4s4p4d5s}$. These special PAW potentials were constructed by Kresse and coworkers in their RPA calculations [55, 56], with accurate scattering properties up to ~10 Ry above the vacuum level. The core radii for Si, O and Zr pseudo-atoms were 0.840 Å, 0.672 Å and 1.06 Å, respectively. The energy integrations were performed in the first irreducible Brillouin zone, and the methods used for generating the k mesh depended on the space group of the crystal structures. For cubic (D-Si and β-Zr) and tetragonal (β-tin Si and stishovite) phases, we used the Monkhorst-Pack method to generate 16 × 16 × 16 and 12 × 12 × 14 k meshes for optimizing the crystal structures, respectively [106]. The k grids used for α-quartz (trigonal) and ω-Zr (hexagonal) were 14 × 14 × 10 and 15 × 15 × 19, respectively, and were generated by the Gamma-centered method. Similar k-grids were also used to calculate the energy-volume curve for each phase. Using the present settings, the total energy was converged to 1 meV.

The exchange-correlation energy was approximated using functionals on the first three rungs of Jacob's ladder, including the Perdew-Zunger local density approximation (LDA) [19], the Perdew-Burke-Ernzerhof (PBE) GGA [25], PBE modified for solids (PBEsol) [30], the Tao-Perdew-Staroverov-Scuseria meta-GGA (TPSS) [37], the revised TPSS (revTPSS) [39], the regularized revTPSS (regTPSS) [40], the meta-GGA made simple (MGGA_MS0) [41] and its other two variants (MGGA_MS1 and MGGA_MS2) [42, 43].

For some structures, the transition pressures were also estimated from other exchange-correlation functionals, including the Heyd-Scuseria-Ernzerhof screened hybrid functional (HSE06, which mixes the nonlocal Hartree-Fock-type exchange in the short-

range portion of the electron-electron interaction with PBE exchange) [50-52], and various GGAs: Perdew-Wang 91 (PW91, a parent of PBE) [21], Armiento-Mattsson (AM05, an early GGA for solids) [28], Wu and Cohen (WC06) [29] and RPBE [27].

For the screened hybrid functional HSE06, we employed different k meshes for all six phases, i.e., D-Si (10 × 10 × 10), β-tin Si (8 × 8 × 10), α-quartz SiO_2 (8 × 8 × 6), stishovite (8 × 8 × 10), ω-Zr (8 × 8 × 10) and β-Zr (10 × 10 × 10). Employing the *downsampling* method reduces the computing time significantly. The total energy was converged to 5 meV/atom. In the *VASP* code, the default range separation parameter μ is 0.20 $Å^{-1}$ for the semilocal and nonlocal parts of the exchange functional [50, 51]. The same value was used in our current work.

The GW_0 calculations were performed for D-Si and stishovite phases with their experimental lattice constants using the VASP code [107]. The calculation parameters we applied are given below for stishovite: The kinetic energy cutoff (E_{cut}) was set to 400 eV, and the k mesh to 7 × 7 × 9. The frequency dependence of the dielectric function was evaluated using 300 Kohn-Sham LDA orbitals. The convergence of the band gap has been carefully confirmed using smaller E_{cut} (380 eV) and k mesh (6 × 6 × 8), and also fewer Kohn-Sham orbitals (200). For D-Si phase, we used 350 eV, 8 × 8 × 8 and 96 for E_{cut}, k mesh and the number of Kohn-Sham LDA orbital, respectively. Within the present settings, the quasi-particle band gap was converged to 0.01 eV.

The calculations using the PW91 and WC functionals were carried out in the *CASTEP* code [108, 109]. The crystal structures were re-optimized by ultrasoft

pseudopotentials (USPPs) for Si, O and Zr atoms [95]. The plane-wave cutoff was set to 500 eV, and k grids similar to those presented previously were employed.

3.2.2 Thermal Corrections to Phase Transition Pressure

The experimental transition pressure is usually measured at room temperature. Meanwhile, the DFT calculations are performed by default at 0 K. Therefore, it is necessary to include the phonon effects in the computed phase transition parameters. The thermal effects such as zero point energy and phonon excitations can be obtained from phonon spectrum using the following expressions:

$$E_{ZPE} = 3N \int_0^{\omega_{\max}} \frac{1}{2} \hbar \omega g(\omega) d\omega \tag{3.1}$$

$$A(N,V,T) = 3Nk_B T \int_0^{\omega_{\max}} \ln(1 - e^{-\hbar\omega/k_B T}) g(\omega) d\omega \tag{3.2}$$

with

$$\int_0^{\omega_{\max}} g(\omega) d\omega = 1 \tag{3.3}$$

where E_{ZPE} is the zero point energy, N is the total number of atoms in the unit cell, k_B and $\hbar$ are the Boltamann constant and reduced Planck constant, respectively, ω is the phonon frequency, and $g(\omega)$ gives the phonon density of states. Note that the phonon density of states must be normalized correctly according to equation 3.3.

In this dissertation, we have calculated the phonon spectra of SiO_2 structures using density functional perturbation theory (DFPT) in the *CASTEP* code [109]. For Si and Zr systems, the phonon effects on the transition pressures were taken from the

literature. In our phonon calculations, the plane-wave basis set was expanded in reciprocal space with a kinetic energy cutoff of 550 eV. USPPs were used to represent the pseudo-atoms of Si and O, i.e., Si ($3s^2 3p^2$) and O ($2s^2 2p^4$). For the energy integrations in the first irreducible Brillouin zone, the Monkhorst-Pack method was used to generate 6 × 6 × 8 and 4 × 4 × 4 k-meshes for stishovite and α-quartz, respectively. The convergence tests with respect to k-points were carefully conducted. For the exchange-correlation energy, only the PBE GGA was employed, because previous studies showed that different density functionals usually give quite similar results for the zero-point energy (ZPE) and thermal correction to the phase transition pressure [110]. The obtained ZPE and finite-temperature correction at each cell volume were added to the energy-volume curves. The change of the transition pressure induced by these two factors can be calculated from the change of the common tangent line of the energy-volume curves for the two phases.

The predicted lattice constants tabulated in this paper do not include the small phonon effects. This makes them more comparable to results in the earlier literature.

3.2.3 Euqation of State

The phase transition pressure is calculated from slope of the common tangential line of two energy versus volume curves for a solid. The common tangential line can be computed analytically using the equations of state (EOS) of two ploymorphs. In addition to phase transition pressure, other structural parameters are also obtained at the same time. In this work, we use the third order Birch-Murnaghan EOS, expressed as:

$$E(V) = \frac{9}{16} V_0 B_0 \left\{ \left[\left(\frac{V_0}{V} \right)^{\frac{2}{3}} - 1 \right]^3 B_0^{'} + \left[\left(\frac{V_0}{V} \right)^{\frac{2}{3}} - 1 \right]^2 \left[6 - 4 \left(\frac{V_0}{V} \right)^{\frac{2}{3}} \right] \right\} + E_0 \qquad (3.4)$$

where E_0 (the equilibrium energy) and V_0 (the equilibrium cell volume), as well as B_0 and B_0' (the bulk modulus and its pressure derivative dB/dP). The pressure of a single phase at volume V is $-dE/dV$.

In this paper, we have also evaluated the transition volume (V_t) for each phase, which is given by the solution of

$$P(V_t) = \frac{3}{2} B_0 [(\frac{V_0}{V_t})^{7/3} - (\frac{V_0}{V_t})^{5/3}] \times \{1 + \frac{3}{4}(B_0^{'} - 4)[(\frac{V_0}{V_t})^{2/3} - 1]\} \qquad (3.5)$$

here $P(V_t)$ is the pressure, which we set to the *experimental* transition pressure before the corresponding transition volume V_t is computed for comparison with experiment [111]. The theoretical transition pressures are sometimes inaccurate, due mainly to errors in E_0 and not to errors in the other parameters of the equation of state. In other words, the largest error in the theoretical transition pressure arises because the EOS of one phase displays an erroneous rigid vertical shift with respect to that of the other.

3.2.4 Ingredients of Meta-GGAs

The exchange energy density of a meta-GGA can be computed if its three ingredients such as Wigner-Seitz radius (r_s), reduced density gradient (s) and α are known. In this dissertation, the three parameters are calculated on the crystallographic plane within the expressions:

$$r_s = \left(\frac{3}{4\pi n} \right)^{1/3} \tag{3.6}$$

$$s = \frac{\sqrt{\left(\nabla_x n(x,y)\right)^2 + \left(\nabla_y n(x,y)\right)^2}}{2(3\pi^2 n)^{1/3} n} \tag{3.7}$$

$$\mathrm{ELF} = \frac{1}{1+\alpha^2} \tag{3.8}$$

where n is the valence electron density at a specific crystallographic plane. The density gradients in the x and y directions are evaluated in order to obtain the total density gradient $\nabla n(x,y)$. ELF refers to the electron localization function, calculated directly by the *VASP* code. For all calculations, the ground state electron density was obtained by the LDA method. The lattice constants and atomic positions were fixed to their experimental values.

3.3 Diamond-Si to β-tin Si Transition

3.3.1 Optimized Structures

Figure 3.4 shows the calculated energy-volume curves of D-Si and β-tin Si phases using the meta-GGA functionals TPSS, revTPSS, regTPSS and MGGA_MS0. The results for other functionals are not given in the figure for simplicity. The figure shows that the functional errors are reflected mainly in erroneous vertical displacements of the curve for one phase with respect to that for the other.

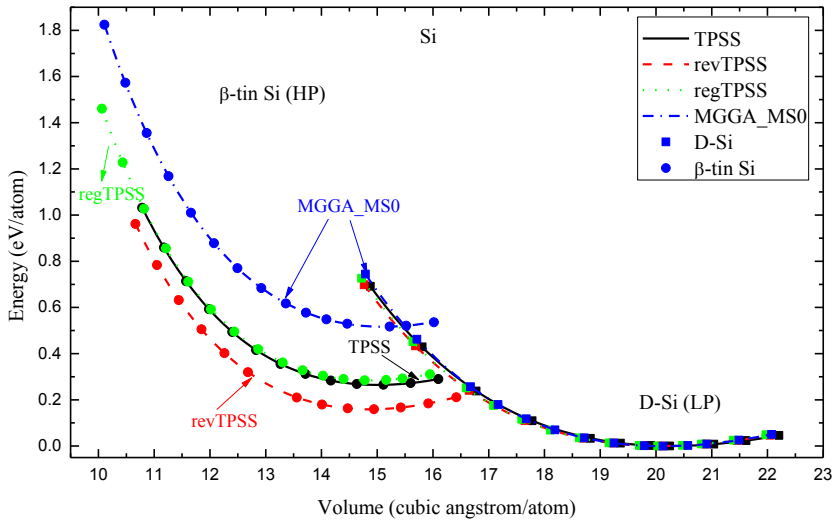

Figure 3.4: The total energies of D-Si (LP) and β-tin Si (HP) phases are calculated as a function of cell volume by four different meta-GGA exchange-correlation functionals. The total energies are given relative to the cell energy of the D-Si phase at the equilibrium volume for each meta-GGA functional. The dotted and solid lines are obtained from the third-order Birch-Murnaghan equation of state.

In Tables 3.1 and 3.2, the optimized lattice properties and phase transition parameters of the D-Si and β-tin Si phases from different exchange-correlation functionals are compared with available experimental results. The equilibrium lattice constant of D-Si shows typical trends: too small in LDA, too large in PBE, about right in PBEsol, too large but improved over PBE in TPSS, and about right in the other meta-GGAs.

For the β-tin Si phase, the MGGA_MS family behaves differently from the other density functionals, giving a larger c/a ratio and thus apparently favoring cubic symmetry too much. The lattice constants of the β-tin Si phase measured at the transition pressure (11.3 GPa) are a = 4.6900 Å, and c = 2.5780 Å, with c/a = 0.5496 [101].

Table 3.1: The structural parameters of diamond-structure Si (D-Si) (LP) computed by different exchange-correlation functionals. D-Si is cubic, thus the lattice constants are given by a, and V_0 is the equilibrium cell volume. B_0 and B' are bulk modulus and its pressure derivative. The cell volume at transition pressure is defined as V_t, computed from equation 3.5 where P_t = 11.7 GPa is Si system.

E_{xc}	a (Å)	V_0 (Å^3/atom)	B (GPa)	B'	V_t (Å^3/atom)
LDA	5.4025	19.71 19.72[a], 17.61[b]	97.1 96.4[a], 97[b]	4.03 4.13[a], 4.0[b]	17.87 17.86[a]
PBE	5.4650	20.40 20.48[a], 18.28[b]	89.4 89.0[a], 91[b]	4.07 4.12[a], 3.7[b]	18.38 18.42[a]
PBEsol	5.4305	20.02 20.06[a]	94.4 93.9[a]	4.02 4.09[a]	18.10 18.13[a]
AM05	5.4315	20.03 20.07[a]	93.6 93.1[a]	4.01 4.08[a]	18.10 18.13[a]
TPSS	5.4516	20.25	92.4	4.03	18.28
revTPSS	5.4380	20.10	94.1	4.00	18.17
regTPSS	5.4324	20.04	99.0	3.94	18.19
MGGA_MS0	5.4408	20.13	101.8	3.92	18.29
MGGA_MS1	5.4464	20.19	99.9	3.93	18.34
MGGA_MS2	5.4270	19.98	102.1	3.93	18.18
HSE06	5.4335	20.05 20.07[a]	101.5 99.1[a]	4.06 4.00[a]	17.90 18.21[a]
Expt	5.4288[a]	20.0[a]	99.2[a] 97.88[c]	4.11[a] 4.24[c]	18.15[a]

[a]Ref [111]; [b]Ref [112] ; [c]Ref [101].

The computed bulk moduli of D-Si and β-tin Si are given in Tables 3.1 and 3.2. Experimentally, the bulk modulus of D-Si is 99.2 GPa [111]. Hu et al. [101] found 97.88 GPa using the measured elastic constants. Most functionals underestimate the bulk modulus of D-Si, but the screened hybrid functional HSE06 gives 101.49 GPa and 99.1 GPa in this paper and in Ref. 111, respectively, with both values in good agreement with experiment. The MGGA_MS family of density functionals and regTPSS give the bulk modulus in better agreement with experiment than other semilocal functionals. For the β-tin Si phase in HSE06, we find a bulk modulus of 119.0 GPa, in good agreement with a

previous reference [112]. Finally, for the calculated B`, our results are slightly different from other references [111, 112]. However, the agreement among reference values is also poor, indicating that $B$` is sensitive to the parametric fitting.

Table 3.2: The structural parameters of β-tin Si (HP) computed by different exchange-correlation functionals. D-Si is tetragonal, thus the lattice constants are given by a and ratio c/a, and V_0 is the equilibrium cell volume. B_0 and B' are bulk modulus and its pressure derivative. The cell volume at transition pressure is defined as V_t, computed from equation 3.5 where P_t = 11.7 GPa is Si system. Since D-Si to β-tin Si transformation is revesible, the experimental cell volume of latter phase is not available.

E_{xc}	a (Å)	c/a	V_0 (Å^3/atom)	B (GPa)	B'	V_t (Å^3/atom)	a_t (Å)	c_t/a_t
LDA	4.7613	0.5489 0.548[a] 0.546[b]	14.81 14.82[a], 13.22[b]	120.4 116.0[a] 117[b]	4.1 4.59[a] 4.3[b]	13.66 13.63[a]	4.6456	0.5411 0.544[a]
PBE	4.8138	0.5487 0.550[a] 0.547[b]	15.30 15.36[a] 13.69[b]	109.7 106.4[a] 109[b]	4.3 4.57[a] 4.1[b]	14.03 14.04[a]	4.6862	0.5449 0.544[a]
PBEsol	4.7801	0.5487 0.548[a]	14.98 15.02[a]	119.1 115.0[a]	4.13 4.52[a]	13.80 13.80[a]	4.6707	0.5376 0.543[a]
AM05	4.7609	0.5484 0.546[a]	14.80 14.82[a]	124.1 120.5[a]	4.08 4.54[a]	13.67 13.67[a]	4.6499	0.5434 0.543[a]
TPSS	4.7787	0.5504	15.02	116.3	4.24	13.79	4.6581	0.5458
revTPSS	4.7650	0.5489	14.85	122.9	4.15	13.72	4.6552	0.5397
regTPSS	4.7520	0.5615	15.06	127.3	4.01	13.74	4.5992	0.5658
MGGA_MS0	4.6568	0.5977	15.09	131.3	3.95	13.99	4.6064	0.5681
MGGA_MS1	4.6758	0.5921	15.13	128.6	4.01	13.99	4.6159	0.5647
MGGA_MS2	4.6738	0.5876	15.00	130.4	3.99	13.90	4.6023	0.5673
HSE06	4.7602	0.5491 0.565[a]	14.81 15.10[a]	119.0 117.0[a]	4.32 4.35[a]	13.67 13.89[a]	4.6611	0.5462 0.557[a]
Expt	—	—	—	—	—	13.96[a]	4.6900[c]	0.550[a,c]

[a]Ref [111]; [b]Ref [112]; [c]Ref [101].

3.3.2 Phase Transition Parameters

The computed phase transition pressure and energy difference are summarized in Table 3.3. Hennig et al. [111] have calculated the energy difference between the two polymorphs using various methods, and their results are also shown in Table 3.3. In their calculations, the quantum diffusion Monte Carlo (DMC) method gives the most accurate

values, which were found to be 0.48 eV/atom in Ref. 111 and 0.424 eV/atom in Ref. 113, respectively. LDA, the PBEsol GGA, and all of the meta-GGAs outside the MGGA_MS family seriously underestimate this energy difference, while the screened hybrid HSE06 performs well for it. Interestingly, regTPSS gives 0.285 eV/atom, which strongly improves the poor performance of revTPSS, suggesting that the order-of-limits error in revTPSS is significant here.

The errors of the various functionals for the transition energy are reflected in the transition pressure, which is seriously too low in LDA, PBEsol, and the meta-GGAs outside the MGGA_MS family. The phase transition pressure from D-Si to β-tin Si was found to be in the range of 10~15 GPa from QMC [110, 111]. Without including the ZPE and finite-T effect, the value obtained by HSE06 in this paper is 14.6 GPa. The finite-T and ZPE corrections further reduce the transition pressure from D-Si to β-tin Si by 1.3 GPa in Ref. 114 and 1.0 GPa in a recent calculation [110]. With these thermal corrections, HSE06 gives 13.3 GPa, which is larger than the 12.4 GPa reported in Ref. 111. The transition volumes, calculated as described around equation 3.5, are reasonably good for all tested functionals.

Table 3.3: The calculated phase transition parameters for D-Si to β-tin Si transformation by different exchange-correlation functionals. The zero point energy and finite-temperature (300 K) correction to transition pressure were estimated from the phonon spetra of the two phases using PBE functional, and the value was found to be -1.3 GPa (Refs. 111 and 114). We define ΔE_0 and ΔV_0 as $\Delta E_0 = E_{HP} - E_{LP}$ and $\Delta V_0 = V_{HP} - V_{LP}$, where LP and HP refer to the high and low pressure phases, respectively.

E_{xc}	ΔE_0 (eV/atom)	ΔV_0 (Å^3/atom)	P_t (GPa)
LDA	0.206 0.206[a], 0.216[d]	4.90	5.7 5.8[a], 6.7[b]
PBE	0.290 0.287[a], 0.299[d]	5.10	8.4 8.4[a], 9.2[b]
PBEsol	0.185 0.184[a]	5.04	4.8 4.8[a]
AM05	0.153 0.152[a]	5.24	3.5 3.5[a]
TPSS	0.265 0.266[d]	5.24	7.3
revTPSS	0.160	5.25	3.7
regTPSS	0.285	4.98	8.0
MGGA_MS0	0.517	5.04	17.3
MGGA_MS1	0.475	5.06	15.4
MGGA_MS2	0.429	4.98	13.9
HSE06	0.398 0.390[a], 0.447[d]	5.35	13.3 12.4[a]
Expt	—	—	10∼14[a, c] 11∼15[e]

[a]Ref [111]; [b]Ref [112]; [c]Ref [100]; [d]Ref [113]; [e]Ref [101].

3.4 α-Quartz to Stishovite Transition

3.4.1 Optimized Structures

The computed energy versus volume curves of two SiO_2 polymorphs are shown in Figure 3.5 for meta-GGAs. The GGAs and LDA resutls are omitted here.

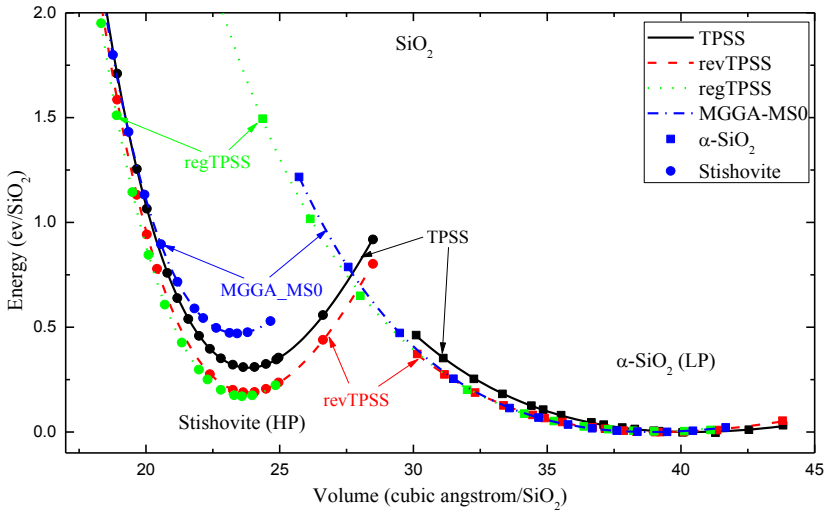

Figure 3.5: The calculated energy-volume curves of the α-quartz and stishovite phases. The total energies obtained by meta-GGA functionals are given relative to the cell energy of the α-quartz phase at the equilibrium volume for each functional.

Table 3.4: The optimized equilibrium structural parameters of α-quartz (LP) are given for different exchange-correlation functionals. V_t is the cell value computed at transition pressure (7.46 GPa) using equation 3.5.

E_{xc}	a (Å)	c/a	V_0 (Å^3/SiO$_2$)	B (GPa)	B'	V_t (Å^3/SiO$_2$)
LDA	4.9041 4.84[a]	1.0969 1.1177[a] 1.104[b]	36.95	36.95 45[a] 35[b]	5.48 4.9[a] 7.1[b]	—
PBE	5.0153 4.97[a]	1.0951 1.1107[a] 1.099[b]	39.41	35.59 48[a], 44[b], 43[b]	4.68 3.0[a], 3.2[b], 3.3[b]	34.62
PBEsol	4.9605	1.0996	38.63	32.08	6.05	33.48
AM05	4.9613	1.1004	38.74	33.07	4.58	34.05
TPSS	5.0186	1.0922	39.17	34.84	3.92	34.51
revTPSS	5.0044	1.0954	39.15	36.42	4.07	33.71
regTPSS	5.0005	1.0936	39.00	43.08	3.88	33.82
MGGA_MS0	4.9740	1.0933	38.37	38.4	4.97	33.87
MGGA_MS1	4.9869	1.0953	38.95	43.42	4.19	34.30
MGGA_MS2	4.9736	1.0933	38.39	46.9	3.86	33.69
HSE06	4.9568	1.0961	38.28	33.33	5.44	33.90
Expt	4.92[a] 4.921[d]	1.099[a] 1.097[d]	37.73[c]	38[a], 37.2[c] 36.5[d], 37.4[d]	6[a], 6.0[c] 5.9[c], 6.3[d]	—

[a]Ref [99]; [b]Ref [112]; [c]Ref [115]; [d]Ref [116].

We show the calculated structural properties of the SiO_2 phases in Table 3.4 and Table 3.5. As can be seen from Table 3.4, the lattice constants of α-quartz are overestimated by most exchange-correlation functionals other than LDA, suggesting that a long-range vdW correction might be needed to shrink the lattice constants. In earlier work by Hamann [99], the lattice constants of α-quartz were found to be a = 4.84 Å and c = 5.41 Å by LDA, but our calculation using LDA gives a = 4.9041 Å and c = 5.3790 Å. The large differences between the two results are probably associated with the different pseudopotentials used in Ref. 99 and in our paper. Below the meta-GGA level, PBEsol gives better lattice constants and equilibrium cell volume than other semi-local functionals. The lattice constants of α-quartz from the MGGA_MS functionals are only slightly worse than those of PBEsol and AM05. The MGGA_MS functionals are the only ones in Table 3.4 to include a reliable estimate of intermediate-range vdW effects [40-43]; none of these functionals includes the long-range effects.

Table 3.5: The optimized equilibrium structural parameters of stishovite-SiO_2 (HP) are given for different exchange-correlation functionals. The definition of V_t is similar to previous Tables.

E_{xc}	a (Å)	c/a	V_0 (Å^3/SiO_2)	B (GPa)	B'	V_t (Å^3/SiO_2)
LDA	4.1516 4.20[a] 4.157[c]	0.6417 0.6309[a] 0.642[b] 0.6394[c]	22.96 22.96[c]	321.57 286[a] 303[b] 313[c]	4.21 4.6[a] 4.8[b] 4.24[c]	
PBE	4.225 4.29[a]	0.6374 0.6247[a] 0.636[b]	24.04	270.36 260[a], 257[b], 249[b]	4.42 3.0[a], 4.9[b], 5.0[b]	23.54
PBEsol	4.1892	0.6394	23.51	277.85	4.52	23.08
AM05	4.1935	0.6377	23.52	295.79	4.32	23.02
TPSS	4.1984	0.6400	23.68	296.5	4.22	23.28
revTPSS	4.1972	0.6403	23.68	296.13	4.23	23.27
regTPSS	4.1932	0.6399	23.59	308.72	4.14	23.10
MGGA_MS0	4.1901	0.6365	23.42	318.72	4.12	22.88
MGGA_MS1	4.1890	0.6380	23.45	306.41	4.35	23.01
MGGA_MS2	4.1717	0.6402	23.24	305.40	6.09	22.78
HSE06	4.1751	0.6382	23.22	327.30	4.11	22.72
Expt	4.18[a] 4.1777[c]	0.6387[a] 0.6381[c]	23.30[c]	313[a], 306[c] 295[d]	2.8~6[a] 1.3[d]	—

[a]Ref [99]; [b]Ref [112]; [c]Ref [117]; [d]Ref [115].

In Figure 3.6, we show the equilibrium cell volumes of α-quartz obtained by different density functionals. The results of semilocal functionals are compared with the random phase approximation (RPA) (See Chapter 4 for details). RPA is able to capture the long-range vdW interactions in molecules and solids [55]. MGGA_MS0, MGGA_MS2 and HSE06 are better than other tested functionals for the equilibrium volume of α-quartz. In section 3.6.2, we will employ pairwise corrections pioneered by Grimme [84, 85] for the PBE and TPSS functionals to investigate the effect of long-range vdW interaction. The most accurate structural parameters of α-quartz are found from the screened hybrid HSE06. This is surprising, because HSE06 includes no long-range vdW interaction, although it is believed to give a good description of covalent bonds [118].

For the bulk modulus of α–quartz, Zupan et al [112] found a PBE bulk modulus of 44 GPa, which is close to Hamann's value [99] but not to ours.

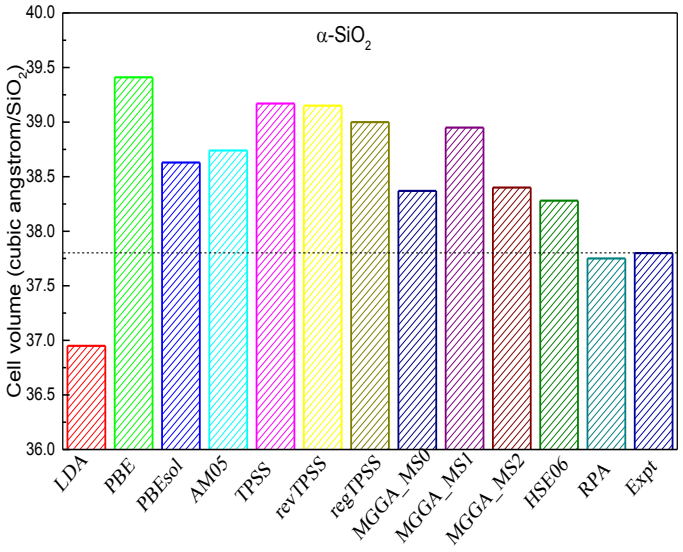

Figure 3.6: The equilibrium volumes of α-quartz calculated by different density functionals on Jacob's ladder. The results are compared with the experimental value. The dashed horizontal line is given to guide the eye.

The lattice constants of stishovite are rather accurate from all tested functionals, as shown in Table 3.5. For the bulk modulus of stishovite, both regTPSS and the MGGA_MS family of density functionals give results in agreement with experiment [99, 115, 119]. More recently, Driver and coworkers [120] have employed the quantum Monte Carlo (QMC) method, finding the bulk moduli of α-quartz and stishovite to be 32 GPa and 305 GPa, respectively, with the former value somewhat different from experiment. Practically, the accuracy of QMC is considered to be comparable to random phase approximation in density functional theory.

3.4.2 Phase Transition Parameters

The calculated energy difference between α-quartz and stishovite is given in Table 3.6. LDA fails to predict that α-quartz is the ground state of SiO_2, so its ΔE_0 is negative (-0.031 eV/SiO_2). In experiment, this energy difference is found to be 0.51~0.54 eV per SiO_2, and the corresponding transition pressure from α-quartz to stishovite is 7.46 GPa [99]. Our PBE results are in good agreement with experiment and with previous PBE calculations. However, as for Si, the meta-GGAs other than those of the MGGA_MS family predict transition energies and pressures that are far too low. Among thrre MGGA_MS variants, MGGA_MS2 is less accurate than other two forms for the transition parameters.

Table 3.6: The computed phase transition parameters of SiO_2 system using different exchange-correlation functionals. The ZPE and finite-temperature correction have been estimated from the phonon calculations using PBE, and are included in the obtained transition pressure.

E_{xc}	ΔE_0 (eV/SiO_2)	ΔV_0 (Å^3/SiO_2)	P_t (GPa)
LDA	-0.031 0.02[a], -0.090[b]	13.99	-0.37
PBE	0.532 0.57[a], 0.445[b]	15.37	6.94 7.2[a], 6.2[b]
PBEsol	0.171	15.12	2.71
AM05	0.292	15.23	3.79
TPSS	0.384	15.46	3.84
revTPSS	0.189	15.47	2.66
regTPSS	0.167	15.41	2.48
MGGA_MS0	0.467	14.96	6.16
MGGA_MS1	0.503	15.50	6.55
MGGA_MS2	0.286	15.16	3.99
HSE06	0.484	15.06	6.24
Expt	0.51~0.54[a] 0.525[d], 0.48[d]	14.43[c]	7.46[a]

[a]Ref [99]; [b]Ref [112]; [c]Ref [117]; [d]Ref [121].

3.5 ω-Zr to β-Zr Transition

3.5.1 Optimized Structures

Both ω-Zr and β-Zr are normal metals, so their electron density distributions should be more uniform than those of the SiO_2 and Si systems. Since the approximate exchange-correlation functionals are usually constructed to be exact for the uniform electron gas, we would expect that the semi-local functionals can give better results for Zr than for the previous cases. As we shall see, that tends to be true, although the LDA and HSE06 transition pressures are rather unrealistic. A countervening effect is that the changes of energy and volume at the transition are much smaller in Zr than in the previous cases, so an accurate transition pressure requires them to have very small absolute errors.

Figure 3.7 shows the dependences of the total energies of the two Zr phases on cell volume per atom using the regTPSS functional. The results for the other meta-GGA functionals are not shown for clarity, because the computed equilibrium cell volumes and energies of ω-Zr and β-Zr structures are too close near the transition pressure. The common tangent line is also given in Figure 3.7 for the two energy versus volume curves.

In Tables 3.7 and 3.8, we show the structural parameters the two structures of Zr using different exchange-correlation functionals. The results are also compared to experiments. The most reliable transition pressure from ω-Zr to β-Zr was measured by Xia *et al*. [105] using the energy-dispersive X-ray diffraction method with a synchrotron light source, and the resulting value is 30 ± 2 GPa. In the same paper, for ω-Zr, the c/a ratio, bulk modulus and pressure derivative of bulk modulus were also reported.

However, the lattice constants and mechanical modulus of β-Zr were not accurately determined due to the limited pressure range applied in that experiment. The calculated lattice constants shown in Tables 3.7 and 3.8 for the two Zr phases are compared with the experimental results reported by Hao *et al*. [103] and Greeff *et al*. [122].

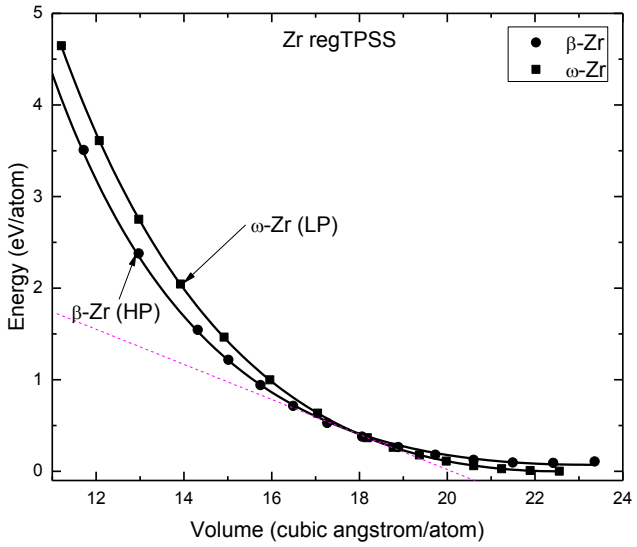

Figure 3.7: The volume dependences of the total energies of the ω-Zr (LP) and β-Zr (HP) phases calculated using regTPSS. The solid lines are obtained by fitting the energy-volume data to the third-order Birch-Murnaghan equation of state and the dashed line is the common tangent of the two energy-volume curves.

All tested functionals yield accurate lattice constants for the Zr phases, with HSE06 the most accurate. The change of the equilibrium cell volume due to thermal expansion may be estimated from the zero-point anharmonic expansion (ZPAE) for cubic crystals [74]. The Debye temperature (Θ_D) in this method can be calculated using the equation given in Ref. 101. For the β-Zr phase, we use $\Theta_D = 269$ K computed using PW91 in a previous paper [123]. We applied the zero-point anharmonic expansion to

correct the PBE cell volume. It was found that cell volume is slightly increased, i.e., 0.066 Å^3/atom, indicating that we can safely use lattice constants obtained at 0 K to draw our conclusion.

Table 3.7: The calculated structural properties of the ω-Zr (LP). Note that ω-Zr is hexagonal, thus the lattice parameters are uniquely defined by a and ratio c/a. The cell volume V_t at transition pressure (30 GPa) is obtained using equation 3.5.

E_{xc}	a (Å)	c/a	V_0 (Å^3/atom)	B (GPa)	B'	V_t (Å^3/atom)
LDA	4.9222	0.6257	21.54	103.84	3.49	17.68
PBE	5.0235 5.056[a]	0.6246 0.6230[a]	22.86	95.90 101.1[a], 95.3[c]	3.43 3.27[a], 3.44[c]	18.60
PBEsol	4.9715	0.6255	22.18	100.24	3.45	18.04
AM05	4.9706	0.6255	22.19	99.0	3.43	18.03
TPSS	5.0045	0.6248	22.61	99.04	3.44	18.46
revTPSS	4.9957	0.6248	22.49	99.73	3.41	18.31
regTPSS	4.9892	0.6250	22.40	99.39	3.41	18.29
MGGA_MS0	5.0030	0.6269	22.66	95.52	3.42	18.50
MGGA_MS1	5.0090	0.6267	22.74	97.24	3.37	18.53
MGGA_MS2	5.0080	0.6244	22.57	100.24	3.34	18.47
HSE06	5.0240	0.6270	22.96	91.05	3.34	
Expt	5.039[a] 5.050[d]	0.6251[a] 0.6237[d]	23.09[a]	104[b], 90[e] 109[e]	2.05[b] 4.0[e]	

[a]Ref [103]; [b]Ref [105]; [c]Ref [124]; [d]Ref [122]; [e]Ref [125].

The computed bulk moduli of two Zr ploymorphs are given in Tables 3.7 and 3.8. The bulk modulus of ω-Zr phase predicted by different exchange-correlation functionals falls in the experimental range.

The LDA lattice constants of β-Zr are too small, which results in the largest bulk modulus for this phase. The AM05 functional gives a rather small bulk modulus for the β-Zr phase, because this functional fails to show a reasonable minimum in the calculated energy-volume curve. The bulk moduli of ω-Zr and β-Zr phases computed from HSE06 are smaller than from the semi-local functionals.

Tables 3.7 and 3.8 suggest that most semilocal functionals overestimate ΔV_0 somewhat in comparison with experiment. PBE and MGGA_MS2 work better than other tested exchange-correlation functionals for this parameter. The computed ΔV_0 for Zr from HSE06 is almost one order of magnitude smaller than those from other semilocal functionals. The main reason is that HSE06 underestimates the cell volume for ω-Zr, but slightly overestimates it for β-Zr, so that the errors reinforce each other instead of cancelling.

Table 3.8: The calculated structural properties of the β-Zr (HP). Note that ω-Zr is cubic, thus the lattice parameters are uniquely defined by a only. The cell volume V_t at transition pressure (30 GPa) is obtained using equation 3.5.

E_{xc}	a (Å)	V_0 (Å^3/atom)	B (GPa)	B'	V_t (Å^3/atom)
LDA	3.4681	20.86	92.48	3.71	17.02
PBE	3.56 3.58[a]	22.56	81.95 89.7[b]	3.60 3.13[b]	17.99
PBEsol	3.5032	21.49	87.52	3.63	17.39
AM05	3.5173	21.76	76.51	3.87	17.28
TPSS	3.5440	22.26	86.08	3.60	17.83
revTPSS	3.5347	22.08	83.95	3.63	17.66
regTPSS	3.5327	22.05	86.40	3.57	17.56
MGGA_MS0	3.5414	22.21	82.14	3.59	17.72
MGGA_MS1	3.5484	22.34	82.17	3.56	17.86
MGGA_MS2	3.5440	22.26	84.93	3.51	17.84
HSE06	3.5774	22.89	78.59	3.52	—
Expt	3.574[a] 3.570[b]	22.82[a]	—	—	—

[a]Ref [103]; [b]Ref [124].

3.5.2 Phase Transition Parameters

In Table 3.9, we show the calculated phase transition parameters for Zr system. For the phase transition parameter ΔE_0, PBE, TPSS, revTPSS and regTPSS values are close to each other. The MGGA_MS values are slightly bigger. HSE06 seems to overestimate the energy difference between ω-Zr and β-Zr.

In contrast to Si and SiO_2 systems, the phonon corrections significantly affect the transition pressure from ω-Zr to β-Zr phases [102]. Hereafter, we only discuss the corrected results for different density functionals. As shown in Table 3.9, PBE gives 23.2 GPa which is slightly smaller than the experimental transition range. Without phonon corrections, our PBE value is in good agreement with Ref. 104. Using the same functional, Ostanin *et al*. [102] report 27.0 GPa at 300 K. The LDA overestimates the stability of the β-Zr phase, and the transition pressure is too small. In Ref. 102, the transition pressure calculated by LDA at 300 K is 18.0 GPa, which is larger than our LDA result (9.17 GPa). Cazorla *et al.* [104] obtained a value of 22 GPa from the WC functional, smaller than from PBE. Using a very rough relationship $P_t = \Delta E_0/\Delta V_0$ to estimate ω-Zr to β-Zr transition pressure, we find that the transition pressure is strongly overestimated by HSE06 (over 200 GPa). MGGA_MS0 yields 35.3 GPa without phonon effects (ZPE and finite T = 300 K). The transition pressure from ω-Zr to β-Zr phases is reduced to 31.3 GPa (very close to experiment) by including the two phonon corrections.

Table 3.9: The phase transition parameters of Zr system. The ZPE and finite-temperature correction for the transition pressure have been evaluated from Debye's quasi-harmonic approximation [102]. LDA and PBE give slightly different corrections for transition pressure due to ZPE and finite T-effect. For example, at 300 K, PBE gives -4 GPa and LDA gives -6 GPa. Our results in this paper were corrected by the PBE value reported in Ref. 102 for all functionals other than LDA, and by the LDA correction for the LDA functional.

E_{xc}	ΔE_0 (eV/atom)	ΔV_0 (Å^3/atom)	P_t (GPa)
LDA	0.059	0.690	9.17 5-24[b]
PBE	0.084	0.300	23.21 26.8[a], 28.2[d], 27[e], 22[b]
PBEsol	0.075	0.685	17.06
AM05	0.078	0.432	23.28
TPSS	0.087	0.352	22.56
revTPSS	0.087	0.410	21.78
regTPSS	0.088	0.362	26.62
MGGA_MS0	0.113	0.450	31.25
MGGA_MS1	0.109	0.400	27.01
MGGA_MS2	0.123	0.320	28.08
HSE06	0.200	0.065	—
Expt	—	0.270[a]	30 ± 2[c]

[a]Ref [103]; [b]Ref [104]; [c]Ref [105]; [d]Ref [126]; [e]Ref [127].

3.6 Effects of van der Waals Interactions

As can be seen from Figure 3.6, the van der Waals interactions are important in α-quartz, because semilocal functionals overestimate the equilibrium cell volume. It seems that only RPA gives good accurate value. It is known that RPA captures the van der Waals interactions naturally due to its nonlocal correlation functional. Besides RPA, the van der Waals corrections can also be computed by DFT+D2 and vdW-DF methods. The latter two methods are less expensive than RPA. In this section, we would like to study the effects of van der Waals interactions on structural and phase transition properties of

Si, SiO_2 and Zr systems. In the calculations, we employed the pairwise-interaction DFT+D2 method of Grimme [84, 85] and the nonlocal density functional optB86b-vdW [86] method, both available in the *VASP* code. Table 3.10 shows the equilibrium volumes predicted by these methods for our six phases. By comparison with Tables 3.1, 3.2, 3.4, 3.5, 3.7 and 3.8, we see that the long-range corrections tend to decrease the cell volumes. OptB86b-vdW gives better cell volumes for stishovite, D-Si and β-tin Si than DFT+D2 does. For α-quartz, the cell volume predicted by optB86b-vdW is too small, and RPA gives the best value. The non-empirical MGGA_MS0 functionals, which include some intermediate-range dispersion effects, give the best overall performance for equilibrium cell volume among all the tested methods.

Table 3.10: The equilibrium cell volumes of the Si, SiO_2 and Zr structures computed by DFT+D2 and optB86b-vdW methods, which introduce long-range van der Waals attraction. For the SiO_2 system, the unit is $Å^3/SiO_2$; for the other two systems it is $Å^3$/atom. The experimental values are not corrected for thermal effects, and the RPA value is used instead of the Expt value for β-tin Si to calculate the mean absolute error (MAE) of each functional. LP and HP indicate the low-pressure and high-pressure structures.

Structures	PBE+D2	TPSS+D2	optB86b-vdW	MGGA_MS0	RPA	Expt
D-Si (LP)	19.81	19.44	19.98	20.13	20.02	20.00[a]
β-tin Si (HP)	15.03	14.46	15.21	15.09	15.24	—
α-quartz (LP)	38.75	37.02	34.56	38.37	37.75	37.73[b]
Stishovite (HP)	23.83	23.49	23.29	23.42	23.66	23.30[b]
ω-Zr (LP)	23.17	22.90	21.46	22.66	—	23.09[c]
β-Zr (HP)	22.53	22.19	21.13	22.21	—	22.82[c]
MAE	0.38	0.51	1.09	0.35	—	—

[a]Ref [111]; [b]Ref [117]; [c]Ref [103].

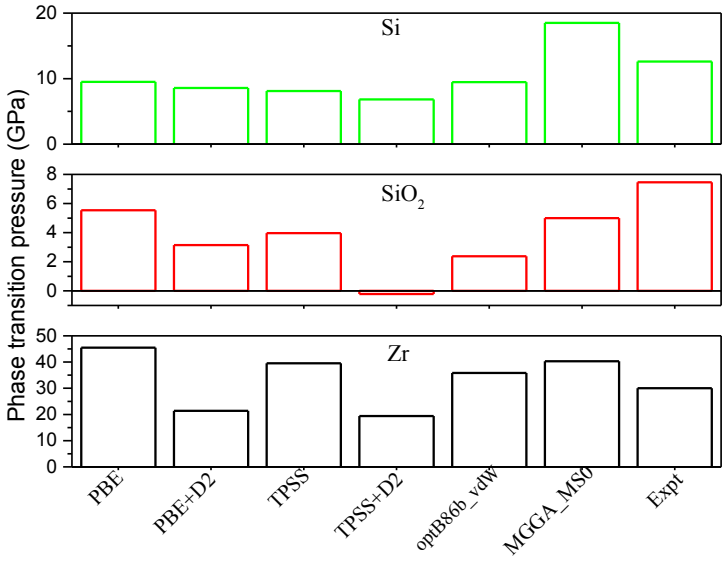

Figure 3.8: The phase transition parameters of Si, SiO_2 and Zr systems computed by DFT+D2 and optB86b-vdW methods. The resutls are compared to semilocal functionals without long-range van der Waals corrections and experimental results.

The calculated phase transition pressures are illustrated in Figure 3.8. For all three considered systems, the DFT+D2 methods are less accurate for phase transition pressure than their DFT counterparts. The TPSS+D2 method even predicts a negative transition pressure in the SiO_2 system. The optB86b-vdW works better for Si and Zr systems than for SiO_2. In the latter case, the transition pressure obtained from optB86b-vdW is smaller and less realistic than that from PBE and TPSS. In all three systems, MGGA_MS0 gives the best performance. Therefore, our calculations indicate that, for solids that are not primarily van-der-Waals-bound, one should be cautious about using long-range vdW corrections for phase transition parameters and equilibrium lattice geometry.

3.7 Effect of Band Gap

The calculated fundamental band gaps for D-Si, α-quartz and stishovite by LDA, GGAs, meta-GGAs, HSE06 and GW_0 are given in Table 3.11. Clearly, the most accurate band gaps are found by the HSE06 and GW_0 methods, in comparison with experimental values. Similar to LDA and GGAs, all tested meta-GGA functionals underestimate the band gaps for these three solids.

The underestimation of the fundamental band gap does not necessarily result in a poor phase transition parameters for Si and SiO_2 systems, contrary to the suggestion of Ref. 111. The exact Kohn-Sham method should yield the exact transition parameters, but the band structure from even the exact Kohn-Sham multiplicative potential would underestimate the gap [128, 129].

In our calculations, only LDA and GGA have a multiplicative Kohn-Sham exchange-correlation potential $\delta E_{xc} / \delta n(\vec{r})$, and they do indeed underestimate the gap. For computational convenience, our meta-GGA results employ a non-multiplicative exchange-correlation potential which tends to underestimate the gap even more, and even when the transition parameters are good. The screened hybrid functional HSE06 includes a fraction of the non-multiplicative Hartree-Fock exact exchange potential which increases and improves the single-particle band gap, in the same general way that the non-multiplicative GW_0 self-energy does. With some effort, one could construct a multiplicative exchange-correlation potential for the meta-GGAs or hybrid functionals, which might yield GGA-like gaps without much changing the predicted transition parameters for these functionals.

Table 3.11: The electronic band gaps of the D-Si, α-quartz and stishovite structures estimated from the calculated band-structure densities of states by semilocal and non-local functionals. The results of PW91 and WC were obtained using the CASTEP code. Our band gaps of the Si and SiO_2 systems were estimated from the calculated band dispersions using optimized crystal structures. Notice that the band gap of Si is indirect [Γ= (0, 0, 0) to X = (2π/a) (1, 1, 0)]; α-quartz also has an indirect band gap [K= ((2π/a) (1/√3, 1/3, 0) to Γ]; the band gap of stishovite is direct at the Γ point.

E_{xc}	D-Si	α-quartz	Stishovite
LDA	0.49	5.68	5.90
PBE	0.62	5.70	5.13
PW91	0.73	6.06	5.77
PBEsol	0.49	5.70	5.47
AM05	0.52	5.84	5.42
WC06	0.57	5.94	5.68
RPBE	0.70	5.70	4.95
TPSS	0.38	5.94	5.56
revTPSS	0.25	5.50	5.17
regTPSS	0.25	5.52	5.17
MGGA_MS0	0.17	5.60	4.25
MGGA_MS1	0.22	5.55	4.28
MGGA_MS2	0.22	5.59	4.38
HSE06	1.14	7.50	8.06
GW_0	1.22	9.40[b]	8.90
Expt	1.17[a]	8.90[c]	5~6[d], 8.75[e]

[a]Ref [52]; [b]Ref [130]; [c]Ref [131], [d]Ref [132]; [e]Ref [133].

3.8 Effect of Exchange Enhancement Factor

In some cases, we can relate a functional's performance for the transition parameters to the behavior of its plottable exchange enhancement factor F_x. Exchange is of course more important than correlation in the higher-density regions that contribute more to the total energy. Bonding regions also tend to have small *s*.

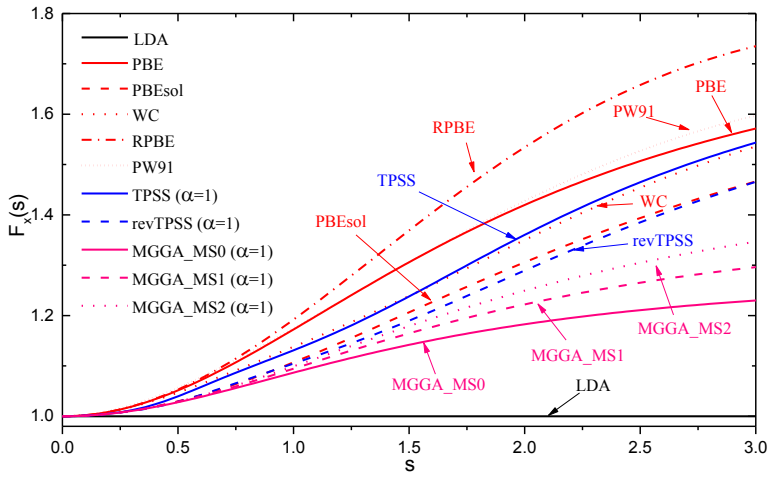

Figure 3.9: The exchange enhancement factors for various semi-local functionals. For meta-GGAs, $\alpha = 1$ and $s = 0$ correspond to uniform electron density.

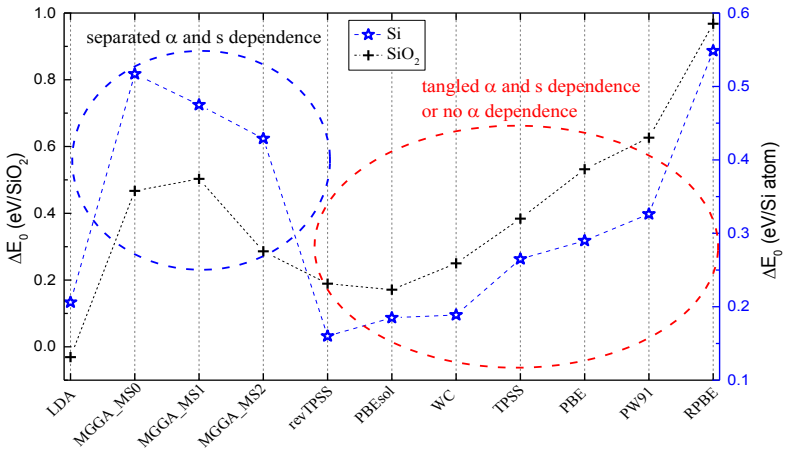

Figure 3.10: The calculated structural energy differences of Si (right vertical scale) and SiO_2 (left vertical scale) polymorphs from semilocal functionals on the first three rungs at Jacob's ladder. The results imply that an α dependence of F_x separated from the s dependence can significantly improve the energy difference between two polymorphs of a solid.

First consider the LDA and GGA functionals. Figure 3.9 shows $F_x(s)$ in the physically important range $0 < s < 3$. $F_x(s)$ equals 1 in LDA at all s and in GGA at $s = 0$. Within GGA, it increases with s, and the initial strength of this increase grows from LDA

to PBEsol to PBE to RPBE. Tables 3.3, 3.6 and 3.9 suggest that the predicted transition pressures tend to increase in the same order.

For the phase transition parameters, systematic improvement over GGAs and LDA is not seen for most meta-GGAs, but only for the MGGA_MS variants. The main difference between the MGGA_MS family of density functionals and other tested functionals lies in the exchange enhancement factor $F_x(s,\alpha)$, where the weaker s-dependence in MGGA_MS (Figure 3.9) is countered by a stronger α dependence. Our recent works has revealed the significance of α for identifying different bonds in molecules and solids [42, 134]. The covalent-single and metallic bonds are characterized by $\alpha = 0$ and 1, respectively. Weak bonds such as van der Waals are characterized by $\alpha >> 1$. By carefully manipulating both α and s dependences in a meta-GGA exchange functional, one can describe all different types of chemical bonds more accurately than with the ordinary GGAs and LDA. The influences of α and s on the calculated phase transition parameters for Si and SiO_2 systems are illustrated in Figure. 3.10.

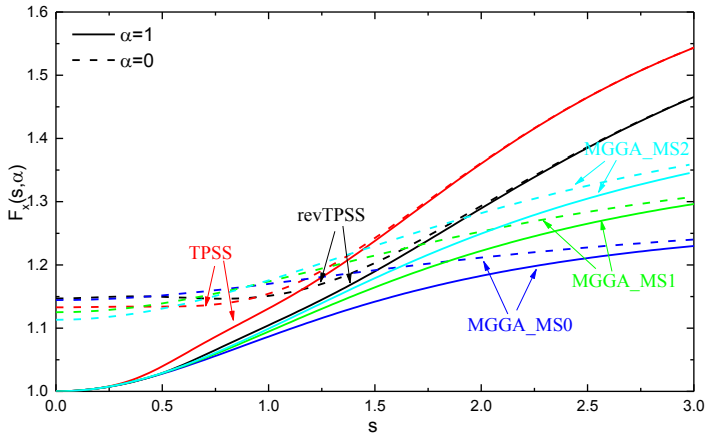

Figure 3.11: The exchange enhancement factors of meta-GGA functionals for the $\alpha = 0$ and $\alpha = 1$ limits.

Figure 3.11: shows the enhancement factors of various meta-GGAs at $\alpha = 0$ and 1. The small-s behavior is like that of GGA ($F_x \approx 1$) only for $\alpha = 1$, with $F_x \approx 1.15$ at $\alpha = 0$.

Figures 3.12 and 3.13 show in detail how $F_x(s,\alpha)$ varies over the s-α plane, first for revTPSS (which yields unrealistically low transition pressures for Si and SiO_2), and then for MGGA_MS (which is much more realistic). The α dependence at $s \approx 0$ reveals two qualitative differences between these two meta-GGAs: (1) The MGGA_MS F_x drops gradually from ~1.15 to ~1 as α increases from 0 to 1, while the revTPSS F_x drops abruptly near $\alpha = 0$ and then remains close to 1. (2) The MGGA_MS continues to drop well below 1 as α increases above 1, while the revTPSS does not. Feature (2) is responsible for the much better description of intermediate-range van der Waals interaction by MGGA_MS.

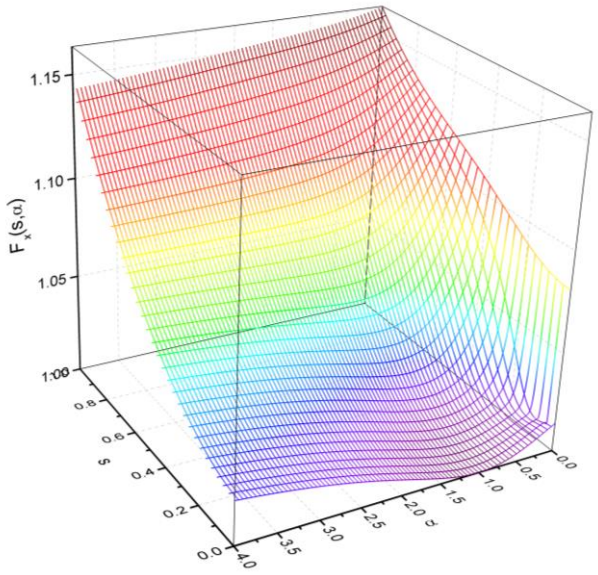

Figure 3.12: The exchange enhancement factor of revTPSS, showing the order of limits problem at small s and α.

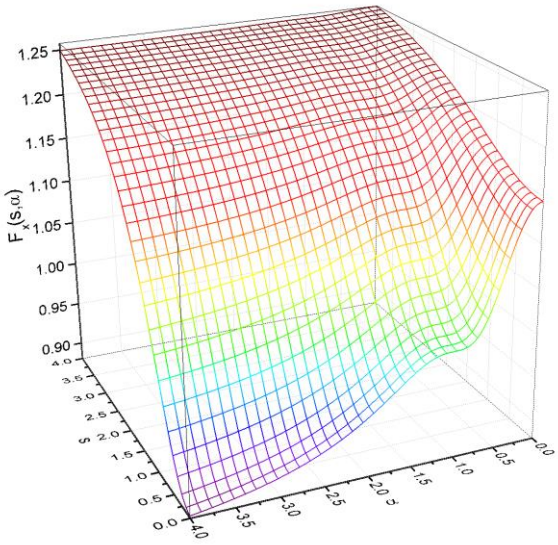

Figure 3.13: The exchange enhancement factor of MGGA_MS0,

Figures 3.14 and 3.15 plot $r_s = (3/[4\pi n])^{1/3}$, s and α along a line through a bond in the low-pressure phases of Si and SiO_2. The line for each solid is defined in the Figures 3.16 and 3.17, which also provide more detailed two-dimensional contour plots. Figures. 3.14 and 3.15 also show the meta-GGA exchange energy density $n\varepsilon_x^{unif} F_x$ (which need not be in the same gauge as the conventional exact exchange energy density). Note that we use pseudo-atoms instead of real ones, and that the pseudo-density is low (i.e., r_s is large) in the core regions.

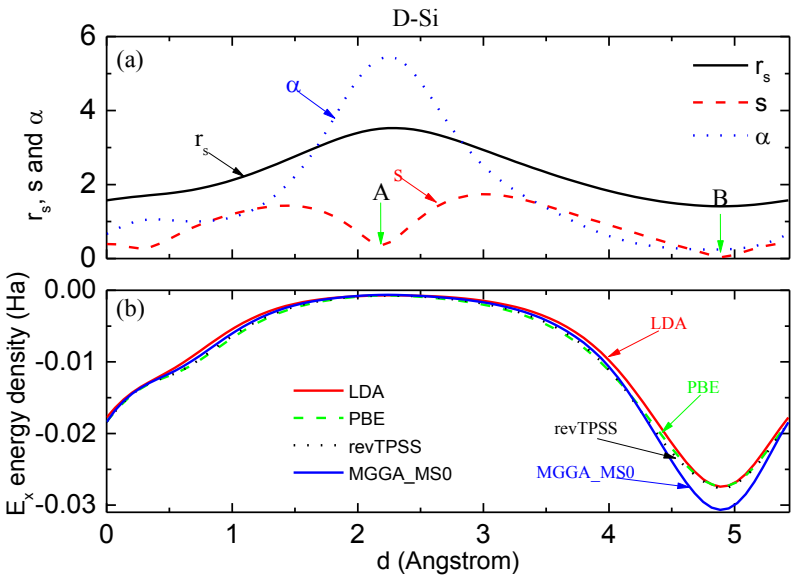

Figure 3.14: (a): The computed r_s, s and α distributions for the pseudo-density along a line in the [001] direction within the (110) plane, passing through the bond center, for the D-Si (LP) crystal using the LDA density (b): The exchange energy densities along the same path by LDA, GGAs and meta-GGAs. A and B indicate the interstitial and single bond regions, respectively.

First consider the phase transition in Si. The high-pressure phase β-tin is metallic, with $s \ll 1$ and $\alpha \approx 1$ in the bonding regions, so all tested functionals have similar exchange energy density there. But the low-pressure phase D-Si gets a much more negative exchange energy density in the bonding regions from MGGA_MS than from PBE or revTPSS, as shown in Figure 3.14. This arises because of feature (1) above, since the covalent single-bonding regions of D-Si have both small s and small α. Thus MGGA_MS energetically stabilizes D-Si with respect to β-tin, increasing the transition energy difference and the transition pressure.

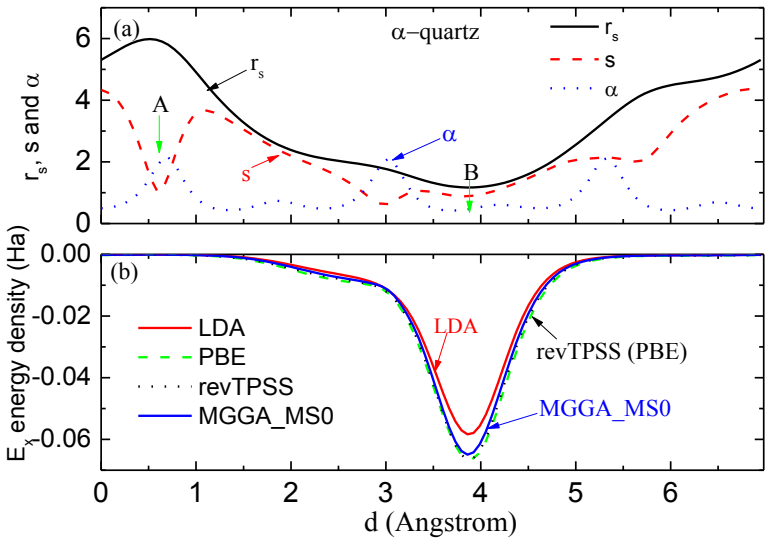

Figure 3.15: The same as Figure 3.14, but for α-quartz SiO_2 (LP). A and B label the interstitial and Si-O bond regions along a line in the [001] direction on the (100) plane.

Next consider the transition in SiO_2, where there is strong electron transfer from Si to O in each phase. Ref. 135 indicates that Si-O bonds in stishovite even show stronger ionic character than those of α-quartz. As a result, in stishovite, we have O^{2-} ions weakly overlapped with Si^{4+} ions. The overlap of the two 10–electron closed shells leads to large α in the bond region, just as we would have for two overlapped Ne atoms. But in this case the resulting van der Waals interactions are totally overwhelmed by the electrostatic attraction. Therefore, the tested functionals yield similar exchange energy densities for the low-pressure phase α-quartz, as shown in Figure 3.15. But the high-pressure phase stishovite has large values of α in the bonding region, so feature (2) above yields a much less negative exchange energy density from MGGA_MS than from PBE or revTPSS. This MGGA_MS energetically destabilizes stishovite with respect to α-quartz, again increasing the transition energy difference and the transition pressure.

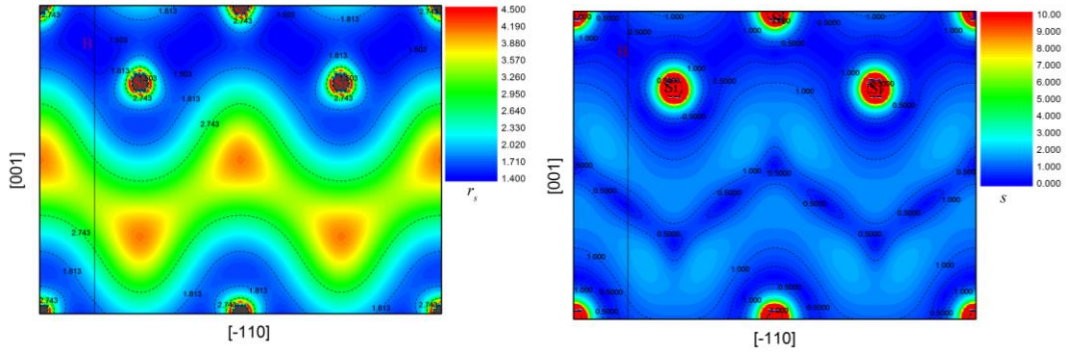

(a) (b)

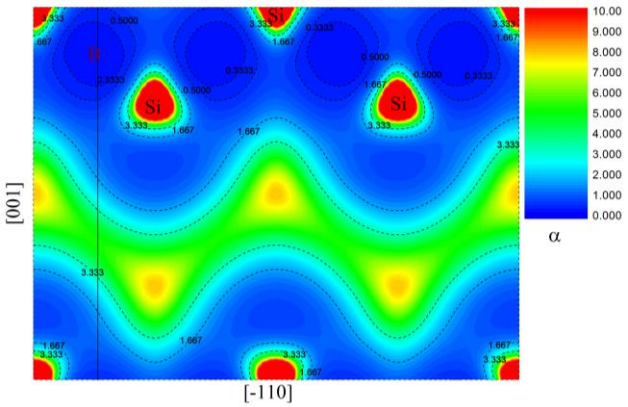

(c)

Figure 3.16: The two-dimensional contour plots of the r_s, s and α distributions of the D-Si phase on the (110) plane using the LDA density. (a): r_s ; (b): s; (c): α. Note that the vertical line refers to the one-dimensional path in [001] direction mentioned in the main text. B indicates the bonding region.

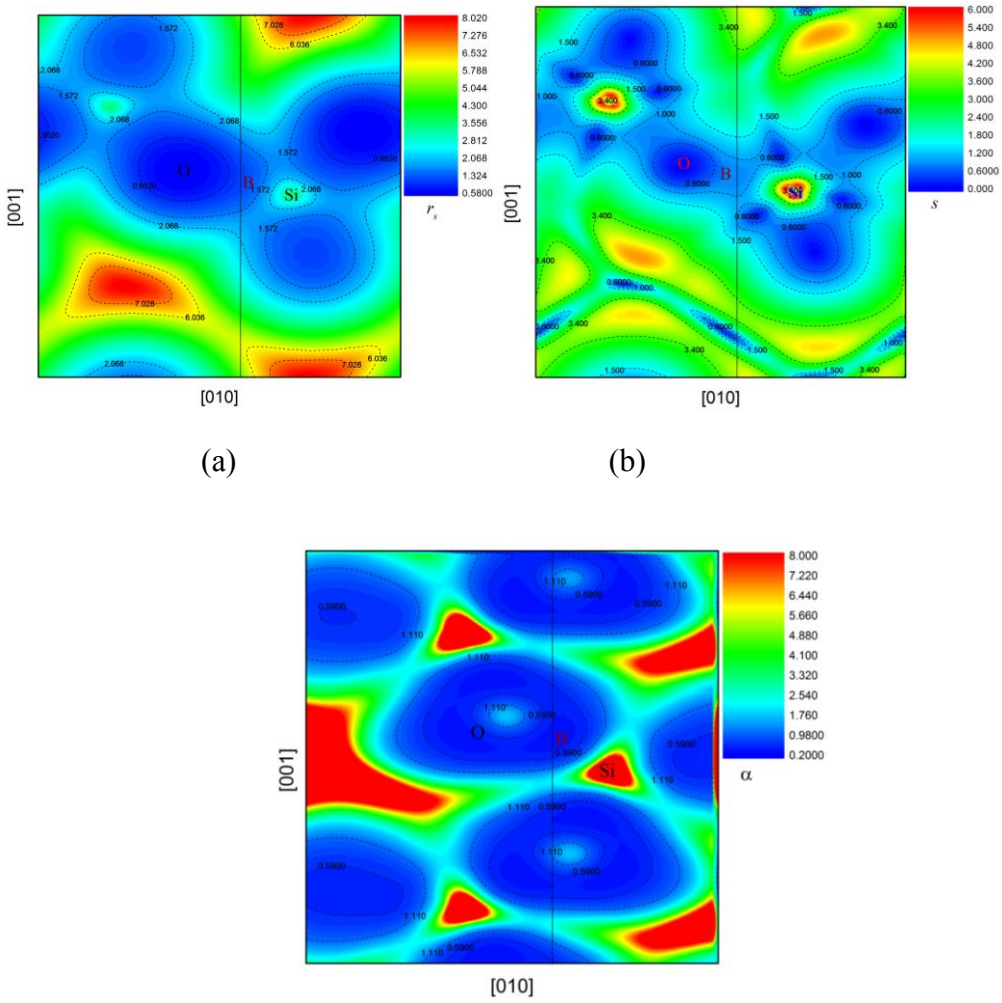

(a) (b)

(c)

Figure 3.17: Contour plots of r_s, s and α for the α-quartz phase of SiO_2 on the (100) plane. (a): r_s; (b): s; (c): α. The vertical line specifies the one-dimensional path in the main text, where the exchange energy density has been calculated for this phase. B indicates the bonding region.

3.9 Structural versus Transition Properties

The meta-GGAs are generally good for structural properties. Except in α-quartz, all tested meta-GGAs perform as well as or better than even the PBEsol and AM05

GGAs for the equilibrium lattice constants and bulk moduli. Their overall performance for these two properties is strongly better than that of the LDA and PBE functionals.

From the results shown in Tables 3.3-3.9 in the previous section, we find that the calculated phase transition parameters are strongly dependent on the exchange-correlation functional employed, and even on the choice of meta-GGA, for all three solids, with the MGGA_MS meta-GGAs giving typically the best results. This intriguing conclusion may always be true as long as the energy and volume differences between the high- and low-pressure phases are small. The simplest explanation is suggested by the estimate $P_t = \Delta E_0/\Delta V_0$: A small change in either energy difference (ΔE_0) or volume difference (ΔV_0) affects the transition pressure significantly when the two quantities are very small.

The different behaviors of the screened hybrid functional HSE06 for insulating and metallic structures have been well documented and explained in previous works by Scuseria and coworkers [136-138]. They found that HSE functional has the right screening for semiconductors, but too much for large band gap insulators and not enough for metals.

CHAPTER 4

ASSESSING RANDOM PHASE APPROXIMATION FOR PRESSURE INDUCED PHASE TRANSITIONS IN Si AND SiO_2 SYSTEMS

In Chapter 3, we have computed the structural and phase transition parameters of Si, SiO_2 and Zr systems by semilocal and hybrid functionals on Jacob's ladder. The random phase approximation is the fifth rung on this ladder, and which is also supposed to be the most accurate DFT method for isolectronic energy differences in solids. Therefore, this Chapter will be dovoted to apply RPA to calculate the similar properties for Si and SiO_2 systems. Zr system is not considered here because of the high computational costs in this particular system within RPA method.

Recently, Maezono *et al*. [110] and Hennig *et al*. [111] calculated the phase transition parameters of Si systems using diffusion quantum Monte-Carlo method (DMC). Meanwhile, Driver *et al*. [120] applied the similar method to SiO_2 system. It will be interesting to compare our RPA results for Si and SiO_2 systems to those of DMC results.

4.1 Methods and Details

4.1.1 Computational Parameters

Our calculations were performed using the Vienna ab-initio simulation program (*VASP*), where the RPA method is implemented non-selfconsistently [56-58]. The projector augmented wave (PAW) method within the frozen-core approximation was

employed for the pseudopotentials of Si and O atoms, i.e., Si_{3s3p3d} and O_{2s2p}, respectively [97]. The non-overlapping core radii for pseudo-Si and O atoms are 0.840 Å and 0.672 Å. The cutoff radii for generating partial waves for different angular quantum numbers, the number of partial waves and projectors of Si and O PAW potentials can be found in Ref. [58]. These special PAW pseudopotentials were built to describe the scattering properties of atoms accurately up to 10 Ry above the vacuum level. Their reliability and transferability have been extensively tested in Refs. [15] and [58]. We used GGA-PBE structures and orbitals as the initial input information for the following RPA calculations. The detailed computational parameters of RPA method will be presented in the next section.

The phase transition parameters were also compared to other semilocal and non-local functionals, including LDA [19], PBE [25], PBEsol [30], TPSS [37], revTPSS [39], regTPSS [40], MGGA_MS variants [41, 42] and HSE06 [50, 51], and also to those DMC calculations [110, 111, 120].

4.1.2 Convergence Tests

In contrast to the conventional DFT calculations, the RPA total energy must be calculated separately as RPA correlation energy and Hartree-Fock energy, and both parts converge independently [15, 58]. We have performed extensive tests on three parameters for the RPA method: kinetic energy cutoff (E_{cut}), k-mesh and E_{cut}^{GW}. The last parameter determines the size of the auxiliary plane wave basis for the response function, and the

value is usually chosen to be between $E_{cut}/3$ and $2E_{cut}/3$ [15, 58]. From the convergence tests, we determined some parameters for the RPA calculations, given in Table 4.1.

Table 4.1: Calculation parameters used for the RPA method. The convergence tests were performed for the Hartree-Fock total and RPA correlation energies of α-quartz, stishovite, and diamond-Si independently. For metallic beta-tin Si, the total energy converges much faster than any individual contribution. The errors shown in the last column are meV/SiO_2 and meV/atom for SiO_2 and Si polymorphs, respectively.

Phase		k-point mesh	E_{cut}	E_{cut}^{GW}	Error (meV)
α-quartz	E_{HF}	7×7×8	500		±1
	E_c	3×3×3	700	420	±10
Stishovite	E_{HF}	10×10×12	500		±2
	E_c	5×5×6	650	420	±20
Diamond-Si	E_{HF}	7×7×7	500		±1
	E_c	8×8×8	450	350	±5
β-tin Si	$E_{HF}+E_c$	8×8×10	500	350	±10

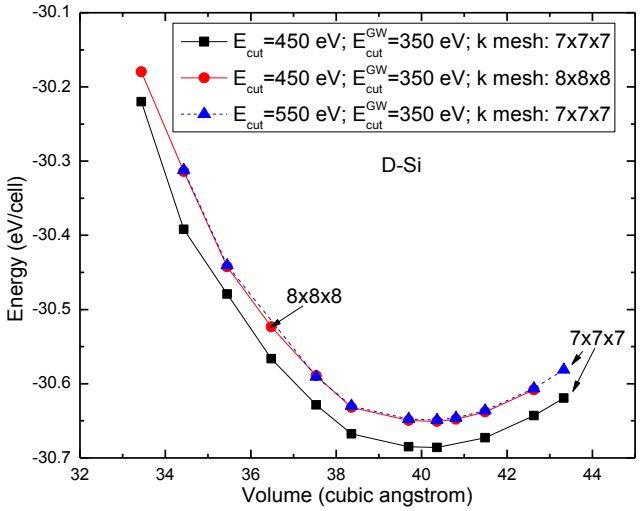

Figure 4.1: The convergence of RPA total energy versus volume curve of D-Si phase with respect to k-mesh and E_{cut}. Using the present settings (E_{cut}=450 eV, E_{cut}^{GW}=350 eV and 8×8×8 k mesh), the total energy and equilibrium cell volume can be obtained accurately.

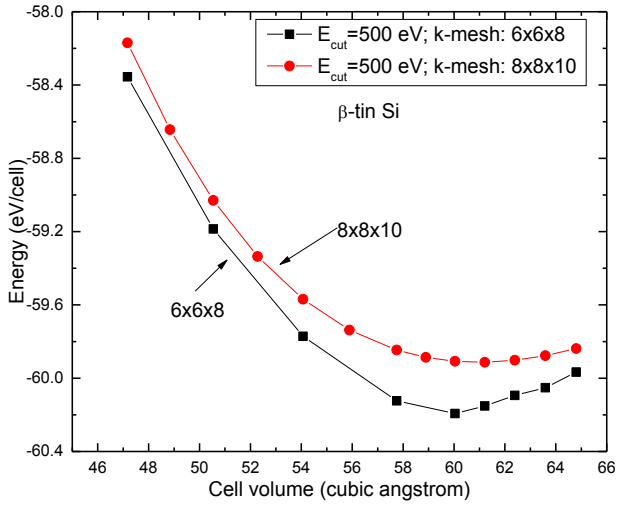

Figure 4.2: The convergence of RPA total energy versus volume curve with respect to k-mesh for metallic β-tin Si phase.

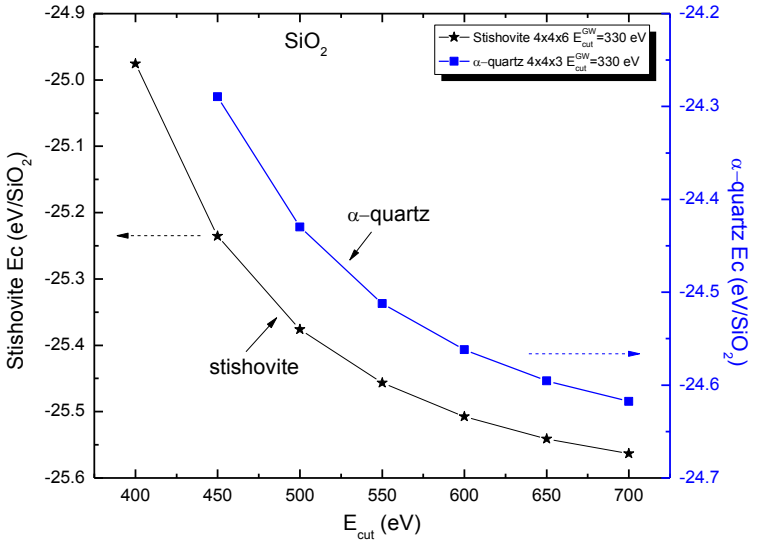

Figure 4.3: Convergence of the RPA correlation energies of α-quartz and stishovite with respect to kinetic energy cutoff values (E_{cut}). The k-mesh and the auxiliary kinetic energy cutoff for the linear response function (E_{cut}^{GW}) of each phase are fixed at the indicated values.

In Figures 4.1 and 4.2, the RPA total energy versus volume curves are shown for D-Si and β-tin Sn structures using different k-meshes. In Figure 4.3, the convergence of correlation energy with respect to kinetic energy cutoff value is also illustrated for SiO_2 system. We found that for insulators or semiconductors such as SiO_2 and D-Si, both Hartree-Fock and RPA correlation energies converge rapidly under increase of the k-point mesh. The main error in the correlation energies is caused by the finite value of E_{cut}, because for semiconductors or insulators the RPA correlation energy usually converges as

$$E_c(E_{cut}) = E_c^{\infty} + \frac{A}{(E_{cut})^{3/2}} \tag{4.1}$$

where E_c^{∞} is the converged RPA correlation energy and A is a fitting parameter which characterizes the error due to the finite E_{cut}. In our calculations, we found that the worst case was stishovite, where the absolute error without the extrapolation was predicted to be 20 meV/SiO_2. For the metallic β-tin Si phase, E_{HF} and E_c were always calculated using the same E_{cut} and k mesh. In addition, the long wave-length part ($\vec{q} \to 0$) of the exchange-correlation energy was excluded in RPA calculation for this phase in order to achieve the fastest convergence [58]. For a system with a band gap, the calculations of E_{HF} and E_c energies with and without including the long wave-length part give almost the same results for the present calculation parameters. For instance, the difference for the calculated E_{total} ($E_{total} = E_{HF} + E_c$) by the two methods for D-Si phase is 2 meV/atom.

4.2 D-Si to β-tin Si Transition

4.2.1 Structural and Phase Transition Properties

The computed energy versus volume curves of D-Si and β-tin Si are shown in Figure 4.4. In the same figure, the common tangential line of them is also illustrated as dashed line, and where the transition pressure from D-Si to β-tin Si can be obtained.

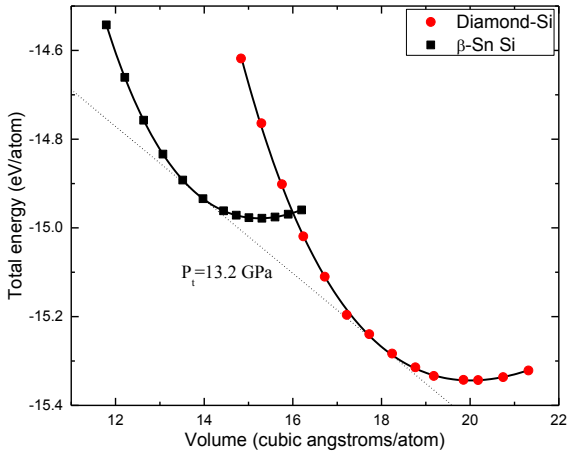

Figure 4.4: The energy versus volume curves of the Si structures. The dotted line is the common tangent line obtained from the Birch-Murnaghan third-order EOS, and the solid lines in the graphs are fitted to the data points by the same EOS.

From Table 4.2, we can see that RPA predicts good equilibrium lattice properties of Si polymorphs. The lattice constant and bulk modulus of D-Si have been calculated by RPA in Ref. 58, and the values are given as 5.432 Å and 99 GPa, respectively. Our RPA calculation gives 5.431 Å and 97.0 GPa for these two properties. The agreement between experimental results and RPA calculations is satisfactory for D-Si. Since the D-Si to β-tin Si transformation is kinematically reversible, the calculated equilibrium lattice properties of β-tin Si phase at 0 GPa can not be compared directly with experiments. However, the transition volume can be measured by experiment at the transition pressure. Using the

Birch-Murnaghan third-order EOS, we also calculated this quantity and the results are given in Table 4.2. The obtained results are slightly larger than the measured ones for Si polymorphs. Hennig *et al*. [111] reported the transition volumes of Si polymorphs from diffusion Monte Carlo simulation (DMC); the values are also shown in Table 4.2. The RPA calculations are generally in agreement with DMC results. In addition, in the case of β-tin Si, our RPA value is slightly better than the DMC value when compared to experimental results.

Table 4.2: Equilibrium lattice properties of Si structures from RPA calculations, including cell volume (V), c/a ratio, bulk modulus (B), pressure derivative of bulk modulus (B`), transition volume (V_t), energy different between two structures (ΔE) and transition pressure (P_t) The results are compared with experimental values and also with DMC calculations. The transition pressure has been corrected by ZPE and finite-temperature correction (300 K) [114].

Structure	Properties	RPA	Exp[a]	DMC[a]
D-Si	V (Å^3/cell)	160.17	160.00	159.84
	c/a	1.0000	1.0000	1.0000
	B (GPa)	97.0	99.2	98.0
	B`	4.84	4.11	4.60
	V_t (Å^3/Si)	18.19	18.15	18.14
			Exp[a]	DMC[a]
β-tin Si	V (Å^3/cell)	60.99	—	60.08
	c/a	0.5487	0.5500	0.5500
	B (GPa)	113.5	—	107.0
	B`	4.27	—	4.60
	V_t (Å^3/Si)	13.99	13.96	13.90
ΔE (eV/atom)	0.37			
P_t (GPa)	12.2			

[a]Ref [111].

The calculated phase transition parameters of Si system are given in Table 4.2. For the ZPE and FT correction to transition pressure, we simply cite the values from published results [110, 114]. The ZPE and FT correction (300 K) shift the D-Si to β-tin Si transition pressure by -1.3 GPa in Ref. 114 and -1.0 GPa in a recent study [110]. For the D-Si to β-tin Si phase transition, RPA gives a good energy difference and transition pressure.

The RPA phase transition parameters are also compared to other semilocal and hybrid functionals in Table 4.3. We can see that semilocal functionals underestimate the transition pressure, because the calculated energy difference is not sufficiently large to give the correct transition pressure. PBE and TPSS give better energy differences than other semilocal functionals. Moreover, both PBEsol and revTPSS predict the phase transition parameters less accurately than LDA. We also found that the calculated energy difference in RPA is situated between those of HSE06 and DMC. The obtained RPA transition pressure is in excellent agreement with experiments.

4.2.2 Discussion

A reason why most semilocal functionals might perform badly for the D-Si to β-tin Si phase transition has been discussed in Ref. 111. Since D-Si is a semiconductor and β-tin Si is a metal, the phase transition from the former structure to the latter is an insulator-to-metal transformation. The electronic structures of the two Si polymorphs are significantly different from each other. The well-known disadvantage of semilocal exchange-correlation functionals is that they usually underestimate physically-correct

energy gaps for semiconductors and insulators because they miss the derivative discontinuity in the Kohn-Sham potential at integer electron number [128, 139]. Errors in the gap as a second difference of total energies are reflected by errors in the band gap in a *generalized* Kohn-Sham band structure [139]. (While the Kohn-Sham exchange-correlation potential is a functional derivative with respect to the density, the generalized one is with respect to the nondiagonal Kohn-Sham density matrix.) The abrupt change of band structure from the semiconducting D-Si phase to metallic β-Sn Si is associated with overlapping of the valence and conduction bands and shrinking of the band gap. Therefore, the nonlocal functionals such as HSE06 have an advantage in this case, because the band gap can be better described by them than by semilocal functionals [111, 140], and a larger gap presumably tends to stabilize the semiconducting D-Si phase with respect to the metallic β-tin phase. In this work, ACFDT-RPA calculation uses the exact exchange energy (EXX), and the non-local correlation part (RPA) is calculated using linear response theory from the GW approximation (GWA) [107]. The generalized Kohn-Sham band structure of the present method (EXX+RPA) would resemble the physically-meaningful GW_0 band structure [53]. As a result, the ground-state energy of the D-Si phase is equally well described by either HSE06 or RPA. Moreover, the ground-state properties of the β-tin Si phase are somewhat similar for different semilocal and nonlocal functionals. Thus the good performance of RPA on the D-Si to β-tin Si phase transition can be explained.

Table 4.3: The phase transition parameters computed from semilocal functionals (LDA, GGA and meta-GGAs), hybrid functional (HSE06), RPA and many-body method (DMC). The experimental results are given for comparision. Note that theoretical P_t values have been corrected by ZPE and finite-temperature correction (300 K) [114].

E_{xc}	ΔE (eV/atom)	P_t (GPa)
LDA	0.206	5.7
PBE	0.290	8.4
PBEsol	0.185	4.8
AM05	0.153	3.5
TPSS	0.265	7.3
revTPSS	0.160	3.7
regTPSS	0.285	8.0
MGGA_MS0	0.517	17.3
MGGA_MS1	0.475	15.4
MGGA_MS2	0.429	13.9
HSE06	0.398	13.3
RPA	0.370	12.2
DMC[a]	0.420	14.0±1.0
Expt[a]	—	11.3~12.6

[a]Ref [111].

4.3 α-Quartz to Stishovite Transition

4.3.1 Structural and Phase Transition Properties

Figure 4.5 shows the calculated energy versus volume curves for α-quartz and stishovite by RPA. In Table. 4.4, the structural properties of them are given, and which are compared to experimental values and DMC calculations. Note that both DMC and RPA are considered as the benchmarks among the theoretical methods.

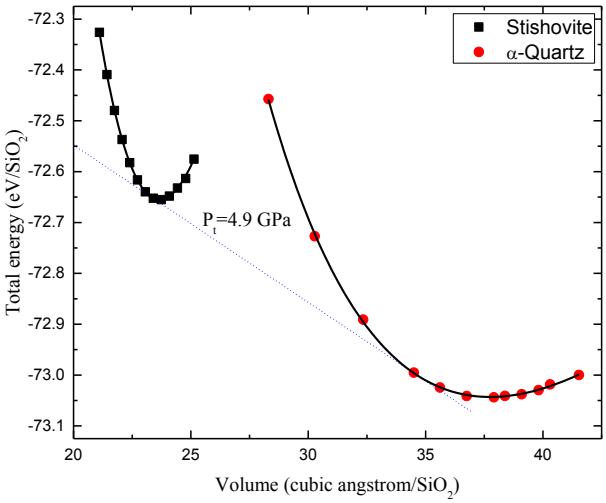

Figure 4.5: The energy versus volume curves of the SiO_2 structures. The dotted line is the common tangent line obtained from the Birch-Murnaghan third-order EOS, and the solid lines in the graphs are fitted to the data points by the same EOS.

For the SiO_2 system, the RPA also gives a good equilibrium cell volume for the α-quartz phase, where it only slightly underestimates the equilibrium cell volume by 0.13 %. However, the calculated bulk modulus of α-quartz is obviously larger than the experimental value. Hamann *et al*. [99] used both LDA and PBE to calculate the bulk modulus of α-quartz and stishovite. Interestingly, the RPA calculation overestimates the bulk modulus of α-quartz by the same amount as in LDA and PBE. In contrast to α-quartz, RPA gives a good bulk modulus for stishovite, but the equilibrium cell volume is overestimated. One should bear in mind that the present RPA calculations are non-selfconsistent, and the input structures were optimized using PBE. From Table 4.4, we can see that for α-quartz the c/a ratio obtained from PBE agrees less well with experiment than for stishovite. The c/a ratio of stishovite deviates from the corresponding experimental value by -0.2 %, and that of α-quartz is -0.4 %. Recently, the DMC method

has been applied to calculate the phase transition properties of SiO_2 polymorphs at ultrahigh pressures [120], and the DMC also gave similar results to our RPA calculations for α-quartz and stishovite. It can be seen clearly from Table 4.4 that DMC and RPA actually predict the same equilibrium cell volume for stishovite.

Table 4.4: The structural parameters of SiO_2 phases computed from RPA. DMC and the experimental results are given for comparision. Note that theoretical P_t values have been corrected by ZPE and finite-temperature correction (300 K) using PBE phonon spectra.

Structure	Properties	RPA	Exp[a]	DMC[b]
α-quartz	V (Å^3/cell)	113.26	113.41	113.44
	c/a	1.0950	1.0995	—
	B (GPa)	44.8	38.0	32.0
	B`	4.89	6.0	7.0
	V_t (Å^3/SiO_2)	31.81	—	—
			Exp[a]	DMC[b]
Stishovite	V (Å^3/cell)	47.32	46.65	47.34
	c/a	0.6373	0.6387	—
	B (GPa)	311.7	313.0	305.0
	B`	4.26	2.8~6.0	3.7
	V_t (Å^3/SiO_2)	22.85	—	—
ΔE (eV/atom)	0.39			
P_t (GPa)	5.6			

[a]Ref [99]; [b]Ref [120].

In Table 4.5, we show the calculated phase transition parameters for SiO_2 by various semilocal and nolocal density functionals. It is found that the transition pressure from α-quartz to stishovite is increased by 0.57 GPa after including ZPE and FT correction (300 K). For the α-quartz to stishovite phase transition, PBE gives the best

phase transition parameters, and the results are comparable to the benchmark DMC calculations [120]. The transition pressures calculated by two meta-GGA functionals named TPSS and revTPSS are less accurate than PBE results. The hybrid functional HSE06 performs well for SiO_2 and the corresponding phase transition parameters are similar to DMC results. However, for the same system, RPA shows relatively poor performance for transition parameters compared to DMC, HSE06, and PBE. The calculated non-selfconsistent RPA energy difference between α-quartz and stishovite is smaller than the experimental value by 26.8 %. (RPA selfconsistency might reduce this error, if it lowered the energy more for the lower-symmetry α-quartz structure.) Therefore, the estimated non-selfconsistent RPA α-quartz to stishovite transition pressure is too small. The results shown in Table 4.5 for SiO_2 also indicate that both RPA and TPSS give similar values for the energy differences between stishovite and α-quartz. However, the transition pressure predicted by RPA is larger than that of TPSS; the main reason is that TPSS gives a too-large equilibrium cell volume for the quartz phase. Similarly, PBE gives the best energy difference for SiO_2, but the cell volumes of both phases are overestimated, especially for α-quartz (See Tables 3.4-3.6 in Chapter 3).

Table 4.5: The phase transition parameters of SiO_2 system computed from semilocal functionals (LDA, GGA and meta-GGAs), hybrid functional (HSE06), RPA and many-body method (DMC). The experimental results are given for comparision. Note that theoretical P_t values have been corrected by ZPE and finite-temperature correction (300 K).

E_{xc}	ΔE (eV/atom)	P_t (GPa)
LDA	-0.031	-0.37
PBE	0.532	6.94
PBEsol	0.171	2.71
AM05	0.292	3.79
TPSS	0.384	3.84
revTPSS	0.189	2.66
regTPSS	0.167	2.48
MGGA_MS0	0.467	6.16
MGGA_MS1	0.503	6.55
MGGA_MS2	0.286	3.99
HSE06	0.484	6.24
RPA	0.39	5.6
DMC[a]	0.50	6.2~6.5
Expt	0.51~0.54[b] 0.525[c], 0.48[c]	7.46[b]

[a]Ref [120]; [b]Ref [99]; [c]Ref [121].

4.3.2 Discussion

The good performance of nonlocal RPA for the equilibrium cell volume of α-quartz is partly related to the van der Waals interaction in the structure. The RPA captures the van der Waals interaction in various solids, including the strongly polarizable covalent and ionic solids and molecular crystal structures. For stishovite, the main reason for the observed discrepancies between the experimental cell volume and those of DMC and RPA is not clear at the moment. Does the underestimation of the energy difference by RPA arise from fixing the c/a ratios of α-quartz and stishovite at

their PBE values? The previous tests of the non-selfconsistent RPA algorithm on simple cubic solids give equilibrium lattice constants in good agreement with experiments [58]. Whether this is also true for low-symmetry crystal structures (like α-quartz with four internal degrees of freedom associated with atomic positions) is not known. In Figure 4.6, we show the calculated energy landscapes of SiO_2 structures near their equilibrium geometries. The results indicate that the present RPA method does not provide satisfactory equilibrium properties (cell volume and c/a ratio) for SiO_2 system. From the energy landscapes shown in Figure 4.6, the estimated energy difference between stishovite and α-quartz is even smaller than that given by using PBE geometries. Notice that in calculating the energy landscapes for SiO_2 phases, the internal degrees of freedom were relaxed using the PBE functional.

A likelier possibility is that low symmetry solids are more like molecules, in which the errors of the RPA correlation energy cancel out of iso-electronic energy differences less perfectly than they do for high symmetry solids [141, 142]. Ruzsinszky et al. [59] pointed out that the isoelectronic energy differences in solids are typically well-described by either RPA or RPA+, but a global hybrid functional such as equation 4.2 is more accurate for calculating the isoelectronic energy changes in molecules.

$$E_{total}(\text{Hybrid}) = \frac{1}{2} E_{total}(\text{PBE}) + \frac{1}{2} E_{total}(\text{RPA}) \tag{4.2}$$

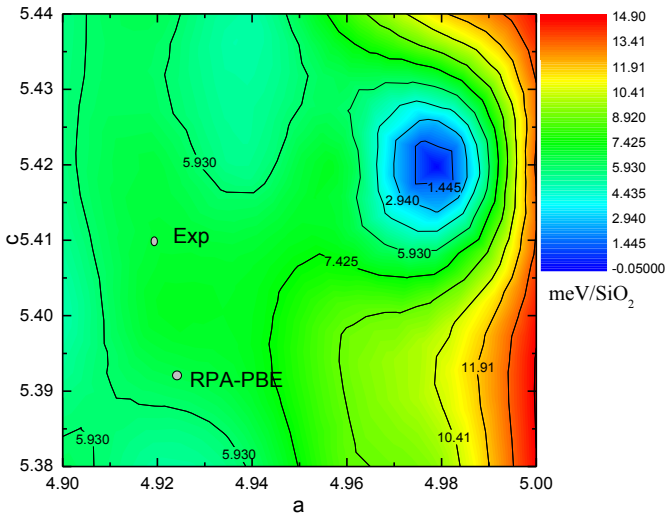

(a)

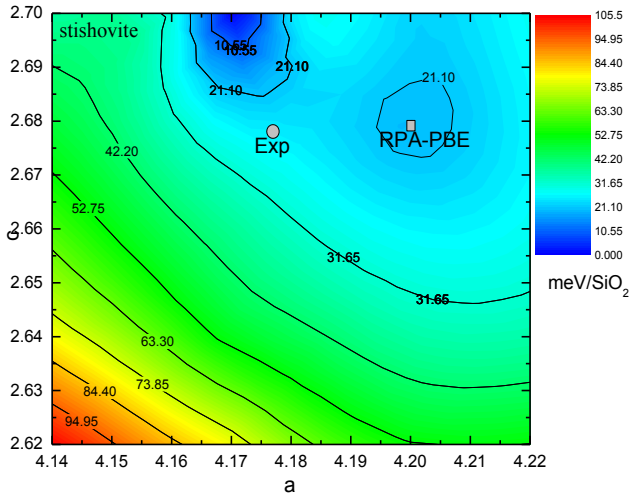

(b)

Figure 4.6: The energy landscapes of α-quartz and stishovite computed from RPA method, with all geometry parameters other than the lattice constants c and a from PBE. The energy minimum is in the darkest blue area. The experimental lattice constants are indicated by gray circles. The gray squares show the lattice constants found by minimizing the RPA energy with respect to a only, at fixed PBE c/a. The unit for lattice constants is Å. The local minimum is chosen to be the zero reference energy. (a): α-quartz (b): stishovite.

In order to verify our conjecture on the molecular nature of SiO_2 phases due to their low symmetry, we have recalculated the energy differences for Si and SiO_2 systems roughly using equation 4.3, and the corresponding values are 0.33 eV/atom and 0.46 eV/SiO_2, respectively.

$$\Delta E(\text{Hybrid}) = \frac{1}{2}\Delta E(\text{PBE}) + \frac{1}{2}\Delta E(\text{RPA}) \tag{4.3}$$

We can see that the calculated energy difference is improved for SiO_2, but it is worsened for Si.

CHAPTER 5

MAGNETISM AND ELECTRONIC STRUCTURES OF RUTILE-TYPE VO_2 PREDICTED BY JACOB'S LADDER OF DENSITY FUNCTIONALS

In this Chapter, we will test various exchange-correlation functionals for the ground state properties of Rutile-type VO_2. Similar to some well-known transition metal oxides such as FeO, NiO and CoO, R-VO_2 is also a strongly correlated system. The conventional semilocal functionals do not work properly for such systems. DFT+U and hybrid functionals are the two most- used remediations for strongly correlated systems. The meta-GGAs and non-self consistent random phase approximation (RPA) have not been tested for strongly correlated transition metal oxides. Since meta-GGAs are semilocal functionals, they may still fail for those systems. We are particularly interested in the non-self consistent RPA method, it is still a puzzle whether if it can give the correct ground state energy for R-VO_2.

5.1 VO_2 Ground State Puzzle

Vanadium dioxide (VO_2) has three known ploymorphs. The tetragonal rutile-type VO_2 is stable above 340 K at ambient pressure [143]. This high symmetry phase has a simple tegtragonal unit cell with space group $P4_2/mnm$ (136). There are two formula units in the unit cell. The vanadium atoms occupy the special 2a Wyckoff sites: V_I (0, 0, 0) and V_{II} (0.5, 0.5, 0.5). Meanwhile, the oxygens are located at 4f Wyckoff positions: $\pm$(u, u, 0), $\pm$(1/2+u, 1/2-u, 1/2), where u is the internal degree of freedom. In R-VO2, the

basic structural unit is VO_6 octahedral, aligned in $[1\bar{1}0]$ direction. The VO_6 octahedral is slightly distorted from the ideal geometry, i.e., the six V-O bonds are divided into two longer apical bonds and other four shorter equatorial bonds. The crystal structure of R-VO_2 is shown in Figure 5.1. The ground state electronic structure of R-VO_2 is a non-magnetic metal. Experimentally, it has been shown that the measured magnetic susceptibility above the transition temperature exhibits the paramagnetism [143].

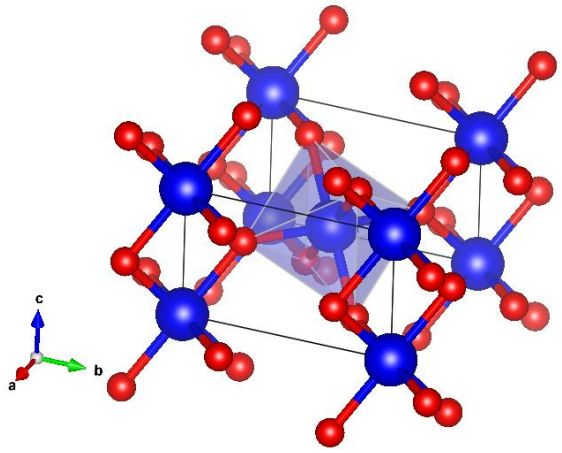

Figure 5.1: The crystal structure of Rutile-type VO_2. The small-red balls are oxygens, and the large-blue ones are vanadium atoms. The VO_6 octahedral is also highlighted in the cell.

Below 340 K, R-VO_2 is destabilized, and it transforms into a lower symmetry monoclinic phase (M-VO_2). The M-VO_2 has simple monoclinic lattice with space group $P2_1/c$ (14). The crystallographic parameters of M-VO_2 were reported before by Anderson [144] and Longo *et al*. [145]. The crystal structure is illustrated in Figure 5.2. The cell volume is doubled, compared to R-VO_2 phase. As a result, the M-VO_2 has four formula units in the unit cell. Vanadium and oxygen atoms occupy the subsets of general 4e Wyckoff site: $\pm$(x, y, z), $\pm$ (x, ½-y, ½+y), here x, y, z are internal degrees of freedom,

and which are different for V and O atoms. The electronic structure of M-VO_2 is a non-magnetic insulator.

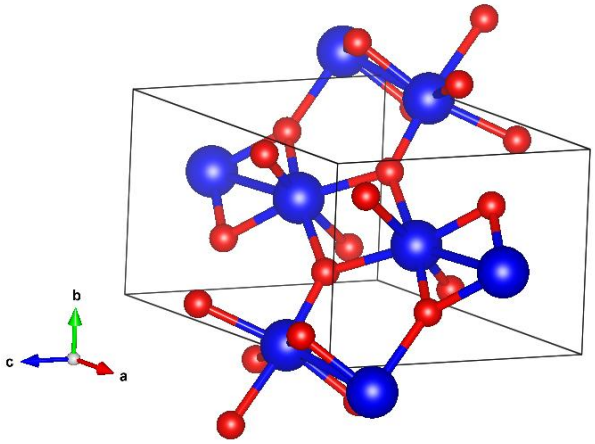

Figure 5.2: The crystal structure of low temperature M-VO_2 phase. The V-V bond in V_2 dimer is also shown.

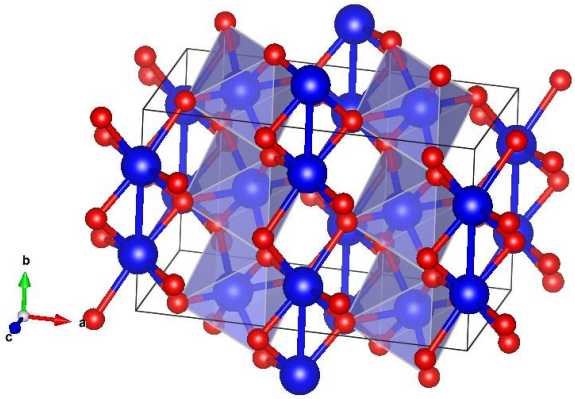

Figure 5.3: The crystal structure of M2-VO_2. Both the dimerized V_2 pair and VO_6 octahedral are highlighted.

It is believed that M2-VO_2 is an intermediate phase between R-VO_2 and M-VO_2. The existence of M2-VO_2 has been confirmed experimentally [146]. The conventional cell of M2-VO_2 adopts a c-centered monoclinic lattice with space group C2/m. In the

conventional cell, there are two different types of metal atoms and three types of oxygens. The M2-VO_2 has eight formula units in the conventional cell, and all 8 vanadium and 16 oxygen atoms occupy different subsets of 8j Wyckoff site: ± (x, y, z), ±(x, -y, z), (1/2, 1/2, 0)±(x, y, z), and (1/2, 1/2, 0)±(x, -y, z). The crystal structure in displayed in Figure 5.3. The electronic structure of M2-VO_2 phase is under debate at the moment, because half of the V atoms show the similar chemical envoirment to R-VO_2, while the remaining V atoms are dimerized, and the isolated V-V pairs are formed. Since M2-VO_2 is an insulator, it is believed that the strong correlation plays the essential role in this phase [143].

The exact transition mechanism from R-VO_2 to M-VO_2 is unclear at the moment [147-154]. In some earlier works, using the information obtained either from phonon dispersions or electronic structures, the phase transition was found to be driven by the structural distortion or Peierls transition [143, 148-150]. Such mechanism is supported by some experimental results [152, 153]. Havorkort and coworkers [154] studied the changes of orbital occupation numbers due to phase transition in VO_2 system by measuring the V $L_{2,3}$ XAS spectrum near the transition temperature. They found that the localization of 3*d* electrons is the prerequisite for occurence of the Peierls distortions. On the other hand, Korotin *et al*., [147] calculated the electronic structures of both M-VO_2 and R-VO_2 using LSDA and LSDA+U methods. Their results strongly implied a Mott-Hubbard transition in this system. More recently, Eyert [148] applied HSE06 functional to study the magnetism and electronic structures of VO_2 structures. It was found that HSE06 functional gave the better descriptions for the ground state properties of VO_2

polymorphs, compared to other semilocal functionals. However, Grau-Crespo *et al*., [155] revisited the magnetic structures and ground state energies evaluated by the HSE06 functional. They concluded that HSE06 opens the band gap for metallic R-VO_2 phase, and the obtained magnetic state is wrong for this structure. For example, the HSE06 functional significantly stabilizes the spurious spin polarized phases (ferromagnetic and anti-ferromagnetic states), and its results are even less accurate than the results computed by semilocal functionals tested previously.

In this dissertation, we will only study the R-VO_2 phase. The previous DFT results suggest that none of the exchange-correlation approximations on Jacob's ladder could predict the correct ground energy even for this simpliest VO_2 phase. We are mainly interested in using meta-GGAs and non-self consistent RPA to revisit the ground state properties of R-VO_2. The results may provide some valuable information for developing better exchange-correlation functionals in the future.

5.2 Methods and Details

5.2.1 DFT Calculations

The calculations were performed using the projector augmented wave (PAW) method in Vienna *ab-initio* simulation program (*VASP*) [97]. The PAW pseudopotentials employed in this work for V and O atoms were V_{3p3d4s} and O_{2s2p} within the frozen core approximation. The plane wave basis was expanded in the reciprocal space using kinetic energy cutoff of 500 eV. The evaluations of ground state energy and electron density were conducted in the first irreducible Brillouin zone using 12 × 12 × 16 k-mesh of

Monkhorst-Pack type [106]. In this paper, we have considered the following meta-GGA level of exchange-correlation functionals including TPSS [37], revTPSS [39], regTPSS [40], meta-GGA made simple (MGGA_MS0 [41] and MGGA_MS2 [42, 43]). The first two meta-GGA functionals have been widely tested for various systems such as atoms, molecules and solids [73]. The latter two functionals were devised recently in order to further improve the performances of TPSS and revTPSS for some specified issues [40, 43]. Nevertheless, none of these non-empirically derived meta-GGA functionals have been tested for magnetic transition metal oxides. The calculations were also performed within local spin polarized density approximation (LSDA) by means of the Perdew-Zunger scheme [19] and the generalized gradient approximation (GGA) in terms of the Perdew-Burke-Ernzerhof (PBE) functional [25]. For the PBE+U method, we have employed an earlier implementation of LSDA+U method proposed by Dudarev [156] in VASP code, and the effective U_{eff} = 3.32 eV (U = 4.0 eV and J = 0.68 eV) was used for *3d* shells of V atom [157]. The calculations within the range separated hybrid functional in terms of HSE06 were also conducted for the different magnetic states of R-VO_2. Our calculation parameters were 400 eV for kinetic energy cutoff and 6 × 6 × 8 k mesh generated by Γ-centered method, which are similar to those employed in Ref. [155]. The default range separation parameter (μ = 0.20 $Å^{-1}$) in VASP code was used in the current work [50-52].

For the RPA calculations, the total energy consists of two different parts, i.e., the correlation energy (E_c) and Hartree-Fock exact exchange energy (E_{HFx}). The classic Hartree energy and exact exchange energy are included in E_{HFx} term. In the current paper,

the R-VO_2 was treated as metallic phase. For metallic structure, the special strategy must be employed to achieve the numerical convergence [15, 58]. In our RPA calculations, the kinetic energy cutoff was set as 430 eV for FM and spin compensated PM states. Meanwhile, the AFM required 480 eV to reach the convergence. The k-point mesh was generated using the similar method employed in other semilocal functionals. The convergence tests were conducted for the calculated energy differences between non-magnetic and magnetic states of R-VO_2 by varying the kinetic energy cutoff and k grid. We found that a 6 × 6 × 8 k grid was sufficient to get the converged energy difference between the magnetic and non-magnetic states at the satisfactory level (±10 meV/VO_2) (Details will be presented in next section).

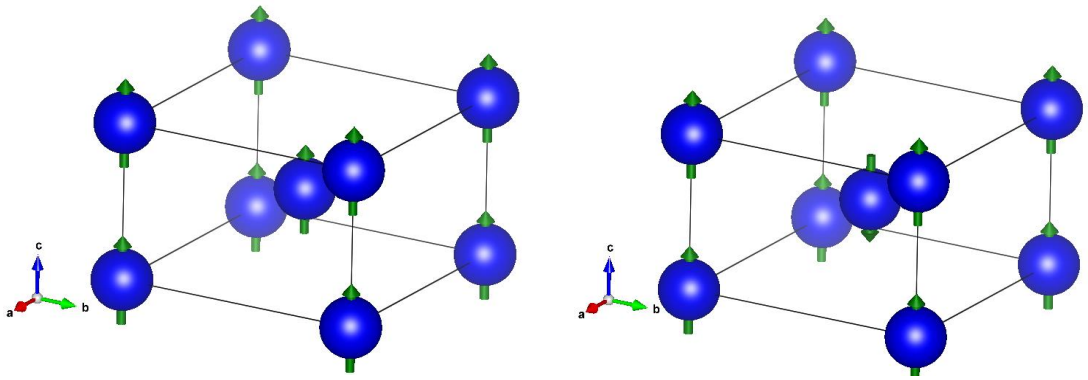

(a) (b)

Figure 5.4: Local spin directions in ferromagnetic (FM) and anti-ferromagnetic (AFM) states of vanadium sublattice. The oxygens atoms are not shown in the unit cell.

For rutile-type VO_2, the calculations were carried out for three different magnetic configurations by assuming the local magnetic moments of V atoms in different magnitudes and directions, i.e., ferromagnetic (FM, with initial local magnetic moment as

$2\mu_B$), anti-ferromagnetic (AFM, the initial guess of local moment has the similar magnitude to FM state) and spin compensated paramagnetic (PM, $0.1\mu_B$ as the initial local moment) states. Note that the spin compensated PM state is different to a realistic PM phase. In the former case, the local moment is zero for each magnetic ion, because the majority and minority spin densities have the same magnitude at the same atomic site. Meanwhile, the local moments carried by magnetic ions in the latter case are not only randomly distributed but also vary strongly in magnitude. In Figure 5.4, the crystal structure of R-VO_2 is illustrated for FM and AFM states. All DFT calculations were spin polarized. Additionally, the experimental lattice constants of R-VO_2 were used in our paper, i.e., a=4.5546 Å and c=2.8514 Å [143]. The internal degrees of freedom of rutile-type VO_2 were optimized accordingly for each exchange-correlation functional. Using the current settings, the total energy was converged to 0.001 meV/atom and the mean Hellmann-Feynman force acting on atoms was reduced to 0.01 eV/Å.

5.2.2 Convergence Tests for RPA

The convergence tests have been carried out for all three magnetic states of R-VO_2, using different k-meshes and kinetic energy cutoff values. In this dissertation, some main results are presented.

The absolute convergence of RPA total energy is difficult to reach. From our previous work on phase transition in solid using RPA and Refs. 15 and 58, we found that the kinetic energy cutoff value and k-mesh are the two most important parameters controlling the final quality of the numerical results. In our current paper, the RPA was

employed to compute the total energy versus volume curves for three different magnetic states of Rutile-type VO_2. The criteria for determining the convergence of total RPA energy with respect to k mesh is simple. By fixing the size of the plane wave basis (ENCUT in vasp input), we have computed the energy versus volume profile for R-VO_2 using different k meshes. As long as the computed energy versus volume curve is smooth, for example, the curve does not show any obvious kinks or large fluctuation in the magnitude. Then, it is safe to use the k mesh determined in this way for the following RPA calculations. For R-VO_2, the Γ -centered $6 \times 6 \times 8$ k-mesh is sufficient for RPA method. Note that due to the symmetry breaking in different magnetic states, such k-mesh is equivalent to 50 irreducible k-points in first Brillouin zone (IBZ) for FM state and spin compensated PM state. In the case of AFM phase, there are 65 k points in IBZ using this k-mesh.

The next step is to fix the k-mesh, and computing the RPA total energy with different kinetic energy cutoff values. However, as discussed in Ref. 15, as long as we use finite plane wave basis (ENCUT is finite value), the absolute convergence of RPA correlation energy is intractable. Otherwise, the computational costs will be unaffordable if the kinetic energy cutoff is too high. In Ref. 61, the authors tested the convergence of RPA calculation for a single layer graphite adsorbed on transition metal surfaces using the binding energy as the criteria. The similar strategy was employed in this work. We have computed the energy differences between two spin polarized magnetic states and the spin compensated PM state by varying the ENCUT value in input. It was found that for PM and FM states, the energy difference between them is converged to ± 10 meV/VO_2 by

setting ENCUT to 430 eV. Meanwhile, the energy difference of AFM and PM states requires 480 eV to reduce the error below ±10 meV/VO_2. Due to the hardware limitations (WALLTIME limit and Memory per core), the increase of ENCUT further above 500 eV were not conducted.

In Figure 5.5, the total RPA energy versus volume curve are shown. We can see that the obtained curves in different magnetic states are smooth. Next, we recalculated the energy versus volume curve for FM R-VO_2 using a larger kinetic energy cutoff value, i.e., 430 eV. The obtained profile is shown in Figure 5.6 together with that of using 350 eV. The main effect of increasing the ENCUT is to shift the entire curve evenly downward. In addition, the computed energy difference between spin compensated PM and other two magnetic states (FM and AFM) are illustrated in Figure 5.7.

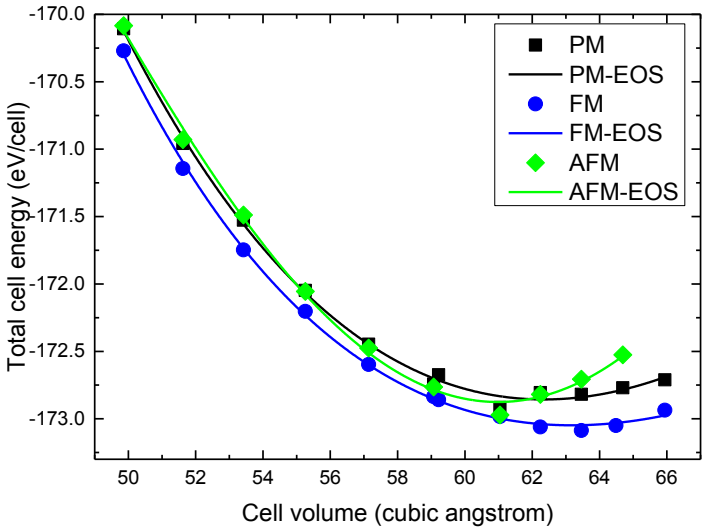

Figure 5.5: The computed total energy versus cell volume curves for FM, AFM and PM states of R-VO_2 by RPA using PBE inputs (charge density, Kohn-Sham single particle energies and geometry.). The computing parameters ENCUT = 350 eV and k-mesh 6 × 6 × 8 were used in the calculations. The solid lines are obtained by fitting the data to equation of state (EOS).

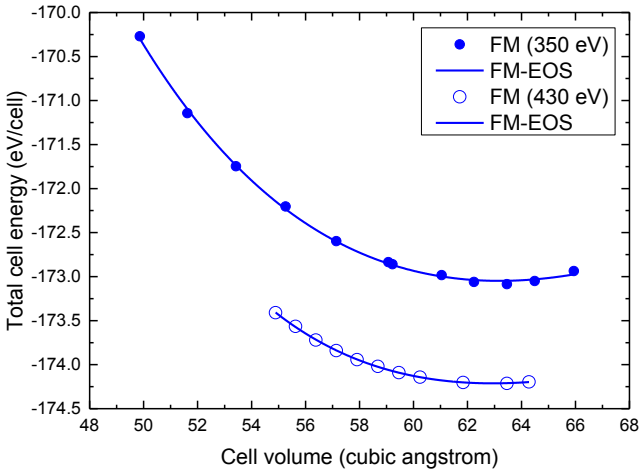

Figure 5.6: The energy versus volume curves computed at two different kinetic energy cutoff values by RPA. Similar to Figure 5.5, the solid lines are obtained from EOS fitting.

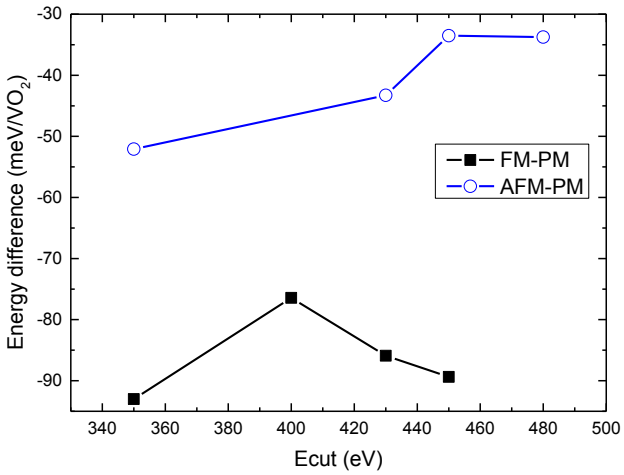

Figure 5.7: The convergence tests for the computed energy differences between spin compensated PM state and other two magnetic states using RPA. Note that in all calculations, the k mesh was fixed to 6 × 6 × 8.

5.2.3 Construction of Proper Local 3*d* States

Since the octahedral of VO_6 unit in R-VO_2 is aligned in [110] and [1$\bar{1}$0] directions, therefore, the principal axes of crystallographic coordinates can be different to

those axes of local Cartesian coordinates for V atoms. The relationship between two sets of coordinate systems is illustrated in Figure 5.8. It is found that the computed angular momentum projected density of states of R-VO_2 in different magnetic states can be only explained using the appropriate 3*d* orbital sets in the local coordinates. The splitting of 3*d* orbitals in different crystal fields is also depicted in Figure 5.9. Without considering the tetragonal distortions, the five-fold degenerated 3*d* orbitals of V in O_3 symmetry split into E_g and T_{2g} groups in an octahedral crystal field (O_h). As shown in Figure 5.8, the local coordinates for V_I or V_{II} atoms are aligned in such way that the local z axis is pointed to apical O atoms; x and y axes are aligned to the equatorial O atoms. For the tetragonal symmetry, the further splitting of either E_g or T_{2g} groups of orbitals can be easily obtained from character table of D_{4h} point group, i.e., $E_g = A_{1g} + B_{2g}$ and $T_{2g} = B_{1g} + E_g$ (See Figure 5.9). As pointed out in Ref. 143, the deviation of VO_6 polyhedral in R-VO_2 from perfect cubic O_h symmetry is usually quite small. Therefore, the notations of cubic symmetry are still applicable to the computed electronic structures of R-VO_2. The proper local *d'* orbitals (d'_{z^2}, $d'_{x^2-y^2}$, d'_{xy}, d'_{yz} and d'_{xz}) can be represented by the appropriate linear combinations of five normal *d* orbitals under global crystallographic coordinates (X-Y-Z system). For V_I and V_{II}, the expressions for local $3d'$ orbitals are given as

$$V_I \rightarrow \begin{cases} d'_{z^2} = d_{xy} \\ d'_{x^2-y^2} = \frac{4}{3} d_{yz} - \frac{4}{3} d_{xz}) \\ d'_{xy} = \frac{2}{3} d_{xy} + \frac{1}{3} d_{z^2} \\ d'_{xz} = \frac{1}{\sqrt{6}} d_{xz} + \frac{1}{\sqrt{6}} d_{yz} - \frac{1}{\sqrt{6}} d_{x^2-y^2} \\ d'_{yz} = \frac{1}{\sqrt{6}} d_{xz} + \frac{1}{\sqrt{6}} d_{yz} + \frac{1}{\sqrt{6}} d_{x^2-y^2} \end{cases} \quad (5.1)$$

$$V_{II} \rightarrow \begin{cases} d'_{z^2} = d_{xy} \\ d'_{x^2-y^2} = \frac{4}{3} d_{yz} + \frac{4}{3} d_{xz} \\ d'_{xy} = -\frac{2}{3} d_{xy} + \frac{1}{3} d_{z^2} \\ d'_{xz} = \frac{1}{\sqrt{6}} d_{xz} - \frac{1}{\sqrt{6}} d_{yz} + \frac{1}{\sqrt{6}} d_{x^2-y^2} \\ d'_{yz} = \frac{1}{\sqrt{6}} d_{xz} + \frac{1}{\sqrt{6}} d_{yz} - \frac{1}{\sqrt{6}} d_{x^2-y^2} \end{cases} \quad (5.2)$$

Note that, the five 3*d*` orbitals given in equations 5.1 and 5.2 are not rigorously normalized. VO_2 also crystallizes into a monoclinic phase (M_1-VO_2) at low temperature (below 340 K). The phase transformation of R-VO_2 into M_1-VO_2 is a metal to insulator transition, which is accompanied by the dimerization of V atoms in [001] direction. This structural transition is also associated with the overlapping of *d* orbitals with the two nearest V atoms in the same direction. Based on the resulting chemical bond types due to 3*d*-3*d* overlapping, the lower laying T_{2g} orbitals can be identified as π and σ orbital symmetry [143, 150]. As can be seen from Figure 5.9, d'_{xy} forms the strongest σ-type

bond in the sublattice consisting of V_{II} (V_I) in [001] direction. Otherwise, the π-bonds are dominated by d'_{yz} and d'_{xz} orbitals.

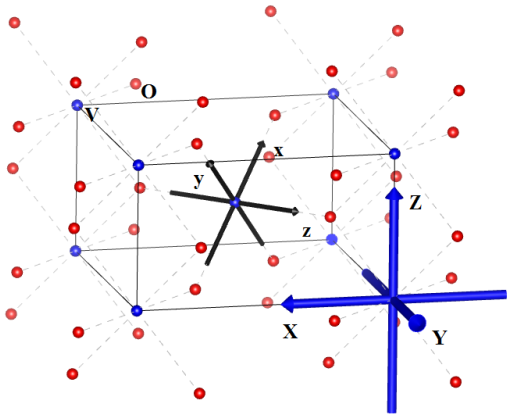

Figure 5.8: The global crystallographic coordinates (X-Y-Z) and local vanadium Cartesian coordinates (x-y-z) in R-VO_2 crystal structure.

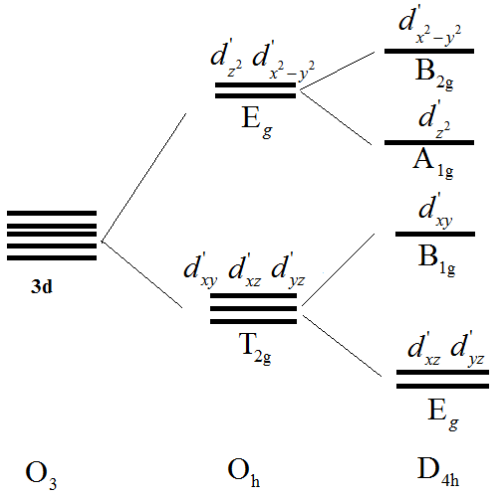

Figure 5.9: The irreducible representations of local 3*d* states in different crystal fields. Note that O_3 represents the spherical symmetry ($D_{\infty h}$).

5.3 Stability of Different Magnetic States

Experimentally, the ground state of R-VO_2 at room temperature is a non-magnetic metal. The previous calculations based on either semi-local functionals (LSDA and

GGA) or orbital dependent DFT methods (DFT+U and HSE06) could not reproduce the correct ground state of this phase using the experimental lattice constants [148, 155]. The obtained total energies of spurious spin polarized (FM and AFM) states are always lower than that of spin compensated PM state. For example, Williams *et al*., [158] have calculated the energy differences of R-VO_2 in magnetic states (AFM and FM) with respect to non-magnetic state. It was found that the energies of FM and AFM phases are lowered by 135 meV/ VO_2 and 56 meV/VO_2 using PBE functional, compared to non-magnetic phase. HSE06 and DFT+U are less accurate than PBE for the ground state energy of PM R-VO_2 [155]. One should note that in the works of Williams and coworkers [158], both the lattice constants and atomic positions were fixed to their experimental values. However, the atomic positions are allowed to relax in our calculations. We have applied the exchange-correlation functionals of all five rungs on Jacob's ladder (LSDA, PBE, meta-GGAs, HSE06 and RPA) to calculate the energy differences between two magnetic states (FM and AFM) and spin compensated PM state. The results are given in Table 5.1. Clearly, none of the tested methods can reproduce the experimental ground state of R-VO_2. The spurious FM and AFM states are always more stable than spin compensated PM state. Otherwise, the FM state has much lower energy than AFM state. All exchange-correlation functionals predict the FM state is the ground state for R-VO_2 except that of LSDA+U. In the latter method, AFM state is slightly more stable than FM state by nearly 7 meV per VO_2 unit. DFT+U method favors the strong localization of 3*d* electrons, and the electrons of R-VO_2 in AFM state are more localized than FM state. Therefore, LSDA+U may tend to overestimate the electron localization

and which lowers the total energy of AFM below that of FM state. Otherwise, the energy differences given by LSDA+U and HSE06 are significantly more negative than semilocal functionals and RPA. Our HSE06 values are similar to those reported in Ref. 155. For RPA, the starting Kohn-Sham single particle energy and orbitals were computed by PBE. The obtained energy difference by non self-consistent RPA is better than PBE for FM state, but it is worse than that of PBE in AFM state. Among the five meta-GGA functionals, the FM and AFM states of R-VO_2 phase are strongly favored by MGGA_MS0 and MGGA_MS2, because the calculated energy differences between two magnetic states and PM state are significantly more negative than TPSS, revTPSS and regTPSS. Meanwhile, TPSS and revTPSS give similar results for the calculated energies. The magnetization energies of regTPSS are slightly more negative than revTPSS and TPSS. Moreover, the best overall performance for the ground state energy of R-VO_2 is surprisingly attributed to LSDA method. The total energies of spurious FM and AFM states calculated with LSDA are quite close to the spin compensated non-magnetic state, indicating that LSDA is more accurate than other DFT methods for ground state energy of non-magnetic spin singlet R-VO_2 phase.

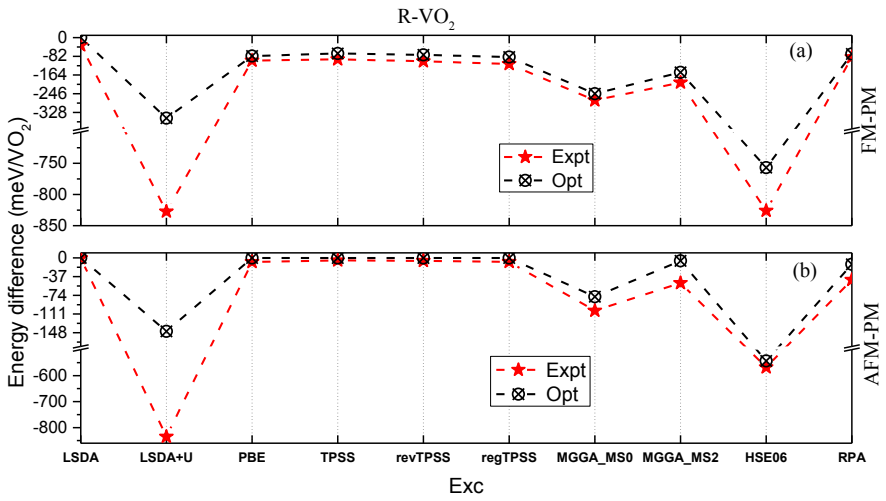

Figure 5.10: The energy differences between two spurious magnetic states (FM and AFM) and spin compensated non-magnetic state are calculated using the experimental lattice constants and fully relaxed geometry, respectively. Note that for RPA, the values marked as "OPT" are obtained by minimizing the total energy with respect to PBE cell volume.

Table 5.1: The computed energy differences of R-VO_2 in three magnetic states by different exchange-correlation functionals on Jacob's ladder using the experimental lattice parameters.

E_{xc}	ΔE_{FM-PM} (meV/VO_2)	ΔE_{AFM-PM} (meV/VO_2)
LSDA	-33.50	-0.40
LSDA+U	-827.36	-834.80
PBE	-100.71	-8.13
TPSS	-95.24	-4.96
revTPSS	-103.70	-5.83
regTPSS	-115.59	-7.80
MGGA_MS0	-257.07	-104.38
MGGA_MS2	-196.94	-49.66
HSE06	-826.09 -739.0[a]	-567.95 -700.0[a]
RPA	-85.90	-43.27

[a]Ref [155].

Table 5.2: The similar quantities to Table 5.1 are evaluated, but using the optimized geometries.

E_{xc}	$\Delta E_{FM\text{-}PM}$ (meV/VO_2)	$\Delta E_{AFM\text{-}PM}$ (meV/VO_2)
LSDA	-0.11	+0.08
LSDA+U	-352.94	-145.20
PBE	-80.66	-0.09
TPSS	-69.74	-0.12
revTPSS	-75.85	-0.12
regTPSS	-85.15	-0.17
MGGA_MS0	-245.69	-76.71
MGGA_MS2	-152.23	-5.83
HSE06	-756.84	-543.33
RPA	-75.55	-12.50

Using the fully relaxed unit cell, we recalculate the energy differences for R-VO_2. The results are illustrated in Figure 5.10, and also are given in Table 5.2. We can see that the computed energy differences generally show a dependence on the geometry. Especially for LSDA+U and HSE06, the errors in energy differences between spurious magnetic states and non-magnetic state are greatly reduced using the optimized geometry. It is also worth noting that LSDA now stabilizes spin compensated PM state over the AFM state. The total energy of AFM state is slightly higher than PM state by 0.08 meV per VO_2. Meanwhile, the total energy of FM state is almost identical to non-magnetic phase by LSDA. Moreover, the relative stability of PM state is comparable to AFM state by the semilocal functional. The RPA results are also improved through the energy minimization strategy. In summary, in the fully relaxed case, LSDA still gives the best ground state energy for R-VO_2 among all tested density functional methods.

In Figure 5.11, the calculated total magnetic moments of V atoms are given according to their Wyckoff positions. For R-VO_2, the covalent state of V is +4, implying a $3d^1$ configuration. Therefore, the nominal magnetic moment of V is 1 μ_B. Our calculations for FM state of R-VO_2 are roughly in agreement with this conjecture for all tested density functionals. One should note that obtained magnetic moments of V atoms by MGGA_MS0, MGGA_MS2, LSDA+U and HSE06 for R-VO_2 in FM state are larger than 1μ_B. Meanwhile, LSDA and TPSS slightly underestimate the local moments in FM state. We find that RPA give the exact 1μ_B in the same magnetic state. In the FM state, the RPA local moment for V atom was obtained by minimizing the total cell energy with respect to magnetic moment. On the other hand, the results are quite different for AFM state. Among semilocal functionals, LSDA, PBE, TPSS, revTPSS and regTPSS predict much smaller magnetic moments for V atoms than MGGA_MS variants. The values of former exchange-correlation functionals are only 30%~50% of other functionals (LSDA+U, MGGA_MS0, MGGA_MS2 and HSE06). HSE06 gives the largest local moment for AFM state. The local moments obtained by LSDA+U, MGGA_MS2 and HSE06 are close to the exact value of 1μ_B for V^{4+} cation. For semilocal functionals, the underestimation of local magnetic moment in AFM state implies that the spin up and down components are compensated to each other at V site, resulting in an electron distribution similar to spin compensated PM state. Sun *et al*., [159] have tested TPSS and revTPSS for the magnetic moments of Fe, Co and Ni in their ferromagnetic state. The obtained magnetic moments of these 3*d* transition metals are in good agreement with experimental values. Our results for the R-VO_2 and also those of Ref. 159 imply that

TPSS and revTPSS describe magnetic moments of ferromagnetic state more accurate than anti-ferromagnetic phase. Basically, we found that TPSS and revTPSS give a different electronic structure of R-VO_2 to other semilocal functionals. The computed electronic structures of R-VO_2 by regTPSS are somewhat situated between MGGA_MS family of density functionals and TPSS or revTPSS.

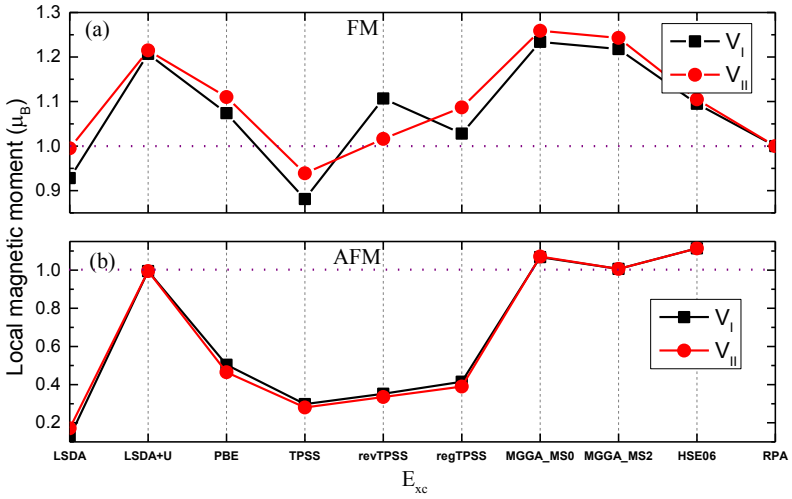

Figure 5.11: The computed local magnetic moments of V atoms by different exchange-correlation functionals. The horizontal line represents the exact value of local magnetic moment carried by a V^{4+} cation. (a): FM; (b): AFM. The fractional coordinates for V_I and V_{II} are (0, 0, 0) and (0.5, 0.5, 0.5), respectively.

5.4 3*d* States Weighted Band Dispersions

The weighted band dispersions of ferromagnetic R-VO_2 in the up spin direction are shown in Figure 5.12 for the tested exchange-correlation functionals. The results for the spin down electrons are quite similar to those of up spin channel except the band energies are shifted due to the exchange splitting. The unit cell of R-VO_2 has two VO_2 structural units, implying that total number of bands in each spin channel is doubled,

compared to one VO_2 formula unit. In our plots, the four lowest laying bands (below -15 eV) mainly consist of 2*s* orbitals of O atoms. The 2*s* bands are less dispersive and their band energies are also far below the Fermi level. Therefore, the overlap of *2s* orbitals with other nearest atoms are expected to be negligible. From Figure 5.13, we find that meta-GGAs predict more negative energy for 2*s* bands than LSDA, LSDA+U and PBE. Among meta-GGAs, MGGA_MS0 and MGGA_MS2 give less negative band energy than TPSS, revTPSS and regTPSS for 2*s* orbitals. Meanwhile, MGGA_MS variants also predict the narrower band widths for 2*s* orbitals than other functionals. The main reason why meta-GGAs tend to lower the 2*s* band energy can be explained using their exchange gradient enhancement factors in limit of small *s* when α is zero. Unlike LSDA and PBE, meta-GGAs tested in this paper use α to distinguish the single orbital region ($\alpha = 0$) and uniform electron gas ($\alpha = 1$) having the same *s* [36, 37, 39, 41]. In the single orbital region, we have $\alpha = 0$ and small *s*. The exchange gradient enhancement factor in a meta-GGA is always larger than LDA and PBE in such case. Therefore, meta-GGAs lower the energy of 2*s* orbital further below that the latter functionals.

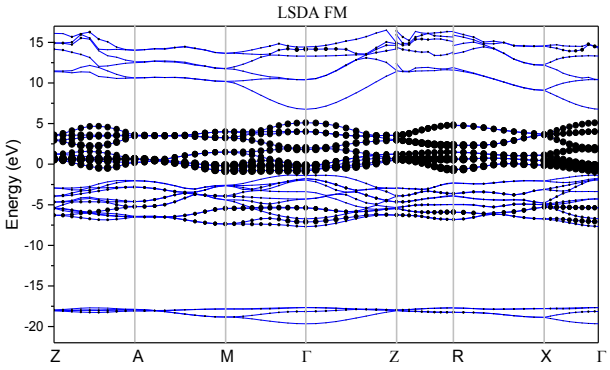
LSDA FM
Energy (eV)
15
10
5
0
-5
-10
-15
-20
Z
A
M
Γ
Z
R
X
Γ

(a)

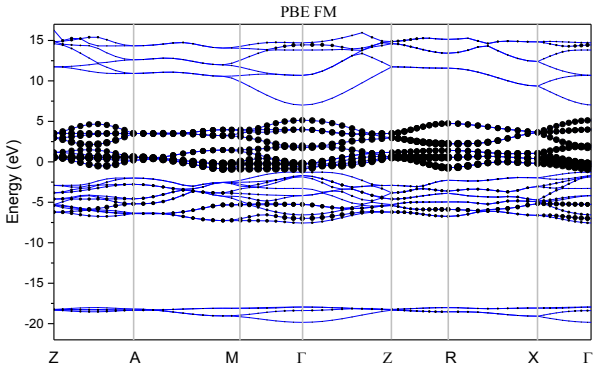
PBE FM
Energy (eV)
15
10
5
0
-5
-10
-15
-20
Z
A
M
Γ
Z
R
X
Γ

(b)

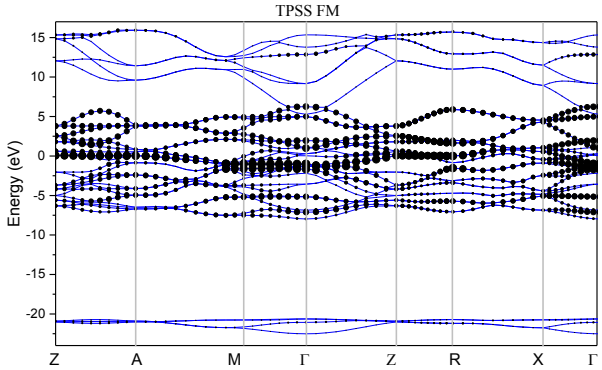
TPSS FM
Energy (eV)
15
10
5
0
-5
-10
-15
-20
Z
A
M
Γ
Z
R
X
Γ

(c)

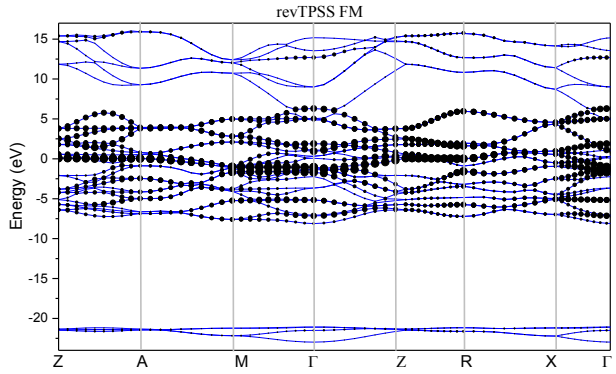
revTPSS FM
Energy (eV)
15
10
5
0
-5
-10
-15
-20
Z
A
M
Γ
Z
R
X
Γ

(d)

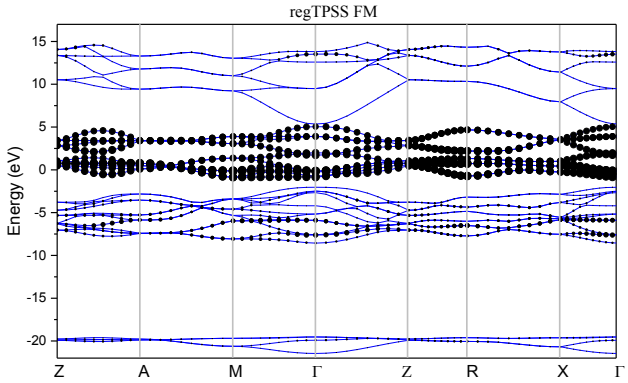
regTPSS FM
Energy (eV)
15
10
5
0
-5
-10
-15
-20
Z
A
M
Γ
Z
R
X
Γ

(e)

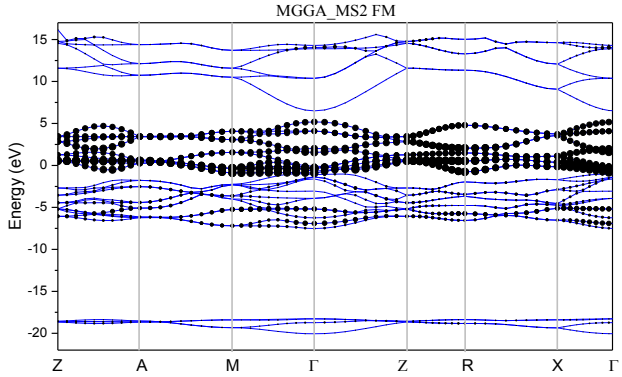
MGGA_MS2 FM
Energy (eV)
15
10
5
0
-5
-10
-15
-20
Z
A
M
Γ
Z
R
X
Γ

(f)

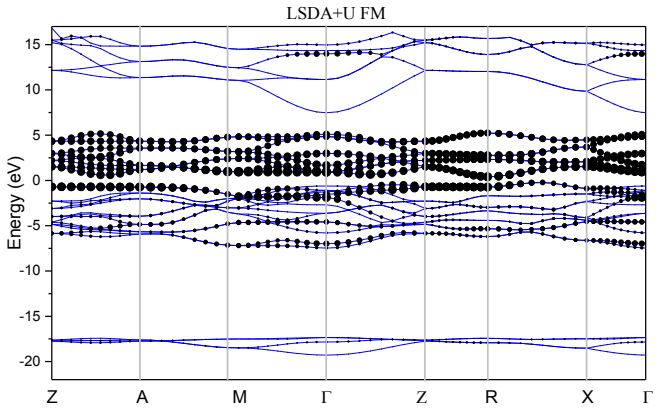

(g)

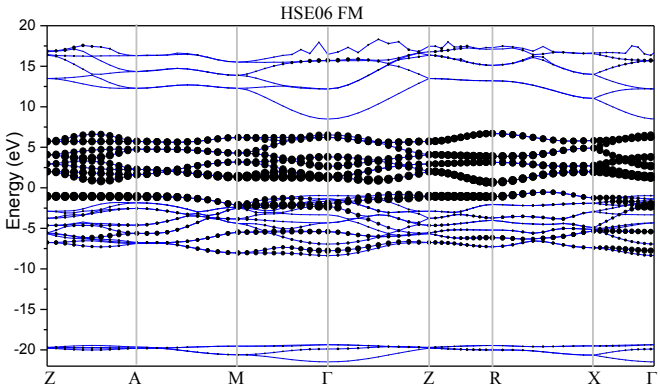

(h)

Figure 5.12: The weighted up spin band dispersions of rutile-type VO_2 calculated by semilocal functionals and also PBE+U. The size of black dots represents the weights of 3*d* orbitals of V atoms. The solid-blue lines are the band dispersions of bulk R-VO_2. The fractional coordinates for these special high symmetry k points are Z (0, 0, 1/2), A (1/2, 1/2, ½), M (1/2, 1/2, 0), Γ (0, 0, 0), R (0, 1/2, 1/2) and X (0, 1/2, 0). (a): LSDA; (b): PBE; (c): TPSS; (d): revTPSS; (e): regTPSS; (f): MGGA_MS2; (g): LSDA+U; (h): HSE06. The Fermi level is set as zero at the top of valence band.

It can be clearly seen from Figure 5.12 that the conduction bands of R-VO_2 are mainly attributed to 3*d* states of V atoms. The lower part of *d* bands is made of six T_{2g} type orbitals (d'_{xy}, d'_{yz} and d'_{xz}). Otherwise, the upper *d* bands consist of other four E_g

type orbitals (d'_{z^2} and $d'_{x^2-y^2}$). The band gap of E_g-T_{2g} splitting due to O_h (or D_{4h}) crystal field for 3*d* states in R-VO_2 was described in some previous works [143, 147]. In our calculations, the tail of T_{2g} states are always overlapped with the head of E_g bands. Therefore, no obvious crystal field created band gap can be observed between E_g and T_{2g} bands. The mixture of 3*d* bands with 2*p* states determines the strength of V-O covalent bonds in the structure. For TPSS and revTPSS, the 2*p*-3*d* hybridizations are significantly stronger than other tested functionals, and which have been clearly illustrated in the calculated 3*d* weighted band dispersions in Figure 5.12. For example, the entire 2*p* bands predicted by revTPSS and TPSS exhibit the strong 3*d* character. This can be also seen from the computed band widths of 2*p* states. TPSS, revTPSS give the larger band width for 2*p* band than other tested functionals. In the case of PBE+U and HSE06, two 3*d* states, mainly consist of d_{z^2} (or d'_{xy} in local x-y-z coordinates) orbital, are fully occupied and their positions can be even lower than 2*p* bands at Γ point. The band gap is opened between occupied and unoccupied 3*d* states. As a result, in LSDA+U and HSE06 calculations, the R-VO_2 is the Mott insulator in FM and AFM states. Interestingly, one can see the bands below Fermi level at Γ point show very strong 3*d* character in TPSS and revTPSS calculations. Unlike LSDA+U and HSE06, TPSS and revTPSS are unable to open the band gap between occupied and empty 3*d* bands, both 3*d* and 2*p* bands make contributions to the density of states at Fermi level. In contrast to TPSS and revTPSS, the Fermi surface is mainly dominated by 3*d* states for the remaining density functionals.

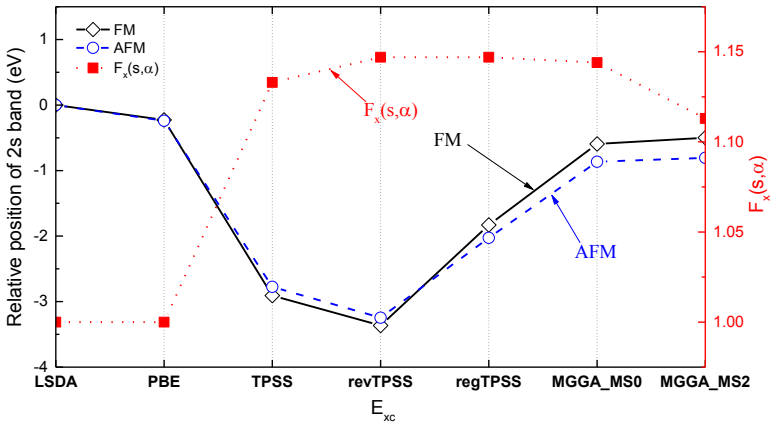

Figure 5.13: The relative positions of 2*s* bands computed by semilocal functionals in FM and AFM states. The 2*s* band positions obtained from LSDA are set as zero. The value of $F_x(s, \alpha)$ is evaluated with the assumptions that $s \rightarrow 0$ and $\alpha = 0$ for the spherical-like single orbital region.

5.5 Angular Momentum Projected Density of States

The construction of proper local $3d'$ orbitals is the essential step to explain the computed density of states. In Figures 5.14 and 5.15, we show the spin polarized density of states of FM, AFM and spin compensated PM phases of R-VO_2. The results of FM phase will be discussed first. As can be seen from Figure 5.14, the electronic structures of R-VO_2 in FM state can be identified as three different categories. PBE, regTPSS and two MGGA_MS functionals predict the half-metal for ferromagnetic R-VO_2; LSDA+U and HSE06 give a Mott-Hubbard insulator; TPSS and revTPSS compute it as normal magnetic metal. Experimentally, the true ground state of R-VO_2 at room temperature is a non-magnetic metal. Although, Eyert [148] claimed that the recently developed HSE06 hybrid functional can provide the good results for electronic structure and magnetic property of VO_2 structures, the later works done by Grau-Crespo and coworkers [155] revealed that HSE06 strongly stabilizes the magnetic phases.

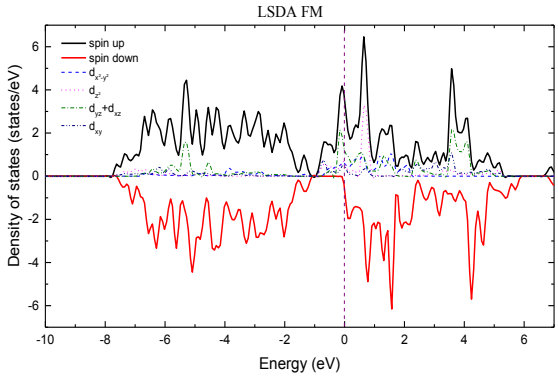
LSDA FM
spin up
spin down
$d_{x^2-y^2}$
d_{z^2}
$d_{yz}+d_{xz}$
d_{xy}
Density of states (states/eV)
Energy (eV)

(a)

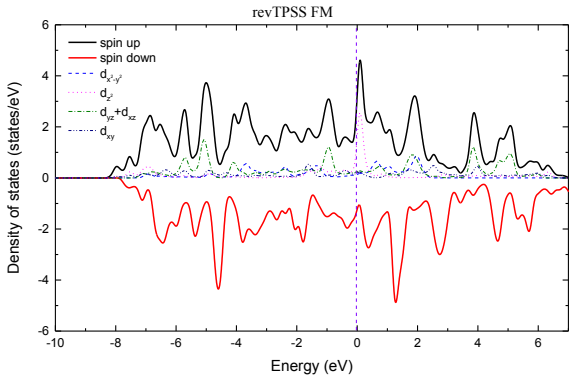
revTPSS FM
spin up
spin down
$d_{x^2-y^2}$
d_{z^2}
$d_{yz}+d_{xz}$
d_{xy}
Density of states (states/eV)
Energy (eV)

(b)

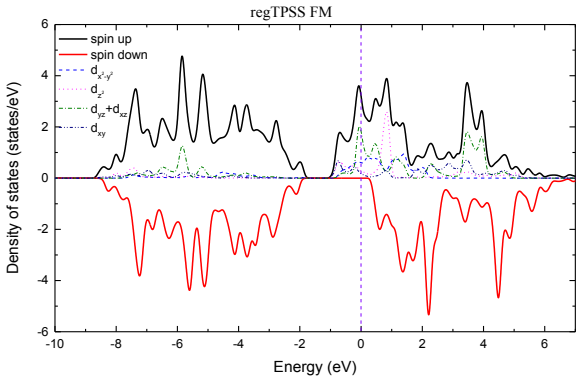
regTPSS FM
spin up
spin down
$d_{x^2-y^2}$
d_{z^2}
$d_{yz}+d_{xz}$
d_{xy}
Density of states (states/eV)
Energy (eV)

(c)

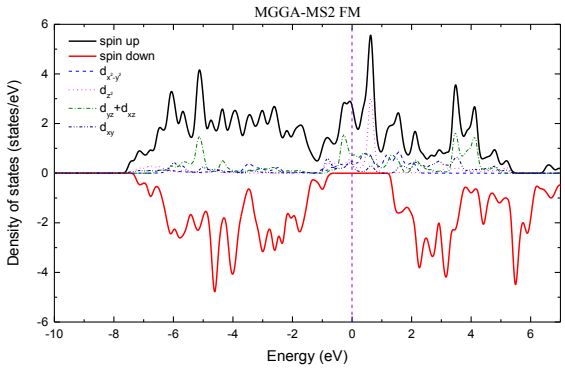

(d)

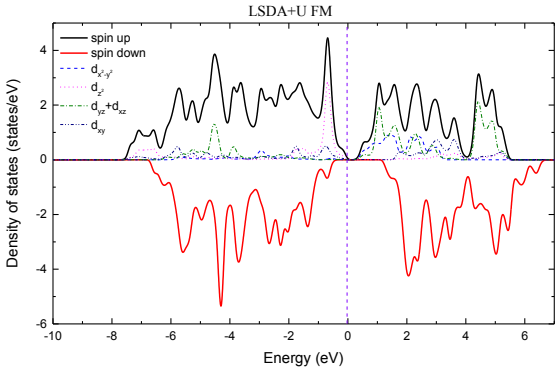

(e)

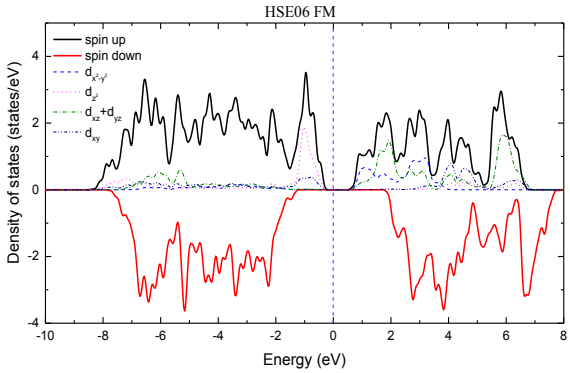

(f)

Figure 5.14: The calculated spin polarized density of states of R-VO_2 by different exchange-correlation functionals. The angular momentum projected densities of states on to 3*d* orbitals are also shown for up spin direction. The vertical line refers to Fermi level. (a): LSDA; (b): revTPSS; (c): regTPSS; (d): MGGA_MS2; (e): LSDA+U; (f): HSE06.

In FM R-VO_2, the main part of electronic states below the Fermi level is attributed to 2*p* bands of O atoms. The hybridization between 2*p* and 3*d* orbitals is seen in Figure 5.14. Using the symmetry of local $3d'$ orbitals, E_g orbitals (d'_{z^2} and $d'_{x^2-y^2}$) and the appropriate linear combinations of 2*p* shells of O atoms form *p-d* σ bonds. On the other hand, the remaining three-fold degenerated T_{2g} orbitals (d'_{xy}, d'_{yz} and d'_{xz}) interact with 2*p* orbitals in terms of *p-d* π bonds. The bonding *p-d* π and σ bonding states below the Fermi level are predominated by 2*p* character. Meanwhile, those of anti-bonding π and σ states above the Fermi level are mainly consisted of 3*d* orbitals of V atoms. From equations 5.1 and 5.2, in the local coordinates, d_{z^2} and $d_{x^2-y^2}$ only show T_{2g} symmetry. Meanwhile, the linear combinations of d_{xy}, d_{yz} and d_{xz} can have both T_{2g} and E_g characters. In our calculations, the strongest mixing of 2*p* with 3*d* states is ascribed to $d_{yz} \pm d_{xz}$ and p_z orbitals at the lower part of 2*p* bands, and which correspond to the well-known *p-d* σ-bonds in transition metal oxides. Otherwise, the mixture of d'_{z^2} (or d_{xy}) with $p_x + p_y$ is also mainly σ-type bonds. At the lower tail of 2*p* bands, d_{z^2} is also hybridized with $p_x + p_y$ states. In our local coordinates of V atoms, $d_{xy} + d_{z^2}$ is equivalent to d'_{xy} orbital. The crystal orbital formed between them is mainly *p-d* π type. The chemical interactions discussed above in this paper are in agreement with Ref. 160. For semilocal functionals, E_g and T_{2g} orbitals are situated mostly above the Fermi level. The computed *3d* projected density of states (DOS) imply that all five 3*d* orbitals (d_{xy}, d_{yz}, d_{xz}, d_{z^2} and $d_{x^2-y^2}$) make contributions to T_{2g} states (d'_{xy}, d'_{yz} and d'_{xz}) near the Fermi level, in

agreement with group theory prediction. For TPSS and revTPSS, d_{z^2} character dominates the DOS at Fermi level. The occupied 3*d* bands on the top of valence band by HSE06 and LSDA+U also mainly consist of d_{z^2} orbitals. Furthermore, in R-VO_2, d'_{xy} has a higher energy than d'_{yz} and d'_{xz} because of D_{4h} symmetry of the distorted VO_6 octahedral (See Figure. 5.5). This may explain why the position of d_{z^2} (T_{2g} symmetry) is relatively higher than other *d* orbitals with the same symmetry. The E_g type crystal orbitals can be recognized as $A_{1g}(d'_{z^2})$ and $B_{2g}(d'_{x^2-y^2})$ representations in D_{4h} symmetry. The former one lies in lower energy than the latter one. As can be seen from Figure 5.14, we find that two d_{xy} bands consist of the lower laying E_g bands. Additionally, $d_{yz} \pm d_{xz}$ states play the key role in the upper E_g bands. This clearly shows the weak tetragonal distortion of VO_6 octahedral has some effects on the electronic states of 3*d* bands.

The computed electronic densities of states in AFM and spin compensated PM phases by different DFT methods are shown in Figure 5.15. The electronic structures of AFM and PM states resemble to each other. TPSS and revTPSS close the band gap between 3*d* and 2*p* states. Similar to FM phase, the mixing of 3*d* and 2*p* bands predicted by these two meta-GGAs is too strong in AFM and PM states. Other tested exchange correlation functionals create the band gap between 2*p* and 3*d* states. Besides LSDA+U and HSE06, AFM states are found to be metallic by semilocal functionals. Meanwhile, it is a Mott-Hubbard insulator in LSDA+U and HSE06 calculations. For the insulating AFM R-VO_2, the density of states at the top of valence band is also dominated by d_{z^2}

orbital, completely similar to FM case. On the other hand, semilocal functionals (LSDA, PBE, meta-GGAs) show an evenly occupied 3*d* states near the Fermi level. In the spin compensated PM state, HSE06 opens a band gap between T_{2g} and E_g states. The density of states obtained by the same hybrid functional at the Fermi level shows strong $d_{x^2-y^2}$ character.

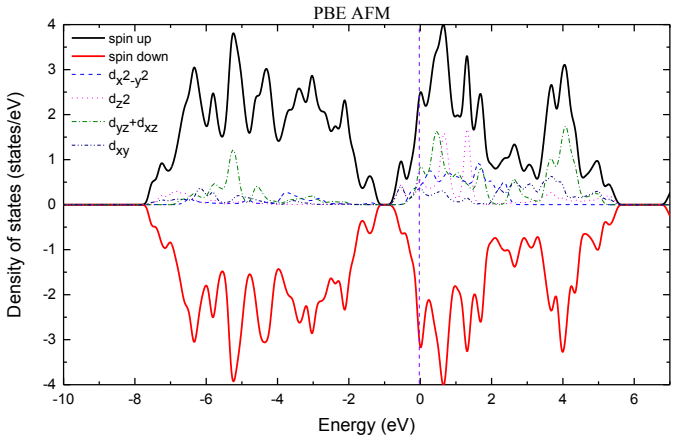

(a)

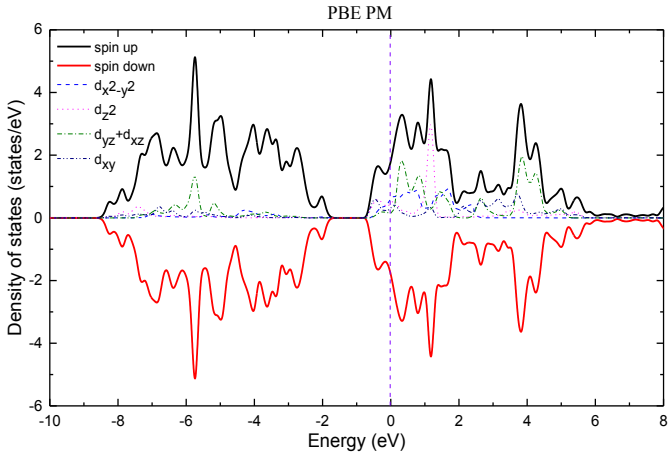

(b)

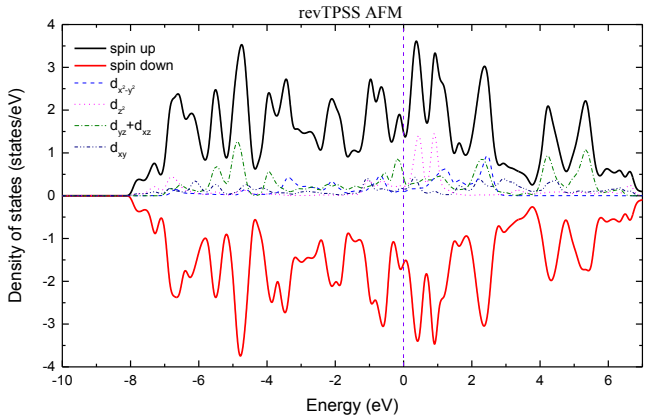
revTPSS AFM
spin up
spin down
$d_{x^2-y^2}$
d_{z^2}
$d_{yz}+d_{xz}$
d_{xy}
Density of states (states/eV)
Energy (eV)

(c)

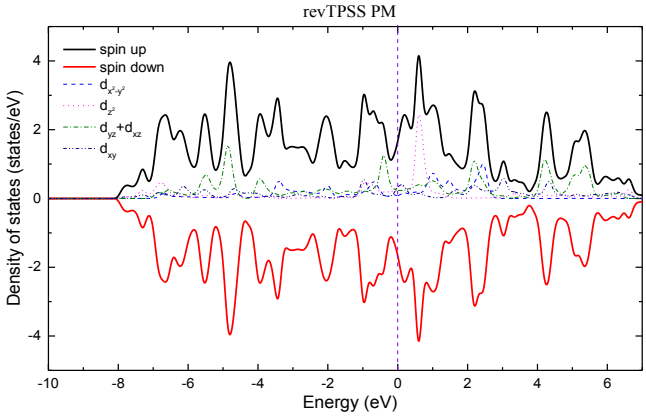
revTPSS PM
spin up
spin down
$d_{x^2-y^2}$
d_{z^2}
$d_{yz}+d_{xz}$
d_{xy}
Density of states (states/eV)
Energy (eV)

(d)

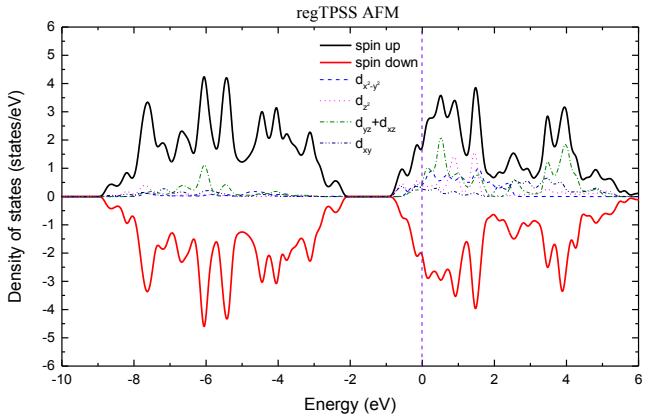
regTPSS AFM
spin up
spin down
$d_{x^2-y^2}$
d_{z^2}
$d_{yz}+d_{xz}$
d_{xy}
Density of states (states/eV)
Energy (eV)

(e)

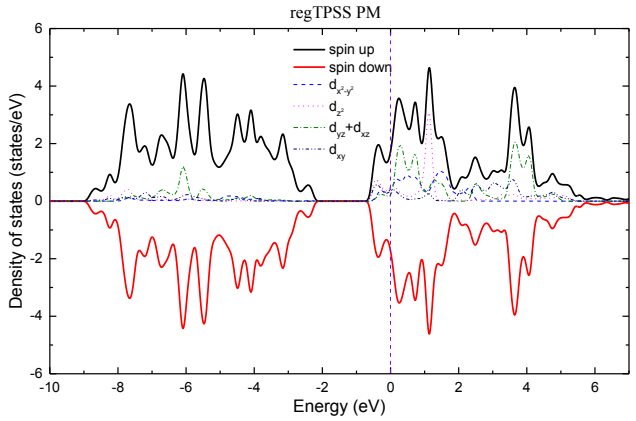
regTPSS PM
spin up
spin down
$d_{x^2-y^2}$
d_{z^2}
$d_{yz}+d_{xz}$
d_{xy}
Density of states (states/eV)
Energy (eV)

(f)

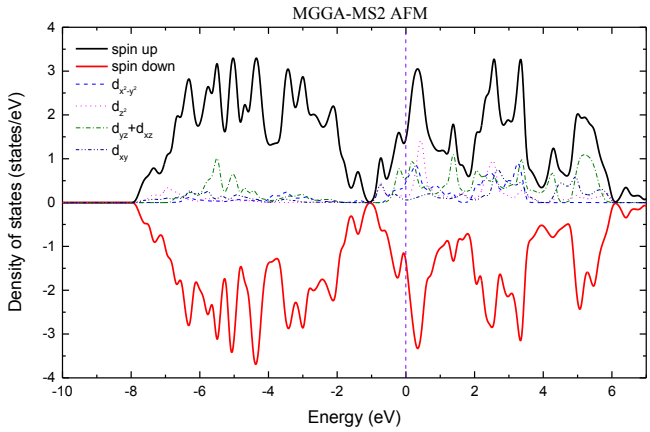
MGGA-MS2 AFM
spin up
spin down
$d_{x^2-y^2}$
d_{z^2}
$d_{yz}+d_{xz}$
d_{xy}
Density of states (states/eV)
Energy (eV)

(g)

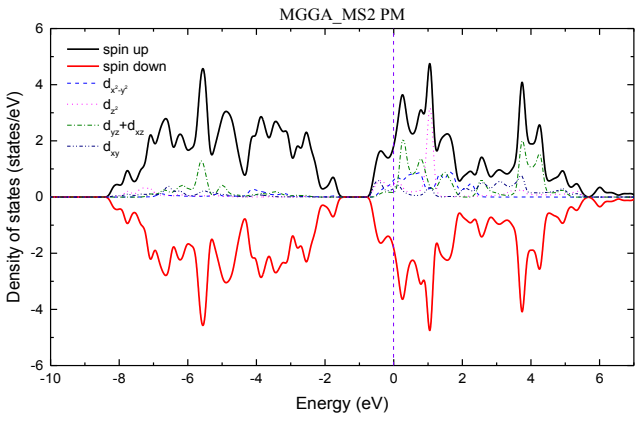
MGGA_MS2 PM
spin up
spin down
$d_{x^2-y^2}$
d_{z^2}
$d_{yz}+d_{xz}$
d_{xy}
Density of states (states/eV)
Energy (eV)

(h)

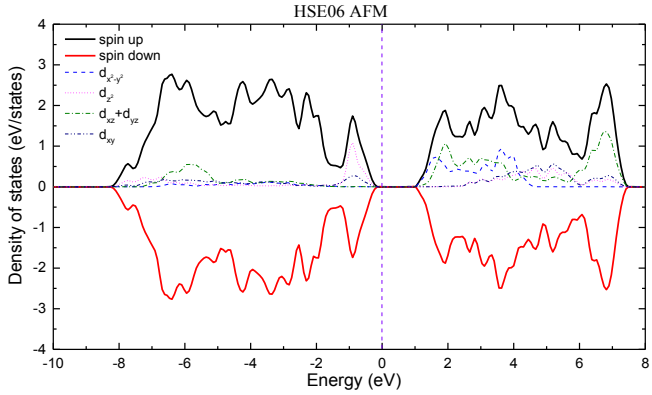

(i)

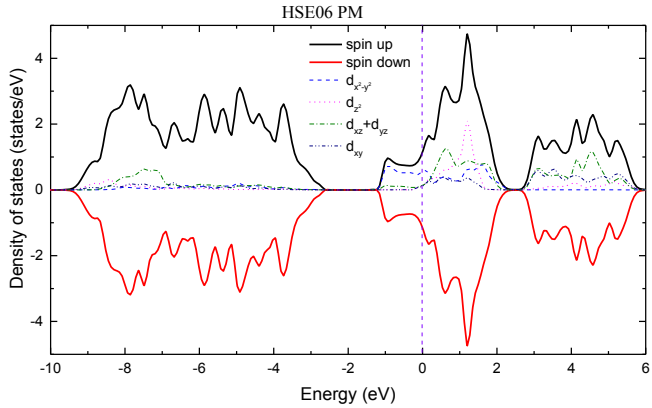

(j)

Figure 5.15: The spin polarized densities of states of AFM and spin compensated PM phases. (a): PBE-AFM; (b): PBE-PM; (c): revTPSS-AFM; (d): revTPSS-PM; (e): regTPSS-AFM; (f): regTPSS-PM; (g): MGGA_MS2-AFM; (h): MGGA_MS2-PM; (i): HSE06-AFM; (j): HSE06-PM. The vertical dashed line represents Fermi level. Note that the plots for LSDA, revTPSS, MGGA_MS0 and LSDA+U are not given here, because they are similar to the corresponding profiles of PBE, TPSS, MGGA_MS2 and HSE06, respectively. The definitions for 3d states are the same as Figure 5.14.

In [001] direction, the sublattice of V atoms can form *d-d* σ-bonds through the overlapping of d'_{xy} orbitals between the nearest unit cells, and which has been considered as one possible driven force for tetragonal VO_2 transforming into monoclinic phase at

low temperature (below 340 K) [143]. Korotin *et al*. [147] have applied LSDA+U method to study the electron localizations in 3*d* states of M_1-VO_2 and R-VO_2 phases. They found the electrons are localized on d'_{xy} bands at V sites in the monoclinic phase. In our calculations, LSDA+U and HSE06 match this picture not only for M_1-VO_2, but also for R-VO_2 in their FM and AFM states. In all three magnetic states, d'_{xy} bands are pushed above the Fermi level and mostly not occupied in the computed densities of states by semilocal functionals (Figures 5.14 and 5.15).

5.6 Orbital and Atomic Electron Populations

Since the obtained electronic structures of FM and AFM phases of R-VO_2 by TPSS and revTPSS are different to regTPSS, MGGA_MS0 and MGGA_MS2. In this section, the orbital occupation numbers for V and O atoms are computed for AFM or FM phases using semilocal functionals (LSDA, GGA, meta-GGAs), LSDA+U and range-separated hybrid functional HSE06. The computed orbital occupation numbers are given in Figure 5.16 for FM and AFM states and spin compensated PM state. Clearly, the 2*p*-3*d* hybridizations cause the electron transfer between V and O atoms. As a result, the occupation number of 2*p* bands determines how strong the 2*p*-3*d* interactions are in R-VO_2 phase. The on-site U correction only changes the orbital populations for 3*d* states. LSDA and LSDA+U give the similar occupation numbers for 2*p* states. The main influence of U on the computed electronic structure of R-VO_2 is that d_{z^2} orbital is completely filled in either FM or AFM phase, i.e., $V_I(d^{\uparrow}_{z^2}) + V_{II}(d^{\uparrow}_{z^2})$ in FM phase and

$V_I(d_{z^2}^{\uparrow}) + V_{II}(d_{z^2}^{\downarrow})$ in AFM case. On the other hand, from the calculated electron populations at 3*d* and 2*p* bands and also the weighted band dispersions shown in Figure 5.12, TPSS and revTPSS predict the different electronic structures for R-VO_2 phase to other DFT methods. The computed orbital occupation numbers for 2*p* bands using TPSS and revTPSS are much smaller than other density functionals. Each oxygen atom losses one more electron in its 2*p* shell, compared to the occupation numbers of the same orbital by other density functionals. Meanwhile, TPSS and revTPSS predict that the 3*d* bands trap two more electrons, leading to a half-filled d^5 ($t_{2g}^3 e_g^2$) configuration. The overestimation of 2*p*-3*d* orbital hybridizations facilitates the electron transfer from O to V in R-VO_2. Otherwise, we have also computed the orbital occupation for each of five 3*d* states, the results are omitted here. It is found that the occupation numbers of 3*d* states obtained by most tested DFT methods are anisotropic, showing that the five 3*d* orbitals are not evenly populated with electrons. LSDA+U and HSE06 represent two extreme cases where only one *d* orbital (d_z^2 in X-Y-Z crystallographic coordinates or d_{xy}' in local x-y-z coordinates) is fully occupied. On the other hand, TPSS and revTPSS give the isotropic orbital occupations for 3*d* band, resulting in a d^5 configuration as mentioned before. Nevertheless, the electronic structures computed by TPSS and revTPSS for AFM, FM and PM phases are suspicious, because the depopulation of 2*d* bands is somewhat rare and unrealistic in metal oxides.

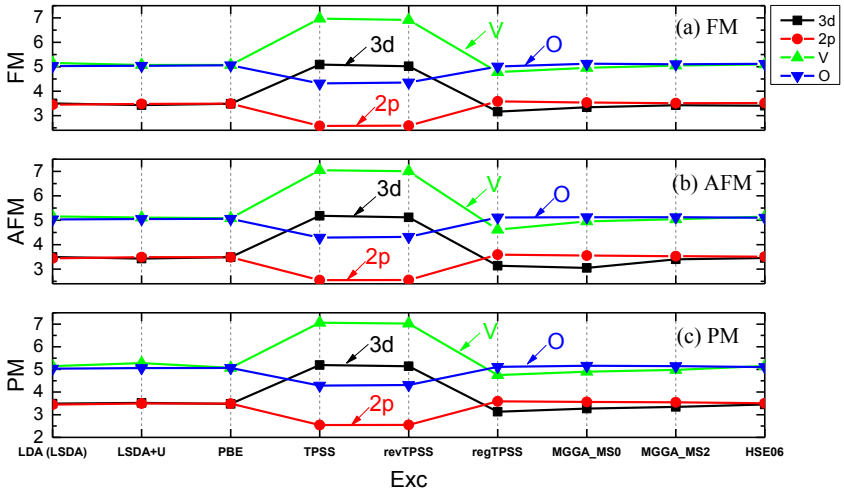

Figure 5.16: The computed electron occupations for different orbitals and atomic species in three magnetic states. (a): FM; (b): AFM; (c): spin compensated PM.

5.7 Error Cancellations in Semilocal Functionals

Rutile-type VO_2 is believed to be a strongly correlated non-magnetic metal at room temperature. Sometimes standard density functionals can imitate strong correlation by developing a spurious spin polarization: The extra exchange then keeps the electrons apart in the way that strong correlation does. The classic example is the stretched H_2 molecule. LSDA and GGA descriptions wrongly localize the spin-up electron on one site and the spin down on the other, but this leads to nearly right energy. Using the correct spin-unpolarized singlet density (spin-compensated PM state in our case) leads to an energy that is much too high. As one of the consequences due to the above reasons, it is expected that ground state energy and equilibrium cell volume of R-VO_2 computed in an energy minimized magnetic phase should be more accurate than spin compensated PM state. In Figure 5.17, we show the calculated percent errors of different DFT methods for equilibrium cell volume. It is generally true that the spurious AFM and FM calculations

predict better lattice geometry than that of spin compensated PM case except LSDA and RPA. One special case is PBE functional whereas the cell volume obtained from AFM state is almost the same as spin-compensated PM state, and both values are in good agreement with experimental value. Otherwise, the optimized cell volumes of R-VO_2 by TPSS, revTPSS and regTPSS in AFM state are identical to the corresponding values in PM state. Since the local magnetic moments given by LSDA, PBE, TPSS, revTPSS and regTPSS are significantly smaller than other tested DFT methods (LSDA+U, HSE06 and two MGGA_MS variants), the ground state electron density distribution of AFM state predicted by them is close to a spin compensated PM solution. Therefore, for LSDA, PBE, TPSS, revTPSS and regTPSS, the ground state energy and equilibrium cell volume in AFM state do not differ too much to those of spin compensated PM state. For LSDA, the predicted local spin magnetic moments are too small for both FM and AFM phase, indicating that the spin compensated PM state is more favored by this functional than other semilocal functionals. As a result, the obtained percent errors for cell volume in three different magnetic states are similar to each other. We have already seen that RPA also predicts the wrong ground state for R-VO_2. The optimized cell volume can be obtained by minimizing the total RPA energy as a function of PBE cell volume through the fitting of the equation of state (EOS). We find that such geometry optimization procedure gives very poor equilibrium cell volume for all three R-VO_2 magnetic states. In contrast to the tested semilocal functionals, LSDA+U and HSE06, the error cancellation is not observed in a spin polarized state for RPA. One possible explanation is that the current RPA is implemented self-consistently. The input single particle orbitals and wave

functions are computed by semilocal functional (PBE in our case) or even from the method mixed with fraction of exact exchange. For a strongly correlated system, the correct behavior of correlation hole is essential to obtain the true ground state. However, all DFT methods employed in this paper rely on the error cancellation between extra deep exchange and less accurate correlation holes, resulting in the nearly correct total exchange-correlation hole, but the actual physics is wrong. The deepening of exchange part rises the total energy of spin unpolarized singlet state too much. Therefore, none of the tested DFT method can give the correct ground state for R-VO_2. Thus, the input information obtained from various DFT methods for non self-consistent RPA calculation may be unreasonable for a strongly correlated system or simply deviate too far from the realistic one. The self-consistency is required in this situation, because it has been confirmed that the large difference between spin up and down channels in exchange potential can be significantly reduced by adding the correlation potential in self-consistent RPA+EXX method [64, 160].

Peng *et al*. [65] showed that RPA method is sensitive to the DFT inputs in the spin polarized case. So far, our RPA calculations are based on self-consistent PBE results. From Tables 5.1 and 5.2, we can see that LSDA is more accurate than other tested semilocal and hybrid functionals. It might be reasonable to assume that LSDA gives more realistic inputs for RPA calculations. Therefore, we have recalculated the energy differences between FM, AFM and PM states within LSDA inputs. It is astonishing to see that RPA then predicts the correct ground state for R-VO_2. The obtained energy difference between FM and PM is +619.64 meV/VO_2, and that between AFM and PM is

+3215.54 meV/VO_2. Using different DFT inputs, the non-self-consistent RPA gives completely different results in spin polarized case, implying that the calculation must be performed self-consistently.

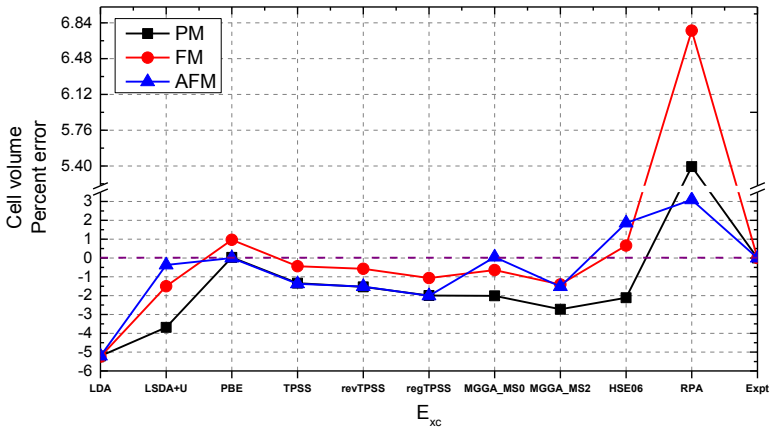

Figure 5.17: The computed percent errors of equilibrium cell volume in three different magnetic states by semilocal and nonlocal functionals. For RPA, the equilibrium cell volume is obtained by fitting the total energy versus volume curve to equation of state.

5.8 Effect of Exchange Enhancement Factor on Magnetism

It can be seen from Figure 5.11 that some semilocal functionals predict too small local magnetic moments for V atoms in AFM state of R-VO_2. Since for semilocal functional, the magnetic property is dominated by exchange energy, the observed extremely small local moments in AFM state could be related to the behaviors of their exchange gradient enhancement factors. We plot the gradient enhancement factors of LDA, PBE, and several meta-GGAs in Figure 5.18. as a function of α. In meta-GGAs, α is used to distinguish different orbital regions and chemical bonds [43]. For PBE, the gradient enhancement factors does not depend on α, its value is explicitly determined by reduced density gradient only (s). Therefore, they are straight lines in different F_x (s, α)

versus α plots. Moreover, LDA is independent on both s and α, implying that LDA profile is always a horizontal line with value of unity. Based on their behaviors at large α and small s, the tested meta-GGAs can be sorted into three different types. The MGGA_MS0 and MGGA_MS2 are the first category, their gradient enhancement factors decrease monotonically as α is increased. Otherwise, those profiles of TPSS and revTPSS are decreased with α for small s at first, but then increased above unity when α is larger than one. Similar to MGGA_MS variants, $F_x(s, \alpha)$ of regTPSS decreases with α monotonically at first and then approaches unity (LDA value) when α is infinity, but only for extremely small s. There is a minimum near $\alpha = 1$ in $F_x(s, \alpha)$ of regTPSS at any finite value of s. For the relatively large s ($s = 1$ as an example), the $F_x(s, \alpha)$ of most meta-GGAs decreases with the increase of α, but their values are still above the LDA limit (Figure 5.17). By analyzing the gradient enhancement factors of the tested semilocal functionals, we can see that TPSS and revTPSS favor the large α region when s is small. Meanwhile, MGGA_MS variants obviously exhibit the opposite trend. Although regTPSS indeed intends to decrease the small s and moderate α region in solid, its actual behavior is similar to LDA, PBE, TPSS and revTPSS for large α. In Table 5.2, the exchange gradient enhancement factors of five meta-GGAs in different limits are summarized. Our following analysis shows that the first limit is related to the magnetic property of a material predicted by semilocal functionals. It is also interesting to note that the same limit is also important for a semilocal functional to capture a portion of intermediate range van der Waals interactions in the density weakly overlapped region [43].

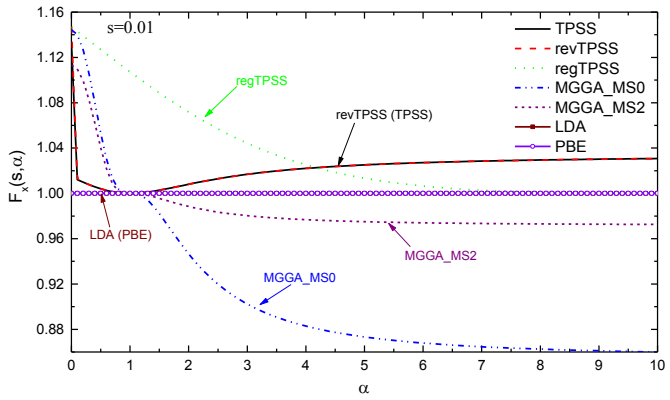

(a)

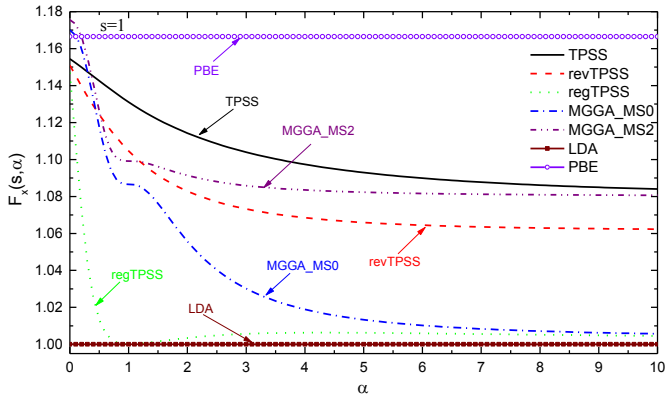

(b)

Figure 5.18: The α dependence of exchange gradient enhancement factors of meta-GGAs for different s values. LDA and PBE are represented by horizontal lines, because both exchange functionals show no dependence on α.

The computed Wigner-Seitz radius ($r_s = (3/[4\pi n])^{1/3}$), reduced density gradient ($s = |\nabla n| / [2(3\pi^2)^{1/3} n^{4/3}]$) and α are shown in Figure 5.19 for AFM R-VO_2 phase using TPSS and LSDA+U. TPSS is a representative for those semilocal functionals where the local magnetic moments are underestimated significantly, compared to an ideal d^1 configuration for V^{4+} ion. On the other hand, LSDA+U results are used to illustrate the

same parameters computed by MGGA_MS variants, HSE06. In Chapter 3, we found that the exchange energy is mainly determined by the behavior of the exchange gradient enhancement in the high density region (or small r_s). The V-O bonds in R-VO_2 show relatively strong ionic character. As a result, the valence electron density is very low in the interstitial region, and its value is much large in the pseudo-core region. From Figures 5.19 (a) and (b), one can see that TPSS (LDA, PBE, revTPSS and regTPSS) gives too small local moment, because local moment from majority spin density is compensated by the minority spin on the same site in AFM state. In the case of LSDA+U (HSE06 and MGGA_MS variants), the spin compensation is weak in the pseudo-core region of each V atom, leading to large local spin moment. On the other hand, the computed reduced density gradient shown in Figure 5.19 (c) and (d) imply that the pseudo-core regions for both V and O atoms have small s ($s < 1$). Meanwhile, the obtained α distribution at V site is different to O site. The pseudo-core regions of V atoms have very large α values, and α is small at O sites. It is also interesting to note that the strong spin polarization increases α for V_I site and reduces it for V_{II} atom for the same spin channel (Figure 5.19 (e)). In a spin compensated AFM state, α is large for V_I and V_{II} atoms in both spin channels (Figure 5.19 (f)). For meta-GGAs, the underestimation of local spin moment in AFM R-VO_2 clearly correlated with behaviors of their exchange gradient enhancement factors for small s and large α region in high density limit. TPSS, revTPSS and regTPSS give too small local moment for AFM R-VO_2, because they prefer the small s and larger α region more than MGGA_MS variants in the crystal structure. In the high density limit, the spin compensated magnetic state maximizes such region in solid. Thus, TPSS, revTPSS and

regTPSS give more negative exchange energy density ($n\varepsilon_x^{unif}[n]\mathrm{F}_x(s,\alpha)$). As can be seen from Figure 5.20, using TPSS ingredients, the obtained exchange energy density at V_{II} position is more negative than that computed from LSDA+U ingredients. Although, the exchange energy density at V_I site using TPSS ingredients now is slightly less negative than that using LSDA+U inputs, the net effect is the decreasing of local magnetic moment in AFM R-VO_2 results in more negative total exchange energy for TPSS. We believe this is also true for revTPSS and regTPSS. In the FM state, the large exchange splitting between majority and minority spins keeps a large local moment surviving for all semilocal functionals. Moreover, MGGA_MS variants give larger local magnetic moment than LSDA+U and HSE06 in FM state, demonstrating that the decreasing of $F_x(s, \alpha)$ monotonically with α is equivalent to introduce more extra exchange in the density functional. In order to verify this conjecture, we have calculated the magnetic moment of Fe in body centered cubic (BCC) structure. It is known that BCC Fe is a ferromagnetic metal below Curie point (1043 K) with a large local moment as 2.22 μ_B per atom. In this case, the local moment is underestimated by LSDA (1.94 μ_B). PBE (2.17 μ_B), TPSS (2.20 μ_B) and revTPSS (2.19 μ_B) give the results in good agreement with experiments. On the other hand, regTPSS (2.46 μ_B), MGGA_MS0 (2.63 μ_B), MGGA_MS2 (2.62 μ_B), LSDA+U (2.60 μ_B) and HSE06 (2.82 μ_B) overestimate the value. We can see the over prediction of local magnetic moment in BCC Fe by regTPSS and two MGGA_MS variants is related to their exchange enhancement factors at large α and small s. The main difference between Fe and R-VO_2 is that the former structure is dominated by metallic bonds resembling the uniform electron gas in the interstitial

regions, indicating that both s and α are not too large there (s < 1.5 and α<3). Meanwhile, V-O bonds in R-VO_2 show strong ionic character, resulting in large s and α in the interstitial regions. However, both structures show large α (>10) and small s (<0.5) in the high density pseudo-core regions.

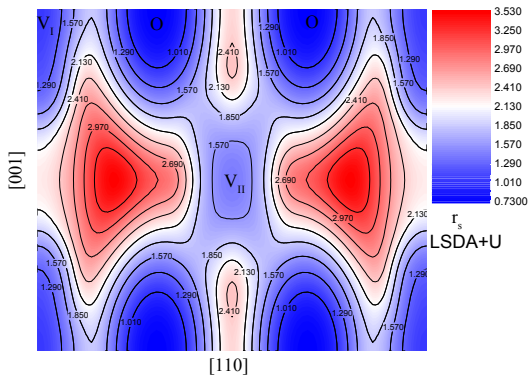

(a)

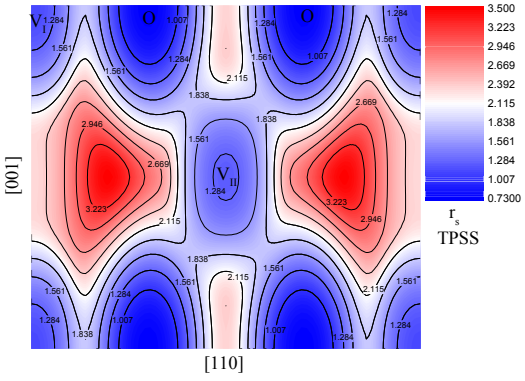

(b)

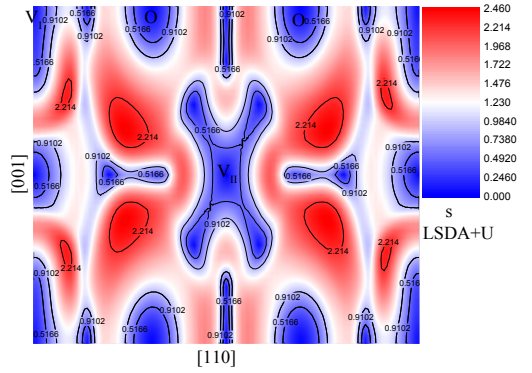

(c)

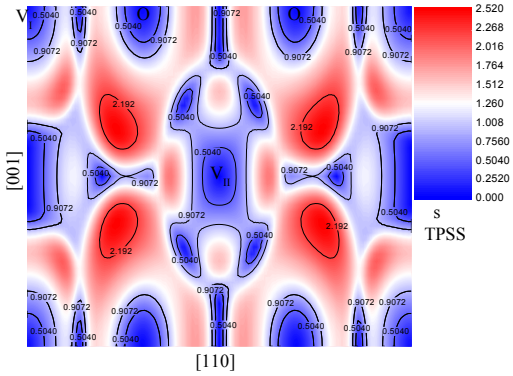

(d)

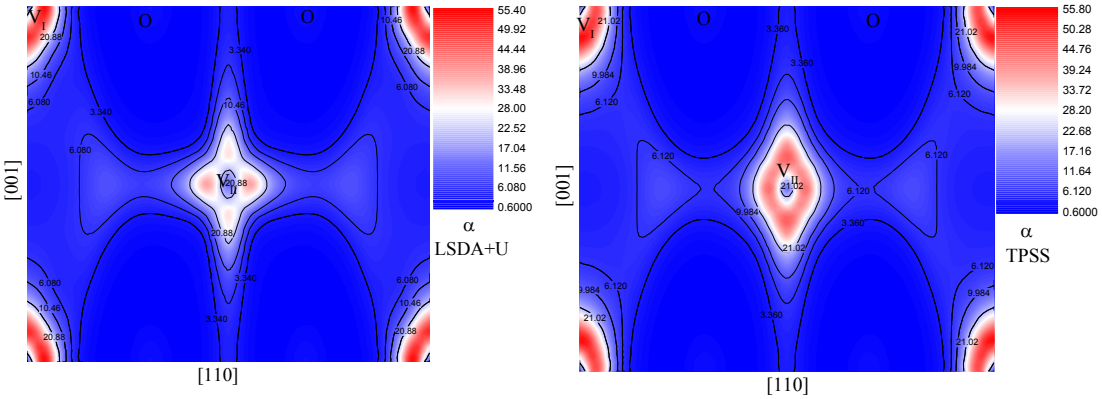

(e) (f)

Figure 5.19: The two-dimensional (2-D) contour plots of Wigner-Seitz radius (r_s), reduced density gradient (s) and α by LSDA+U and TPSS for majority spin density on [$\bar{1}$10] crystallographic plane. (a), (c) and (e) for LSDA+U, and (b), (d) and (f) for TPSS. Note that MGGA-MS variants and HSE06 give the similar results to LSDA+U; meanwhile, LDA, PBE, revTPSS and regTPSS are analog to TPSS.

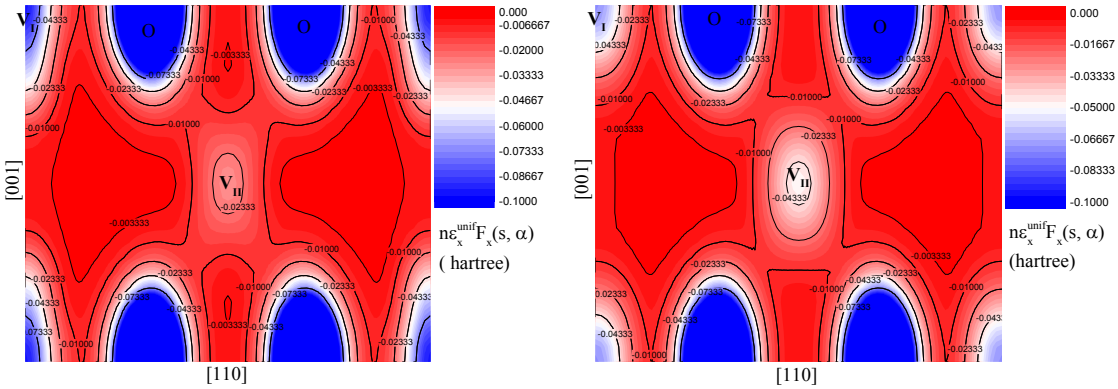

(a) (b)

Figure 5.20: The 2-D contour plots of exchange energy density of TPSS using LSDA+U and TPSS ingredients shown in Figure 5.19, respectively.

Table 5.3: The values of gradient enhancement factor of semilocal functionals in different limits. Note that PBE is independent on α, while LDA has no dependences on both s and α.

$F_x(s,\alpha)$	$\lim_{\alpha\to\infty}\lim_{s\to 0}$	$\lim_{\alpha\to 0}\lim_{s\to 0}$	$\lim_{s\to 0}\lim_{\alpha\to 0}$	$\lim_{\alpha\to 0}\lim_{s\to\infty}$
LDA	1	1	1	1
PBE	1	1	1	1.804
TPSS	1.035	1.014	1.133	1.804
revTPSS	1.035	1.014	1.147	1.804
regTPSS	1	1.147	1.147	1.804
MGGA_MS0	0.856	1.144	1.144	1.290
MGGA_MS2	0.972	1.113	1.113	1.504
Meta-VT{8,4}	1.035	1.014	1.148	0.000
BLOC	1.035	1.014	1.133	1.804

In a strongly correlated system with non-magnetic state as ground state, the ground state energy of spin singlet non-magnetic phase obtained from a meta-GGA with exchange enhancement factor similar to those of MGGA_MS variants will be less accurate than TPSS and revTPSS (See Table 5.3). More recently, two new non-empirical meta-GGAs have been published, i.e., meta-VT{8, 4} proposed by Campo and coworkers [44] and BLOC meta-GGA derived by Constantin and collaborators [45]. The exchange part of both meta-GGAs still suffers from the order of limits problem as TPSS and revTPSS do (See Table 5.3). Additionally, the large α and small s behaviors of them are also exactly the same as TPSS and revTPSS. Therefore, these new meta-GGAs perform similarly to TPSS and revTPSS for the magnetic property of a solid.

CHAPTER 6

PHYSISORPTION OF CO_2 MOLECULE ON Pt (111) SURFACE

In this Chapter, we will employ some semilocal and nonlocal functionals to study the surface adsorption problem in surface science. The main motivation is to test several density functionals for van der Waals interactions, incluing PBE, PBE+D2, MGGA_MS2 and vdw-DF. In the PBE+D2 and vdw-DF, the long-range van der Waals intractions are captured either through the pair-wise corrections or by the non-local correlation functional. Recently, it was shown that MGGA_MS2 is also able to describe a portion of van der Waals interactions in graphene absorbed on transition metal surfaces [43]. In contrast to other three methods, MGGA_MS2 is an empirical semilocal functional. We would like to apply this meta-GGA to another particular interesting problem in surface science: the physisorption of CO_2 molecule on Pt (111) surface. The interactions between absorbent and metallic surface are pure van der Waals interactions in this case. The computed binding curves will be compared with those of PBE, DFT+D2 and vdW_DF. Our earlier tests showed that computational costs of RPA method are completely unaffordable within the current hardware, even using the smallest supercell model (19 atoms). So, RPA method is disregarded in our discussions. The main purpose is to show that the semilocal functional at meta-GGA level is able to describe a portion of van der Waals interactions at the equilibirum geometry.

6.1 CO_2 Sequestration

The CO_2 sequestration is aimed to capture and store a large amount of atomspheric CO_2 molecules produced during the human activities by using either chemical or physical methods. The ultimate goal is to reduce or stabilize the CO_2 concentration in atmosphere, probobaly slowing down the global warming process. Recent years, the field has attracted much attentation from both academe and industries, mainly facilitating by various projects of US Department of Energy (DOE).

The materials, which have been considered for CO_2 sequestration, are basically these two catergories: the meta-organic frameworks (MOFs) and surfaces (graphene, transition metals and transition metal oxides). The MOFs usually exhibit large pores in the crystal structures [162]. Due to the different sizes, those MOFs can be highly selective for a particular type of molecule (See Figure 6.1). The properties of these pores also determine the uptake capacity of a MOF. In most cases, CO_2 molecule is simply attached inside the pore by van der Waals interactions [163-166]. With the suitable pore size, each pore can accommodate multiple CO_2 molecules. The interactions between those CO_2 molecules are also dispersion interactions. MOFs are not considered in this work because of the following two reasons. First of all, the physisorption of CO_2 in MOFs has been calculated using various DFT methods with van der Waals corrections [165, 166]. The performances of DFT+D2 and different versions of vdW-DF methods were compared to each other. From Refs. 165 and 166, we can see that the non-empirical vdW-DF methods are more accurate than DFT+D2 approach. However, the main drawback of vdW-DF method is that the overall performance is dependent of the choice

of exchange energy functional. Another reason is obviously related to the computational aspect. The crystal structures of MOFs are very complicated and their primitive cells can have hundreds of atoms. In this case, RPA is not applicable to them even with the modern super-computers. The usage of walltime and memory is huge, because computational costs of RPA scale at least as N^6, where N is the total number of atoms in the system. For semilocal functionals, the calculation is still a challenging task without knowing the CO_2 adsorption geometry from experiments.

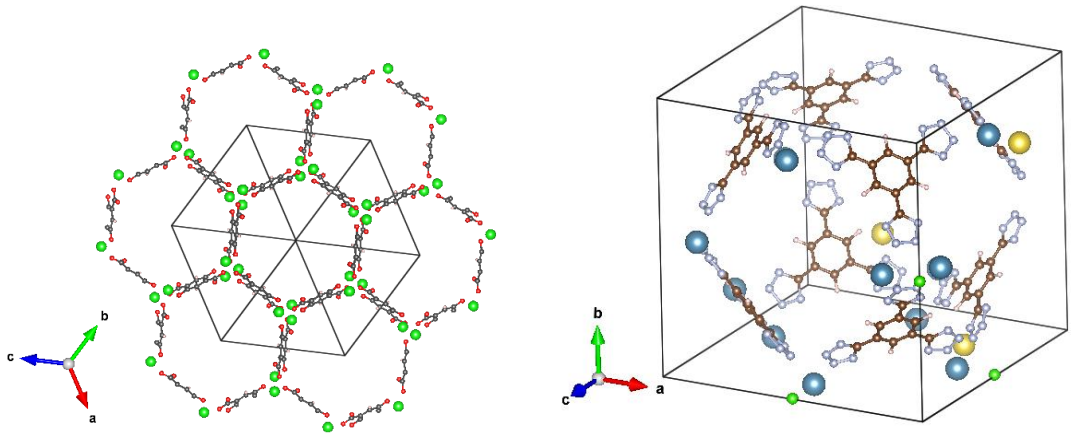

(a) (b)

Figure 6.1: The crystal structures of two widely studied MOFs for CO_2 sequestration problem. (a): Mg-MOF74 [165]; (b): Ca-BTT [166].

In contrast to MOFs, the adsorption of CO_2 on surfaces of transition metals or metal oxides is computationally less expensively for most DFT methods. For small system, RPA method can be also applied in the calculations. Since CO_2 is chemically inert due to its high stability, it interacts with the various surfaces mainly through van der Waals interactions. In an ealier comprehensive review of CO_2 absorbed on transiton metal surfaces given by Freund and Roberts [167], it has been shown that CO_2 adopts the

linear geometry in a physisorption case, similar to isolated CO_2 molecule. In a chemisorption, CO_2 has a bent geometry because of charge transfer between surface and molecule, changing the highest occupied frontier orbital of molecule. The Walsh diagram was used in Ref. 167 to explain the change of CO_2 geometry in the two situations. In some metal or metal oxides surfaces, CO_2 can be highly reactive. It is usually either dissociated into smaller atomic fragments (C, O, CO or other ions) or attached with an extral electron given by the surface to form CO_2^- anion. The carbonate and oxalate were also observed in experiments. The physisorption and chemisorption can occur on the same surface at different distances [167, 168], i.e., Bi (0001), Cu (211), Cu (311), Fe (110), Fe (111), Ni (100), Ni (110) an etc. The pure physisorption was seen on Rh (111), Pt (111), Pd (111), Ni (111) and Cu (111) surfaces. Among the metal oxides, the carnonates and physisorption species have been detected on CaO (100), MgO (100), TiO_2 (110) and ZnO ($000\bar{1}$); the carboxylates and physisorbed CO_2 were seen on Cr_2O_3 (0001) and ZnO (0001) surfaces; only the physisorption was observed on MnO (100), NiO (100), SnO_2 (110) and Cu_2O (111) surfaces [168].

In this dissertation, we are mainly focused on the physisorption of CO_2 on Pt (111) surface. The Pt (111) surface is non-magnetic due to the bulk property of Pt metal. Pt (111) surface is the most compacted crystallographic plane of a face centered cubic metal. The physisorption is much easier to deal with than chemisorption, because CO_2 keeps its linear geometry, and all likely adsorption sites can be obtained from the local symmetry considerations.

6.2 Methods and Details

6.2.1 Adsorption Geometries

In Figure 6.2, the crystal structure of a face centered cubic (FCC) Pt metal is illustrated, and (111) crystallographic plane is also highlighted by the gray polygon. The atomic structure of Pt (111) surface is shown in Figure 6.3 by a 4 × 4 supercell. On (111) surface, each atom has six nearest neighbours, thus the local symmetry of it is C_6. In the bulk FCC metal, the stacking sequence in [111] direction is ABCABCABC⋯. Thus, the supercell of transition metal (111) surface requires at least 4 layers in [111] direction to match with the minimum periodicity of atomic configuration in bulk material.

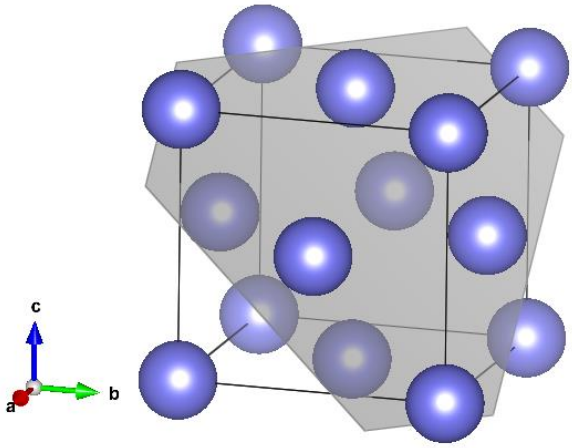

Figure 6.2: The conventional cell of face centered cubic (FCC) Pt crystal structure. The (111) crystallographic plane is shown by the shadowed polygon.

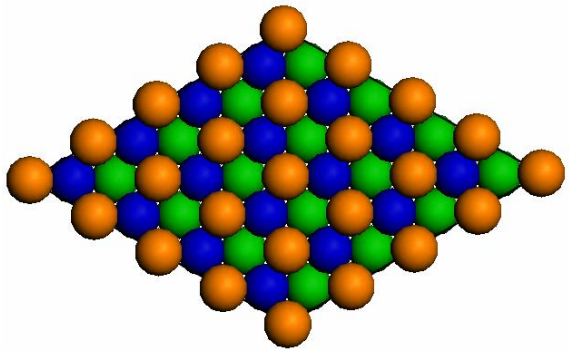

Figure 6.3: The atomic configuration of FCC metal on (111) surface. The atoms in different layers are represented by different colors. The atoms in the top layer are maked by yellow, and those in the second and third layers are indicated by blue and green balls, respectively.

Since in this work we only consider the physisorption of CO_2 on Pt (111) surface, the geometry of CO_2 molecule does not change too much, compared to the isolated case. Otherwise, the possible alignments of CO_2 molecule with respect to surface are only limited to two special cases: the main rotational axis of CO_2 is either parallel or perpendicular to the normal vector of Pt (111) surface. In other words, the CO_2 is allowed to stand or lay on the surface, but not tilting to the surface. Moreover, considering the local symmetry of hexagons formed by atoms on the top layer (See Figure 6.3), there are only seven different adsorption geometries for CO_2 molecule on Pt (111) surface. In Figure 6.4, all seven adsorption geometries are shown. There are three non-equivilent geometries when CO_2 is aligned perpendicular to surface, and four other geometries in the parallel case. It should be noted that since there is no chemical interactions in the physisorption, one may only need to distinguish two different CO_2 configurations on the transition metal (111) surface. This will further reduce the seven possible adosprtion geometries in our case to only two, i.e., parallel and perpendicular cases.

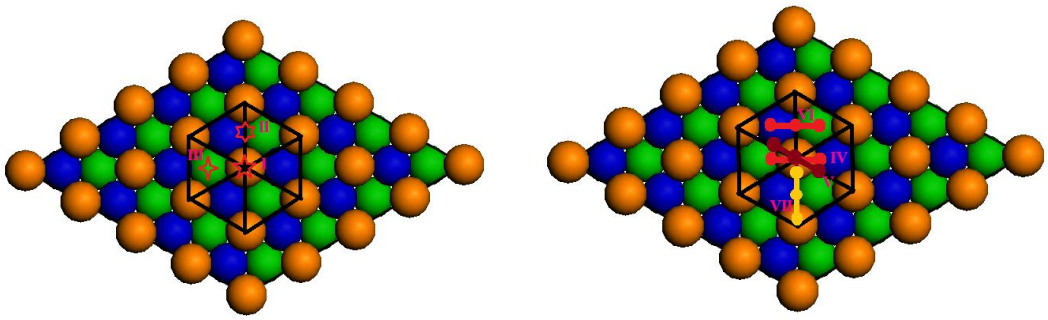

(a) (b)

Figure 6.4: The non-equivilent adsorption geometries of CO_2 molecule on transition metal (111) surface. (a): $CO_2 \perp$ Pt (111) surface; (b): $CO_2 \parallel$ Pt (111) surface. The CO_2 molecule is represented by the ball and stick model in parallel case.

Table 6.1: The seven high symmetry adsorption geometries for CO_2 molecule physisorbed on Pt (111) surface. Their atomic structures are numbered by Roman numerals and also indicated in Figure 6.4.

$CO_2 \perp$ (111) surface			$CO_2 \parallel$ (111) surface			
I	II	III	IV	V	VI	VII
Top	Bridge	Hollow	Top-Hollow	Top-Bridge	Bridge-Hollow	Bridge-Bridge

6.2.2 Computational Parameters

All DFT calculations were perfomed using *VASP* code [97]. The standard PBE-type PAW pseudopotentials were employed in this work for Pt, C and O atoms. For these elements, the the frozen core approximation was applied to the pseudo-atoms, and the orbitals treated as valence shells were Pt_{5d6s}, C_{2s2p} and O_{2s2p}. The kinetic energy cutoff value for plane wave expansion in reciprocal space was set as 550 eV. The Γ-centered k-mesh used in this work was 8 × 8 × 1 for the surface supercell. The Monkhorst-Pack

method was not employed to generated the k-mesh, because in our case, the supercell of (111) surface has hexagonal symmetry. The exchange-correlation functionals considered in the calculations were PBE [25], PBE+D2 [84], optB88-vdW [88] and MGGA_MS2 [42, 43]. Besides PBE, the other three methods are able to describe the van der Waals interactions at the different levels of accuracy. MGGA_MS2 belongs to MGGA_MS family of density functionals, and all of the density functionals in this family can capture a portion of dispersion interactions. All first principles calculations for Pt systems (Pt bulk, Pt (111) surface and Pt surface + CO_2) were carried out using the spin non-polarized method. It is well-known that Pt bulk metal and Pt (111) surface are non-magnetic. Experimentally, CO_2/Pt (111) system is also non-magnetic, because the interactions between the absorbent and substrate are mainly weak van der Waals interactions. In Table 6.2, the computational parameters are shown for PBE+D2 method, including the van der Waals C_6 coefficients and radii of Pt, O and C elements. For other settings, we used the default values in *VASP* program [84].

Table 6.2: The C_6 coefficients and van der Waals radii of Pt, C and O elements employed in the calculations.

Parameter	Pt[a]	C[b]	O[b]
C_6 (J.nm^{-6}/mol)	19.92	1.75	0.70
R_{vdW} (Å)	2.074	1.452	1.342

[a]Ref [169]; [b]Ref [84].

The CO_2 molecule and surface supercells were optimized using each DFT method mentioned above. For isolated CO_2 molecule, the geometry was relaxed in a 10 Å × 14 Å × 10 Å supercell. Then, the total energy of an isolated molecule was computed from the optimized geometry. For bulk Pt crystal structure, the lattice constant was optimized using the PBE functional only. For many transiton metals, PBE usually gives lattice constants in good agreement with experimental results. The (111) surface supercells were built from those optimized for the crystal structure of Pt. The dimensions of the supercell of Pt (111) surfaces were 11.0984 Å × 11.0984 Å × 26.7964 Å ([100]-[010]-[001]). The vacuum layer in [001] direction was set to 20.0 Å, avoiding the artificial interactions between two slabs in the imaging cells. For the Pt (111) surface, the dimensions of supercells were fixed, but the atomic positions in top layer of surface were allowed to relax using the selective dynamics in *VASP* code. Then, the total energy of Pt (111) surface supercell was computed. The supercells of CO_2/Pt (111) system were built using the optimized geometries for the absorbent (CO_2) and substrate ((111) surface). The supercells of combined system have the same dimensions as the Pt (111) surface itself. For our system, the combined CO_2/Pt (111) surface supercell has 69 atoms. Among them, 64 atoms come from the substrate, and the remaining atoms belong to CO_2 molecule. In Figure 6.5, we show the side views of supercells for two different CO_2 configurations.

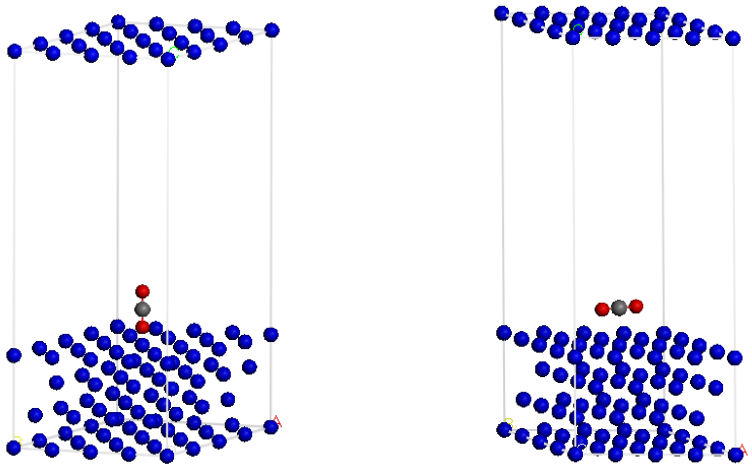

(a) (b)

Figure 6.5: Two different adsorption configurations for CO_2 molecule on Pt (111) surface. Note that (a) and (b) refer to structures I and IV in Table 6.1. (a): Perpendicular configuration; (b): Parallel configuration.

The binding energy curve can be computed from

$$E_{Bind}(CO_2+surface)=E_{total}(CO_2+surface)-[E_{total}(CO_2)+E_{total}(surface)] \quad (6.1)$$

where the binding energy is defined as the energy difference between the combined structure and those of separated subsystems. Using this definition, if the DFT method binds the system, then the computed binding energy should be negative. In our case, the binding energy is mainly attributed to van der Waals interactions. Therefore, it is expected that the magnitude of it is less than 10 kcal/mol (or 0.01 eV/CO_2). In Table 6.3, the optimized bond lengths of CO_2 molecule by different DFT methods are shown and which are also compared with experimental value. The bond length is underestimated by MGGA_MS2, and the values of other three DFT methods are slightly overestimated.

MGGA_MS2 is less accurate for the computed bond length of CO_2 than other three methods.

Table 6.3: The optimized bond lengths of CO_2 molecule by different exchange-correlation functionals. The experimental value is also given.

Bond	PBE	PBE+D2	MGGA_MS2	optB88-vdW	Expt[a]
C=O	1.17639	1.17664	1.13496	1.17308	1.16

[a]Ref [167].

6.2.3 Convergence Tests

For the convergence tests, we will first consider the effects of supercell size on the computed binding curve. The optB88-vdW functional was used in the tests, because it captures long-range van der Waals interactions, and the computational costs are comparable to semilocal functionals (PBE and meta-GGAs). In the tests, we compute the binding curves for structures I and IV in Pt system using two different supercells (See Figure 6.4 and Table 6.1 for more details): the default supercell (64 Pt atoms + CO_2) and a small supercell (36 Pt atoms + CO_2). Note that in both supercells, the substrate consists of 4 atomic layers (Pt atoms). The obtained binding curves are shown in Figure 6.6.

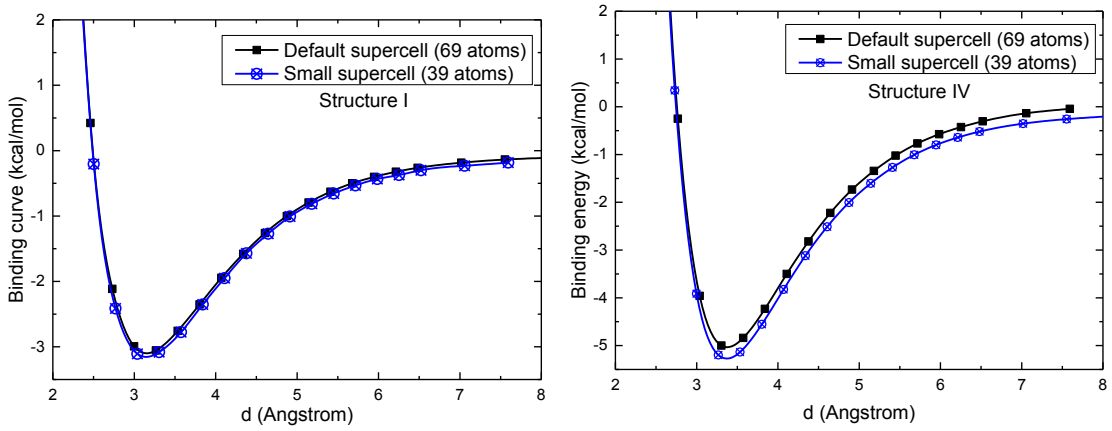

(a) (b)

Figure 6.6: The computed binding curves for Pt (111) surface + CO_2 system from optB88-vdW method. (a): Structure I (Perpendicular configuration); (b): Structure IV (Parallel configuration).

From Figure 6.6 (a), we can see that for the perpendicular configuration, the size of the supercell has minor effect on the computed binding curve. The equilibrium distance is not affected at all, only the binding energy gets more negative when using smaller supercell. On the other hand, the binding curve for the parallel configuration shows stronger dependence on supercell size, compared to perpendicular case. However, the change of the binding energy is not significant, i.e., 0.5 kcal/mol. Similar to perpendicular configuration, the equilibrium binding distance is also not sensitive to the supercell size for parallel configuration. One should note that the van der Waals interactions are stronger in parallel case than perpendicular configuration, considering all three atoms in CO_2 molecule can interact with metal surface at the equivalent distance in the former case. In our latter discussions, all results are computed using the large supercell (64 metal atoms and CO_2 molecule).

6.3 CO_2 Physisorbed on Pt (111) Surface

6.3.1 Binding Curves

The computed binding curves for all seven possible adsorption geometries shown in Figure 6.4 are calculated using PBE and optB88-vdW functionals. Those two methods are chosen here, because the former functional is a representative for those semilocal functionals which can not capture the long-range van der Waals interactions; otherwise, optB88-vdW is a widely used for van der Waals bound systems, and is supposed to be more accurate than pair-wise corrections (DFT+D2). Later, we will also compute the binding curves by MGGA_MS2 and PBE+D2.

In Figure 6.7, the binding curves are shown for PBE functional. The first three geometries (I, II and III) refer to the perpendicular configuration for CO_2 molecule. Due the missing of van der Waals interactions in PBE functional, the adosprtion energies are small and the binding curves are not distinguiable in this case. The adsorption energies are more negative for the other four parallel configurations than perpendicular cases, implying the stronger binding between Pt (111) surface and CO_2 molecule. At the large separation, the binding curves of PBE decay very fast to zero, indicating the missing of long-range van der Waals interactions in this semilocal exchange-correlation functional.

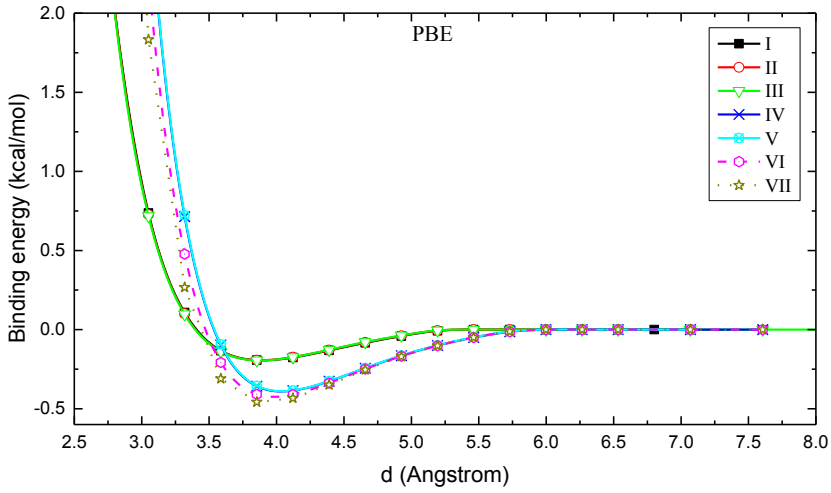

Figure 6.7: The computed binding curves of seven different adsorption geometries of CO_2 on Pt (111) surface using PBE.

In Figure 6.8, the calculated binding curves are shown for optB88-vdW functional. Comparing to PBE binding energies and adsorption distances at the minima, the optB88-vdW strongly binds the CO_2 molecule on Pt (111) surface. For either perpendicular or parallel adsorption geometries, the obtained binding energies are nearly ten times more negative than PBE values. Otherwise, the equilibrium binding distances are also shorter than those of PBE. It is also interesting to note that optB88-vdW is also unable to distinguish I, II and III adsorption geometries. For both PBE and optB88-vdW, the bonding energies of four adosprtion geometries in parallel configuration are more negative than those in perpendicular case, but the equilibrium distances between absorbent and Pt (111) surface in the former cases are longer than later situations. The main reason is the electron-electron repulsion between two closed-shell systems, due to the Pauli exclusive principle. All adsorption geometries in the parallel configuration exhibit stronger such repulsion than perpendicular ones, because CO_2 has a linear shape.

Among the adsorption geometries IV-VII, the binding energy of VII computed by either PBE or optB88-vdW is more negative than others. Note that geometry VII corresponds to bridge (C)-bridge (O) site on Pt (111) surface. In the case of IV and V, the carbon atom in CO_2 molecule is always placed on the top of Pt atom. From the computed binding energy curves, these two adsorption geometries are less favored than VI and VII by PBE and optB88-vdW in current calculations. In VI and VII, none of atoms in CO_2 molecule is placed directly above the Pt atoms on the top layer at (111) surface.

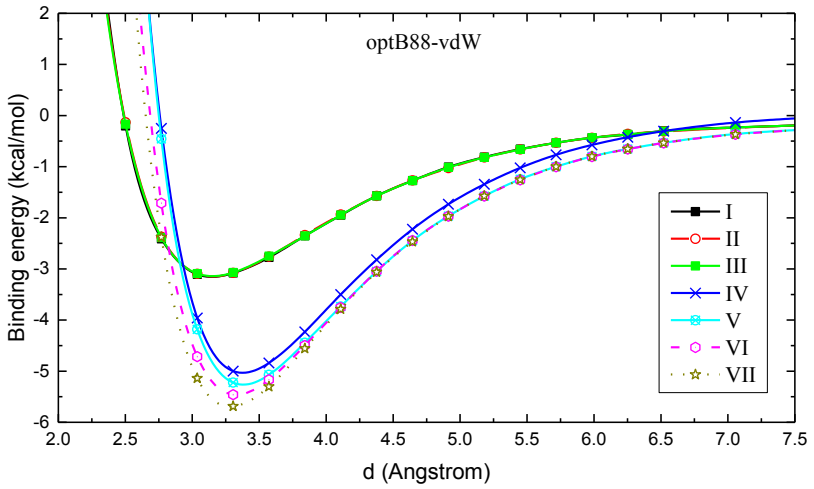

Figure 6.8: The calculated binding curves of CO_2 on Pt (111) surface using optB88-vdW functional.

Now, we will compute the binding curves of I, III and IV adsorption structures by MGGA_MS2 and PBE+D2. In Figures 6.9-6.11, the binding curves of structures I, III and IV are shown for PBE, PBE+D2, optB88-vdW and MGGA_MS2. As can be seen from Figures 6.9 and 6.10, MGGA_MS2 performes similarly for the two adsorption geometries. In our future discussions, we will focus on the results of I and IV. The two

adsorption geometries are considered as the representatives for two CO_2 configurations on Pt (111) surface.

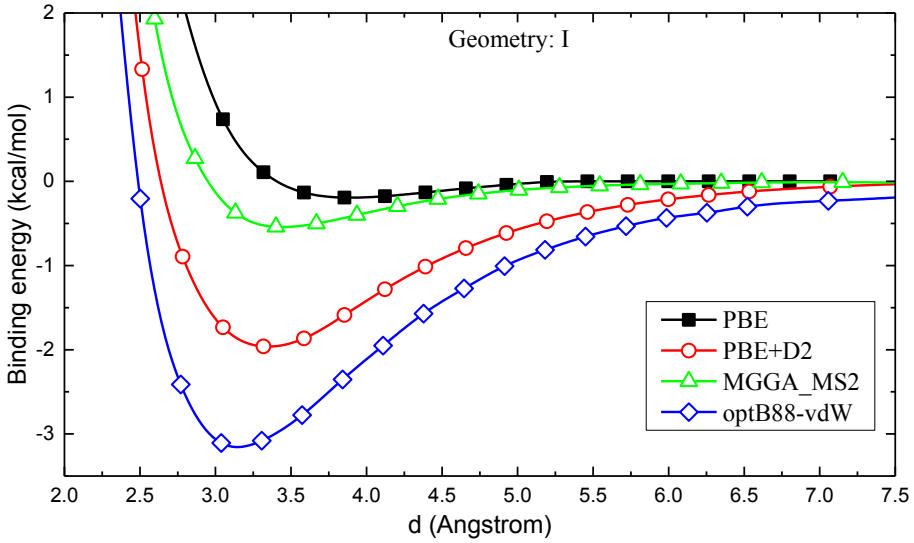

Figure 6.9: The computed binding curves of adosprtion geometry I by PBE, PBE+D2, MGGA_MS2 and optB88-vdW.

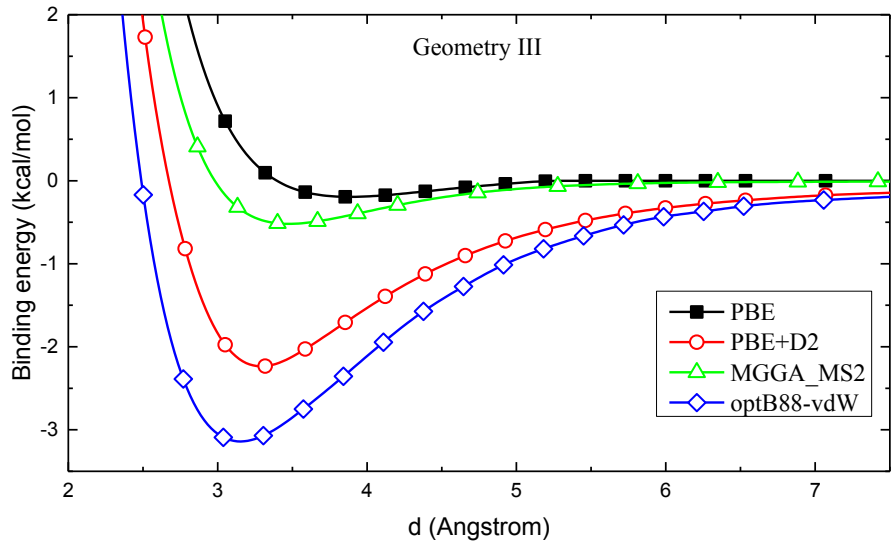

Figure 6.10: The binding curves of adsorption-geomtry III computed by PBE, PBE+D2, MGGA_MS2 and optB88-vdW.

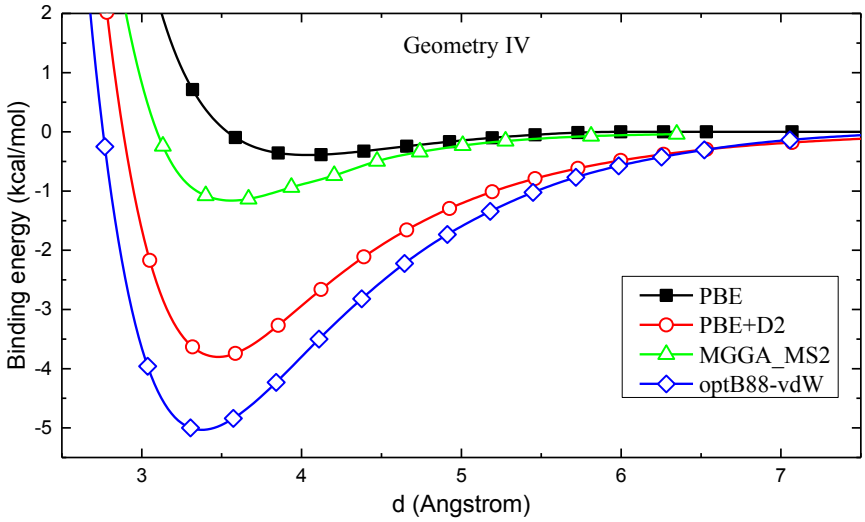

Figure 6.11: The binding curves of adsorption-geometry IV obtained from PBE, PBE+D2, MGGA_MS2 and optB88-vdW.

MGGA_MS2 captures a portion of van der Waals interactions. The equilibrium distance predicted by this exchange-correlation functional is usually comparable to PBE+D2 and optB88-vdW methods. The magnitude of binding energy at the equilibrium distance obtained by MGGA_MS2 is smaller than latter two method, i.e., the value is usually 1/3 of van der Waals DFT methods.

6.3.2 Adsorption Geometry and Energy

From the computed binding energy curves for different adsorption-geometries, the equilibrium distance and binding energy for each geometry can be extracted. First, we show the two quantities for all seven adsorption-geometries using PBE and optB88-vdW methods in Table 6.4. From the resutls given in the table, we can clearly see that PBE binds the system, but the obtained absolute values of binding energy are too small. As a

result, the equilibrium binding distances predicted by PBE are much larger than those of optB88-vdW method. Since the experimental values are not available for the studied systems, we have computed the two parameters for geometries I and IV using MGGA_MS2 and PBE+D2, and the results are compared with PBE and optB88-vdW methods in Table 6.5. MGGA_MS2 binds the two structures more than PBE does, and the predicted binding distances are more close to PBE+D2 and optB88-vdW methods than PBE. The optB88-vdW gives the strongest binding among four DFT methods. MGGA_MS2 is situated between PBE+D2 and PBE.

Table 6.4: The calculated binding energies and equilibrium binding distances for seven adsorption geometries by PBE and optB88-vdW.

Structure	PBE		optB88-vdW	
	E_{bind} (kcal/mol)	d_{bind} (Å)	E_{bind} (kcal/mol)	d_{bind} (Å)
I	-0.1939	3.8971	-3.1527	3.1468
II	-0.1935	3.8890	-3.1473	3.1468
III	-0.1948	3.8809	-3.1406	3.1490
IV	-0.3913	4.0318	-5.0328	3.3779
V	-0.3894	4.0409	-5.2608	3.3859
VI	-0.4250	3.9770	-5.4617	3.3312
VII	-0.4618	3.9223	-5.6879	3.2957

Table 6.5: The calculated binding energies and equilibrium distances of structures I and IV by different DFT methods.

E_{xc}	Structure I		Structure IV	
	E_{bind} (kcal/mol)	d_{bind} (Å)	E_{bind} (kcal/mol)	d_{bind} (Å)
PBE	-0.1939	3.8971	-0.3913	4.0318
PBE+D2	-1.9631	3.3525	-3.8020	3.4814
MGGA_MS2	-0.5419	3.4478	-1.1632	3.5607
optB88-vdW	-3.1527	3.1468	-5.0328	3.3779

6.3.3 Point Charge Model for CO_2 Interacting with Metal Surface

Although the CO_2 molecule interacts with Pt (111) surface through the van der Waals forces, the semilocal functional like PBE still binds them together. In the case CO_2 absorbed in MOF, sometimes the binding energy is attributed to the electrostatic attraction between CO_2 and MOF [165, 166]. This is indeed possible, because the covalent bonds in CO_2 are highly polarized, due to the big difference of eletronegativities of O and C elements. Maurin *et al*. [170] employed an atomic point charge model to study the CO_2 molecule in the force field method. The nominal charges assigned to C and O atoms are + 0.72 e and – 0.36 e, respectively. Since the valence electron density on Pt (111) surface is relatively uniform, it can be treated as the jellium surface. Therefore, the electrostatic interacting energy between CO_2 and Pt (111) surface might be calculated

from a well-known classic model in electrodynamics, i.e., the point charge interacts with a metal surface [171], as illustrated in Figure 6.12.

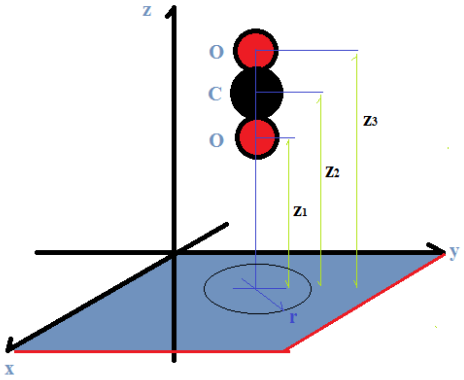

Figure 6.12: The point charge model of CO_2 molecule physisorbed on metallic surface.

In the classic electrostatics, the induced surface-charge density due to the point charge outside the conducting half-space can be computed by

$$n_{ind}(r) = \frac{-q(z-z_0)}{\{2\pi[r^2+(z-z_0)^2]^{3/2}\}} \tag{6.2}$$

where q represents the point charge outside the metallic surface, and $n_{ind}(r)$ is the induced surface charge density, and z is the distance between external charge and surface, z_0 refers to the center of gravity of induced charge density. The total induced surface charge density is obtained from equation 6.3.

$$q_{ind} = \int n_{ind}(r)dr \tag{6.3}$$

The integral is only performed for r, because the induced density is confined on surface for an ideal conducting surface. Otherwise, if we only consider the perpendicular configuration for CO_2 molecule on Pt (111) surface, and we have $z_0 = 0$ due to the local

symmetry in adsorption-geometry I. For the same adsorption geometry, if we employ the structural parameters of CO_2 (Bond length = 1.17 Å) and the equilibrium distance (~3.85 Å) in the binding curve computed from PBE, the induced surface charge densities by O and C atoms are given by

$$n_{O_1}(r) = \frac{0.220589}{(14.8225 + r^2)^{3/2}} \tag{6.4}$$

$$n_{O_2}(r) = \frac{0.354661}{(38.3161 + r^2)^{3/2}} \tag{6.5}$$

$$n_C(r) = -\frac{0.57525}{(25.2004 + r^2)^{3/2}} \tag{6.6}$$

In Figure 6.13 (a), we plot the three-dimensional contour of the total induced surface charge density $n_{ind}(r) = n_{O_1}(r) + n_C(r) + n_{O_2}(r)$. Meanwhile, we also plot the radial distributions of the induced and the total surface charge densities in Figure 6.13 (b). We can see that from this simple point charge model, the induced charge density right below the CO_2 molecule is positive, while the negative charges are also seen around the positive region near the center of the gravity of total induced charge density $n_{ind}(r)$. The positive surface charge density caused by one of the O atoms closest to the surface cancels most negative charges induced by C atom very near z_0. After the integration of equation 6.3, the total induced charge is + 0.00131 e. Therefore, the point charges of O atoms determine the sign of image charge on Pt (111) surface.

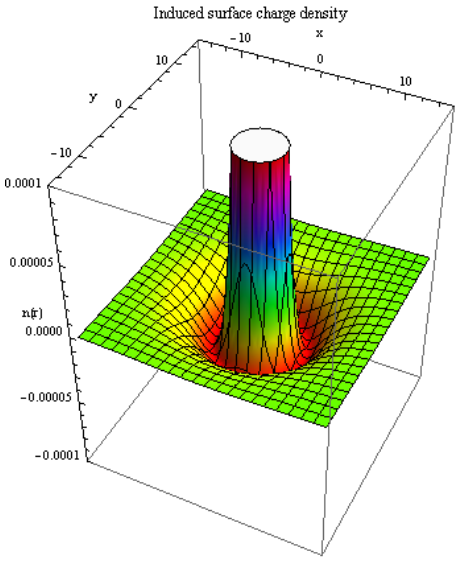

(a)

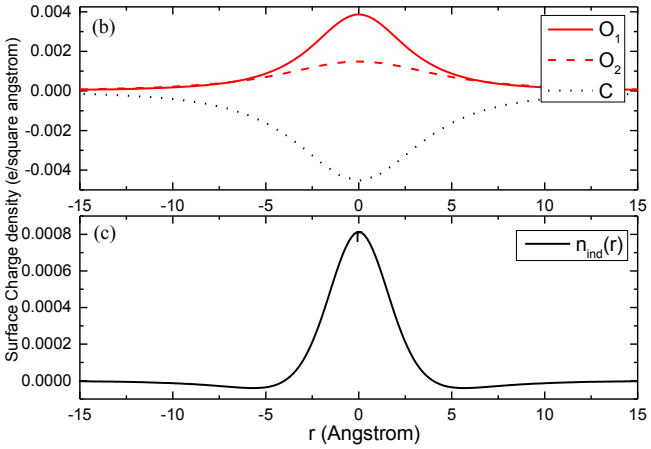

Figure 6.13: The induced surface charge densities in a point charge model of CO_2 molecule on metallic surface. (a): The three-dimensional contour plot of total induced surface charge density; (b) and (c): The radial distributions.

The total electrostatic potential energy between point charges of CO_2 molecule and the metallic surface can be roughly estimated from the following expression

$$U = \frac{e^2}{4\pi\varepsilon_0}\sum_i \frac{q_{ind}q_i}{z_i} \tag{6.7}$$

where the elementary charge is given by $e = 1.60217657 \times 10^{-19}$ coulombs, and the dielectric constant $\varepsilon_0 = 8.8542 \times 10^{-12}$ F/m, z_i is the coordinate of atoms in CO_2 molecule. It is found that the total electrostatic potential energy in the adsorption geometry shown in Figure 6.12 is only -0.00358 kcal/mol. The value is 50 times less negative than the computed value (-0.1932 kcal/mol) for structure I by PBE. Therefore, the simple electrostatic attactions between CO_2 and Pt (111) surface can not explain why PBE binds the system.

In order to go beyond the simple point charge model, the electron density difference maps (EDDM) are calculated for CO_2 physisorbed on Pt (111) surface by PBE and optB88-vdW functionals. EDDM is defined as

$$\rho_{\mathrm{EDDM}}(r) = \rho_{\mathrm{CO_2+Pt(111)}}(r) - (\rho_{\mathrm{CO_2}}(r) + \rho_{\mathrm{Pt(111)}}(r)) \tag{6.8}$$

here the three terms on the right-hand side of equation are the electron densities of combined and the two separated subsystems, respectively. By the definition, the increasing of electron density at r implies the positive sign of $\rho_{\mathrm{EDDM}}(r)$. The change of the electron density in the space of the combined structure is usually due to the interactions between two subsystems. In Figures 6.14 (a) and (b), the three-dimensional contours of EDDM are shown for structure I, computed from PBE and optB88-vdW methods at their equilibrium distances. For a better comparison of EDDM of PBE with optB88-vdW, the EDDM has been recalculated within the former functional at the equilibrium distance of latter one. The new EDDM contour is displayed in Figure 6.14 (c).

From Figure 6.14, it is seen that the valence electron density on Pt (111) surface right below the CO_2 molecule is decreased. The effect is enhanced by decreasing the

disctance between CO_2 and Pt (111) surface. This can be understood from the Pauli exclusive principle between the systems with closed shells.

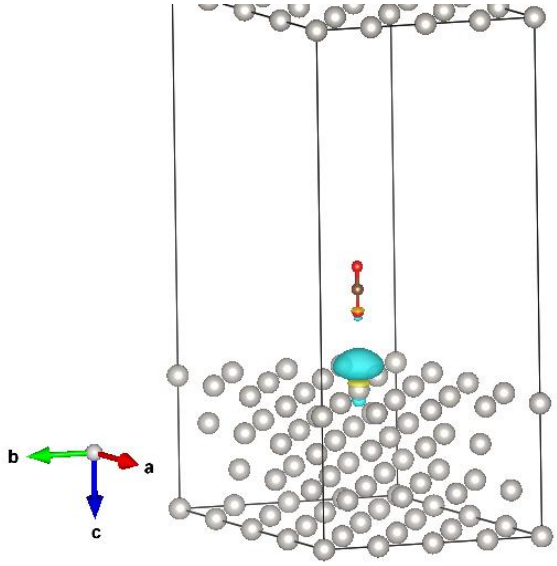

(a)

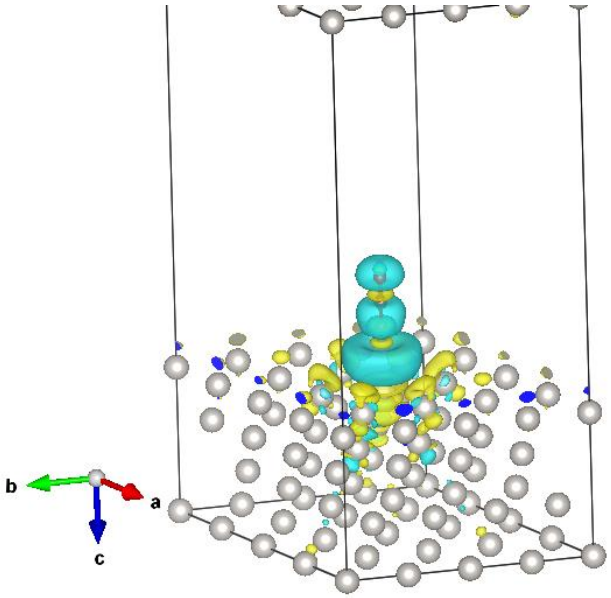

(b)

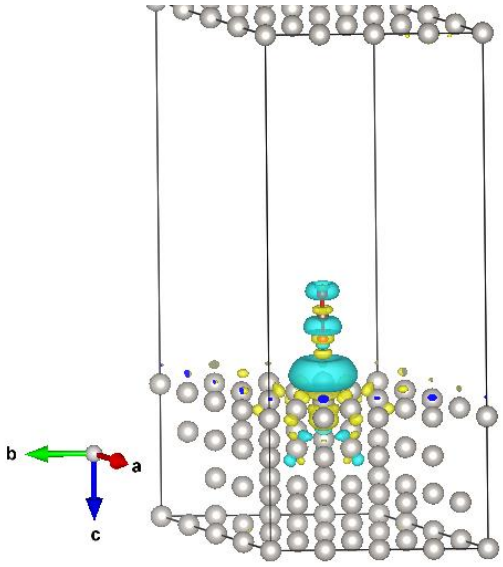

(c)

Figure 6.14: The three-dimensional isovalue contours of EDDM of CO_2 physisorbed on Pt (111) surface. (a): d = 3.85 Å with PBE; (b): d = 3.037 Å with optB88-vdW; (c): d = 3.037 Å with PBE. Note that in all graphs, the cyan color indicates the decrease of electron density, and yellow-blue region refers to the increase of electron density. The magnitude of isovalue contours is 0.0001 e/Å^3.

In the case of PBE, there is the weak redistribution of charge density on CO_2 molecule at the equilibrium distance, which can not be predicted from the simple point charge model. The charges are accumulated on one O atom at the bottom of CO_2 molecule and Pt atom right below it. Therefore, both CO_2 and Pt (111) surface are slightly polarized even in the PBE calculation. At the short distance (See Figures 6.14 (b) and (c)), the CO_2 is significantly polarized due to the redistribution of charge density on it. PBE and optB88-vdW give similar contours. However, for the metallic substrate, the increase of surface charge density in optB88-vdW method is much stronger than in PBE. From Figure 6.14 (b), we find that the electron density is accumulated at the Pt atoms

right below CO_2 molecule and next to it. If the interactions between CO_2 and Pt (111) surface is mainly caused by the induced dipoles of molecule and substrate, then the non-local van der Waals functional (optB88-vdW) indeed can reproduce this mechanism. For semilocal functional like PBE, the induced dipoles on both molecule and metallic substrate are too weak; meanwhile, the repulsion due to the Pauli exclusive principle between them is enhanced and also dominates the computed binding energy at short distance.

For MGGA_MS2, the EDDM is also computed at the equilibrium adsorption distance (~3.40 Å). The 3-D isovalue contours are similar to Figure 6.14 (c) for PBE at short distance. This demonstrates that the polarization of electron density in MGGA_MS2 is stronger than that of PBE at the same adsorption distance. As a result, MGGA_MS2 predicts more negative binding energy and shorter binding distance than PBE does. MGGA_MS2 captures the portion of van der Waals interactions, because of its large α dependence in the exchange enhancement factor. In a meta-GGA, we can use α to distinguish three different types of chemical bond. For van der Waals bound system, we expect to observe $\alpha \gg 1$ and $s \approx 0$ [41-43]. Basically, MGGA_MS2 disfavors the large α region in the computed structure. In the large separation of CO_2 from the Pt (111) surface, α is increased significantly in the region between the two fragments due to the decrease of electron density.

CHAPTER 7

SUMMARY AND CONCLUSIONS

In this dissertation, we have assessed the performances of exchange-correlation functionals of all five rungs on Jacob's ladder on three particular problems: the phase transitions between two polymorphs of a solid, a strongly correlated transition metal oxide, and the physisorption of molecule on metal surface. Each problem represents a challenge for current density functional theory (DFT).

In Chapter 3, we have tested the performance of LSDA, the PBE GGA, and several meta-GGA functionals (TPSS, revTPSS, regTPSS, and MGGA_MS) on the structural properties and phase transition parameters for three different systems, i.e., Si, SiO_2 and Zr. For the structural properties, all tested meta-GGAs are better than the PBE GGA, as expected, but for the phase transition pressures the earlier meta-GGAs are worse than PBE for Si and SiO_2, and only the members of the MGGA_MS family are able to predict realistic values. The quality of the results is sensitive to the details of the exchange functional. At least for the insulator-to-metal transition in Si, the relative performance of various functionals can be understood simply in terms of their plottable exchange enhancement factors. We suggest that further improvements to the meta-GGA will lead to further improvements in the predicted properties of most molecules and solids near equilibrium and under pressure, without sacrificing computational efficiency.

Our results for normal metals (Zr phases) indicate that all semilocal functionals perform more or less similarly for equilibrium lattice constants and bulk modulus. Some

meta-GGA functionals (regTPSS and MGGA_MS) can predict phase transition parameters for Zr in better agreement with experiment than PBE. For this system, the screened hybrid functional HSE06 significantly overestimates phase transition parameters (transition energy and pressure). Although the tested functionals are all more accurate for the metallic Zr phases than for Si or SiO_2, the exceptionally small structural energy and volume differences for Zr still make this system challenging to approximate calculations.

For the transition pressure in general, the approximate exchange-correlation energy functional must predict a small energy difference with a small relative error. That is not so hard when the small energy difference arises from a small change in the electron density, because then we can expect a great error cancellation in the energy difference between similar densities. That explains how even LSDA can predict rather good lattice constants in some cases: There is a small change of density associated with a small expansion or compression of the lattice. But, for the transition pressure, we have to predict a small energy difference arising from a large change of density, and less error cancellation can be expected. Therefore, the calculation of transition pressures for structural phase transitions remains a challenging test of density functionals. The challenge is especially great for silicon dioxide, where the average valence electron density changes so strongly at the transition.

In Chapter 4, we have studied the phase transition parameters of the α-quartz to stishovite and D-Si to β-tin Si phase transformations using non-selfconsistent RPA calculations. The obtained equilibrium lattice volumes of most structures are in good agreement with DMC (or QMC) simulations and experimental results. The calculated phase transition pressure and transition volume of Si are also in excellent agreement with

experimental values. On the other hand, the energy difference between α-quartz and stishovite is underestimated by RPA and thus the corresponding transition pressure is smaller than those of experiment and several other local and nonlocal functionals. While non-selfconsistent RPA seems to work well for the difficult insulator-to-metal transition in Si, selfconsistent and geometry-optimized RPA calculations may be needed for the low-symmetry crystal structures of SiO_2. While non-selfconsistent RPA seems to work well for the difficult insulator-to-metal transition in Si, the RPA error cancellation may be less perfect in SiO_2, as in molecules.

In Chapter 5, we have assessed the performances of many semilocal (LSDA, LSDA+U, GGA and meta-GGAs) and nonlocal (HSE06) density functionals on the ground state energy, electronic structures and magnetic property of strong correlated R-VO_2. Our calculations indicate that none of them gives the correct ground state for this metal oxide. The spurious spin polarized magnetic phases (FM and AFM) are always more stable than spin compensated singlet state. Besides LSDA+U, all semilocal functionals predict R-VO_2 to be a metallic magnetic phase. Meanwhile, LSDA+U and HSE06 give a Mott-Hubbard insulating phase with large local magnetic moments. In addition, the widely tested TPSS and revTPSS functionals give the qualitatively different electronic structures for R-VO_2 to either widely used LSDA and PBE functionals or the recently developed meta-GGA functionals (regTPSS and MGGA_MS family of density functionals).

The non-self-consistent RPA calculations based on PBE inputs slightly improve the stability of spin-singlet nonmagnetic phase of R-VO_2, but it is not sufficient to reverse the wrong results given by PBE calculations. Using PBE inputs, the ground state of R-

VO_2 is found to be a ferromagnetic metal by RPA. Meanwhile, the RPA stabilizes the spin-compensated PM R-VO_2 over FM and AFM states when the inputs are computed from LSDA. For most semilocal functionals, the development of spurious magnetic states (FM or AFM) gives more accurate equilibrium lattice geometry than that of the spin singlet non-magnetic state by the total energy minimization. LSDA and RPA (with PBE inputs) are the two exceptions where in the former case all three computed magnetic states (FM, AFM and spin compensated PM) underestimate equilibrium cell volume with similar percent errors; while in the latter case, the optimized cell volume for a spurious magnetic state is significantly overestimated. For strong correlated R-VO_2, the error cancellation between the extra exchange and less realistic correlation holes in the semilocal functionals is not seen in RPA calculations. For normal solids, RPA is always employed as a benchmark method. Our results for R-VO_2 suggest that the self-consistency is required for a strongly correlated system.

In meta-GGAs, there is a correlation between the predicted magnetic moment and the behavior of exchange enhancement factor. Our calculations for either R-VO_2 or BCC Fe imply that a meta-GGA is capable of giving the accurate local magnetic moment by carefully controlling its exchange enhancement factor ($F_x(s, \alpha)$) in the small s and large α regime. The monotonic decrease of $F_x(s, \alpha)$ with α for small s enhances the exchange energy, resulting in the large local magnetic moment for magnetic phase. Although, the meta-GGAs exhibiting the exchange enhancement factor similar to MGGA_MS variants are less accurate than other tested semilocal functionals for the ground state energy of R-VO_2, they are able to capture a portion of van der Waals interactions in the density

weakly overlapped case due to the same reason as they overestimate the local magnetic moment.

In Chapter 6, we have computed the binding energy curves of CO_2 molecule physisorbed on the Pt (111) surface using PBE, PBE+D2, MGGA_MS2 and optB88-vdW. We are particularly interested in the comparison of binding energy and binding distance predicted by MGGA_MS2 to those of PBE+D2 and optB88-vdW methods. Our results confirmed that MGGA_MS2 captures a portion of van der Waals interactions, and it gives binding distance in good agreement with PBE+D2 and optB88-vdW methods. Although MGGA_MS2 significantly improves the description of physisorption problem among semilocal functionals, the obtained binding energy is usually ~30% of the latter two methods.

We developed a simple point charge model for CO_2 molecule on Pt (111) surface. The binding energy estimated from such model is 50 times less negative than the computed value. Thus, the electrostatic potential energy along can not explain why a semilocal functional like PBE can still bind CO_2 on Pt (111) surface. From the obtained electron density difference maps (EDDM), we discovered that optB88-vdW predicts the strongest electron-density polarizations for both CO_2 and Pt (111) surface. For PBE, such effect is very weak, but it is not completely negligible. At the short distance, the binding energy is dominated by the strong repulsion between electron densities of the two fragments due to the Pauli exclusive principle. The advantage of MGGA_MS2 for weak van der Waals interactions is mainly attributed to its α dependence in the exchange enhancement factor.

The results presented in this dissertation for the new meta-GGA functionals and random phase approximation reveal the great success and failure of current density functional methods on Jacob's ladder. The need for the development of more advanced exchange-correlation functional is ever-growing.

PUBLICATIONS

[1] B. Xiao, J. Sun, A. Ruzsinszky, J. Feng, J.P. Perdew, *Structural phase transition in Si and SiO_2 crystals via the random phase approximation*, Phys. Rev. B. **86**, 094109 (1-6) (2012).

[2] B. Xiao, J. Sun, A, Ruzsinszky, J. Feng, R. Haunschild, G.E. Scuseria, J.P. Perdew, *Testing density functionals for structural phase transitions of solids under pressures: Si, SiO_2, and Zr*, Phys. Rev. B. **88**, 184103 (1-17) (2013).

[3] B. Xiao, J. Sun, A. Ruzsinszky, J.P. Perdew, *Testing the Jacob's ladder of density functionals for the electronic structures and magnetism of rutile-type VO_2*, in preparation (2014).

[4] Y. Fang, B. Xiao, J. Tao, J. Sun, J.P. Perdew, *Ice phases under ambient and high pressure: Insights from density functional theory*, Phys. Rev. B. **87**, 214101 (1-6) (2013).

[5] J. Sun, B. Xiao, Y. Fang, R. Haunschild, P. Hao, A. Ruzsinszky, G.I. Csonka, G.E. Scuseria, J.P. Perdew, *Density functionals that recognize covalent, metallic and weak bonds*, Phys. Rev. Lett. **111**, 106401 (1-5) (2013).

[6] J. Sun, B. Xiao, A. Ruzsinzsky, *Communication: Effect of the orbital-overlap dependence in the meta generalized gradient approximation*, J. Chem. Phys. **137**, 051101 (1-5) (2012).

[7] P. Hao, J. Sun, B. Xiao, A. Ruzsinszky, G.I. Csonka, J. Tao, S. Glindmeyer, J.P. Perdew, *Performance of meta-GGA functionals on general main group thermochemistry, kinetics, and noncovalent interactions*, J. Chem. Theory Comput. **9**, 355-363 (2013).

[8] J. Sun, R. Haunschild, B. Xiao, I.W. Bulik, G.E. Scuseria, J.P. Perdew, *Semilocal and hybrid meta-generalized gradient approximations based on the understanding of the kinetic-energy-density dependence*, J. Chem. Phys. **138**, 044113 (1-9) (2013).

[9] A. Ruzsinszky, J. Sun, B. Xiao, G.I. Csonka, *A meta-GGA made free of the order of limits anomaly*, J. Chem. Theory Comput. **8**, 2078-2087 (2012).

BIBLIOGRAPHY

[1] P. Dirac, *Quantum mechanics of many-electron systems*, Proc. R. Soc. Lond. **A123**, 714-733 (1929).

[2] W. Kohn, *Nobel lecture: Electronic structure of matter-wave functions and density functionals*, Rev. Mod. Phys. **71**, 1253-1266 (1999).

[3] M. Born and J.R. Oppenheimer, *On the quantum theory of molecules*, Annalen der Physik, **389**, 457-484 (1927).

[4] L.H. Thomas, The calculation of atomic fields, Proc. Cambride Phil. Soc. 23, 542-548 (1927).

[5] E. Fermi, *Un metodo statistic per la determinazione di alcune prioprietà dell' atomo*, Rend. Accad. Naz. Lincei. **6**, 602-607 (1927).

[6] R.G. Parr and W. Yang, *Density-Functional Theory of Atoms and Molecules*. New York: Oxford University Press (1989). ISBN 978-0-19-509276-9.

[7] W. Teller, *On the stability of molecules in the Thomas-Fermi theory*, Rev. Mod. Phys. **34**, 627-631 (1962).

[8] P. Csavinszky, *Approximation analytical solutions of the Thomas-Fermi-Dirac and Thomas-Fermi-Dirac-Gombás equations*, J. Chem. Phys. **50**, 2476-2485 (1969).

[9] E. Engel and J.P. Perdew, *Theory of metallic clusters: Asymptotic size dependence of electronic properties*, Phys. Rev. B. **43**, 1331-1337 (1991).

[10] E.H. Lieb, *Density functionals for Coulomb systems, In Physics as Natural Philosophy, Essays in Honor Laszlo Tisza on his 75th Birthday*, (M. Feshbach and A. Shimony eds.). Cambridge: MIT Press, 111-149 (1982).

[11] J.E. Harriman, *Orthonormal orbitals for the representation of an arbitrary density*, Phys. Rev. A. **24**, 680-682 (1981).

[12] P. Hohenberg and W. Kohn, *Inhomogeneous electron gas*, Phys. Rev. **136**, 864-871 (1964).

[13] W. Kohn and L.J. Sham, *Self-consistent equations including exchange and correlation effects*, Phys. Rev. **140**, 1133-1138 (1965).

[14] M. Levy, *Electron densities in search of Hamiltonians*, Phys. Rev. A. **26**, 1200-1208 (1982).

[15] J. Harl, *The linear response function in density functional theory: Optical spectra and improved description of the electron correlation*, Ph.D. thesis, Universität Wien, Austria, 36-37 (2008).

[16] S. Kurth and J.P. Perdew, *Role of the exchange-correlation energy: Nature's glue*, Int. J. Quant. Chem. **77**, 814-818 (2000).

[17] J.P. Perdew and K. Schmidt, *in Density Functional Theory and Its Application to Materials*, (V. Van Doren, C. Van Alsenoy, and P. Geerlings, eds). AIP, Melville, New York (2001).

[18] S.H. Vosko, L. Wilk and M. Nusair, *Accurate spin-dependent electron liquid correlation energies for local spin density calculations: a critical analysis*, Can. J. Phys. **58**, 1200-1211 (1980).

[19] J.P. Perdew and A. Zunger, *Self-interaction correction to density-functional approximation for many-electron systems*, Phys. Rev. B. **23**, 5048-5079 (1981).

[20] L.A. Cole and J.P. Perdew, *Calculated electron affinities of the elements*, Phys. Rev. A. **25**, 1265-1271 (1982).

[21] J.P. Perdew and Y. Wang, *Accurate and simple analytic representation of the electron-gas correlation energy*, Phys. Rev. B. **45**, 13244-13249 (1992).

[22] J.P. Perdew, K. Burke and Y. Wang, *Generalized gradient approximation for the exchange-correlation hole of a many-electron system*, Phys. Rev. B. **54**, 16533-16539 (1996).

[23] S-K. Ma and K.A. Brueckner, *Correlation energy of an electron gas with a slowly varying high density*, Phys. Rev. **165**, 18-31 (1968).

[24] J.P. Perdew, J.A. Chevary, S.H. Vosko, K.A. Jackson, M.R. Pederson, D.J. Singh and C. Fiolhais, *Atoms, molecules, solids and surfaces: Applications of the generalized gradient approximation for exchange and correlation*, Phys. Rev. B. **46**, 6671-6687 (1992).

[25] J.P. Perdew, K. Burke and M. Ernzerhof*, Generalized gradient approximation made simple*, Phys. Rev. Lett. **77**, 3865-3868 (1996).

[26] Y. Zhang and W. Yang, *Comment on "Generalized gradient approximation made simple*", Phys. Rev. Lett. **80**, 890-890 (1998).

[27] B. Hammer, L.B. Hansen and J.K. Nørskov, *Improved adsorption energies with density-functional theory using revised Perdew-Burke-Ernzerhof functionals*, Phys. Rev. B. **59**, 7413-7421 (1999).

[28] R. Armiento and A.E. Mattsson, *Functional designed to include surface effects in self-consistent density functional theory*, Phys. Rev. B. **72**, 085108 (1-5) (2005).

[29] Z. Wu and R.E. Cohen, More accurate generalized gradient approximation for solids, Phys. Rev. B. 73, 235116 (1-6) (2006).

[30] J.P. Perdew, A. Ruzsinszky, G.I. Csonka, O.A. Vydrov, G.E. Scuseria, L.A. Constantin, X. Zhou and K. Burke, *Restoring the density-gradient expansion for exchange in solids and surfaces*, Phys. Rev. Lett. **100**, 136406 (1-4) (2008).

[31] Y. Zhao and D.G. Truhlar, *Construction of a generalized gradient approximation by restoring the density-gradient expansion and enforcing a tight Leib-Oxford bound*, J. Chem. Phys. **129**, 184109 (1-8) (2008).

[32] J.P. Perdew, *Accurate density functional for the energy: Real-space cutoff of the gradient expansion for the exchange hole*, Phys. Rev. Lett. **55**, 1665-1668 (1985).

[33] S.K. Ghosh and R.G. Parr, *Phase-space approach to the exchange-energy functional of density-functional theory*, Phys. Rev. A. **34**, 785-791 (1986).

[34] A.D. Becke and M.R. Roussel, *Exchnage holes in inhomogeneous systems: A coordinate-space model*, Phys. Rev. A. **39**, 3761-3767 (1989).

[35] T. Van Voorhis and G.E. Scuseria, *A novel form for the exchange-correlation energy functional*, J. Chem. Phys. **109**, 400-410 (1998).

[36] J.P. Perdew, S. Kurth, A. Zupan and P. Blaha, *Accurate density functional with correct formal properties: A step beyond the generalized gradient approximation*, Phys. Rev. Lett. **82**, 2544-2547 (1999).

[37] J. Tao, J.P. Perdew, V.N. Staroverov and G.E. Scueria, *Climbing the density functional ladder: Nonempirical meta-generalized gradient approximation designed for molecules and solids*, Phys. Rev. Lett. **91**, 146401 (1-4) (2003).

[38] Y. Zhao and D.G. Truhlar, *A new local density functional for main-group thermochemistry, transition metal bonding, thermochemical kinetics, and noncovalent interactions*, J. Chem. Phys. **125**, 194101 (1-8) (2006).

[39] J.P. Perdew, A. Ruzsinszky, G.I. Csonka, L.A. Constantin and J. Sun, *Workhorse semilocal density functional for condensed matter physics and quantum chemistry*, Phys. Rev. Lett. **103**, 026403 (1-4) (2009).

[40] A. Ruzsinzsky, J. Sun, B. Xiao and G.I. Csonka, *A meta-GGA made free of the order of limits anomaly*, J. Chem. Theory Comput. **8**, 2078-2087 (2012).

[41] J. Sun, B. Xiao and A. Ruzsinszky, *Communication: Effect of the orbital-overlap dependence in the meta generalized gradient approximation*, J. Chem. Phys. **137**, 051101 (1-4) (2012).

[42] J. Sun, R. Haunschild, B. Xiao, I.W. Bulik, G.E. Scuseria and J.P. Perdew, *Semilocal and hybrid meta-generalized gradient approximations based on the understanding of the kinetic-energy-density dependence*, J. Chem. Phys. **138**, 044113 (1-8) (2013).

[43] J. Sun, B. Xiao, Y. Fang, R. Haunschild, P. Hao, A. Ruzsinszky, G.I. Csonka, G.E. Scuseria and J.P. Perdew, *Density functionals that recognize covalent, metallic, and weak bonds*, Phys. Rev. Lett. **111**, 106401 (1-5) (2013).

[44] J.M. del Campo, J.L. Gázquez, S.B. Trickey and A. Vela, *A new meta-GGA exchange functional based on an improved constraint-based GGA*, Chem. Phys. Lett. **543**, 179-183 (2012).

[45] L.A. Constantin, E. Fabiano and F.D. Sala, *Meta-GGA exchange-correlation functional with a balanced treatment of nonlocality*, J. Chem. Theory Comput. **9**, 2256-2263 (2013).

[46] A.D. Becke, *A new mixing of Hartree-Fock and local density-functional theories*, J. Chem. Phys. **98**, 1372-1377 (1993).

[47] Y. Zhao and D.G. Truhlar, *The Mo6 suite of density functionals for main group thermochemistry, thermochemical kinetics, noncovalent interactions, excited states, and transition elements: two new functionals and systematic testing of four Mo6-class functionals and 12 other functionals*, Theor. Chem. Account. **120**, 215-241 (2008).

[48] Y. Zhao and D.G. Truhlar, *Density functional for spectroscopy: No long-range self-interaction error, good performance for Rydbergy and charge-transfer states, and better performance on average than B3LYP for ground states*, J. Phys. Chem. A. **110**, 13126-13130 (2006).

[49] C. Adamo and V. Barone, *Toward reliable density functional methods without adjustable parameters: The PBE0 model*, J. Chem. Phys. **110**, 6158-6170 (1999).

[50] J. Heyd, G.E. Scuseria and M. Ernzerhof, *Hybrid functionals based on a screened Coulomb potential*, J. Chem. Phys. **118**, 8207-8215 (2003).

[51] J. Heyd and G.E. Scuseria, *Efficient hybrid density functional calculations in solids: Assessment of the Heyd-Scuseria-Ernzerhof screened Coulomb hybrid functional*, J. Chem. Phys. **121**, 1187-1192 (2004).

[52] L. Schimka, J. Harl and G. Kresse, *Improved hybrid functional for solids: The HSEsol functional*, J. Chem. Phys. **134**, 024116 (1-11) (2011).

[53] M. Grüning, A. Marini and A. Rubio, *Density functionals from many-body perturbation theory: The band gap for semiconductors and insulators*, J. Chem. Phys. **124**, 154108 (1-9) (2006).

[54] P. García-González, J.J. Fernández, A. Marini and A. Rubio, *Advanced correlation functionals: Application to bulk materials and localized systems*, J. Phys. Chem. A. **111**, 12458-12465 (2007).

[55] J. Harl and G. Kresse, *Cohesive energy curves for noble gas solids calculated by adiabatic connection fluctuation-dissipation theory*, Phys. Rev. B. **77**, 045136 (1-8) (2008).

[56] J. Harl and G. Kresse, *Accurate bulk properties from approximate many-body techniques*, Phys. Rev. Lett. **103**, 056401 (1-4) (2009).

[57] Huy-Viet Nguyen and S. de Gironcoli, *Efficient calculation of exact exchange and RPA correlation energies in the adiabatic-connection-fluctuation-dissipation theory*, Phys. Rev. B. **79**, 205114 (1-12) (2009).

[58] J. Harl, L. Schimka and G. Kresse, *Assessing the quality of random phase approximation for lattice constants and atomization energies of solids*, Phys. Rev. B. **81**, 115216 (1-18) (2010).

[59] A. Ruzsinszky, J.P. Perdew and G.I. Csonka, *The RPA atomization energy puzzle*, J. Chem. Theory Comput. **6**, 127-134 (2010).

[60] L. Schimka, J. Harl, A. Stroppa, A. Grüneis, M. Marsman, F. Mittendorfer and G. Kresse, *Accurate surface and adsorption energies from many-body perturbation theory*, Nature Materials, **9**, 741-744 (2010).

[61] T. Olsen, J. Yan, J.J. Mortensen and K.S. Thygesen, *Dispersive and covalent interactions between graphene and metal surfaces from the random phase approximation*, Phys. Rev. Lett. **107**, 156401 (1-5) (2011).

[62] M. Hellgren, D.R. Rohr and E.K.U. Gross, *Correlation potentials for molecular bond dissociation within the self-consistent random phase approximation*, J. Chem. Phys. **136**, 034106 (1-9) (2012).

[63] F. Mittendorfer, A. Garhofer, J. Redinger, J. Klimeš, J. Harl and G. Kresse, *Graphene on Ni(111): Strong interaction and weak adsorption*, Phys. Rev. B. **84**, 201401 (R) (1-4) (2011).

[64] T. Kotani and H. Akai, *Optimized-effective-potential method with exact exchange and exact RPA correlation-3d metals*, J. Magn. Magn. Mater. **177-181**, 569-570 (1998).

[65] H. Peng and S. Lany, *Polymorphic energy ordering of MgO, ZnO, GaN, and MnO within the random phase approximation*, Phys. Rev. B. **87**, 174113 (1-5) (2013).

[66] L. Schimka, R. Gaudoin, J. Klimeš, M. Marsman and G. Kresse, *Lattice constants and cohesive energies of alkali, alkaline-earth, and transition metals: Random phase approximation and density functional theory resutls*, Phys. Rev. B. **87**, 214102 (1-8) (2013).

[67] D. Ceperley, *Ground state of the fermion one-component plasma: A Monte Carlo study in two and three dimensions*, Phys. Rev. B. **18**, 3126-3138 (1978).

[68] D.M. Ceperley and B.J. Alder, *Ground state of the electron gas by a stochastic method*, Phys. Rev. Lett. **45**, 566-569 (1980).

[69] O. Gunnarsson and B.I. Lundqvist, *Exchange and correlation in atoms, molecules, and solids by the spin-density-functional formalism*, Phys. Rev. B. **13**, 4274-4298 (1976).

[70] J.P. Perdew, A. Ruzsinszky, J. Sun and K. Burke, *Gedanken densities and exact constraints in density functional theory*, J. Chem. Phys. **140**, 18A533 (1-8) (2014).

[71] P.S. Svendsen and U. von Barth, *Gradient expansion of the exchange energy from second-order density response theory*, Phys. Rev. B. **54**, 17402-17413 (1996).

[72] J. Sun, M. Marsman, A. Ruzsinszky, G. Kresse and J.P. Perdew, *Improved lattice constants, surface energies, and CO desorption energies from a semilocal density functional*, Phys. Rev. B. **83**, 121410(R) (1-4) (2011).

[73] V.N. Staroverov, G.E. Scuseria, J. Tao and J.P. Perdew, *Tests of a ladder of density functionals for bulk solids and surfaces*, Phys. Rev. B. **69**, 075102 (1-11) (2004).

[74] G.I. Csonka, J.P. Perdew, A. Ruzsinszky, P.H.T. Philipsen, S. Lebègue, J. Paier, O.A. Vydrov and J.G. Ángyán, *Assessing the performance of recent density functionals for bulk solids*, Phys. Rev. B. **79**, 155107 (1-14) (2009).

[75] J.P. Perdew, A. Ruzsinszky, J. Tao, V.N. Staroverov and G.E. Scuseria, *Prescription for the design and selection of density functional approximations: More constraint satisfaction with fewer fits*, J. Chem. Phys. **123**, 062201 (1-9) (2005)

[76] J.P. Perdew, A. Ruzsinszky, L.A. Constantin, J. Sun and G.I. Csonka, *Some fundamental issues in ground-state density functional theory: A guide for the perplexed*, J. Chem. Theory Comput. **5**, 902-908 (2009). (Invited article for the John P. Perdew special issue).

[77] V.I. Anisimov, J. Zaanen and O.K. Andersen, *Band theory and Mott insualtors: Hubbard U instead of Stoner I*, Phys. Rev. B. **44**, 943-954 (1991).

[78] V.I. Anisimov, I.V. Solovyev, M.A. Korotin, M.T. Czyżyk and G.A. Sawatzky, *Density-functional theory and NiO photoemission spectra*, Phys. Rev. B. **48**, 16929-16934 (1993).

[79] I.V Solovyev, P.H. Dederichs and V.I. Anisimov, *Corrected atomic limit in the local-density approximation and the electronic structure of d imprities in Rb*, Phys. Rev. B. **50**, 16861-16871 (1994).

[80] V.I. Anisimov, F. Aryasetiawan and A.I. Lichtenstein, *First-principles calculations of the electronic structure and spectra of strongly correlated systems: the LDA+U method*, J. Phys.: Condens. Matter. **9**, 767-808 (1997).

[81] A.E. Bocquet, T. Mizokawa, K. Morikawa, A. Fujimori, S.R. Barman, K. Maiti, D.D. Sarma, Y. Tokura and M. Onoda, *Electronic structure of early 3d-transition-metal oxides by analysis of 2p core-level phonemission spectra*, Phys. Rev. B. **53**, 1161-1170 (1996).

[82] N.J. Mosey and E.A. Carter, Ab initio evaluation of Coulomb and exchange parameters for DFT+U calculations, Phys. Rev. B. 76, 155123 (1-13) (2007).

[83] M. Cococcioni and S. de Gironcoli, *Linear response approach to the calculation of the effective interaction parameters in the LDA+U method*, Phys. Rev. B. **71**, 035105 (1-16) (2005).

[84] S. Grimme, *Semiempirical GGA-type density functional constructed with a long-range dispersion correction*, J. Comput. Chem. **27**, 1787-1799 (2006).

[85] S. Grimme, J. Antony, S. Ehrlich and H. Krieg, *A consistent and accurate ab initio parameterization of density functional dispersion correction (DFT-D) for the 94 elements H-Pu*, J. Chem. Phys. **132**, 154104 (1-19) (2010).

[86] J. Klimeš and A. Michaelides, *Perspective: Advances and challenges in treating van der Waals dispersion forces in density functional theory*, J. Chem. Phys. **137**, 120901 (1-12) (2012).

[87] M. Dion, H. Rydberg, E. Schröder, D.C. Langreth and B.I. Lundqvist, *Van der Waals density functional for general geometries*, Phys. Rev. Lett. **92**, 246401 (1-4) (2004).

[88] J. Klimeš, D.R. Bowler and A. Michaelides, *Van der Waals density functionals applied to solids*, Phys. Rev. B. **83** 195131 (1-13) (2011).

[89] T. Thonhauser, V.R. Cooper, S. Li, A. Puzder, P. Hyldgaard and D.C. Langreth, *Van der Waals density functional: Self-consistent potential and the nature of the van der Waals bond*, Phys. Rev. B. **76**, 125112 (1-11) (2007).

[90] O.A. Vydrov and T.V. Voorhis, *Nonlocal van der Waals density functional: This simpler the better*, J. Chem. Phys. **133**, 244103 (1-9) (2010).

[91] D.R. Hamann, *Generalized normal-conserving pseudopotentials*, Phys. Rev. B. **40**, 2980-2987 (1989).

[92] S.G. Louie, S. Froyen and M.L. Cohen, *Nonlinear ionic pseudopotentials in spin-density-functional calculations*, Phys. Rev. B. **26**, 1738-1742 (1982).

[93] G.P. Kerker, *Non-singular atomic pseudopotentials for solid state applications*, J. Phys. C: Solid St. Phys. **13**, L189-94 (1980).

[94] G.B. Bachelet, D.R. Hamann and M. Schlüter, *Pseudopotentials that work: From H to Pu*, Phys. Rev. B. **26**, 4199-4228 (1982).

[95] D. Vanderbilt, *Soft self-consistent pesudopotentials in a generalized eigenvalue formalism*, Phys. Rev. B. **41**, 7892-7895 (1990).

[96] P.E. Blöchl, *Projector augmented-wave method*, Phys. Rev. B. **50**, 17953-17979 (1994).

[97] G. Kresse and D. Joubert, *From ultrasoft pseudopotentials to the projector augmented-wave method*, Phys. Rev. B. **59**, 1758-1775 (1999).

[98] X. Zhang, Z. Li and G. Lu, *A non-self-consistent range-separated time-dependent density functional approach for large-scale simulations*, J. Phys.: Conden Matter. **24**, 205801 (1-8) (2012).

[99] D.R. Hamann, *Generalized gradient theory for silica phase transition*, Phys. Rev. Lett. **76**, 660-663 (1996).

[100] K.J. Chang and M.L. Cohen, *Solid-solid phase transitions and soft phonon modes in highly condensed Si*, Phys. Rev. B. **31**, 7819-7826 (1985).

[101] J.Z. Hu, L.D. Merkle, C.S. Menoni and I.L. Spain, *Crystal data for high-pressure phases of silicon*, Phys. Rev. B. **34**, 4679-4684 (1986).

[102] S.A. Ostanin and V. Yu. Trubitsin, *Calculation of the P-T phase diagram of Zr in different approximations for the exchange-correlation energy*, Phys. Rev. B. **57**, 13485-13491 (1998).

[103] Y.J. Hao, L. Zhang, X.R. Chen, Y.H. Li and H.L. He, *Phase transition and elastic constants of zirconium from first-principles calculations*, J. Phys.: Condens. Matter. **20**, 235230 (1-5) (2008).

[104] C. Cazorla, D. Alfè and M.J. Gillian, *Zero-temperature generalized phase diagram of the 4d transition metals under pressure*, Phys. Rev. B. **77**, 224103 (1-11) (2008).

[105] H. Xia, S.J. Duclos, A.L. Ruoff and Y.K. Vohra, *New high-pressure phase transition in Zirconium metal*, Phys. Rev. Lett. **64**, 204-207 (1990).

[106] H.J. Monkhorst and J.D. Pack, *Special points for Brillouin-zone integrations*, Phys. Rev. B. **13**, 5188-5192 (1976).

[107] M. Shishkin and G. Kresse, *Implementation and performance of the frequency-dependent GW method within the PAW framework*, Phys. Rev. B. **74**, 035101 (1-13) (2006).

[108] S.J. Clark, M.D. Segall, C.J. Pickard, P.J. Hasnip, M.I.J. Probert, K. Refson and M.C. Payne, *First principles methods using CASTEP*, Z. Kristallogr. **220**, 567-570 (2005).

[109] M.D. Segall, P.J.D. Lindan, M.J. Probert, C.J. Pickard, P.J. Hasnip, S.J. Clark and M.C. Payne, *First-principles simulation: ideals, illustrations and the CASTEP code*, J. Phys.: Condens. Matter. **14**, 2717-2744 (2002).

[110] R. Maezono, N.D. Drummond, A. Ma and R.J. Needs, *Diamond to β-tin phase transition in Si within diffusion quantum Monte Carlo*, Phys. Rev. B. **82**, 184108 (1-7) (2010).

[111] R.G. Hennig, A. Wadehra, K.P. Driver, W.D. Parker, C.J. Umrigar and J.W. Wilkins, *Phase transformation in Si from semiconducting diamond to metallic β-Sn phase in QMC and DFT under hydrostatic and anisotropic stress*, Phys. Rev. B. **82**, 014101 (1-9) (2010).

[112] A. Zupan, P. Blaha, K. Schwarz and J.P. Perdew, *Pressure-induced phase transitions in solid Si, SiO_2, and Fe: Performance of local-spin-density and generalized-gradient-apprximation density functionals*, Phys. Rev. B. **58**, 11266-11272 (1998).

[113] E.R. Batista, J. Hyed, R.G. Hennig, B.P. Uberuaga, R.L. Martin, G.E. Scuseira, C.J. Umrigar and J.W. Wilkins, *Comparison of screened hybrid density functional theory to diffusion Monte Carlo in calculations of total energies of silicon phases and defects*, Phys. Rev. B. **74**, 121102 (R) (1-4) (2006).

[114] K. Gaal-Nagy, A. Bauer, M. Schmitt, K. Karch, P. Pavone and D. Strauch, *Temperature and dynamical effects on the high-pressure cubic-diamond ↔ β-tin phase transition in Si and Ge*, Phys. Stat. Sol. (b) **211**, 275-280 (1999).

[115] L.G. Liu, *Bulk moduli of SiO_2 polymorphs: Quartz, coesite and stishovite, Mech. Mater*. **14**, 283-290 (1992).

[116] H. D'Amour, W. Denner and H. Schulz, *Structure determination of α-Quartz up to 68×10^8 Pa*, Acta. Crystallogr., Sect. B: Struct. Crystallogr. Cryst. Chem. **B35**, 550-555 (1979).

[117] B.B. Karki, M.C. Warren, L. Stixrude, G.J. Ackland and J. Crain, *Ab-initio studies of high-pressure structural phase transformations in silica*, Phys. Rev. B. **55**, 3465-3471 (1997).

[118] J. Paier, M. Marsman, K. Hummer, G. Kresse, I.C. Gerber and J.G. Ángyán, *Screened hybrid density functionals applied to solids*, J. Chem. Phys. **124**, 154709 (2006).

[119] J.S. Weaver, D.W. Chipman and T. Takahashi, *Comparison between thermochemical and phase stability data for the quartz-coesite-stishovite transformations*, Am. Mineral. **64**, 604-614 (1979).

[120] K.P. Driver, R.E. Cohen, Z. Wu, B. Militzer, P. López Ríos, M.D. Towler, R.J. Needs and J.W. Wilkins, *Quantum Monte Carlo computations of phase stability, equations of state, and elasticity of high-pressure silica*, Proc. Ncad. Sci. USA. **107**, 9519-9524 (2010).

[121] J.C. Boettger, *New model for the shock-induced α-quartz → stishovite phase transition*, J. Appl. Phys. **72**, 5500-5508 (1992).

[122] C.W. Greeff, *Phase changes and the equation of state of Zr*, Modelling Simul. Mater. Sci. Eng. **13**, 1015-1028 (2005).

[123] Q. Chen and B. Sundman, *Calculation of debye temperature for crystalline structures—a case study on Ti, Zr and Hf*, Acta. Mater. **49**, 947-961 (2001).

[124] S.L. Shang, A. Saengdeejing, Z.G. Mei, D.E. Kim, H. Zhang, S. Ganeshan, Y. Wang and Z.K. Liu, *First-principles calculations of pure elements: Equations of state and elastic stiffness constants*, Comput. Mater. Sci. **48**, 813-826 (2010).

[125] Y. Zhao, J. Zhang, C. Pantea, J. Qian, L.L. Daemen, P.A. Rigg, R.S. Hixson, G.T. Gray, Y. Yang, L. Wang, Y. Wang and T. Uchida, *Thermal equations of state of the α, β, and ω phases of zirconium*, Phys. Rev. B. **71**, 184119 (1-6) (2005).

[126] I. Schnell and R.C. Albers, *Zirconium under pressure: phase transitions and thermodynamics*, J. Phys.: Condens. Matter. **18**, 1483-1494 (2006).

[127] K.D. Joshi, G. Jyoti, S.C. Gupta and S.K. Sikka, *Some aspects of pressure-induced $\omega \rightarrow \beta$ transformation in group IVB elements,* J. Phys.: Condens. Matter. **14**, 10921-10925 (2002).

[128] J.P. Perdew, R.G. Parr, M. Levy and Jose L. Balduz, *Density-functional theory for fractional particle number: Derivative discontinuities of the energy*, Phys. Rev. Lett. **49**, 1691-1694 (1982).

[129] C.C. Wang, J.V. James and J. Xia, *Line broadening in multiphoton processes with a resonant intermediate transition*, Phys. Rev. Lett. **51**, 184-187 (1983).

[130] G. Kresse, M. Marsman, L.E. Hintsche and E. Flage-Larsen, *Optical and electronic properties of Si_3N_4 and α-SiO_2*, Phys. Rev. B. **85**, 045205 (1-7) (2012).

[131] R.B. Laughlin, *Optical absorption edge of SiO_2*, Phys. Rev. B. **22**, 3021-3029 (1980).

[132] G. Wiech, *X-ray spectroscopic investigation of the electronic structure of α-quartz and stishovite (SiO_2)*, Solid State Commun. **52**, 807-809 (1984).

[133] A.N. Trukhin, T.I. Dyuzheva, L.M. Lityagina and N.A. Bendelinai, *Intrinsic absorption threshold of stishovite and coesite*, Solid State Commun. **131**, 1-5 (2004).

[134] Y. Fang, B. Xiao, J. Tao, J. Sun and J.P. Perdew, *Ice phases under ambient and high pressure: Insights from density functional theory*, Phys. Rev. B. **87**, 214101 (1-6) (2013).

[135] D. Li, G.M. Bancroft, M. Kasrai, M.E. Fleet, R.A. Secco, X.H. Feng, K.H. Tan and B.X. Yang, *X-ray absorption spectroscopy of silicon dioxide (SiO_2) polymorphs: the structural characterization of opal*, Am. Mineral. **79**, 622-632 (1994).

[136] T.M. Henderson, J. Paier and G.E. Scuseria, *Accurate treatment of solids with the HSE screen hybrid*, Phys. Status Solidi B. **248**, 767-774 (2011).

[137] M.J. Lucero, T.M. Henderson and G.E. Scuseria, *Improved semiconductor lattice parameters and band gaps from a middle-range screened hybrid exchange functional*, J. Phys.: Condens. Matter. **24**, 145504 (1-11) (2012).

[138] X. Wen, R.L. Martin, T.M. Henderson and G.E. Scuseria, *Density functional theory studies of the electronic structure of solid state actinide oxides*, Chem. Rev. **113**, 1063-1096 (2013).

[139] J.P. Perdew and M Levy, *Physical content of the exact Kohn-Sham orbital energies: Band gaps and derivative discontinuities*, Phys. Rev. Lett. **51**, 1884-1887 (1983).

[140] A.J. Cohen, P. Mori-Sánchez and W. Yang, *Insights into current limitations of density functional theory*, **321**, 792-794 (2008).

[141] A. Ruzsinszky, J.P. Perdew and G.I. Csonka, *A simple but fully nonlocal correction to the random phase approximation*, J. Chem. Phys. **134**, 114110 (1-6) (2011).

[142] F. Furche, *Molecular tests of the random phase approximation to the exchange-correlation energy functional*, Phys. Rev. B. **64**, 195120 (1-8) (2001).

[143] V. Eyert, *The metal-insulator transitions of VO_2: A band theoretical approach,* Ann. Phys. (Leipzig), **11**, 1-61 (2002).

[144] G. Anderson, *Studies on vanadium oxides. II. The crystal structure of vanadium dioxide*, Acta. Chem. Scand. **10**, 623-628 (1956).

[145] J.M. Longo and P. Kierkegarrd, *A refinement of the structure of VO_2*, Acta. Chem. Scand. **24**, 420-426 (1970).

[146] M. Marezio, D.B. McWhan, J.P. Remeika and P.D. Dernier, *Structural aspects of the metal-insulator transitions in Cr-doped VO_2*, Phys. Rev. B. **5**, 2541-2551 (1972).

[147] M.A. Korotin, N.A. Skorikov and V.I. Anisimov, *Variation of orbital symmetry of the localized $3d^1$ electron of the V^{4+} ion upon the metal-insulator transition in VO_2*, Phys. of Metals and Metallography (USSR). **94**, 17-23 (2002).

[148] V. Eyert, *VO_2: A novel view from band theory*, Phys. Rev. Lett. **107**, 016401 (1-4) (2011).

[149] F. Gervais and W. Kress, *Lattice dynamics of oxides with rutile structure and instabilities at the metal-semiconductor phase transition of NbO_2 and VO_2*, Phys. Rev. B. **31**, 4809-4814 (1985).

[150] J.B. Goodenough, *The two components of the crystallographic transition in VO_2*, J. Solid. State. Chem. **3**, 490-500 (1971).

[151] K. Okazaki, A. Fujimori and M. Onoda, *Temperature-dependent electronic structure of VO_2 in the insulating phase*, J. Phys. Soc. Jpn. **71**, 822-825 (2002).

[152] A. Cavalleri, Th. Dekorsy, H.H.W. Chong, J.C. Kieffer and R.W. Schoenlein, *Evidence for a structurally-driven insulator-to-metal transition in VO_2: A view from the ultrafast timescale*, Phys. Rev. B. **70**, 161102® (1-4) (2004).

[153] Y. Muraoka, Y. Ueda and Z. Hiroi, *Large modification of metal-insulator transition temperature in strained VO_2 films grown on TiO_2 substrates*, J. Phys. Chem. Solids. **63**, 965-967 (2002).

[154] M.W. Haverkort, Z. Hu, A. Tanaka, W. Reichelt, S.V. Streltsov, M.A. Korotin, V.I. Anisimov, H.H. Hsieh, H.-J. Lin, C.T. Chen, D.I. Khomskii and L.H. Tjeng, *Orbital-assisted metal-insulator transiton in VO_2*, Phys. Rev. Lett. **95**, 196404 (1-4) (2005).

[155] R. Grau-Crepo, H. Wang and U. Schwingenschlögl, *Mind the gap but also the spin: why the Heyd-Scuseria-Ernzerhof hybrid functional description of VO_2 phases is not correct*, arXiv: 1207.5624 (2012).

[156] S.L. Dudarev, G.A. Botton, S.Y. Savrasov, C.J. Humphreys and A.P. Sutton, *Electron-energy-loss spectra and the structural stability of nickel oxide: An LSDA+U study*, Phys. Rev. B. **57**, 1505-1509 (1998).

[157] S. Biermann, A. Poteryaev, A.I. Lichtenstein and A. Georges, *Dynamical singlets and correlation-assisted Peierls transition in VO_2*, Phys. Rev. Lett. **94**, 026404 (1-4) (2005).

[158] M.E. Williams, W.H. Butler, C.K. Mewes, H. Sims, M. Chshiev and S.K. Sarker, *Calculated electronic and magnetic structure of rutile phase $V_{1-x}Cr_xO_2$*, J. Appl. Phys. **105**, 07E510 (1-3) (2009).

[159] J. Sun, M. Marsman, G. Csonka, A. Ruzsinszky, P. Hao, Y.S. Kim, G. Kresse and J.P. Perdew, *Self-consistent meta-generalized gradient approximation within the projector-augmented-wave method*, Phys. Rev. B. **84**, 035117 (1-12) (2011).

[160] T. Kotani, *An optimized-effective-potential method for solids with exact exchange and random-phase approximation correlation*, J. Phys.: Condens. Matter. **10**, 9214-9261 (1998).

[161] P.I. Sorantin and K. Schwarz, *Chemical bonding in Rutile-type compounds*, Inorg. Chem. **31**, 567-576 (1992).

[162] C. Janiak and J.K. Vieth, *MOFs, MILs and more: concepts, properties and applications for porous coordination networks (PCNs)*, New J. Chem. **34**, 2366-2388 (2010).

[163] W. Morris, B. Leung, H. Furukawa, O.K. Yaghi, N. He, H. Hayashi, Y. Houndonougbo, M. Asta, B.B. Laird and O.M. Yaghi, *A combined experimental-computational investigation of carbon dioxide capture in a series of isoreticular zeolitic imidazolate framworks*, J. Am. Chem. Soc. **132**, 11006-11008 (2010).

[164] Stephen S.-Y. Chui, Samuel M.-F. Lo, Jonathan P.H. Charmant, A.G. Orpen and I.D. Williams, *A chemically functionalizable nanoporous material* $[Cu_3(TMA)_2(H_2O)_3]_n$, Science. **283**, 1148-1150 (1999).

[165] R. Poloni, B. Smit and J.B. Neaton, *CO_2 capture by metal-organic frameworks with van der Waals density functionals*, J. Phys. Chem. A. **116**, 4957-4964 (2012).

[166] M.K. Rana, H.S. Koh, J. Hwang and D.J. Siegel, *Comapring van der Waals density functionals for CO_2 adsorption in metal-organic frameworks*, J. Phys. Chem. C. **116**, 16957-16968 (2012).

[167] H.-J. Freund and M.W. Roberts, *Surface chemistry of carbon dioxide*, Surf. Sci. Rep. **25**, 225-273 (1996).

[168] M.W. Abee, *Interaction of acid/base probe molecules with specific features on well-defined metal oxide single-crystal surfaces*, Ph.D. thesis, Virginia Polytechnic Institute and State University, United States, 61-90 (2001).

[169] W. Liu, V.G. Ruiz, G. Zhang, B. Santra, X. Ren, M. Scheffler and A. Tkatchenko, *Structure and energetics of benzene adsorbed on transition-metal surfaces: density-functional theory with van der Waals interactions including collective substrate response*, New J. Phys. **15**, 053046 (1-25) (2013).

[170] G. Maurin, P.L. Liewellyn and R.G. Bell, *Adsorption mechanism of carbon dioxide in faujasites: grand canonical monte carlo simulations and microcalorimetry measurements*, J. Phys. Chem B. **109**, 16084-16091 (2005).

[171] M.W. Finnis, R. Kaschner and C. Kruse, J. Furthmüller, M. Scheffler, *The interaction of a point charge with a metal surface: theory and calculations for (111), (100) and (110) aluminium surfaces*, J. Phys.: Condens. Matter. **7**, 2001-2019 (1995).